

AD-A186 799

DTIC FILE COPY

2

Bulletin 51
(Part 2 of 3 Parts)

THE SHOCK AND VIBRATION BULLETIN

Part 2
Environmental Testing,
Shock Testing, Shock Analysis

MAY 1981

DTIC
ELECTE
NOV 19 1987
S D
C&D

A Publication of
THE SHOCK AND VIBRATION
INFORMATION CENTER
Naval Research Laboratory, Washington, D.C.



Office of
The Under Secretary of Defense
for Research and Engineering

Approved for public release; distribution unlimited

87 10 28 007

SYMPOSIUM MANAGEMENT

THE SHOCK AND VIBRATION INFORMATION CENTER

Henry C. Pusey, Director

Rudolph H. Volin

J. Gordan Showalter

Carol Healey

Elizabeth A. McLaughlin

Bulletin Production

**Publications Branch, Technical Information Division,
Naval Research Laboratory**

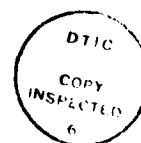
Bulletin 51
(Part 2 of 3 Parts)

THE SHOCK AND VIBRATION BULLETIN

MAY 1981

**A Publication of
THE SHOCK AND VIBRATION
INFORMATION CENTER
Naval Research Laboratory, Washington, D.C.**

The 51st Symposium on Shock and Vibration was held at the Holiday Inn at the Embarcadero, San Diego, CA on October 21-23, 1980. The Naval Ocean Systems Center, San Diego CA was the Host.



**Office of
The Under Secretary of Defense
for Research and Engineering**

Accession For	
NTIS CRA&I	<input checked="" type="checkbox"/>
DTIC TAB	<input type="checkbox"/>
Unannounced	<input type="checkbox"/>
Justification	
By	
Distribution	
Availability Codes	
DTIC	DTIC
A-1	

CONTENTS

PAPERS APPEARING IN PART 2

Environmental Testing

OPTIMIZING PRE AND POST PULSES FOR SHAKER SHOCK TESTING ; R. T. Fandrich, Harris Corporation, Melbourne, FL	1
SHOCK, VIBRATION AND FATIGUE IN TRANSPORTATION INDUSTRIES ; T. V. Seshadri, Fruehauf Corporation, Detroit, MI	15
RANDOM IMPACT VIBRATION TESTOR ; W. D. Everett, Pacific Missile Test Center, Point Mugu, CA	23
PARAMETERS FOR DESIGN OF REVERBERANT ACOUSTIC CHAMBERS FOR TESTING AIR-CARRIED MISSILES ; T. W. Elliott, Pacific Missile Test Center, Point Mugu, CA	31
SPACECRAFT MODAL TESTING USING SYSTEMATIC MULTI-SHAKERS SINE-DWELL TESTING TECHNIQUES ; F. H. Chu, C. Voohees, W. W. Metzger and R. Wilding, RCA Astro-Electronics, Princeton, NJ	41
DEVELOPMENT OF A MULTIAXIAL FORCE-PULSE GENERATOR ; R. D. Crowson, U.S. Army Waterways Experiment Station, Vicksburg, MS, F. B. Safford, Agabian Associates, El Segundo, CA, W. J. Schuman, Jr., U.S. Army Ballistic Research Laboratory, Aberdeen Proving Ground, MD and R. Frieberg, U.S. Army Electronic Research and Development Command, Fort Monmouth, NJ	59
VIBRATION QUALIFICATION OF EQUIPMENT MOUNTED IN TURBOPROP AIRCRAFT ; L. G. Smith, Hughes Aircraft Company, Fullerton, CA	69
"QUICK LOOK" ASSESSMENT AND COMPARISON OF VIBRATION SPECIFICATIONS ; J. H. Schmidt, The Marquardt Company, Van Nuys, CA	73
VIBRATION TEST LEVEL CRITERIA FOR AIRCRAFT EQUIPMENT ; P. S. Hall, Flight Dynamics Laboratory, Air Force Wright Aeronautical Laboratories, Wright-Patterson AFB, OH	81
CONSERVATISM IN LEAST FAVORABLE RESPONSE ANALYSIS AND TESTING ; T. L. Paez, The University of New Mexico, Albuquerque, NM	93

Shock Testing

CALCULATING RESPONSES IN HULL MOUNTED ITEMS OF EQUIPMENT IN SUBMARINES COMPARED WITH MEASUREMENTS CARRIED OUT DURING SHOCK TESTS ; K. Hellqvist, Kockums AB, Malmo Sweden	111
A COMPUTER-CONTROLLED MEASURING SYSTEM HAVING 128 ANALOG MEASURING CHANNELS AND FACILITIES FOR SIGNAL ANALYSIS ; K. Hellqvist, Kockums AB, Malmo, Sweden	121
A LARGE-SCALE SUBMARINE SHOCK TEST CARRIED OUT AS PART OF THE SWEDISH SHOCK DESIGN DEVELOPMENT PROGRAM ; K. Hellqvist, Kockums AB, Malmo, Sweden	129
EDES, AN ELECTROMAGNETICALLY-DRIVEN EXPLOSIVE-SHOCK SIMULATOR ; F. J. Szama and J. B. Whitt, Naval Surface Weapons Center, White Oak, Silver Spring, MD	137
ANALYSIS OF ENERGY-ABSORBING SHOCK MOUNTS ; V. H. Neubert, The Pennsylvania State University, University Park, PA	149
ANALYSIS OF THE EFFECTS OF EXPLOSIVE FUEL IGNITION ON A AIRCRAFT NOISE SUPPRESSION SYSTEM ; V. R. Miller, E. R. Hotz and D. L. Brown, Flight Dynamics Laboratory, Wright-Patterson AFB, OH	169

FEASIBILITY STUDY FOR THE SURFACE IMPULSE LOADING OF STRUCTURES USING MILD DETONATING FUZE	177
D. L. Shirey and F. H. Mathews, Sandia National Laboratories, Albuquerque, NM	

A THEORY FOR THE CALCULATION OF EXPLOSIVE DEPOSITION PROFILES FROM THE SPRAY PAINTING OF LIGHT INITIATED EXPLOSIVE	189
F. H. Mathews, Sandia National Laboratories, Albuquerque, NM	

Shock Analysis

THE RESPONSE SPECTRUM METHOD OF SOLUTION FOR DISPLACEMENT EXCITATION	205
F. C. Nelson, College of Engineering, Tufts University, Medford, MA	

AN IMPROVED RECURSIVE FORMULA FOR CALCULATING SHOCK RESPONSE SPECTRA	211
D. O. Smallwood, Sandia National Laboratories, Albuquerque, NM	

A FINITE ELEMENT MODEL FOR FAILURE INITIATION IN SHOCK LOADED STRUCTURAL MATERIALS	219
D. W. Nicholson, Naval Surface Weapons Center, White Oak, Silver Spring, MD	

STUDY OF PENETRATION FORCES FOR SUPERSONIC WARHEAD DESIGNS	227
R. Hassett, J. C. S. Yang, J. Richardson and H. Walpert, Naval Surface Weapons Center, Silver Spring, MD	

PAPERS APPEARING IN PART 1

Keynote Address

KEYNOTE ADDRESS

Mr. James E. Colvard, Naval Material Command, Washington, DC

Invited Papers

AN APPROACH TO THE LIMITATION AND CONTROL OF SHIPBOARD VIBRATION
Edward F. Noonan, NKF Engineering Associates, Inc., Vienna, VA

STATE-OF-THE-ART ASSESSMENT OF MOBILITY MEASUREMENTS — A SUMMARY OF EUROPEAN RESULTS
David J. Ewins, Imperial College of London, London, England

DEPARTMENT OF DEFENSE POLICY ON RELIABILITY AND MAINTAINABILITY
Colonel Ben H. Swett, USAF Director of Engineering and Standardization, Defense Industrial Supply Center, Philadelphia, PA

NECESSARY AND SUFFICIENT QUALIFICATION FOR SHOCK
Robert Dyrdaht, The Boeing Company, Seattle, WA

MYTHS AND SACRED COWS IN SHOCK AND VIBRATION
Henry Caruso, Westinghouse Electric Corporation, Baltimore, MD

Damping

ON MODELING VISCOELASTIC BEHAVIOR
L.C. Rogers, Flight Dynamics Laboratory, AFWAL/FIBA, Wright-Patterson AFB, OH

FINITE ELEMENT PREDICTION OF DAMPING IN BEAMS WITH CONSTRAINED VISCOELASTIC LAYERS
C. D. Johnson, D. A. Keinholz, Anamet Laboratories, Inc., San Carlos, CA and
L. C. Rogers, Air Force Wright Aeronautical Laboratories, Flight Dynamics Laboratory, WPAFB, OH

DYNAMIC BEHAVIOR OF LATHE SPINDLES WITH ELASTIC SUPPORTS INCLUDING DAMPING BY FINITE ELEMENT ANALYSIS
A. M. Sharan, T. S. Sankar and S. Sankar, Department of Mechanical Engineering, Concordia University, Montreal, Canada

FINITE ELEMENT ANALYSIS OF VISCOELASTICALLY DAMPED SANDWICH STRUCTURES

M. L. Soni, University of Dayton Research Institute, Dayton, OH

PNEUMATIC VIBRATION CONTROL USING ACTIVE FORCE GENERATORS

S. Sankar and R. R. Guntur, Department of Mechanical Engineering, Concordia University, Montreal, Canada

THE EXPERIMENTAL PERFORMANCE OF AN "ON-OFF" ACTIVE DAMPER

E. J. Krahnicki, Lord Kinematics, Erie, PA

Fluid-Structure Interaction

AN EVALUATION OF: DOUBLE ASYMPTOTIC APPROXIMATION; STAGGERED SOLUTION SCHEMES; USA-STAGS

R. S. Dunham, R. J. James, A. S. Kushner and D. E. Ranta, Pacifica Technology, San Diego, CA

MEDIA-STRUCTURE INTERACTION COMPUTATIONS EMPLOYING FREQUENCY DEPENDENT MESH SIZES WITH THE FINITE ELEMENT METHOD

A. J. Kalinowski and C. W. Nebelung, Naval Underwater Systems Center, New London, CT

SIMILITUDE ANALYSIS AND TESTING OF PROTOTYPE AND 1:13.8 SCALE MODEL OF AN OFFSHORE PLATFORM

C. S. Li, National Taiwan University, Taipei and C. S. Yang, N. G. Dagalakis, W. Messick, University of Maryland, College Park, MD

SOUND PROPAGATION THROUGH LIQUIDS IN VISCOELASTIC CIRCULAR CYLINDERS

R. A. Skop, Naval Research Laboratory, Washington, DC

PAPERS APPEARING IN PART 3

Analytical Methods

AN IMPROVEMENT TO SHAIKH'S METHOD FOR THE TORSIONAL VIBRATION ANALYSIS OF BRANCHED SYSTEMS

B. Dawson, Polytechnic of Central London, London, England and M. Davies, University of Surrey, Surrey, England

STUDY OF GUYAN REDUCTION OF TWO DEGREE OF FREEDOM SYSTEMS

F. H. Wolff, A. J. Molnar, Westinghouse R&D Center, Pittsburgh, PA and J. A. Gribik, Basic Technology, Inc., Pittsburgh, PA

A METHOD FOR ESTIMATING THE ERROR INDUCED BY THE GUYAN REDUCTION

G. L. Fox, NKF Engineering Associates, Inc., Vienna, VA

CRITICAL SPEEDS OF MULTI-THROW CRANKSHAFTS USING SPATIAL LINE ELEMENT METHOD

C. Bagci, Department of Mechanical Engineering, Tennessee Technological University, Cookeville, TN and D. R. Falconer, Duriron Valve Division, Cookeville, TN

Dynamic Analysis

A PARAMETRIC STUDY OF THE IBRAHIM TIME DOMAIN MODAL IDENTIFICATION ALGORITHM

R. S. Pappa, NASA Langley Research Center, Hampton, VA and S. R. Ibrahim, Old Dominion University, Norfolk, VA

EFFECTIVE DYNAMIC REANALYSIS OF LARGE STRUCTURES

B. P. Wang, University of Virginia, Charlottesville, VA and F. H. Chu, RCA/ASTRO, Princeton, NJ

EFFECT OF STIFFENER ARRANGEMENT ON THE RANDOM RESPONSE OF A FLAT PANEL

R. B. Bhat and T. S. Sankar, Department of Mechanical Engineering, Concordia University, Montreal, Quebec, Canada

ON NONLINEAR RESPONSE OF MULTIPLE BLADE SYSTEMS

A. Muszynska, University of Dayton Research Institute, Dayton, OH, D. I. G. Jones and T. Lagness, Air Force Wright Aeronautical Laboratories, Wright-Patterson AFB, OH and L. Whitford, Aeronautical Systems Division Computer Center, Wright-Patterson AFB, OH

**VIBRATIONS OF A BEAM UNDER MOVING LOADS BY A FINITE ELEMENT FORMULATION
CONSISTENT IN THE TIME AND SPATIAL COORDINATES**

J. J. Wu, U.S. Army Armament Research and Development Command, Benet Weapons Laboratory, Watervliet, NY

THE BEND-BUCKLING OF A RING-STIFFENED CYLINDRICAL SHELL DUE TO WHIPPING EXCITATIONS

K. A. Bannister, Naval Surface Weapons Center, White Oak, Silver Spring, MD

RESPONSE OF HYDROFOIL STRUT-FOIL SYSTEMS AFTER IMPACT WITH "DEAD-HEAD" LOGS

H. S. Levine, Weidlinger Associates, Menlo Park, CA and A. P. Misovec, Weidlinger Associates, Chesapeake, VA

TRANSIENT RESPONSE ANALYSIS OF A LARGE RADAR ANTENNA

E. Meller, W. A. Loden, Lockheed Palo Alto Research Laboratory, Palo Alto, CA and
W. Woltornist, Lockheed Electronics Company, Inc., Plainfield, NJ

**FATIGUE LIFE PREDICTION FOR SIMULTANEOUS STRESS AND STRENGTH VARIANCES UNDER
RANDOM VIBRATION**

R. G. Lambert, General Electric Company, Aircraft Equipment Division, Utica, NY

DYNAMIC RESPONSE OF THE PROGRESSIVELY DAMAGING STRUCTURES

M. G. Srinivasan, Argonne National Laboratory, Argonne, IL and G. U. Fonseka and
D. Krajcinovic, University of Illinois at Chicago Circle, Chicago, IL

Vehicle Systems

LATERAL DYNAMICS OF C4 MISSILE

F. H. Wolff, Westinghouse R&D Center, Pittsburgh, PA

ANALYSIS OF SUBCRITICAL RESPONSE MEASUREMENTS FROM AIRCRAFT FLUTTER TESTS

J. C. Copley, Royal Aircraft Establishment, Farnborough, Hampshire, England

**AIRCRAFT RESPONSE TO OPERATIONS ON RAPIDLY REPAIRED BATTLE DAMAGED RUNWAYS
AND TAXIWAYS**

T. Gerardi, Air Force Wright Aeronautical Laboratories, Wright-Patterson AFB, OH and
L. R. Caldwell, Lt Col, Air Force Engineering Services Center, Tyndall AFB, FL

**A METHOD FOR DETERMINING THE EFFECT OF TRANSPORTATION VIBRATION ON
UNITIZED CORRUGATED CONTAINERS**

T. J. Urbanik, U.S. Department of Agriculture, Madison, WI

**ACOUSTIC ENVIRONMENT ON THE SURFACE OF A LARGE-SCALE POWERED MODEL OF A
VECTORED-ENGINE-OVER-THE-WING STOL CONFIGURATION**

L. L. Shaw, Air Force Wright Aeronautical Laboratories, Flight Dynamics Laboratory, Wright-Patterson AFB, OH and
S. Y. Lee, Agency for Defense Development, Republic of Korea

ACTIVE STABILIZATION OF A SHIP BORNE CRANE

S. Sankar and J. Svoboda, Department of Mechanical Engineering, Concordia University, Montreal,
Quebec, Canada

**TITLES AND AUTHORS OF PAPERS
PRESENTED IN THE
SHORT DISCUSSION TOPICS SESSION**

NOTE: These papers were only presented at the Symposium. They are not published
in the Bulletin and are only listed here as a convenience.

ERROR EVALUATION OF INELASTIC RESPONSE SPECTRUM METHOD FOR EARTHQUAKE DESIGN

M. Paz, University of Louisville, Louisville, KY

**EXPERIMENTAL EVALUATION OF APPROXIMATIONS OF RESPONSE TO RANDOM EXCITATION OF
OSCILLATOR WITH NONLINEAR DAMPING**

A. E. Galef, TRW, Redondo Beach, CA

NONLINEAR SHOCK ANALYSIS OF RESILIENTLY MOUNTED SHIPBOARD EQUIPMENT SYSTEMS

M. P. Pakstys, General Dynamics/Electric Boat Division, Groton, CT

**THE APPLICATION OF VIBRATION THEORY TO THE DESIGN OF ACCELERATION RESISTANT
MAN-MACHINE DEVICES**

D. W. Reppeger, Air Force Aerospace Medical Research Laboratory, Wright-Patterson AFB, OH

HUMAN VIBRATION TESTING USING FREQUENCY AND ACCELERATION SWEEPS

J.C. Guignard, Naval Biodynamics Laboratory, New Orleans, LA

BLADE FLUTTER INSTABILITY OF A HORIZONTAL AXIS WIND POWERED GENERATOR

A. Muszynska, University of Dayton Research Institute, Dayton, OH and G.T.S. Done, The City University, London, UK

SPIN PIT TESTS OF DAMPED TURBINE BLADES

R. Doninic, University of Dayton Research Institute, Dayton, OH

DYNAMIC AND THERMAL STRESS ANALYSIS OF AN 'MIC' MODULE

V. R. Beatty, Harris GISD, Melbourne, FL

DAMPING MATERIAL PROPERTIES FROM SANDWICH BEAM DATA USING SIXTH ORDER THEORY

L. Rogers and R. W. Gordon, Air Force Wright Aeronautical Laboratories, Wright-Patterson AFB, OH

REPORT OF THE I.E.S. SHOCK AND VIBRATION COMMITTEE'S BROADBAND VIBRATION WORKING GROUP ON SCREENING OF ELECTRONIC HARDWARE

W. Silver, Westinghouse Electric Corp., Baltimore, MD

RAILCAR VIBRATION TESTING IN THE RAIL DYNAMICS LABORATORY

W. D. Dorland, DOT-Transportation Test Center, Pueblo, CO

THE HOLOGRAPHIC ANALYSIS OF LARGE VEHICLE STRUCTURES

G. Gerhart and G. Arutunian, U.S. Army Tank-Automotive Research and Development Command, Warren, MI

SWEPT NARROW BAND RANDOM ON RANDOM IMPLEMENTED ON AN HP5451C FOURIER ANALYZER

F. T. Mercer, Sandia National Laboratories, Albuquerque, NM

ON COMPLEX-VALUED MODE SHAPES, MODELS FOR STRUCTURAL DAMPING, AND MINI-COMPUTER MODAL ANALYSIS TECHNIQUES

P. W. Whaley, University of Nebraska, Lincoln, NE

APPLICATION OF THE IEEE-488 INSTRUMENTATION BUS IN THE VIBRATION LABORATORY

L. G. Smith, Hughes Aircraft Company, Fullerton, CA

SHOCK RESPONSE AND SPECTRAL ANALYSIS DEMONSTRATION

C. T. Morrow, Consultant, Encinitas, CA

ENVIRONMENTAL TESTING

OPTIMIZING PRE AND POST PULSES FOR SHAKER SHOCK TESTING

R. T. Fandrich
Harris Corporation
Melbourne, Florida

The method of selecting pre and post pulses described in this paper considers (1) the entire pulse must fit the required tolerances, (2) the optimum initial conditions must exist before the test pulse starts, including optimum velocity, displacement and acceleration, (3) the terminal acceleration, velocity and displacement must be zero and (4) the excursions of acceleration, velocity and displacement must fall within the shaker system capability.

In order to simultaneously consider these four requirements, a computer program was written to generate various shaped pre and post pulses. These shapes were mathematically integrated to find the velocity and displacement profiles, which could then be compared to the requirements. Parametric variation was performed to optimize the shapes.

An example is shown using a MIL-STD 810C, 11 millisecond, 30G half sine pulse with tolerances of $\pm 5\%$ on pre-pulse, $\pm 15\%$ on classic pulse and $+20\%$, -30% on post pulse (as required by the MIL-STD). The results of this example are compared with the results obtained by using present "typical" pre and post pulses.

HISTORY

Impact Shock Testing was developed to evaluate and demonstrate a test item's ability to survive a collision with something. This type shock typically is of half-sine, terminal peak sawtooth or square wave acceleration time history, depending on the nature of the materials involved at the collision interface. The shock involves a change in velocity of the test item, caused by the impact. In the past, this type test was performed by simulating the collision. The test item was attached to a table which was allowed to collide with part of the shock machine. Various materials were placed at the collision interface to obtain the desired time history. Originally, sand was used at the interface. Later it was replaced by lead, rubber, plastic foams, pneumatic programmers and others, all in an attempt to shape the time history. Tolerances were established to insure some degree of validity to the tests. The tolerances were developed on the basis of an actual collision, with some consideration being given to the type of shock machines being used for this test.

The tolerances allow very little motion before the impact, a degree of accuracy during the impact period and fractional "ringing" after impact. See Figure 1 for MIL-STD 810C tolerances. These tolerances tend to encourage a change in test item velocity.

As the age of electronics progressed, the concept of impact testing on a vibration shaker was born. This concept allows great flexibility in time history. Rather than change impact material, dial settings on a pulse generator were changed to produce the desired shapes. Unfortunately, the signal put into a shaker system is not identical to the acceleration it produces because of the transfer function of the system. Various methods of overcoming non-unity transfer functions were developed. During this period, a technical paper describing a closed-loop iterative equalizer costing \$100,000 was followed by a paper describing a \$15 OP-AMP circuit which unitized the system transfer function. Finally, the development of low cost computer controllers has allowed digital control of shock tests in many laboratories.

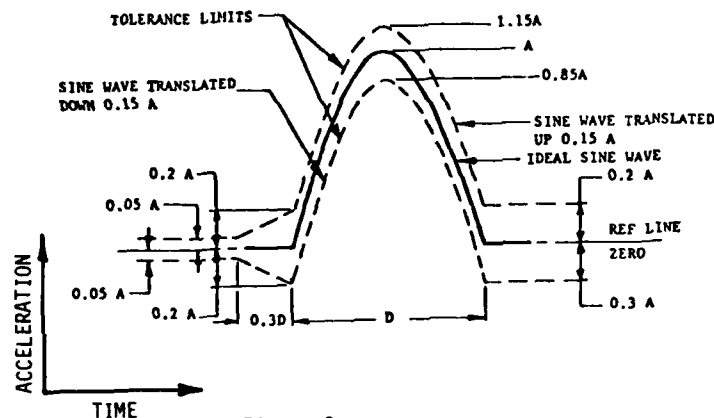


Figure 1
Half-Sine Shock Pulse with
MIL-STD-810C Tolerances

THE PROBLEM

Although impact shock results in a change in velocity an electrodynamic shaker system is not capable of long term velocity change. Typically, the shaker head is constrained to a single location and can deviate from that location by only a centimeter or so. This restriction provides the remaining challenge to impact testing. See Figure II for acceleration, velocity and displacement of an impact shock. In order to overcome the requirement for a change in velocity, the test must possess a second change in velocity being of equal magnitude but opposite direction as the required change. This zeros the long term velocity change and allows testing to be performed on a shaker. The way in which this opposite velocity is obtained is the essence of this paper.

Tolerances on impact testing are applied to acceleration time history. In order to minimize the acceleration required to generate the opposite velocity change, long duration pulses are used. (Since velocity change is the time integral of acceleration, increasing the time and reducing the amplitude of a pulse will result in the same velocity change.) To further reduce the amplitude two pulses are used, one before and one after the impact shock.

It is advantageous to minimize these pre and post pulses to eliminate their damage potential to the test item and to meet pre and post test tolerances.

COMMON SOLUTION

Present canned programs have equal pre and post pulses. See Figure III for acceleration, velocity and displacement of a 30G, 11 millisecond half-sine for a typical canned program pulse test. Notice the pre and post pulse acceleration is equal, the positive velocity equal the negative velocity and the displacement is all negative. The size of the boxes around velocity and displacement represents the shaker system limits, that is, 254 centimeters/second is the maximum velocity possible and 2.54 centimeters is the maximum double amplitude possible for the particular shaker system under consideration. Notice the displacement required for this pulse is greater than allowable for this system. The acceleration magnitude of the pre-pulse is greater than the allowable tolerance. We will see later in this paper, that this shock test can be performed within tolerance, on this system, by optimizing the pre and post pulse.

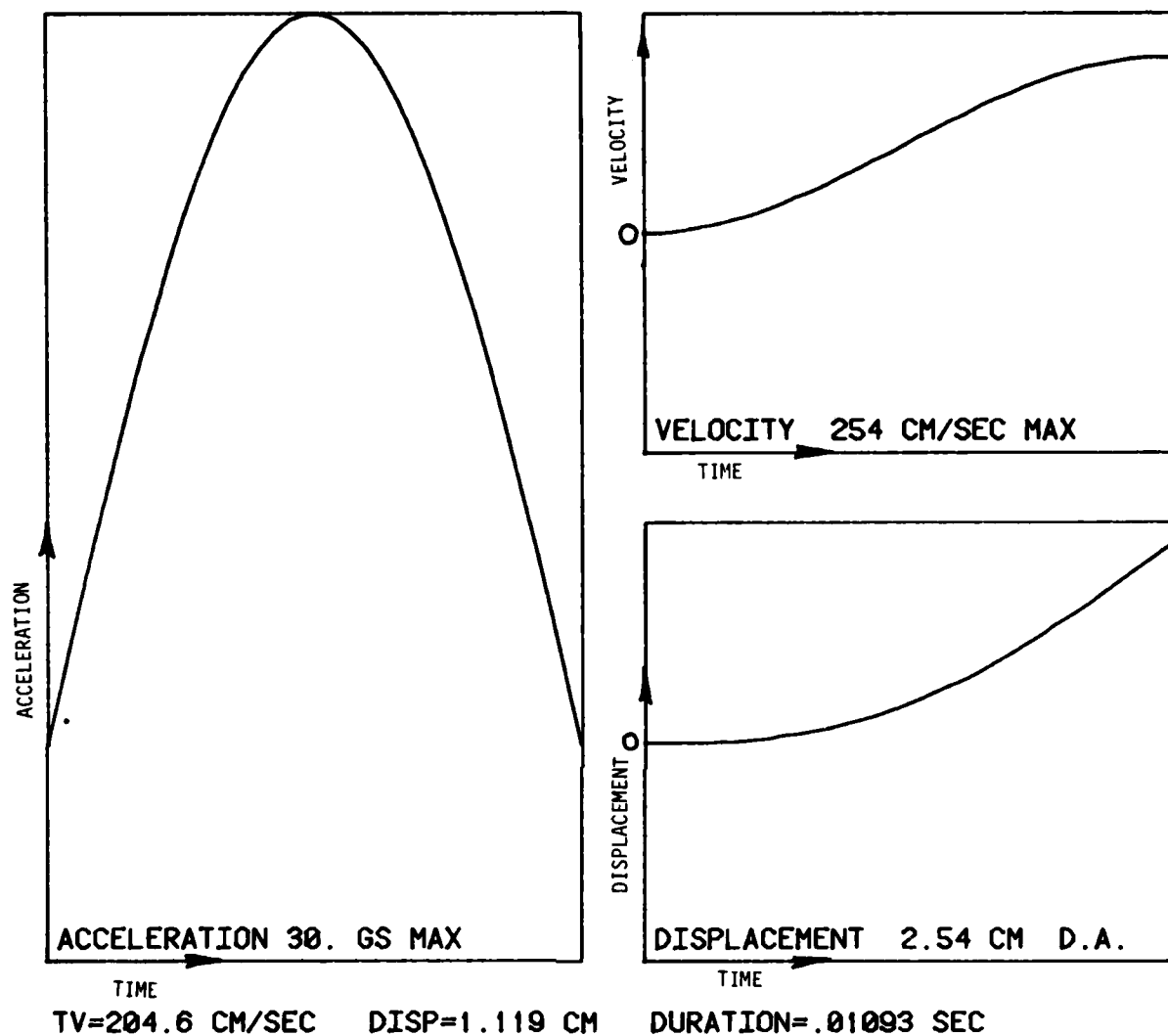


Figure II
30 G, 11 ms Half-Sine
Accel, Vel, and Disp.

OPTIMUM SOLUTION

The following considerations should be made to optimize pre and post pulses: (1) Tolerances, (2) Initial conditions should be optimum, (3) Final conditions should be zero, (4) Excursions should be within shaker system capabilities and (5) Damage potential of pre and post pulses should be minimized. Let us try to consider the first three constraints one at a time, while keeping our solutions within the bounds of the fourth and fifth constraints.

TOLERANCES

In order to meet the tolerances, the pre-pulse must be constrained to 5% of the pulse magnitude. If the shapes are the same for pre, post and shock pulse, and the pre and post pulse magnitudes are equal, then the duration of the pre and post pulse must be ten times the shock pulse. This would result in twenty times the duration at one-twentieth the magnitude to completely cancel the shock

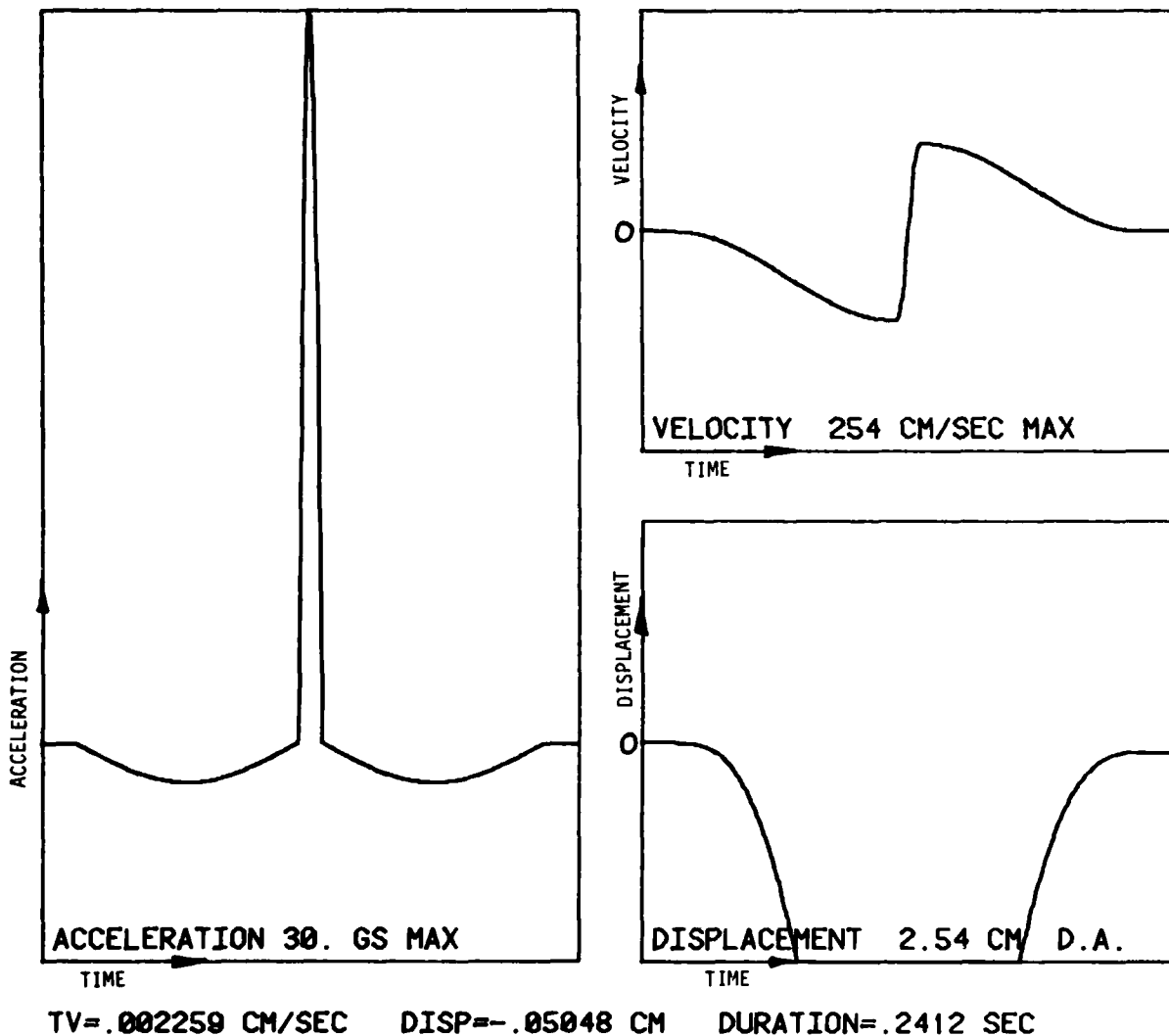


Figure III
"Typical Solution"

pulse velocity. Unfortunately, two problems arise from this approach. First, for an 11 millisecond shock pulse, the pre and post pulses must be 110 milliseconds long. This is too long for the shaker system being considered, since it is limited to testing at 5 Hertz and above and a 110 millisecond half-sine pulse contains a component below 5 Hertz. Secondly, as is seen in Figure III, the displacement of the pre-pulse exceeds the shaker capability. For these reasons, it is not practical to preserve equal pre and post-pulses. The pre-pulse must be designed to fit the tolerance and comply with shaker capabilities, leaving more than 50% of the velocity to be cancelled by the post-pulse. The post pulse,

having greater than 5% tolerance, has the ability to make up for the pre-pulse deficiency.

INITIAL CONDITIONS

Within the constraints of the previous paragraphs, now we must optimize the acceleration, velocity and displacement just prior to the shock pulse.

The optimum acceleration is zero since the shock pulse starts and ends at zero. To comply with this requirement, we will simply define any acceleration before the zero crossing as pre-pulse.

The perfect velocity is a negative velocity representing half the shock pulse velocity. We already know this is impossible so the optimum velocity is the maximum negative velocity obtainable within the 5 hertz and 5% amplitude constraint. This velocity must be obtained without exceeding the displacement limit.

Since amplitude and duration of the pre-pulse are bounded, the only variable left is shape. To obtain the maximum velocity from a pulse of limited amplitude and magnitude, a square wave should be used. Square waves have components at all frequencies and will excite all natural frequencies of a test item. For this reason only the first two components of the square wave are used. This produces a square-like wave with limited damage potential. A 1.155 amplitude half-sine at the

fundamental frequency was added to a 0.231 amplitude sine at the third harmonic to produce a maximum velocity wave of unity magnitude. See Figure IV. This shape was used for the pre-pulse to obtain maximum velocity in minimum time with limited damage potential.

The optimum displacement must be within the 2.54 centimeters of shaker stroke. If we start from center and accelerate downward, the further we can travel; the higher the velocity. For this reason, to maximize velocity, we should start at the top of the allowable stroke, not the center. The optimum initial condition for the pre-pulse, is zero velocity, maximum positive displacement. It is possible to include in the pre-pulse, an initial portion designed to establish this condition.

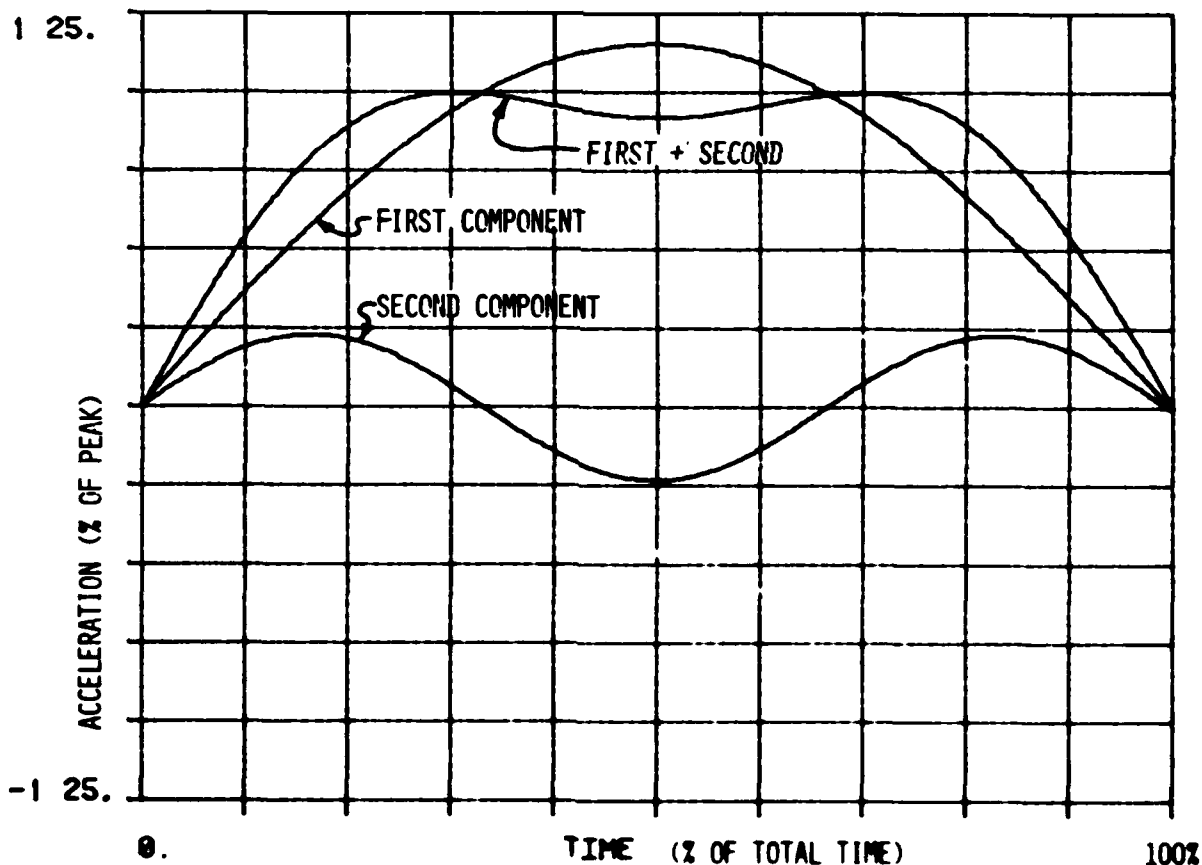


Figure IV
Square-Like Wave
Max. Velocity, Min. Damage

Figure V shows this optimized pre-pulse superimposed on the resulting displacement. The pre-pulse consists of a positive pulse of 0.24 amplitude followed by a negative pulse of unit amplitude. The displacement shows that the first 65% of the pulse is used to obtain the maximum positive displacement/zero velocity condition. The remaining 35% is used to obtain maximum velocity just before reaching maximum negative displacement. A small amount of displacement must remain to perform the shock pulse. Unit amplitude and duration have been used to allow tailoring of this time history to various shock pulses. For the

30G half-sine discussed, the 5% tolerance would allow a magnitude of 1.5G's. This yields a pre-pulse fundamental frequency of 6.1 Hertz, well above the 5 Hertz lower limit.

Note: For the 2.54 centimeter shaker system, the relationship between magnitude (M) and fundamental frequency (F) is:

$$F^2 = 25M \quad \text{Derived from the basic equation of motion:}$$

$$\text{Distance} = \text{Acceleration} \times \text{Time}^2/2$$

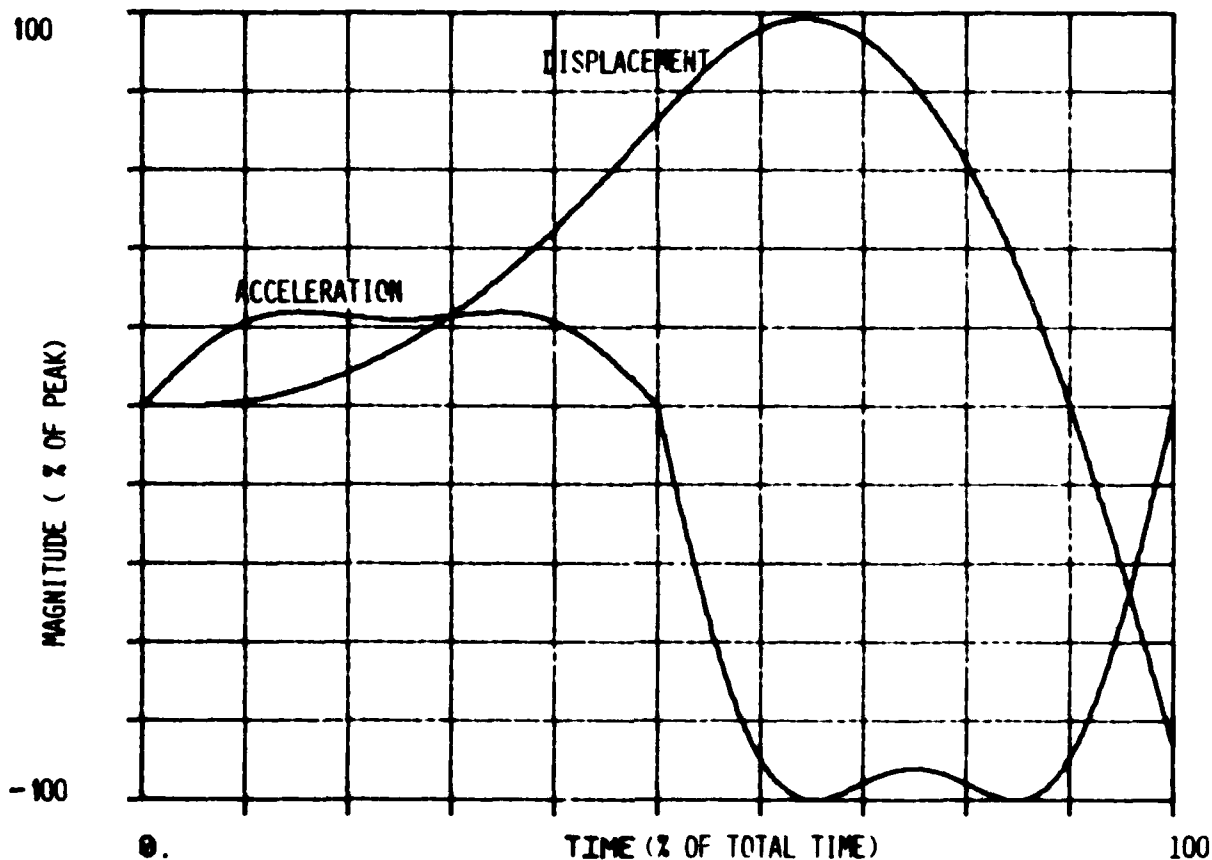


Figure V
Pre-Pulse
Acceleration and Displacement

FINAL CONDITIONS

Having optimized the pre-pulse and performed the required shock pulse, a residual velocity and displacement will exist. A post pulse must be designed to cancel the residual velocity within the displacement constraint, while minimizing the damage potential. Figure VI shows the development of acceleration, velocity and displacement up to the post-pulse. The task

remains to develop a post-pulse which will result in zero acceleration, velocity and displacement at the end of the test. From Figure VI, we see the post-pulse must start at 0.0G acceleration, 133.1 cm/sec velocity and -0.7354 cm displacement and end at zero. It is easier to conceive of a pulse that starts at zero and ends at the above conditions so we will consider this type pulse and simply reverse the time axis polarity when we find a pulse which com-

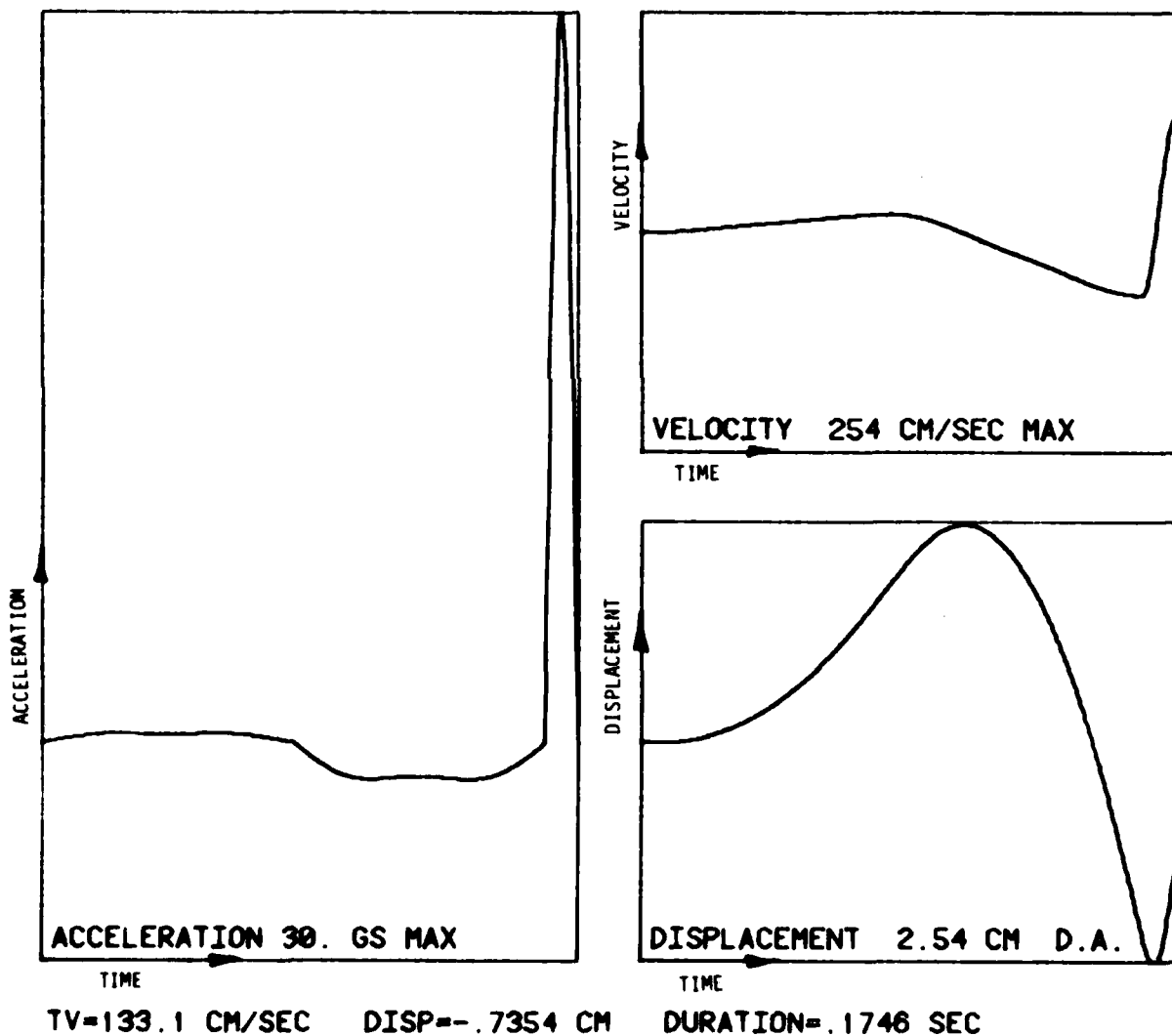


Figure VI
Pre-Pulse and Half-Sine

plies with our requirements. The post-pulse tolerances will limit the amplitude of this pulse to +6 G's and -9 G's. The shape of the post-pulse will establish the resulting velocity to displacement ratio and the magnitude of the post pulse will establish the values for velocity and displacement. For this reason, we will first find a suitable shape, then establish its magnitude.

The velocity/displacement ratio required is:

$$R = \frac{-133.1 \text{ cm/sec}}{+0.7354 \text{ cm}} \\ = -181 \text{ sec}^{-1}$$

If a half-sine is used for the post-pulse, the ratio R, is 2.0 divided by duration. The appropriate duration post-pulse of half-sine shape would be 11 milliseconds. The magnitude required to obtain a -133.1 cm/sec velocity is -20 G's. This is greater than the -9 G's allowed so a different shape of longer duration is required.

To satisfy a large number of possible requirement, a family of curves was investigated. This family possesses (1) smooth displacement, velocity and acceleration time histories, (2) high variation of R, (3) simple and continuous mathematical representation. See Figure VII. The function is one complete cycle

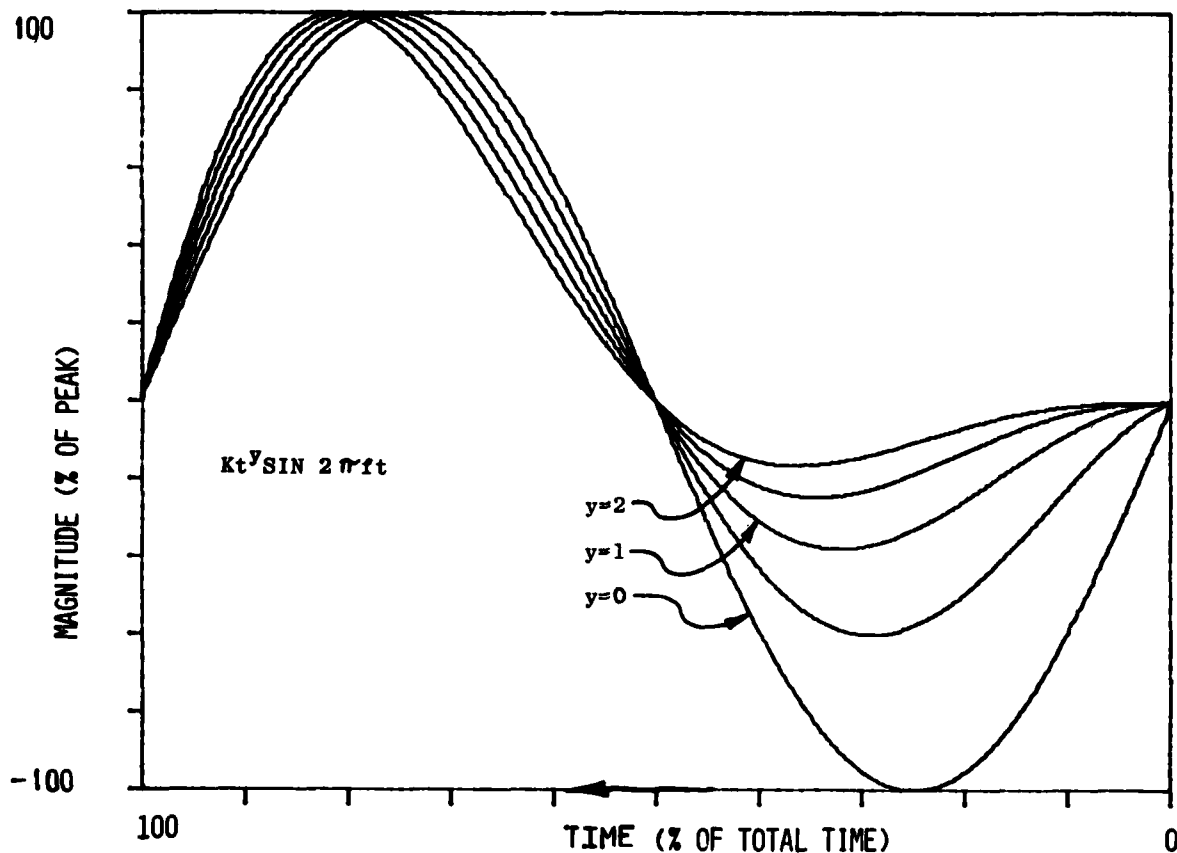


Figure VII
Family of Post-Pulses

of a sine function with amplitude modulated by an exponential, represented:

$$F(t) = K t^y \sin 2\pi ft$$

The frequency (f) and the exponent (y) can be varied to obtain various ratios (R). The equation represents a sine increasing in amplitude. In actual use, the time axis is reversed and the amplitude decays. Figure VIII shows what f and y are required to obtain a desired ratio R.

When the exponent y is between 1 and 2, the ratio varies greatly; when above 2 it remains relatively constant. This occurs because the function looks less like a full cycle of sine and more like a pulse as y is increased and therefore, takes on the pulse-like characteristic of having a single R for a given frequency. Figure VIII can be used to select candidate post-pulses. The maximum acceleration of the candidate must be adjusted to obtain the proper velocity change. This

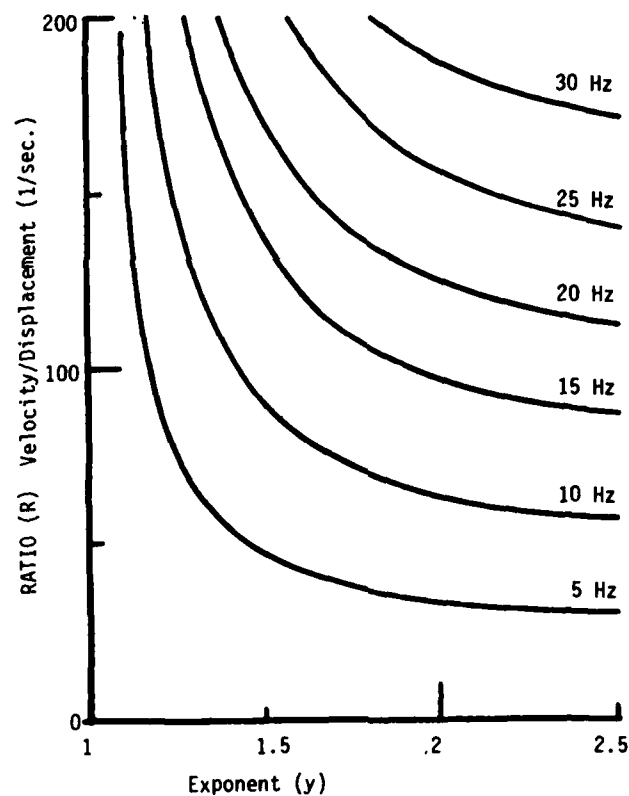


Figure VIII
R Selection Chart

acceleration is limited by the post-pulse tolerance so not all the candidates will suffice. If the post-pulse is limited to -9 G's, the frequency must be 14 Hertz or less to obtain the desired velocity change. Similarly, if the frequency is too low, the displacement exceeds

the shaker capability. For this particular case, the frequency must be between 12 and 14 Hertz. Figure IX shows the total wave shape using a frequency of 14 Hertz, an exponent of 1.29 and an amplitude of -8.17 G's.

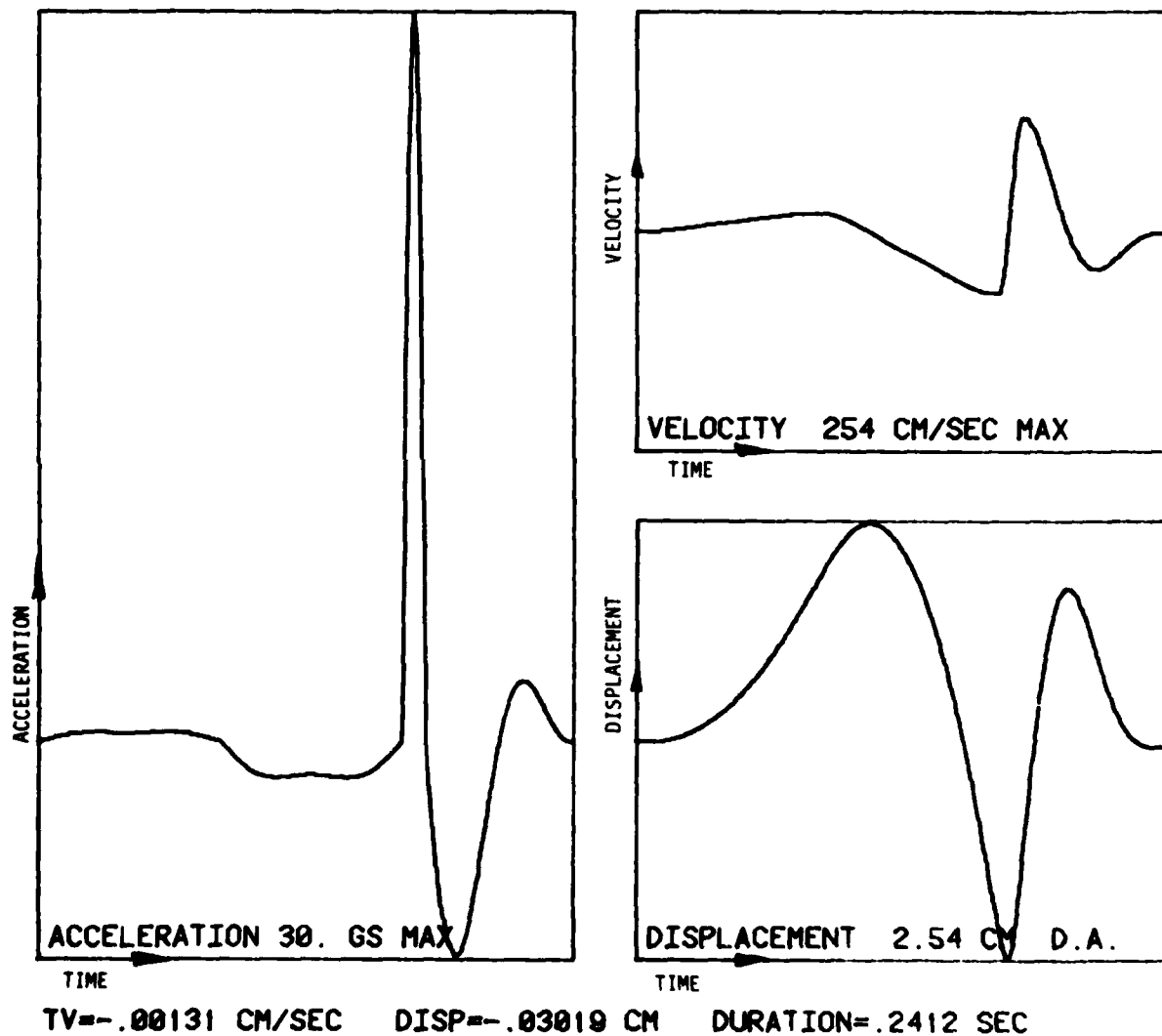
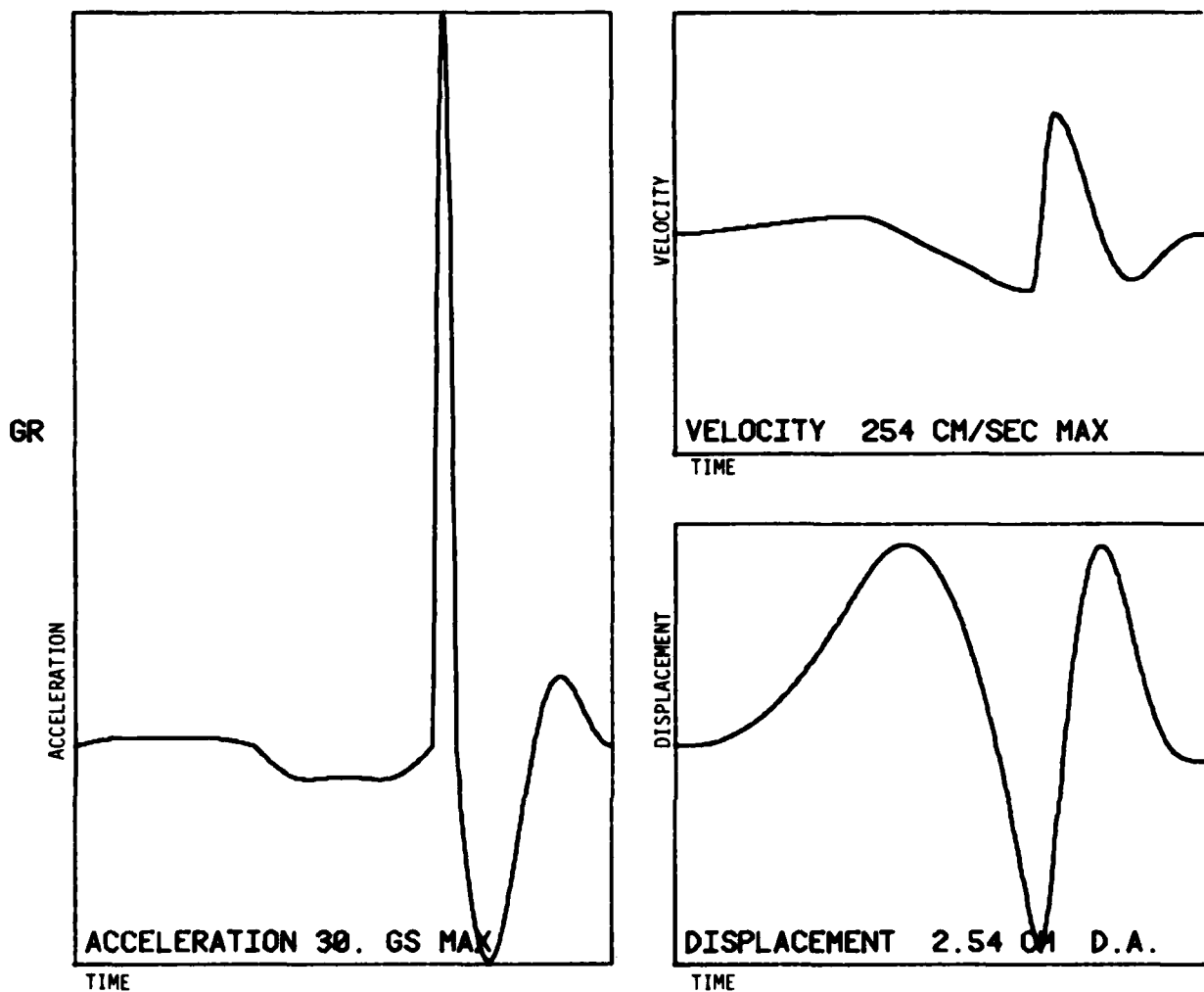


Figure IX
Satisfactory Solution
Displacement Close to Limit



TV=.004476 CM/SEC DISP=-.09274 CM DURATION=.2459 SEC

Figure X

Optimum Solution

This shape completely satisfies the requirements, however, the displacement for the pre-pulse is to the 2.54 cm limit, while the displacement for the post pulse is far from the limit. The pre-pulse was made slightly smaller and the post pulse made larger to even out the displacement. Figure X shows the final shock profile.

The total shock time history can be expressed mathematically in four sections with time equal zero at the start of each section. Section I is the positive pre-pulse, Section II is the negative pre-pulse, Section III is the classic pulse and Section IV is the post-pulse. The chart below shows these equations.

$$\text{ACCELERATION} = \begin{cases} 0.3312 \{1.155 \sin 2\pi(6.1 \text{ Hz})t + 0.231 \sin 2\pi(3 \times 6.1 \text{ Hz})t\} & \text{SEGMENT I} \\ -1.3800 \{1.155 \sin 2\pi(6.1 \text{ Hz})t + 0.231 \sin 2\pi(3 \times 6.1 \text{ Hz})t\} & \text{SEGMENT II} \\ 30.0 \sin 2\pi(500/11 \text{ msec})t & \text{SEGMENT III} \\ -1543.0 (0.0714-t)^{1.29} \sin 2\pi(14 \text{ Hz})(0.0714-t) & \text{SEGMENT IV} \end{cases}$$

EQUATION FOR ACCELERATION

COMPARISON

The 30 G pulse can be performed on a 2.54 cm D.A. machine only because of the pre and post pulse optimization. If a typical 10% half-sine pre and post-pulse were used, the machine would be limited to a 12 G pulse so this optimization procedure has increased the machine capability by a factor of 2½.

Additionally, the tolerances of MIL-STD 810C have been met; but at what price? Figure XI shows the shock-response spectrum ($Q=10$) for the pure pulse, the 10% pre and post pulse solution, and the optimized solution. To accommodate the $\pm 5\%$ pre-pulse tolerance, most of the velocity compensation had to be in the post-pulse, resulting in the -9 G decaying sine. This post pulse is almost three times the post-

pulse amplitude required if the pre-pulse tolerance is not met. Complying with the tolerance results in a 40% increase in the SRS at 25Hz, over the SRS for the classic shape, or the 10% pre-post pulse solution. It is not the intent of the tolerance, to increase the pulse damage potential. For this reason, it is suggested that the pre-pulse tolerance of MIL-STD 810C be increased to $\pm 15\%$ to allow shaker shock testing with no increase in damage potential.

Notice both shaker solutions under-test at frequencies below 10 Hz. This is a disadvantage intrinsic to shaker shock and must be considered for testing low frequency systems such as isolated electronics or packaged equipment.

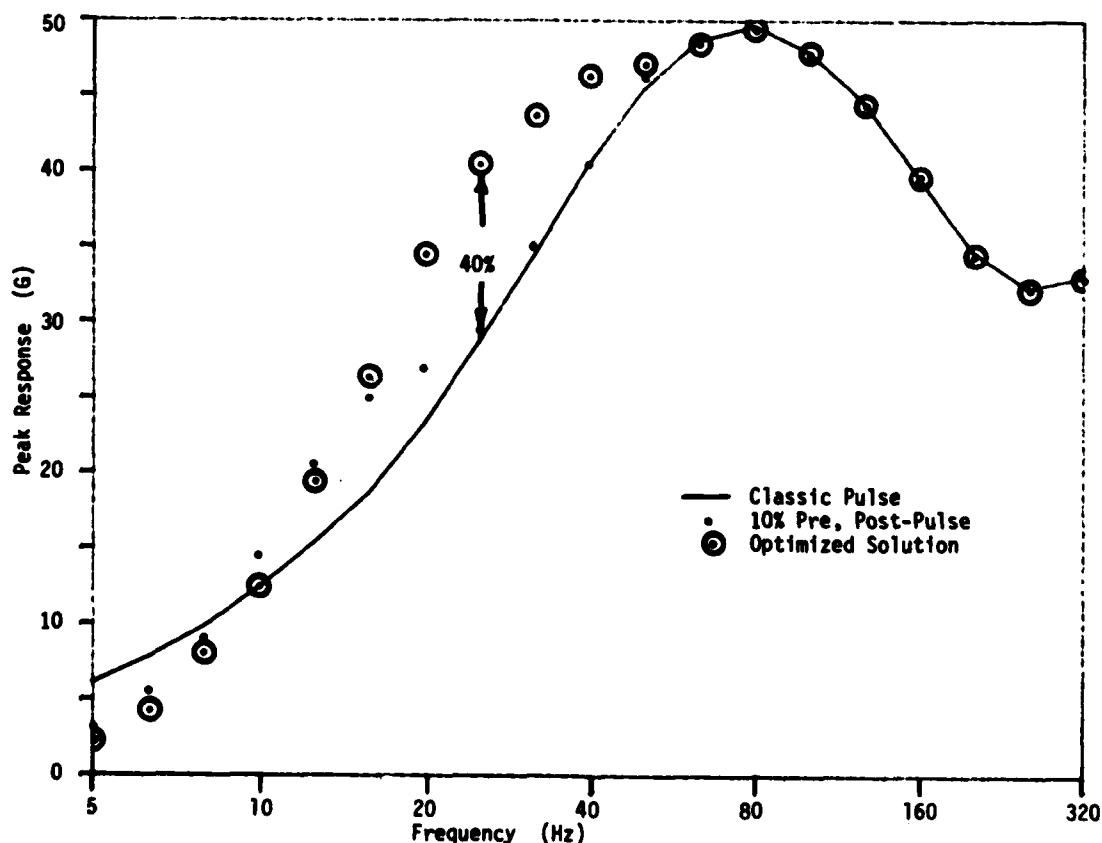


Figure XI
Shock-Response-Spectrum (SRS)

CONCLUSION

This paper has shown how to optimize pre and post-pulse shapes for shaker shock testing and thereby:

1. Meet MIL-STD 810C tolerances
2. Maximize usable range of the shaker system (up to 30 G's, 11ms for a 2.54 shaker).
3. Minimize damage potential of pre and post-pulses.

DISCUSSION

Mr. Rogers (Unholtz-Dickie): Are the digital control people aware of your work and has this been implemented in their software?

Mr. Fandrich: As far as I know at this point in time, it has not been implemented in their software although, some of the technical people in the various companies who sell these programs have been pushing in this direction, they are aware of it. And in fact, after I finished this paper I found that there were some in-house memos in some of these companies that had been written to try and get this kind of solution. And hopefully this will help precipitate that solution also. I have a canned program that will do classic pulses as well as any time history I put into it. So I can program in an optimum pre-in post-pulse and not use their canned solution to the problem which is a good advantage.

Mr. Rogers: Also I noticed your choice of one hundred inches per second. That seems fairly high compared to most shaker system velocity ratings.

Mr. Fandrich: One hundred inches per second is the limit on the shaker that I was using so I think I only needed 40 or 50 inches per second to accomplish all this. Velocity never was a problem on this shaker system.

Mr. Rogers: 40 or 50 seems more consistent with the performance rating of most shaker systems. 100 inch per second velocity capability is fairly rare. So I am glad to see that you stayed within 40 and 50. I think that's good.

Mr. Fandrich: Yes, the velocity was no problem.

SHOCK, VIBRATION AND FATIGUE IN
TRANSPORTATION INDUSTRIES

T. V. Seshadri
Principal Engineer, Systems
Fruehauf Corporation, Detroit, Michigan

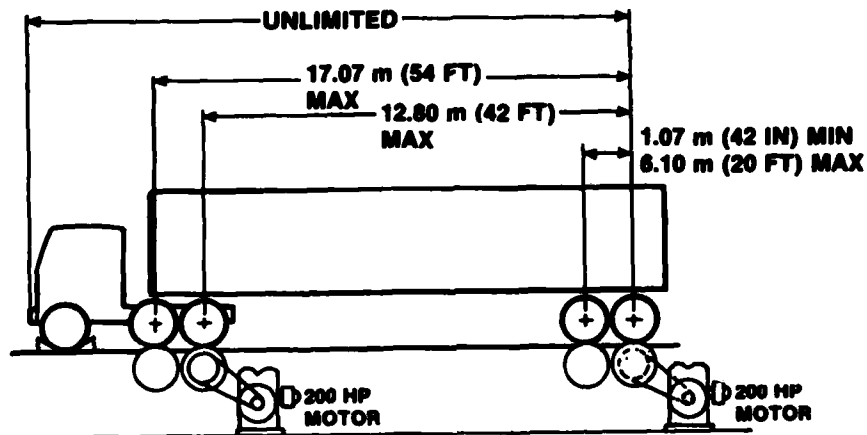
Fatigue failure is the most common form of failure in transportation industries. Design for fatigue loading, taking into account all the variables, is complex. A durability test technique for tractor-trailers is presented. A dynamometer is used which inputs periodic bumps to the vehicle. Even though this technique does not simulate the road loading in real time, it provides an overall view of the adequacy of the design for field loads. Theoretical analysis is performed treating the vehicle as a simple dynamical system. A brief review of fatigue design is included.

In transportation industries, the main cause of product failure is fatigue. The dynamic loading is caused by the service environment. This loading is, in general, random such as the gust loading on an aircraft, wave motion loading on ships and loading caused due to road undulations on road vehicles. The analysis of fatigue for random loading is fairly complex as it involves accurate measurement of the service spectrum, sophisticated counting techniques and reasonably accurate and comprehensive material properties data. This is further complicated by the fact that the service environment will vary from trip to trip. For example, the stresses and strains on an automobile or tractor-trailer will depend on the speed, road surface and loading. The variation of loading conditions is much more drastic in a tractor-trailer than an automobile. There are also additional loading conditions such as braking, hitting a curb or dock, cornering, etc. Accurate fatigue data is also not available for modern lightweight materials such as glass reinforced plastics. Because of these drawbacks, smaller companies resort to some form of durability testing using a constant amplitude or equivalent loading for fatigue design.

Durability testing is used for another reason also. Usually, the road vehicles such as the tractor-trailers are expected to have a useful service life of ten years or a million

miles. Real time testing of actual service environment, if such is available, will take an extensively long time which is not practical. In some industries, accelerated fatigue testing is used either by increasing the magnitude or frequency or both of the service spectrum. This technique may work for some components but will not work for an entire vehicle. Since the stresses caused in the tractor-trailer are a function of the frequency of road undulations, increasing the frequency may not result in the same component response. Increasing the magnitude of loading will result in yielding at some locations which do not yield in actual service. Fatigue performance is significantly altered by the presence of residual stresses which occur after unloading beyond yielding. Therefore, if the service environment is to be simulated, it is more or less mandatory to use real time data with no change in magnitude or frequency.

Durability testing at Fruehauf Corporation is done by using a Chassis Dynamometer (Figure 1). The Chassis Dynamometer consists of a set of rolls on which the trailer wheels are placed. These rolls are 1.02 m (40 in.) in diameter. There are four pairs of rolls, two in front and two in rear. Rolls are wide enough so they can accommodate a set of dual tires. The front of the trailer is restrained at the king pin by a device (dolly) which has a fifth wheel similar to the tractor.

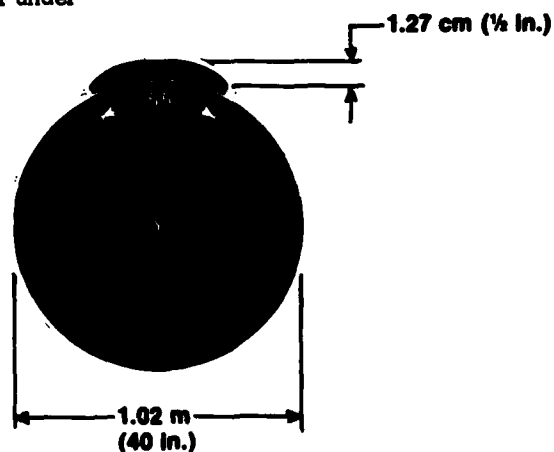


DYNAMOMETER COMPONENTS AND LIMITING DIMENSIONS

Fig. 1

Different height and length of bumps can be installed on the rolls. The speed of the two front and two rear rolls and the phase between them can be varied. The loading on the trailer is therefore, a series of periodic bumps. In most cases, the speed is adjusted until the natural bounce frequency of the trailer is excited. The test is run at this speed for a certain length of time. Effort is still under

way to estimate the required test time which will adequately simulate the actual service life. The test is stopped at periodic intervals to inspect the trailer. Usually 46 cm (18") long, 1.27 cm (1/2") high bumps are used (Figure 2). If the trailer completes the test successfully, it is expected to have adequate service life.

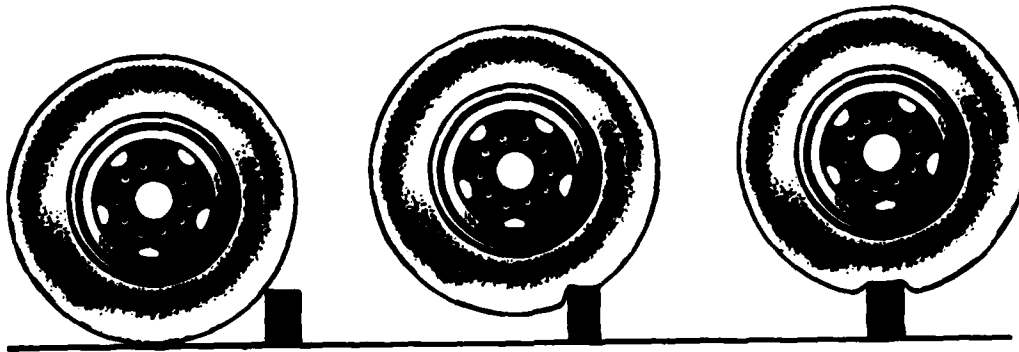


ROLL AND BUMP DIMENSIONS

Fig. 2

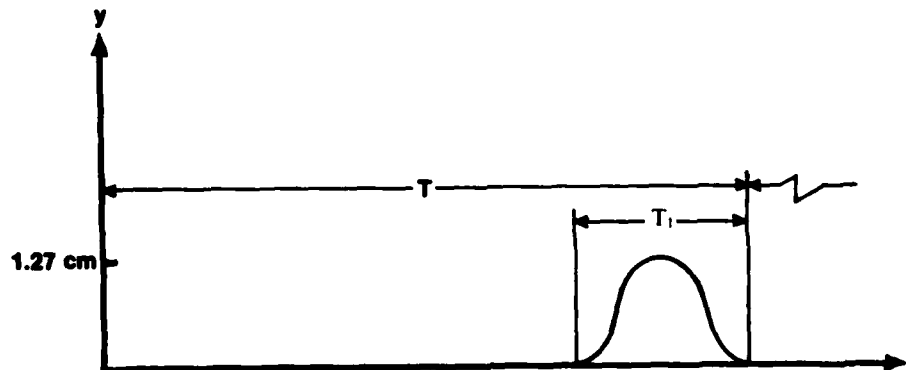
The time history of dynamometer loading will be periodic. The period T is made to correspond to the natural bounce frequency

of the trailer. Since the tire is an elastic body, the actual loading on the tires will be as shown in Figure 3.



TIRE ENVELOPING PROPERTIES

Fig. 3(a)



ONE CYCLE OF LOADING ON TIRE

Fig. 3(b)

A single bump can be represented mathematically by a haversine function

$$y_1(t) = \frac{\delta}{2} (1 - \cos \omega_1 t) \quad \text{-----(1)}$$

where,

δ = Actual bump height
 $\omega_1 = 2\pi/T_1$ where T_1 is the duration of the bump.

Since the loading on the tires is a periodic function, it can be expanded into Fourier series. The function $y(t)$ is then given by,

$$y(t) = \frac{A_0}{2} + \sum_1^{\infty} A_n \cos n\omega t + B_n \sin n\omega t \quad \text{-----(2)}$$

where,

$\omega = 2\pi/T$ (T is the period corresponding to trailer bounce.)

The Fourier series representation of (2) converges rapidly if the ratio T_1/T is 0.5 or more. Since the bump width is 46 cm (18 in.), the ratio of T_1/T is .14 and several terms are needed for proper representation of the function. But as it will be shown later, the contribution of only the first term ($n = 1$) adequately represented the total response.

TRAILER MODEL

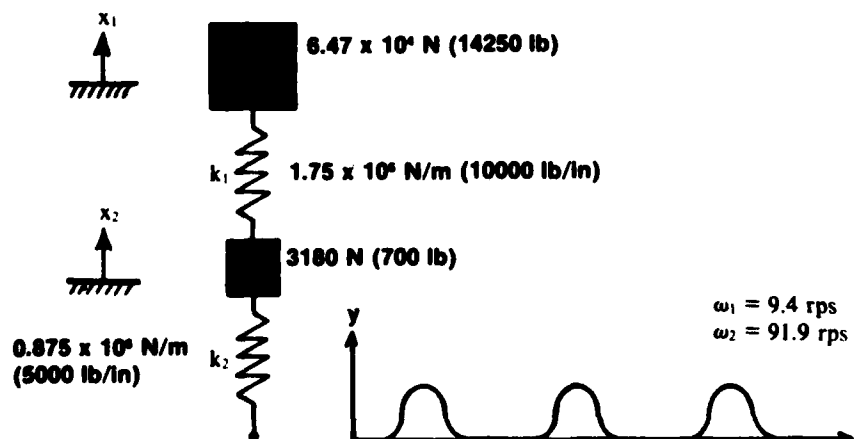
The trailer suspension can be represented as a two degree of freedom system, the masses being the sprung and unsprung masses and the stiffnesses being those of the spring and tires. Taking one set of tires and spring, the parameters are as shown in Figure 4.

The equations of motion for such a system are,

$$\begin{aligned} m_1 \ddot{x}_1 + k_1(x_1 - x_2) &= 0 \\ m_2 \ddot{x}_2 + k_2(x_2 - x_1) + k_2 x_2 &= k_2 y \end{aligned} \quad (3)$$

Using the homogeneous equations, the mode shapes can be found. The mode shape matrix for the chosen parameters is

$$[\Psi] = \begin{bmatrix} 1.48 & -0.033 \\ 1 & 1 \end{bmatrix}$$



TWO DEGREE OF FREEDOM TRAILER MODEL

Fig. 4

This means, in the first mode, which is at 1.5 Hz, the trailer body moves in phase with the axle with about 50% more amplitude. The second mode at 14.6 Hz is basically an axle bounce mode because trailer body is not moving much.

Using normal mode theory, the two degrees of freedom system can be reduced to two single degree of freedom systems, the analysis of which is simpler. The two single degrees of freedom systems and the corresponding loading are shown in Figure 5.

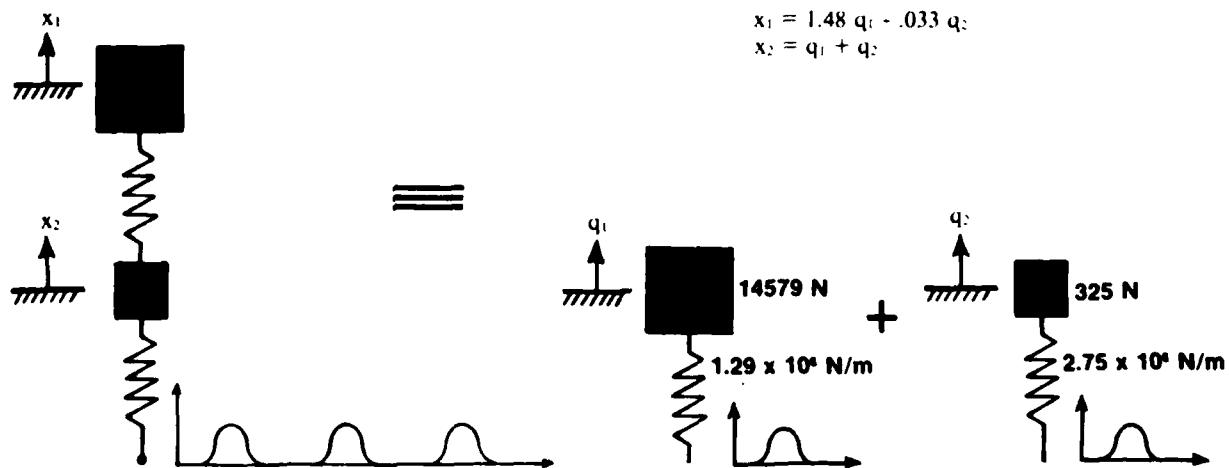
It has to be noted that even though there is loading only at the tires, in the reduced models, there is loading at both springs. But, as stated previously, each single degree of freedom represents one mode and, in the second mode, the motion of the trailer frame is very small. Therefore, for fatigue analysis of the trailer frame, the first mode model of the trailer is adequate. A damping ratio of 0.2% is used in the analysis.

The total response for the periodic input is obtained by adding the response to individual Fourier components. For a 1.27 cm (1/2") bump, the maximum response was found to be 0.62 cm (0.25").

EVALUATION OF STRESSES

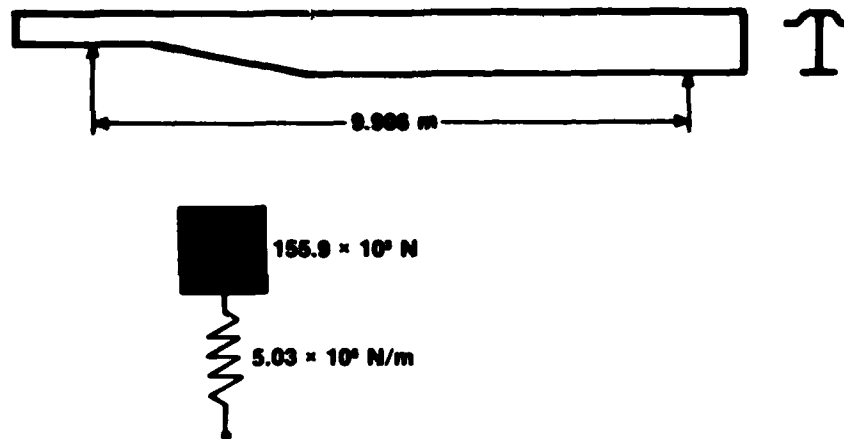
The next step will be to convert this response into meaningful stress values. The life of the trailer for dynamometer loading can be estimated by well known fatigue theories. One of the more popular models of Fruehauf trailers is a platform trailer which is used extensively for carrying steel and aluminum coils, transformers, machinery and construction equipment. It basically consists of two simply supported beams.

Figure 6 shows the dimensions and dynamic properties of this beam. This beam can be represented by a single degree of freedom system model.



EQUIVALENT S.D.O.F. SYSTEMS

Fig. 5



BEAM AND ITS FIRST MODE MODEL

Fig. 6

The equation of motion for such a beam will be

$$\frac{W}{g} \ddot{x} + c\dot{x} + kx = kx_0$$

The natural frequency of the beam is 0.91 Hz and the frequency of excitation is 1.5 Hz. The response for a 0.62 cm (0.25") displacement loading is 0.86 cm (0.34"). Knowing the static displacement and stress of the beam, the dynamic loading is found to fluctuate $\pm 0.28g$. This means the stress fluctuates

from 0.72 to 1.28 times the static stress. The number of cycles per hour can be easily found because the frequency of excitation and response is known.

FATIGUE ANALYSIS

Fatigue analysis for a constant amplitude loading is fairly straightforward if the material fatigue properties are known in the form of S-N curve (Figure 7).

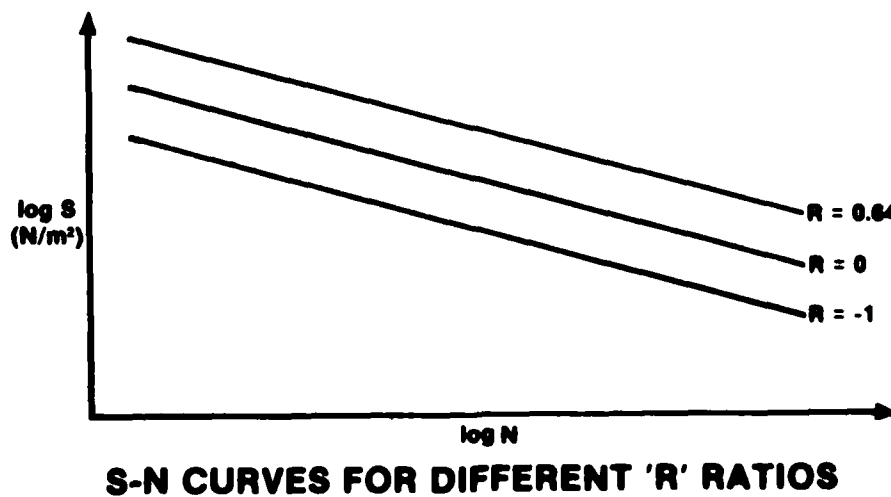


Fig. 7

If test data is not available, SAE recommends several methods to estimate this curve using results of the tensile test.

But fatigue failure usually occurs in a region of stress concentration such as a weld, bolt or rivet hole. The local stress can be obtained by multiplying the nominal stress by a notch factor. Thus, the life of the trailer at a weld detail on the dynamometer can be estimated. Strain measurements can also be made to correlate the theoretical analysis.

Fruehauf is currently working on finding the equivalence of number of hours in the dynamometer to actual service life. Actual strain

measurements are made on the road. The strain history is converted into number of cycles of different magnitudes using rainflow counting. Appropriate notch factor and cumulative damage theories are used to find the fatigue damage. From the fatigue damage coefficients in the dynamometer and road tests, the number of miles corresponding to an hour of dynamometer test can be established.

Thus, using the dynamometer as a tool, the design engineer can verify whether any particular component is overdesigned or underdesigned. This provides a means for optimizing the design resulting in reduced manufacturing and warranty costs.

DISCUSSION

Mr. Gerardi (Flight Dynamics Lab, WPAFB): I have several questions. Did I understand you to say that you used a constant damping force to transmit the force from the dynamometer into the truck frame.

Mr. Seshadri: Yes, it is a constant you use here.

Mr. Gerardi: Were you able to compare any of the forcing functions with the actually measured value? How well did they compare?

Mr. Seshadri: Yes, the measured values in the trailer compared pretty good.

Mr. Gerardi: Had you ever considered the non-linear characteristics of the damper or do you feel that it is just not that important?

Mr. Seshadri: Well right now we don't have any shock absorbers in the trailers. There is really no damping mechanism in the trailer. All there is is friction.

Mr. Gerardi: I didn't know that. So you are just talking basically tire damping then.

Mr. Seshadri: Tire damping, interfacing, interlift friction in the suspension spring and structural damping in the beam.

Mr. Gerardi: I see, thank you.

Mr. Dyrdaahl (Boeing Company): What did you use for road roughness? How did you tackle that problem? Did you establish the bump heights?

Mr. Seshadri: Well this is a simulated dirt road. This is not an actual road.

Mr. Dyrdaahl: Well, I understand that, but you ought to be realistic somewhat.

Mr. Seshadri: Yes, what we think is best based on field failures and failures induced on the dynamometer was a half inch bump. This is based on a lot of trial and error experience and we finally settled on a half an inch bump size.

Mr. Dyrdaahl: I see. You used a half an inch bump and then you tuned it up to resonate the suspension system.

Mr. Seshadri: Right, the fundamental frequency of the trailer.

Mr. Handley (SUP SHIP San Diego): I understand you are using the load of the beam plus a uniformly distributed load above the beam.

Mr. Seshadri: Right.

Mr. Handley: Have you given any consideration to the use of a concentrated load?

Mr. Seshadri: Not really because most of our customers use the trailers for hauling construction equipment where the loads are uniformly distributed. To redo the problem using a concentrated load would not be a difficult task. You would have to change the spring rate of the beam. The natural frequency would be different but you could use the same type of analysis for a concentrated load.

RANDOM IMPACT VIBRATION TESTOR

W. D. Everett
Pacific Missile Test Center
Point Mugu, California

The Random Impact Vibration Testor (RIVT) is a new device that efficiently stimulates realistic vibration in flight vehicles. The stimulus is repetitive impacts by small projectiles on the surface of the test vehicle. The nature of these impacts is random with respect to the relative location, time interval and intensity between successive impacts. The resultant vehicle vibration resembles that of flight with the characteristics of broad band random noise motion, in many directions, throughout the vehicle structure.

BACKGROUND

The RIVT is based on a phenomenon that has become apparent in the study of missile flight vibration. Vibration in missiles during high-speed flight is primarily induced by fluctuating air pressure bearing on the outside surface or skin of the missile. The source of the fluctuating pressure can be jet engine exhaust, unstable aerodynamic flow, oscillating shocks, wakes from nearby flow-distributing structures, the turbulent boundary layer, or some combination of the above. In spite of the possible complexity in the characteristics of the fluctuating pressure, the missile random vibration spectral and spatial characteristics are determined primarily by the mechanical structures. Thus, the fluctuating pressure field can be considered the stimulating, broad frequency energy source to which the missile responds in its characteristic modes. These resonant skin and internal structural modes determine the frequencies (random noise spectral characteristics) and locations and directions (spatial characteristics) of the response vibration.

Shaker Stimulation of Missile Vibration

The conventional means of reproducing flight-like vibration in missiles employs shakers. Typically, the device is an electrodynamic shaker with a random noise vibration output that can be controlled by sophisticated electronic servo systems. One or more of these shakers can be attached to a missile by clamp fixtures, and the missile forced to vibrate. With this system it is possible to force some monitored point in the missile to

vibrate in a manner resembling flight vibration. This forced vibration will be primarily in the direction of the shaker motion, unlike omnidirectional flight vibration, and will not resemble flight vibration at other points in the missile. Clamping the moving element (armature) of the shaker to the missile disturbs the natural vibration modes of the missile. This disturbing effect became more apparent as more thorough measurements of flight vibration were conducted recently (reference 1). One technique to resolve the problem is to clamp additional shakers on the missile at points where flight vibration is measured and to force those points to move in a flight-like manner. This technique further distorts the natural response modes of the missile so that other unmeasured points in the missile vibrate in a progressively less realistic manner.

Acoustic Stimulation of Missile Vibration

Recently, it was shown that reverberant acoustic facilities can recreate flight-like vibration in airborne stores. Typically, one or more stores are suspended near the center of the acoustic chamber and random noise acoustic power is fed into the room creating a diffuse acoustic pressure field sufficient to vibrate the missile. This method has proven effective in vibration tests of several Navy missiles undergoing reliability evaluations (reference 2). It is also a requirement in the MIL-STD-810 vibration test for airborne stores.

The success of the acoustic stimulation in recreating flight vibrations probably is due to similarity in the "forcing function."

In both instances the forcing function, or stimulus, is a broad frequency band of fluctuating pressure acting on the outside surface of the store, yet not interfering with the natural vibration responses that result. The disadvantage of the acoustic stimulation is the requirement for a large, expensive reverberant acoustic chamber and its poor operating efficiency.

RIVT PROTOTYPE AND EVALUATION

The RIVT represents an effort to combine some desirable features of the shaker and acoustic stimulation techniques. Like the acoustic facility it applies fluctuating pressures (the contact pressure during each impact) over the outside surface of the missile. Yet, like shakers, it requires little operational space or power to effect the stimulation of missile vibration.

RIVT Design

The initial prototype for the RIVT is shown in figure 1, connected to an 8 inch diameter missile motor section, to indicate the size and proportions of the device. In figure 2, the device is shown in a cross section sketch to illustrate the functional parts. In this view, three of the four essential functional elements are shown. The element not shown is a set of projectiles, typically small resilient rubber balls, which impart the vibration energy to the missile upon impact. The first element shown in the sketch is the chamber which encloses the test section of a missile, promoting rebound of projectiles for additional impacts. The second element is a motor driven impeller or slinger which restores kinetic energy to spent projectiles within the chamber. The third element is the provision for circulation such that the least energetic projectiles are returned to the slinger for restoration of energy.

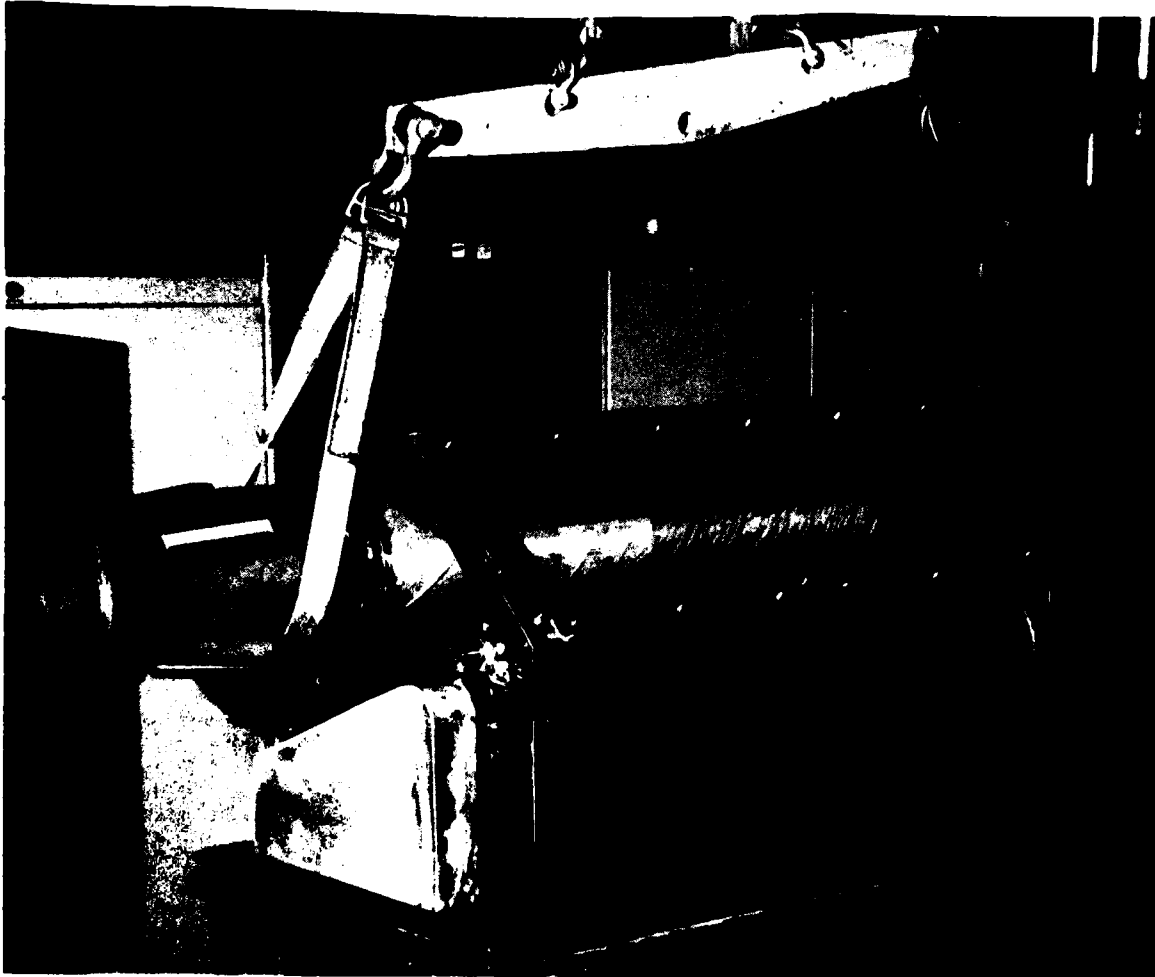


Figure 1. RIVT Attached to 8" Diameter Rocket Motor Section

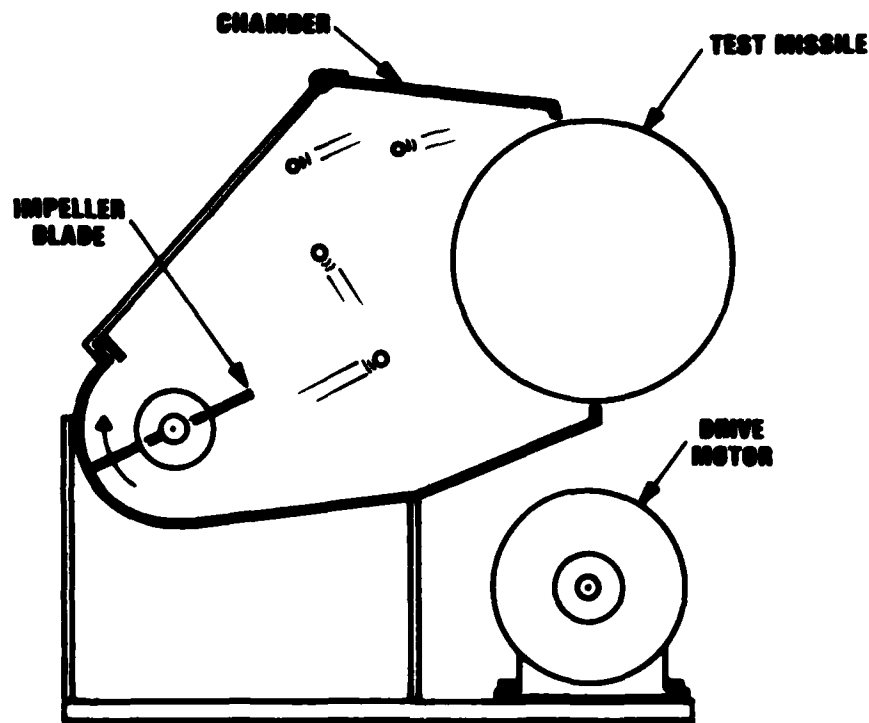


Figure 2. End View of RIVT Showing Functional Elements

Chamber

There are some details associated with each of the functional elements worthy of further discussion. The cross sectional shape of the chamber incorporates an approximation of an elliptical section. The degree and purpose of the approximation is indicated in figure 3, where the two foci positions are indicated by asterisks. The elliptical surface has the property of reflecting any ray leaving one focus toward the other focus. In figure 3, a range of trajectories, over a 90° sector, is indicated as rays starting from the left focus. It can be seen that those balls that don't directly strike the perimeter of circular section of the missile, are reflected toward the center of the circular section, which corresponds to the right focus of the ellipse. Thus, the reflected balls trajectories are normal to the missile surface and there will be maximum effect or energy exchange during impact. The relationship between the dimensions of the elliptical chamber and the cylindrical missile was determined by trial and

error, to give an even distribution of impacts over the missile surface. The even distribution, indicated in figure 3, is dependent upon an even distribution of trajectories starting from the left focus of the ellipse. To achieve that distribution over the 90° sector, there is a deflector at the focus which scatters the balls leaving tangentially from the impeller. This unit has the appearance of a scalloped blade with the peaks or maximum extensions positioned to deflect balls to the lower extreme of the 90° sector and the notches corresponding to a grazing angle of incidence with the tangential path from the impeller, which is the upper extreme of the sector. This description and illustrations refer to a chamber covering one half the surface of the missile and such an arrangement has proven successful. However, a duplicate chamber, to cover the other half of the missile, was added to increase the impact rate and the results reported in a subsequent, evaluation section were acquired with that addition.

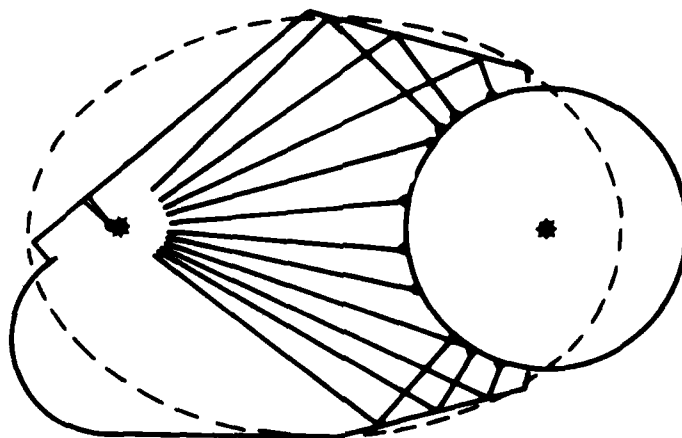


Figure 3. Elliptical Aspect of Chamber Shape with Deflector and Missile Located at Foci

Impeller

The impeller is a paddle wheel which sweeps balls, entering at the bottom, up to the deflector unit with an exit velocity corresponding to the blade tip velocity. The tip section of the blade is made of a flexible material which can deflect when the blade tends to jam on entering balls. The blade diameter is slightly greater than the missile radius, so that the top of its arc corresponds to the focus which is level with the missile centerline and the bottom of the arc is somewhat below the missile to facilitate gravity return of the balls. The shaft of the paddle wheel is driven via a belt drive by a variable speed motor. In the prototype, the resultant impeller speed range is 200 to 1800 rpm which, coupled with the five inch diameter impeller blade dimension, yields a maximum projectile velocity of approximately 40 feet per second.

Circulation

The requirement of circulation is to return spent balls to the impeller with a minimum of interference with the other rebounding balls within the chamber. In this prototype the balls that are not bouncing appreciably will roll to the low point in the chamber which is the inlet to the impeller, thus, satisfying the circulation requirement.

Projectiles

The set of projectiles is the most important functional element of the machine and has been the most difficult to perfect. The choice of a spherical shape seemed appropriate to assure that spent projectiles could roll back to the impeller. The proper choice of size, number and material for those spheres has

been more difficult and is incomplete. The original choice was resilient plastic balls with diameters between 1/2 inch to one inch in sets numbering between 25 and 50. Nylon, phenolic and teflon plastics were used in the prototype machine and the more resilient nylon and phenolic balls performed best. In this instance good performance meant a sustained, lively, erratic motion of the balls within the chamber and infrequent returns to the impeller mechanism. However, when missile sections were exposed to impacts from the plastic balls the response vibration tended to have too much high frequency energy. The first attempt to reduce the high frequency responses used rubber sheeting over the missile skin as a mechanical "low pass" filter. When the thickness of rubber sheeting was sufficient to reduce the high frequency part of the response spectrum there was also a great reduction in the overall vibration effect. Therefore, current efforts to control the spectrum are oriented toward the ball material. An extension of Hertz theory of impact involving solid spheres indicates that the modular of elasticity is an important property of the projectile influencing the response vibration spectrum of an impacted plate (reference 4). This is supported by experience with the RIVT in attempts to match flight vibration spectrums. Best results so far were achieved with a mixture of ball types, with one inch diameter hard rubber balls to excite responses up to 800 Hertz and one half inch diameter nylon balls to excite the higher frequencies. The best mixture for matching flight data at the front section of one missile contained 40 rubber balls and eight nylon balls. Further aft on the same missile the best proportion became 40 rubber and 18 nylon balls to create more high frequency responses that were measured in flight.

RIVT Evaluation

Current efforts to develop the prototype machine have concentrated on the ball material, as it affects response vibration. It has been possible to use the machine with three different Navy missile types for which there were flight vibration measurements. In each instance it was the actual flight test vehicle that was then exposed to the RIVT enabling a direct comparison with the measured flight vibration.

Spatial and Spectral Comparisons

The majority of experimentation has been done with a Navy air-to-air missile as the test vehicle. This missile is 8 inches in diameter and approximately 12 feet long. However, interest in the missile vibration is typically limited to the electronics sections, which for this missile are the seeker section at the front and the control section near the center of the missile. Therefore, the RIVT stimulus

was applied to the forward 30 inch length of the seeker section (immediately aft of the radome) for one experiment and to the center 30 inch length of the missile, including the control section, for a second experiment. The best results for each of these experiments is shown in figure 4. This figure shows the results of the experiments with both sections in terms of power spectral density (PSD) plots for both flight and RIVT stimulated vibration. The small scale and size of the plots provides for an overview of the characteristics of the several vibration responses in the missile. A detailed review of each of the individual comparisons can detect differences greater than would normally be tolerated in a single axis vibration test. The overview shows that the RIVT vibration is similar to flight in terms of spectrum shape, and of perhaps greater significance, both occur simultaneously in the two axes of measurement. This matching of the multi-axis character of flight vibration allows the internal electronic components to respond similarly, thus improving test realism.

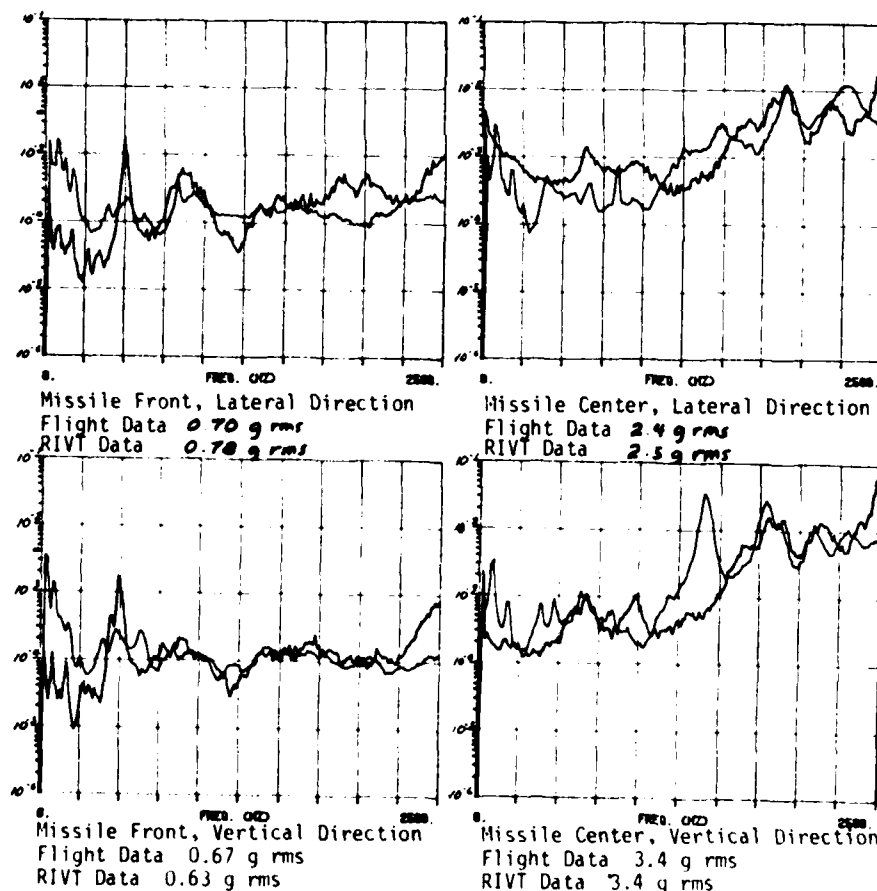


Figure 4. Comparison of flight plots, with 256 degrees of freedom, in units of g^2/Hz vs. Hz , for vibration in eight inch diameter missile

Random Characteristics

Although spatial and spectral characteristics are the conventional way of looking at random noise vibration, the RIVT mechanism invites further analysis. The major concern is the degree of randomness in the missile vibration in response to the discrete impacts. The nature of the impacts tends to be random, particularly with increasing numbers of balls in the chamber. The previous description of the design, described how the chamber geometry and a deflector unit tended to evenly distribute the impacts of balls leaving the impeller. As the number of active balls in the chamber grows large, most impacts will come from balls that have rebounded several times since leaving the impeller and there is an inherent randomness associated with such a phenomenon. This random characteristic can be seen in figure 5, the autocorrelation function

of one of the accelerometer signals from the missile, with the top trace corresponding to flight data and the bottom trace from RIVT stimulation. In each instance the amplitude of the function approaches zero with increasing time delay in a fashion characteristic of band-limited white noise (reference 3). There is also a tendency for the impacts to even out over the exposed missile surface as evidenced in figure 6, which is the pattern of impacts recorded on a carbon backed sheet of paper placed on the impacted surface of the missile. Because all the balls were the same size and material, the variation in dot size in the pattern is an indication of the variation in impact intensity as evidenced by the degree of ball deformation causing carbon transfer. A better measure of the apparently random variation in impact intensity and period shows in the acceleration versus time records in figure 7 of the vibration sensed in

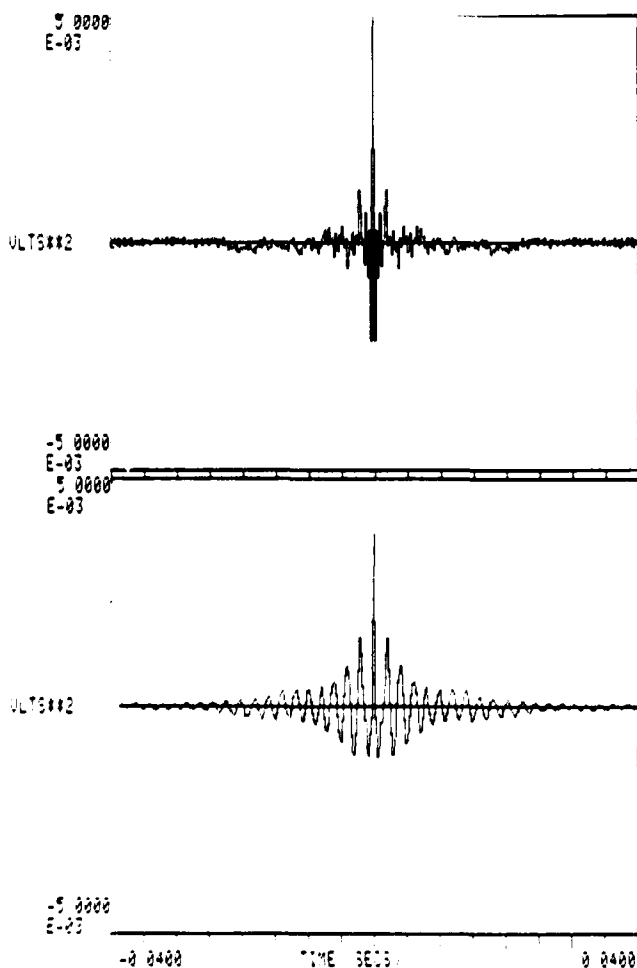


Figure 5. Autocorrelation Function of Missile Vibration (Top Plot of Flight Data and Bottom Plot of RIVT Data)

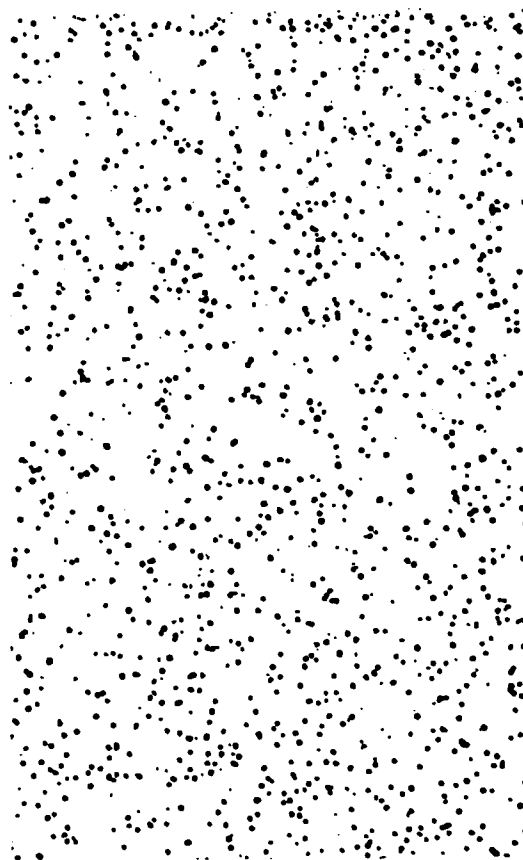


Figure 6. Sample of Impact Pattern Over a Section of Missile Surface

a five inch diameter missile, where the individual traces correspond to bulkhead and internal electronic module responses. In figure 7 it can be seen also that the evidence

of discrete impacts decreases as the vibration energy progresses into the missile electronics equipment.

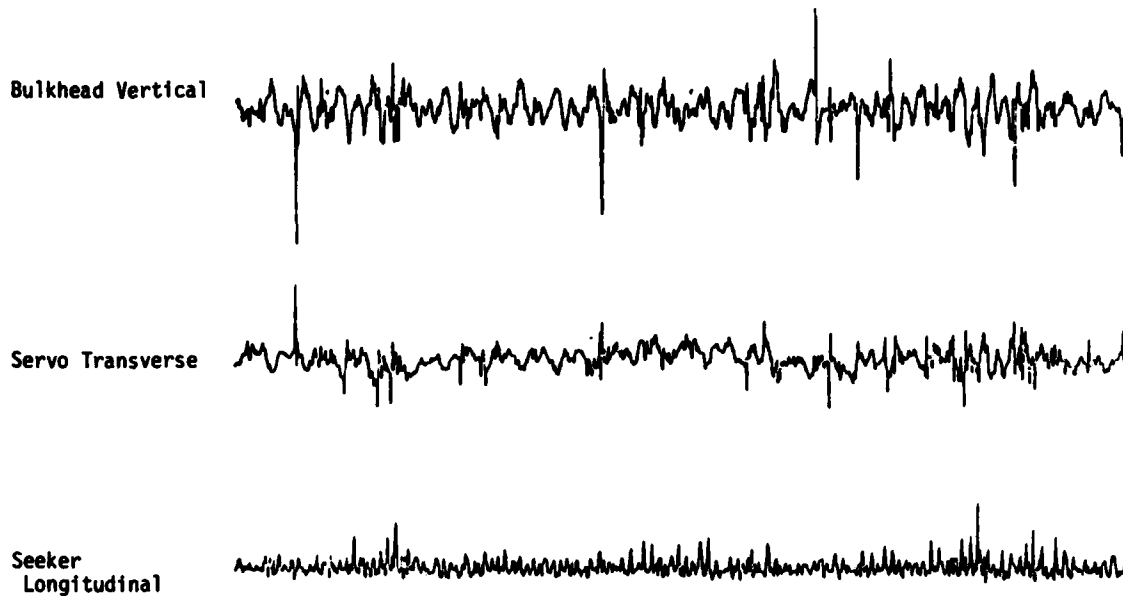


Figure 7. 1 Second Sample of Acceleration versus Time at Bulkhead and Electronic Modules

SUMMARY

The foregoing discussion and figures have described a simple vibration machine and some realistic results achieved with that machine. The machine simplicity is evidenced by its single, motor driven moving part, the impeller and by the total fabrication cost being less than \$2,000. The realism of the vibration was demonstrated for a variety of missile types in terms of both spatial and spectral similarity to flight measurements. The simple machine created realistic vibration when powered by a fractional horsepower motor, thus, presents potential as a cost effective vibration source. Effort is continuing to improve the Gaussian character of the vibration and to adapt the RIVT concept to use with other types of avionic equipment.

REFERENCES

1. Spandrio, A. M. and Burke, M. E. "Acoustics or Shakers for Simulation of Captive Flight Vibration," The Shock and Vibration Bulletin 48, Part 4, pp. 5-14, September 1978.
2. Meeker, D. B. and Everett, W. D. "U.S. Navy Experience on the Effects of Carrier-Aircraft Environment on Guided Missiles," AGARD Conference Proceedings No. CP270 MISSILE SYSTEM FLIGHT MECHANICS, pp. 42-1 through 16, May 1979.
3. Harris, C. M. and Crede, C. E. "Shock and Vibration Handbook," McGraw-Hill Book Co., 1961, pp. 22-25.
4. Ibid., p. 9-3

DISCUSSION

Mr. Sazama (Naval Surface Weapons Center): Is this the first machine of this type that you have built?

Mr. Everett: Yes, it is.

Mr. Sazama: And do you have to replace the balls after awhile?

Mr. Everett: Not yet, because we really haven't put a lot of hours on the balls, in fact, part of the process so far has been determining what kind of ball materials excite the right kind of frequencies in the missiles and my first guess was bad. At first I had a lot of relatively hard plastic balls and they brought out too much high frequency. I'm now investigating the merits of using softer more rubber like balls.

Mr. Werback (Naval Weapons Center): Doug, how do you account for the relatively high level of longitudinal response that you got versus transverse response?

Mr. Everett: It was a resonant response on a module within the missile. It amplified at a certain band of frequencies and the response just happened to be in the longitudinal direction.

PARAMETERS FOR DESIGN OF REVERBERANT ACOUSTIC CHAMBERS FOR TESTING AIR-CARRIED MISSILES

T. W. ELLIOTT
PACMISTESTCEN
POINT MUGU, CALIFORNIA

Rectangular box-shaped reverberant acoustic chambers were theoretically analyzed, using a normal-mode model, for the purpose of optimal design for simulating captive flight vibration of air-carried missiles. A mathematical derivation relating chamber volume to minimum usable frequency was derived. It was determined that minimum usable frequency varied inversely as the square root of the volume ratios. A computer program was generated to investigate the important parameters for design of these chambers. It was found that, apart from some general rules-of-thumb to avoid in acoustic chamber design, there was no over-riding reason to select one configuration over another.

INTRODUCTION

Reverberant acoustic chambers have been extensively analyzed in the literature, particularly the rectangular box-shaped chamber. As new applications for acoustic chambers occur the analysis is extended to investigate optimum criteria for the new application.

The Pacific Missile Test Center (PACMISTESTCEN) has been using rectangular box-shaped reverberant acoustic chambers for several years to simulate the vibration response of an air-carried guided missile during captive flight.

This paper extends the general analysis of these chambers to the application of simulation of vibration response of air-carried guided missiles. In particular, a criteria for minimum usable frequency of a chamber is defined and justified. The relationship between this minimum frequency and chamber volume is derived and the criteria is used to compare several configurations to determine the optimum configuration for testing of air-carried guided missiles.

BACKGROUND

A reverberant acoustic chamber may be defined as an enclosure with rigid reflecting walls excited by an acoustic power source. Sound power emanating into the enclosure is reflected by the walls resulting in a reverberant sound field. The waves of the sound field are known to obey the three-dimensional wave equation

$$\nabla^2 \Phi - \frac{1}{c^2} \frac{\partial^2 \Phi}{\partial t^2} = 0 \quad (1)$$

where Φ = velocity potential

Analytical solutions to the equation are possible for simple geometric figures such as rectangular rooms, sphere, cylinder, etc. The most easily solvable geometric figure is the rectangular box. For this reason, and for the fact it is also the most easily constructed, the rectangular room reverberant acoustic chamber has been extensively studied.

The frequency solution to this equation for the rectangular room, assuming totally reflecting walls, is:

$$f = \frac{c}{2} \sqrt{\frac{N_x^2}{L_x^2} + \frac{N_y^2}{L_y^2} + \frac{N_z^2}{L_z^2}} \quad (2)$$

where c = speed of sound

f = frequency

L_x, L_y, L_z = room dimensions in the x, y, z directions.

N_x, N_y, N_z = integer numbers corresponding to the eigenvalue solution of the equation.

Examination of equation (2) reveals that the spacing between frequencies decreases as frequency increases. Thus, it is generally accepted that the reverberant sound field is diffuse at high frequencies, where the mode density is high, when driven by a source capable of exciting these modes, and is not

diffuse at low frequencies, where mode density is low. Also, when the mode density becomes high it, for most cases, becomes random (reference 1).

The concept of a diffuse sound field assumes that the sound field consists of equal amplitude plane waves traveling with equal probability in all directions as a result of multiple reflections off the boundaries of the chamber. At high frequencies, where modal density is high, a random source excites many chamber resonances, each of which exhibits a preferred direction of propagation. As more modes are excited, the number of directions of wave propagation increases until the sound field exhibits characteristics which are statistical in nature (random). The sound field is then said to be diffuse which assumes uniform distribution of energy density and equal intensity in all directions at all points. The transition point has never been clearly defined, however, the sound field is generally accepted to be diffuse at high frequencies, where modal density is high, and is not diffuse at low frequencies, where modal density is low.

Thus, the concept of a diffuse, and random, sound field assumes:

- a. High modal density - the frequency field should include many resonances.
- b. Smooth frequency distribution - the frequency field should not concentrate energy in certain bands or leave gaps.
- c. Homogeneity - the field should not be dependent upon spatial location.

The Production Acceptance Test and Evaluation Division of the U.S. Navy at PACMISTESTCEN has been using reverberant acoustic chambers for several years to subject Navy air-launched missiles to acoustically induced vibration for the purpose of simulating the missile vibration response that occurs during in-service captive flight. The chamber requirements for simulation of this environment are:

- a. Isotropy - the energy must flow in all directions simultaneously.
- b. Similarity - vibration responses similar to that which occurs in a guided missile during captive-flight.

When compared to vibration simulation results using mechanical shaker systems, the reverberant acoustic chambers fulfill the above requirements sufficiently well that they have become the preferred vibration excitation technique at the PACMISTESTCEN when simulation at all points in all directions simultaneously is desired, and the in-service source excitation is primarily aeroacoustic in nature.

There are currently five reverberant acoustic chambers operating at the PACMISTESTCEN (two more are partially completed chambers and should be operable by the time this paper is published). The first, and smallest, is a pentagonal cross-section shaped cylindrical chamber of 350 ft³. Simulation results from this chamber led to construction of a larger rectangular box shaped chamber of 1993 ft³ and side length ratios of 1.00/0.79/0.63. This volume was selected because it was the largest chamber of this set of side length ratios that would fit within a room selected as a housing for the chamber. Three more duplicates of this chamber were constructed. Two more chambers were constructed of 2900 ft³ in the same shape and side length ratios as the 1993 ft³ chambers. Again the volume was selected for reasons of convenience and the side length ratios were maintained because satisfactory simulation results were obtained from the smaller chambers.

Early test results showed that when simulation required energy at low frequencies it was necessary to augment the acoustic chamber with a mechanical shaker and cross over excitation control at some frequency where the acoustic field became sufficiently broadband and diffuse. As chamber size increases this cross-over point decreases. However, a precise theory relating this cross-over point to chamber size was not known and this point was determined empirically after selection of a size and completion of construction.

RELATIONSHIP BETWEEN MINIMUM USABLE FREQUENCY AND CHAMBER VOLUME

Two different theories relating minimum usable frequency to chamber volume have been published. Each of these were developed from different assumptions of what constituted minimum usable frequency and each resulted in different relationships to volume.

Schroeder, in 1964 (reference 2), required that "the average spacing of the resonance frequencies be smaller than one-third of their 3 dB down bandwidth", or "the normal or eigen modes of an enclosure overlap each other in a ratio of 3:1." Based on this requirement he defines the lowest frequency, f_c , as

$$f_c = 2000 \left(\frac{T_{60}}{V} \right)^{\frac{1}{2}} \quad \text{for } f_c > 300 \text{ Hz} \quad (3)$$

where T_{60} is the reverberation time of the enclosure and V is the volume. Therefore, if T_{60} is constant, f_c varies inversely as the square root of the volume. If T_{60} varies, or is unknown, this relationship is not very useful for design of a new enclosure.

Sepmeyer, in 1965 (reference 3), proposed formulas "for determining the lowest frequency for which a given room meets the criterion for

number of modes in the lowest usable band." His proposals are:

For a 1-octave band containing 20 modes

$$f_0 = 1150/V^{1/3} \quad (4)$$

For a 1/2-octave band containing 12 modes

$$f_0 = 1280/V^{1/3} \quad (5)$$

For a 1/3-octave band containing 9 modes

$$f_0 = 1350/V^{1/3} \quad (6)$$

Thus, the lowest frequency varies inversely as the cube root of the volume. These relationships, however, do not appear to satisfy the broadband requirement, particularly if f_0 is high.

This paper analyzes the same question from the requirements of testing air-carried missiles and uses empirical data gathered from experience in this type of testing.

APPROACH

Equation (2) generates all the frequencies that are compatible with a chamber of given dimensions by letting the mode numbers, N_x , vary from zero to infinity. By truncating the set of mode numbers at some dependent set such that

$$\frac{N_x^2}{L_x^2} + \frac{N_y^2}{L_y^2} + \frac{N_z^2}{L_z^2} \leq \text{constant} \quad (7)$$

equation (2) generates all the compatible frequencies below some upper frequency limit. The solution of this problem for the number of compatible frequencies, or eigentones, below an upper limit has been extensively analyzed. Maa, in 1939 (reference 4) presented the following approximation for the number of eigentones below a given frequency.

$$N = \frac{4\pi Vf^3}{3c^3} \left\{ 1 + \frac{3Sc}{16Vf} + \frac{3Lc^2}{8\pi V f^2} \right\} \quad (8)$$

Where N = no. of eigentones below f
 f = limiting frequency
 V = chamber volume
 c = speed of sound
 S = surface area of chamber
 $L = L_x + L_y + L_z$

The generalized solution for equation (8) is shown in figure 1.

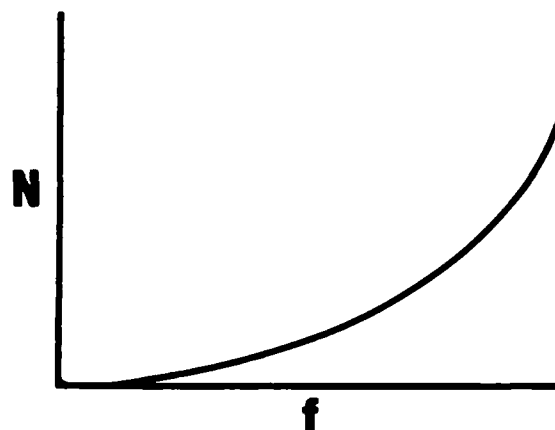


FIGURE 1. Generalized Solution to Equation 8 for Number of Eigentones (N) Below Any Frequency (f)

Examination of figure 1 reveals the lack of continuum, or broadbandness, at low frequencies. Thus at low frequencies the acoustic chamber will not provide broadband diffuse excitation necessary for testing of missiles. Above some minimum frequency the acoustic chamber is satisfactory.

The determination of this minimum frequency is of prime concern. When an acoustic chamber requires the augmentation of a mechanical shaker for testing of missiles, this minimum frequency is the theoretical cross-over point between shaker and chamber control of vibration response. In the PACMISTESTGEN chambers, this cross-over was determined empirically such that missile vibration response closely reproduced vibration measured in captive flight.

One of the purposes of this investigation is to find a definition of the minimum usable frequency which has a theoretical basis, satisfies the criteria for testing of missiles, and agrees with experience. For the purposes of this investigation, after examining the characteristics of the acoustic field predicted by equation (3) and comparing to missile testing requirements, the following definition and criteria is proposed:

"The minimum usable frequency is that frequency which is the lower band edge of the lowest 1/3 octave bandwidth which will contain eigentones in at least 2/3 of the 1 Hz bandwidth windows centered on the integer frequencies."

In other words, if the frequency solutions to equation (2) are rounded to the nearest integer frequency they will include at least

2/3 of the integers in the lowest usable 1/3 octave band.

Most of the empirical data collected on the PACMISTESTCEN acoustic chambers has been on a design of 1993 ft³ with side length ratios of 1/0.79/0.63 which yields side lengths of 15.88 ft, 12.55 ft, 10.00 ft. There are three of these chambers. Initial testing with these chambers to determine optimum techniques for testing air-carried missiles proved that the addition of shakers was necessary to obtain vibrations down to 20 Hz and that a cross-over point between the two excitation techniques was about 150 Hz. Thus vibrations from 20 Hz to 150 Hz were provided primarily from the shakers and the vibrations above 150 Hz were provided by the acoustics. The criteria above was empirically derived from a solution to equation (2) for this design with the desired constraints of using common vibration terms for simplification. Solving for the eigentones (equation (2)) of this chamber yields a theoretical minimum frequency, or cross-over point, of 167 Hz. This is considered to be good agreement when one takes into the account the techniques of mechanical shaker vibration control.

The definition of minimum usable frequency above specifies a minimum acceptable deviation from a vibration spectrum continuum but does not put any criteria on diffusivity. Solving equation (2) for this chamber for all the modes that yield eigentones in the 1/3 octave above 167 Hz yields the following statistics for the two-thirds of the 1 Hz windows which can contain energy:

- a. Fifty percent of the 1 Hz windows couple obliquely - energy will be supported in all three axes.
- b. Forty-five percent of the 1 Hz windows couple tangentially - energy will be supported in two axes.
- c. Five percent of the 1 Hz windows couple axially - energy will be supported in only one axis.

Since the theoretical minimum frequency is in good agreement with experiment the above is considered sufficiently diffuse.

Thus the proposed criteria appears valid enough upon which to base a more detailed analysis.

MATHEMATICAL DERIVATION

This analysis is concerned with determining a mathematical relationship between chamber volume, for a given configuration, and the minimum usable frequency as defined above. The mathematical derivation of this relationship is rendered non-trivial by the limitation

of a constant 1 Hz wide gap as undesirable, independent of chamber volume.

Initially, it might appear that the solution to this problem is trivial and of the form proposed by Sepmeyer: i.e.,

$$f \propto \frac{1}{(V)^{1/3}}$$

This, however, describes the value of the frequency for a consistent set of modal index numbers when chamber volume varies and the side length ratios are held constant. This can be shown most simply by considering a cube, where

$$L_x = L_y = L_z$$

then

$$f = \frac{c}{2} \sqrt{\frac{(N_x)^2 + (N_y)^2 + (N_z)^2}{L_x^2}}$$

and, letting

$$(N_x)^2 + (N_y)^2 + (N_z)^2 = N^2$$

and recognizing that

$$V = L_x^3$$

then

$$f = \frac{c}{2} \sqrt{\frac{N^2}{V^{2/3}}} \quad (9)$$

or

$$f = \frac{cn}{2(V)^{1/3}} \quad (10)$$

Therefore, between two chambers of different volume and constant side length ratios, the value of frequency for constant modal index numbers is so defined. Taking the lower and upper frequencies of a 1/3 octave bandwidth this relationship will define the equivalent frequencies and 1/3 octave bandwidth for the new chamber. However, the number of frequencies within this 1/3 octave will remain constant and, therefore, the modal density will change. It seems reasonable that the lowest usable frequency of the new chamber could be lower than predicted by this relationship if the chamber is larger and, thus, the modal density in this equivalent 1/3 octave is greater.

If a chamber is of a shape such that the modal distribution curve is closely approximated by the smooth curve of figure 1, the modal density, where modal density is defined as,

$$\frac{N_u - N_l}{B} \quad (11)$$

Where B = bandwidth of 1/3 octave
 N_u = number of eigentones below
upper limit of 1/3 octave
 N_L = number of eigentones below
lower limit of 1/3 octave

scales in a simple way with chamber volume when relative dimensions are held constant. The criteria requires that, over the lowest usable 1/3 octave, the density of gaps, or voids, in one chamber is equal to that in another chamber with a different volume but the same dimensional ratios. This relationship will be approximately satisfied by equal modal density of the eigenfrequencies in the lowest usable 1/3 octave. Thus for two chambers of different volumes having the same modal density over bands B_1 and B_2 respectively,

$$\left(\frac{N_u - N_L}{B}\right)_1 = \left(\frac{N_u - N_L}{B}\right)_2 \quad (12)$$

The value of the various M's is given by equation (8) and the bandwidth B is given by

$$B = f_u - f_L \approx \frac{5}{4} f_L - f_L = f_L/4 \quad (13)$$

Solving for chamber 1 from equation (8)

$$N_{L1} = \frac{4\pi V_1 f_{L1}^3}{3c^3} \left\{ 1 + \frac{3S_1 c}{16V_1 f_{L1}} + \frac{3L_1 c^2}{8\pi V_1 f_{L1}^2} \right\} \quad (14)$$

and, since

$$f_{u1} \approx \frac{5}{4} f_{L1}$$

$$N_{u1} = \frac{4\pi V_1 125 f_{L1}^3}{3c^3 64} \left\{ 1 + \frac{3S_1 c}{20 V_1 f_{L1}} + \frac{6 L_1 c^2}{25\pi V_1 f_{L1}^2} \right\} \quad (15)$$

From (13)

$$B_1 = \frac{f_{L1}}{4}$$

Combining (13), (14), and (15) into the form of (12)

$$\left(\frac{N_u - N_L}{B}\right)_1 = \frac{1024\pi V_1 f_{L1}^2}{183 c^3} \left\{ 1 + \frac{27S_1 c}{244 V_1 f_{L1}} + \frac{24L_1 c^2}{244\pi V_1 f_{L1}^2} \right\} \quad (16)$$

By similarity, for chamber 2,

$$\left(\frac{N_u - N_L}{B}\right)_2 = \frac{1024\pi V_2 f_{L2}^2}{183 c^3} \left\{ 1 + \frac{27S_2 c}{244 V_2 f_{L2}} + \frac{24L_2 c^2}{244\pi V_2 f_{L2}^2} \right\} \quad (17)$$

From (12)

$$\frac{1024\pi V_1 f_{L1}^2}{183 c^3} \left\{ 1 + \frac{27S_1 c}{244 V_1 f_{L1}} + \frac{24L_1 c^2}{244\pi V_1 f_{L1}^2} \right\} = \quad (18)$$

$$\frac{1024\pi V_2 f_{L2}^2}{183 c^3} \left\{ 1 + \frac{27S_2 c}{244 V_2 f_{L2}} + \frac{24L_2 c^2}{244\pi V_2 f_{L2}^2} \right\}$$

or

$$V_1 f_{L1}^2 = V_2 f_{L2}^2 \left[\frac{1 + \frac{27S_2 c}{244 V_2 f_{L2}} + \frac{24L_2 c^2}{244\pi V_2 f_{L2}^2}}{1 + \frac{27S_1 c}{244 V_1 f_{L1}} + \frac{24L_1 c^2}{244\pi V_1 f_{L1}^2}} \right] \quad (19)$$

This indicates that the minimum usable frequency ratio varies as the square root of the volume ratio multiplied by the bracketed

term. It will be shown below by numerical analysis for several volume ratios, holding the shape constant, that only a small error is introduced in the calculation of the minimum usable frequency by neglecting the bracketed term of (19). If, for simplification purposes, this term may be neglected,

$$\frac{f_{L1}}{f_{L2}} = \left(\frac{V_2}{V_1}\right)^{1/2} \quad \text{for} \quad \frac{L_y}{L_x} \cdot \frac{L_z}{L_x} = \text{constant} \quad (20)$$

The relationship for minimum usable frequency for testing of air-carried guided missiles follows the same form as proposed by Schroeder (reference 2). Equation (20) then provides a good first approximation to chamber volume requirements for a desired minimum usable frequency when scaling from one chamber to a second of the same side-length ratios. Any real new chamber design must be supported by a complete solution to equation (3).

COMPUTER INVESTIGATION

To determine how closely equation (20) can predict minimum usable frequency a computer analysis was performed. The procedure was as follows:

a. Sets of side length ratios were initialized and allowed to vary as follows:

$$L_x = 1.0$$

$$L_y/L_x = 0.51 \text{ to } 0.96 \text{ at } 0.05 \text{ increments}$$

$$L_z/L_x = L_y/L_x \text{ to } 0.96 \text{ at } 0.05 \text{ increments}$$

b. For each set of side length ratios the volume was doubled from 1000 ft³ to 128,000 ft³, (i.e., 1000, 2000, 4000, 8000, etc.).

c. For each volume and set of side length ratios the minimum usable frequency was determined using the first definition.

d. For each set of side length ratios the calculated minimum usable frequencies and volumes were fitted to a linear curve of the form

$$f = \frac{m}{V^{1/2}} + b \quad (22)$$

and the linear regression coefficient was determined.

This amounted to 55 separate linear regression coefficients being determined for as many sets of side length ratios. To four

decimal places, the linear regression coefficients varied from 0.9642 to 0.9997. The value of b, which is a correction to the value of frequency, varied from 6.4039 to -22.6441. This is considered sufficient support for the validity of equation (20).

INVESTIGATION OF OPTIMUM CHAMBER SHAPE

Other investigations have been performed to define best shapes of rectangular box-shaped acoustic chambers. These were typically performed to determine best shape for general usage rather than for a specific application. The most comprehensive of these is the work conducted by Sepmeyer (reference 3). Sepmeyer studied the modal frequency distribution and angular distribution with a digital computer, developed merit criteria and rated various configurations relative to each other. His merit criteria defined, for each configuration, an average and rms value for, (1) modal spacing irregularity, and (2) angularity of the modes. Angularity was defined as the actual number of modes with direction cosines within a solid angle compared to the expected number of modes. Based on this investigation Sepmeyer recommends, as best shapes, rectangular box-shaped chambers with side length ratios of: (1) 1.00/0.83/0.65, (2) 1.00/0.82/0.72, and (3) 1.00/0.69/0.43. He also discussed a chamber with side length ratios of 1.00/0.79/0.63 as giving good results but comments on its high sensitivity to small variations in dimensionality. It was this last set of side length ratios PACMISTESTCEN selected for the above chambers for reasons of convenience.

COMPUTER INVESTIGATION

A computer program was generated to investigate the important parameters of rectangular box-shaped reverberant acoustic chambers for side length ratios from 1.00/0.50/0.50 to 1.00/1.00/1.00 in increments of 0.01 in the Y and Z dimensions. This program used a constant volume of 1993 ft³ for comparison to one of the acoustic chambers at PACMISTESTCEN. The program first calculated the lengths of each side for the particular set of side length ratios and then calculated all the frequencies generated by equation (2). For ease of determination of which 1 Hz bandwidth each frequency belonged, each calculated frequency was rounded to the nearest integer frequency. The number of calculated frequencies for each integer frequency from 0 to 350 Hz was then calculated and analyzed to determine the minimum usable frequency and the rms value of the frequency count.

The minimum usable frequency was determined from the previous definition. Starting at 1 Hz each integer frequency value was checked to determine whether any calculated frequency value occurred for that frequency. If no calculated frequency had occurred the next

integer frequency was checked. If one or more calculated frequencies occurred at the frequency (f_0), the 1/3 octave bandwidth upper level was calculated ($5 f_0/4$) and rounded upward to the next integer frequency (if not an integer itself). The 1/3 octave bandwidth was checked at each frequency to determine whether calculated frequencies had occurred at 2/3 or more ($5 f_0/16$ or more) of the 1/3 octave. If calculated frequencies occurred at 2/3 or more of the 1/3 octave, the lower band edge, f_0 , was called the minimum usable frequency. If not, the process was repeated until a minimum usable frequency was found.

The rms value of the frequency count was determined by counting the number of times a calculated frequency (rounded off) equaled an integer frequency and then calculating the rms value of these counts for all frequencies from the previously determined minimum usable frequency up to 350 Hz. It is assumed that the rms value provides a measure of the smoothness of the frequency energy field in an acoustic chamber. In other words a chamber that has its energy spread out over the frequencies would have a smoother frequency energy field than a chamber that concentrated its energy in a few number of frequencies. The lower the rms value, the smoother and more desirable a particular chamber configuration appears.

Then, the computer was programmed to do two sorts to provide a list of all chamber configurations, ordered from lowest to highest, by (1) minimum usable frequency, and (2) rms value. From these lists, the preferred chamber configurations could be determined by selecting those that appear in the early parts of both lists.

One final computer program was generated to investigate dimensional sensitivity. Reference 3 recommended a minimum variance of 0.01 in side length ratio for analysis purposes as this was equal to one percent and represents the best tolerance of building trades for this kind of construction (concrete walls). This may be true, however, for the chamber size used in this analysis it represents a deviation of 1.8 inches. If, with detailed attention to dimensions during construction, that tolerance can be reduced, what tolerance is necessary to assure achieving desired chamber characteristics? One particular configuration was selected, which was the "best" from the analysis above, the side length ratios of this configuration were allowed to vary ± 0.01 in increments of 0.001. The minimum usable frequency and the rms value were determined for each of these "new" configurations to investigate dimensional sensitivity.

RESULTS AND DISCUSSION

The lists, ordered from lowest to highest by minimum usable frequency and by rms, were compared for the top 30 in each list and the top 100 in each list. Only one configuration (1.00/0.69/0.98) ranked in the top 30 on both lists. This configuration ranked in the top 10 for minimum usable frequency and the top 20 for rms. Except for this configuration, the lack of correlation between these two lists indicates the difficulty in selecting a preferred configuration. Comparison of the top 100 for both lists revealed a total of 21 configurations that appeared on both lists. Table 1 lists these 21 configurations, the minimum usable frequency, the rms value, and their rank on each list.

TABLE 1

Ly/Lx	Lz/Lx	MF	MF		rms
			rms	Rank	Rank
0.68	0.71	146	1.1906	1	97
0.69	0.98	156	1.1413	9	17
0.74	0.90	157	1.1705	15	48
0.91	0.98	157	1.1706	16	49
0.90	0.98	158	1.1774	20	63
0.55	0.62	159	1.1571	32	31
0.64	0.91	160	1.1682	36	44
0.59	0.92	161	1.1338	39	11
0.63	0.70	163	1.1293	54	7
0.59	0.93	163	1.1797	55	68
0.85	0.93	163	1.1842	56	81
0.68	0.98	165	1.1531	72	25
0.64	0.93	165	1.1803	73	71
0.55	0.91	165	1.1839	74	79
0.66	0.92	166	1.1632	86	37
0.76	0.91	166	1.1648	87	39
0.63	0.69	166	1.1913	88	100
0.52	0.82	167	1.1787	94	65
0.68	0.72	168	1.1463	99	19
0.72	0.76	168	1.1511	100	22

The minimum usable frequency for all configurations was plotted, from lowest to highest, against run number in the sorted list. This is shown in figure 2. The lowest usable frequency ranged from 146 Hz to 278 Hz.

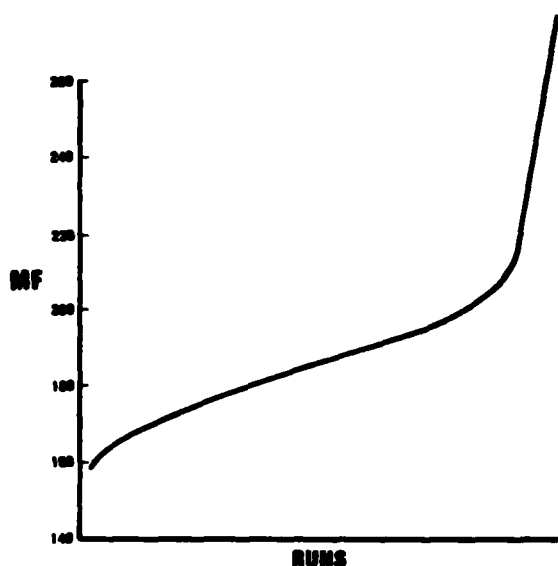


FIGURE 2. Sorted List of Minimum Usable Frequency (MF) for All Runs

The rms value for all configurations was plotted, from lowest to highest, against run number in the sorted list. This is shown in figure 3. The rms value ranged from 1.0799 to 2.2695.

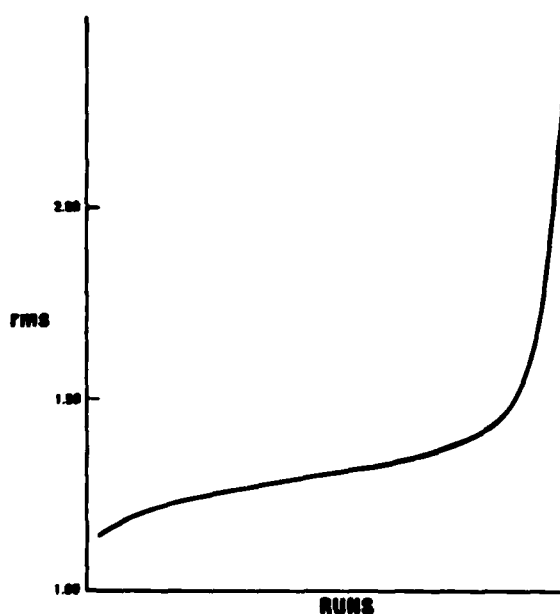


FIGURE 3. Sorted List of RMS for All Runs

Several strong correlations can be determined from comparison of figures 2 and 3. The shapes of the two curves are nearly identical. The first reflection point occurs around 50-100 runs. The second reflection point occurs around 1050 runs. In-between these two reflection points the plot may be represented by a straight line. The minimum usable frequency over the center portion ranges from 168 to 207. The rms value over the center portion ranges from 1.19 to 1.49.

A final correlation can be obtained from an examination of the individual configurations from each sorted list that are beyond the second reflection point. This data represented 230 runs on each test. As opposed to the first 30 or the first 100 there were many configurations that were common to both lists. An examination of all these configurations revealed some commonalities in patterns of these configurations which might be expected. These commonalities are:

1. Two sides equal.
2. One side a low multiple, 1:2, 2:3, 3:4, 3:5 of the other.

Of the last 230 runs, 155 were defined by these commonalities. Thus, while it is difficult to select preferred configurations, it is possible to define rules-of-thumb for configurations to be avoided.

For the final analysis the "best" configuration, 1.00/0.69/0.98, was selected and the Y and Z ratios were allowed to vary from 0.680-0.700 and 0.970 to 0.990 respectively in increments of 0.001. This analysis showed that even dimensional changes of 0.001 in side length ratios gave significant changes in results. Table 2 gives the pertinent characteristics of the range of side length ratios used in this analysis which may be used for comparison.

TABLE 2

CHARACTERISTICS FOR RANGE OF DIMENSIONAL SENSITIVITY ANALYSIS

Ly/Lx	Lz/Lx	Lx, ft	Ly, ft	Lx, ft	M.F.	rms
0.680	0.970	14.46	9.83	14.02	192	1.2526
0.680	0.980	14.41	9.80	14.12	165	1.1531
0.680	0.990	14.36	9.76	14.22	191	1.2065
0.690	0.970	14.39	9.93	13.96	165	1.1884
0.690	0.980	14.34	9.89	14.05	156	1.1413
0.690	0.990	14.29	9.86	14.15	188	1.2292
0.700	0.970	14.32	10.02	13.89	192	1.2924
0.704	0.980	14.27	9.99	13.98	189	1.2411
0.700	0.990	14.22	9.95	14.08	194	1.3833

This analysis looked at a total of 441 configurations within the range of table 2. For these configurations the minimum usable frequency varied from 153 to 218 and the rms value ranged from 1.0804 to 1.4762.

Table 3 shows the pertinent characteristics for some of these configurations. The first half of this table shows the effect of varying $L_y/L_x \pm 0.005$ around 0.980 in increments of 0.001 with L_z/L_x held constant at 0.690. The second half of the table shows the effect of varying $L_z/L_x \pm 0.005$ around 0.690 in increments of 0.001 with L_y/L_x held constant at 0.980. Of these 21 configurations only 11 would rank in the top 100 of minimum usable frequency and only nine would rank in the top 100 for rms value. It can be seen that there is no smooth pattern to the results and values show discrete jumps. The variance in actual dimensions, from configuration to configuration, is less than 1/8 inch which is below the normal tolerance for flatness of a concrete wall of the area used in this analysis. Thus a concrete acoustic chamber cannot be constructed to obtain characteristics derived from an analysis where side length ratios are held to ± 0.001 .

TABLE 3
PARTIAL RESULTS OF DIMENSIONAL
SENSITIVITY ANALYSIS

L_y/L_x	L_z/L_x	L_x , ft	L_y , ft	L_z , ft	M.F.	rms
0.690	0.975	14.36	9.91	14.00	189	1.2862
0.690	0.976	14.36	9.91	14.01	168	1.3025
0.690	0.977	14.35	9.90	14.02	156	1.2199
0.690	0.978	14.35	9.90	14.03	153	1.2371
0.690	0.979	14.34	9.90	14.04	153	1.1477
0.690	0.980	14.34	9.89	14.05	156	1.1413
0.690	0.981	14.33	9.89	14.06	195	1.1608
0.690	0.982	14.33	9.89	14.07	158	1.1276
0.690	0.983	14.32	9.88	14.08	158	1.1460
0.690	0.984	14.32	9.88	14.09	156	1.1548
0.690	0.985	14.31	9.88	14.10	159	1.1528
0.685	0.980	14.37	9.85	14.08	190	1.3265
0.686	0.980	14.37	9.85	14.08	163	1.2420
0.687	0.980	14.36	9.86	14.07	186	1.2138
0.688	0.980	14.35	9.87	14.06	158	1.1639
0.689	0.980	14.34	9.88	14.06	158	1.1818
0.690	0.980	14.34	9.89	14.05	156	1.1413
0.691	0.980	14.33	9.90	14.04	193	1.2151
0.692	0.980	14.32	9.91	14.04	193	1.3245
0.693	0.980	14.32	9.92	14.03	193	1.3856
0.694	0.980	14.31	9.93	14.02	190	1.2923
0.695	0.980	14.30	9.94	14.02	168	1.2058

From consideration of dimensional sensitivity and normal trade tolerances in wall placement and wall flatness an analytical selection of a "best" configuration is an academic exercise at best. As long as certain unfavorable design criteria are avoided, normal trade tolerances in construction probably act to blur distinctions between "best" configurations and configurations selected for other reasons such as convenience or cost.

CONCLUSIONS

A good criteria for determining the lowest usable frequency of a reverberant rectangular box-shaped acoustic chamber for testing of air-carried guided missiles is:

"The minimum usable frequency is that frequency which is the lower band edge of the lowest 1/3 octave bandwidth which will contain eigentones in at least 2/3 of the 1 Hz bandwidth windows centered on the integer frequencies."

Using the above definition, the minimum usable frequency varies as the inverse square root of the volume ratio, as follows:

$$\frac{F_{\ell 1}}{F_{\ell 2}} = \left(\frac{V_2}{V_1}\right)^{\frac{1}{2}}$$

Although it is possible to define best shapes for rectangular box-shaped reverberant acoustic chambers for simulation of captive flight vibration of air-carried guided missiles the dimensional sensitivity of these chambers is such that construction tolerances probably blur the advantage of one configuration over another. As long as some simple rules-of-thumb in design criteria are avoided there is probably no over-riding technical reason for selecting one configuration over another. The rules-of-thumb to avoid are:

1. No two walls the same length.
2. No two walls in low multiples of each other, i.e., 1:2, 2:3, 3:4, 3:5, etc.

REFERENCES

1. Ochs, John Baptist, "An Investigation of the Low Frequency Sound Field of a Reverberant Enclosure and the Effects of Digital Electronic Feedback," TM-79-192, Pennsylvania State College, of 17 Oct 1979.
2. Schroeder, M. R., "Improvement of Acoustic-Feedback Stability of Frequency Shifting," J. Acoust. Soc. Am. 36, 1718-1724, (1964).
3. Sepmeyer, L. W., "Computed Frequency and Angular Distribution of Normal Modes of Vibration in Rectangular Rooms," J. Acoust. Soc. Am. 37, 413-423, (1965).
4. Maa, Dah-You, "Distribution of Eigentones in a Rectangular Chamber at Low Frequency Range," J. Acoust. Soc. Am. 10, 235-238, (1939).

SPACECRAFT MODAL TESTING USING SYSTEMATIC MULTI-SHAKERS SINE-DWELL TESTING TECHNIQUES

F. H. Chu, C. Voorhees, W. W. Metzger, R. Wilding
RCA Astro-Electronics
Princeton, New Jersey

A systematic test procedure is presented for multi-shaker, sine-dwell, modal test of spacecraft. This procedure has been applied to the modal testing of a Defense Meteorological Satellite. Good results were obtained.

INTRODUCTION

The multi-shaker sine-dwell test is a widely accepted method for identifying the dynamic characteristics of aerospace structures. The idea in using multiple shakers is to position the shakers at the proper locations and adjust their forces so as to excite individually each of the modes of the structure. However, the iteration process in adjusting the force ratios among shakers in the modal tuning phase of the test is often difficult and time consuming. This paper describes a procedure which overcomes this difficulty and allows the test to be conducted in a systematic manner.

A single shaker sine sweep test is performed first to identify the resonant frequencies of the spacecraft and the preliminary response data at the possible shaker locations. These preliminary response data for each mode are used to decide the number of shakers, best shaker locations, and the force pattern needed to excite the mode. Usually, the number of shakers needed to excite a particular mode is equal to or less than the number of modes with frequencies close to the mode of interest. The force ratio among shakers is calculated using the method similar to the one proposed by Morosow and Ayre (1, 2). A systematic iteration procedure is also formulated to improve the accuracy of the force pattern.

The test procedure presented in this paper was applied to a modal test of a Defense Meteorological Satellite built

by RCA for USAF. Nine modes below 50 Hz were determined within required accuracy and within cost and schedule constraints.

THEORETICAL BACKGROUND

The equations of motion for an n-degree-of-freedom linear damped system can be written as:

$$[M]\{\ddot{u}\} + [C]\{\dot{u}\} + [K]\{u\} = \{F\} \quad (1)$$

where $[M]$, $[C]$ and $[K]$ are the mass, damping, and stiffness matrices of the structure respectively. $\{u\}$ is the displacement vector and $\{F\}$ is the forcing vector.

Applying modal transformation

$$\{u\} = [\phi]\{q\} \quad (2)$$

to equation (1) and assuming proportional damping, we have:

$$[M]\{\ddot{q}\} + [C]\{\dot{q}\} + [K]\{q\} = [\phi]^T\{F\} \quad (3)$$

where: $[M] = [\phi]^T[M][\phi]$

$$[C] = [\phi]^T[M][\phi]$$

$$[K] = [\phi]^T[K][\phi]$$

and $[\phi]$ contains the mode shapes of the structure and $\{q\}$ is the vector of modal coordinates.

Equation (3) is a set of uncoupled equations which have general form as:

$$\ddot{q}_r + \frac{C_r}{M_r} \dot{q}_r + \omega_r^2 q_r = \frac{[\phi_r]^T \{F\}}{M_r} \quad (4)$$

where M_r and C_r are the generalized mass and modal damping of the structure respectively for mode r and $[\phi_r]^T \{F\}$ is the generalized force in mode r . ω_r is the frequency of mode r .

The solution of equation (4) corresponding to a sinusoidal external force with frequency Ω is:

$$q_r = X_r \cos \Omega t + Y_r \sin \Omega t \quad (5)$$

with

$$X_r = \frac{-[\phi_r]^T \{F\} [C_r \Omega / M_r]}{[\omega_r^2 - \Omega^2]^2 + [C_r \Omega / M_r]^2} \quad (6)$$

$$Y_r = \frac{[\phi_r]^T \{F\} [\omega_r^2 - \Omega^2]}{[\omega_r^2 - \Omega^2]^2 + [C_r \Omega / M_r]^2} \quad (7)$$

From equation (5), we can see that the modal response of the structure has magnitude

$$|q_r| = \sqrt{X_r^2 + Y_r^2} \quad (8)$$

and phase angle

$$\theta_r = \tan^{-1} \frac{X_r}{Y_r} \quad (9)$$

with $\Omega = \omega_r$, the coefficients X_r and Y_r are:

$$X_r = \frac{-[\phi_r]^T \{F\}}{C_r \Omega / M_r} \quad (10)$$

$$Y_r = 0 \quad (11)$$

and hence, $\theta_r = 90^\circ$. In other words, the phase angle between the modal force and the modal displacement is always 90° . However, from equation (2), the phase angle between the physical

displacement and the shaker forces is:

$$\theta = \tan^{-1} \frac{\sum_{r=1}^n \phi_r X_r}{\sum_{r=1}^n \phi_r Y_r} \quad (12)$$

This angle may not be 90° unless

$$\sum_{r=1}^n \phi_r Y_r = 0. \quad \text{This condition can be}$$

achieved by letting the generalized forces associated with the other modes, except the mode to be excited, to be zero. This can be seen from equation (7) which shows that the coefficient Y_r is directly proportional to the generalized force associated with the r th mode of the structure. The force ratio among shakers for exciting the natural mode of the structure can then be calculated such that it will satisfy the above mentioned condition, i.e.:

$$[\phi_r]^T \{F\} = \{F_G\} \quad (13)$$

where $\{F_G\}$ is an $n \times 1$ generalized force vector with null elements except the r th element.

Equation (13) represents a set of n simultaneous linear algebraic equations where n is the number of modes of interest in the test. Out of these n equations, $n-1$ would be homogenous and hence could be used to solve for the force ratio among shakers, assuming the number of shakers is also equal to n . For example, if there are ten modes to be excited for the test using ten shakers, the force ratio among these ten shakers can be calculated by solving a set of nine simultaneous equations with coefficients equal to the mode shape coefficients at exciting locations for each mode. With these forces, the generalized force for exciting a particular mode is represented by the non-zero element in the generalized force vector $\{F_G\}$ for that mode. Conceptually, the generalized force represents the distribution of energy, converted from the work done by exciting forces, among the different modes of the structure. It is reasonable, then, to set the force ratio among shakers such that all the kinetic energy is concentrated to the mode to be excited.

Note that the frequency difference factor $(\omega_r - \Omega)$ involved in equation (7) has second power in the denominator and, hence, Y_r will be smaller for the modes having frequencies widely separated from the frequency of the exciting force. In other words, these modes will have small interference with the mode to be excited. By excluding these modes from the calculation of the force pattern for exciting a particular mode, the number of simultaneous equations to be solved is reduced. For the case of exciting ten modes in the test, it is not always necessary to use ten shakers and solve nine simultaneous equations for the force pattern. The actual number of shakers needed to excite a particular mode can be judged by examining the separation of frequencies between the modes. In general, the number of equations to be solved for the force ratio among shakers to excite a particular mode will be equal to the number of adjacent modes to be suppressed. The number of shakers needed will be equal to the number of equations plus 1.

In case the number of shakers is less than the number of modes to be suppressed for tuning a particular mode, a least square error solution of equation (13) can be obtained as:

$$\{F\} = ([\phi][\phi]^T)^{-1}[\phi] \quad (14)$$

Note that in order to use equations (13) or (14) for the force ratio calculation, the mode shape coefficients at the driving points must be known ahead of time. These can be obtained from the single point sine sweep test or from an analytical finite element model of the structure. A systematic iteration procedure can be used to improve the accuracy of the force ratio calculations.

TEST PROCEDURE

The test procedure is divided into the following main phases:

- a. Single exciter sine-sweeps (modal search).
- b. Multiple exciter mode tuning.
- c. Multiple exciter sine-dwell (mode survey).

The steps involved in each phase are listed below:

A. Single Exciter Sine Sweeps

1. A single exciter sine sweep is performed over the frequency range of interest using one of the initial exciter locations. The other exciters remain disconnected during this sweep.
2. The frequency response function (FRF) between the driving point acceleration and force is calculated and displayed on the digital computer's CRT terminal.
3. The resonant frequencies are determined from inspection of this FRF by observing the frequencies at which the rate of change of phase is maximum (determined from the displayed Nyquist plot).
4. To establish the validity of the FRF, a coherence function is calculated, displayed, and inspected. Also, the results of an MDOF (multi-degree of freedom) curve-fit are displayed to further verify the calculated driving point FRF.
5. Steps 1 through 4 are repeated using each of the initial exciter locations as necessary to reveal all important resonances in the frequency range of interest.
6. After the resonant frequencies of interest have been identified, short, single-exciter sine sweeps are performed for each mode. Responses from the driving point accelerometer and several additional well-spaced accelerometers are recorded for each mode. "Coarse" mode shapes are computed and used to aid in selecting the force pattern and relative phasing of the exciters for each mode.

B. Multiple Exciter Mode Tuning

1. Using the coarse mode shape determined in A.6, the number of shakers, the driving points, and the corresponding force pattern and phasing are determined as follows:
 - 1.1 The modes to be excited within the frequency range of interest are grouped into several units based on the separation of resonant frequencies.

- 1.2 The number of shakers needed to excite the mode within a particular unit is equal to or less than the number of modes within that unit.
- 1.3 The best locations for these shakers and the force pattern to excite a particular mode are determined from equations (13) or (14) and from the resulting generalized force associated with the mode to be excited.
- 1.4 For each mode of a unit, those shakers to be used are connected and the force levels and phases are adjusted accordingly. The excitation frequency is adjusted to match the resonant frequency of the mode to be excited.
- 1.5 The mode coefficients are determined at the driving points from the quadrature values of the measured acceleration response at the resonant frequency.
- 1.6 If the mode coefficients differ from the "coarse" mode coefficients determined from step A.6, repeat steps 1.3 through 1.5 using the updated mode coefficients until final sets of force patterns are obtained.
2. The sweep oscillator is taken out of the dwell mode and the excitation frequency is set to a value slightly below the frequency of the tuned mode. Using the linear sweep setting, the sweep oscillator sweeps the exciters through a peak of the mode to a frequency slightly above the resonant frequency.
3. Additional acceleration data, selected from various locations on the spacecraft, are acquired through the same sweeping operation and the same force signals. The Nyquist circles associated with the acceleration/master force functions are inspected to further verify a properly tuned mode.

C. Multi-Exciter Sine Dwell

1. Once the mode has been tuned as described in Section B, the acceleration data for each group of accelerometers is acquired by dwelling at the resonant peak. The proper force amplitudes are set and controlled through a force feedback loop so that resonance occurs under invariant conditions.
2. The frequency response between the master force and each acceleration signal is calculated.
3. The mode coefficients are determined from the quadrature values of the measured acceleration response at the resonant frequency.

MODAL TEST OF 5D-2 SATELLITE

The test procedure described in the previous section was used for the modal test of a satellite. The spacecraft used in the test was the first Block 5D-2 configuration built by RCA for the Defense Meteorological Satellite Program. The spacecraft was rigidly mounted at its base to a 200-ton seismic block. Figure 1 shows the general setup of the test. Scaffolding was built on the block to completely enclose the spacecraft. It provided a versatile means for supporting the shakers, and provided access to all parts of the ISS during the test. Moving a shaker to a different location on the structure simply involved raising the shaker from the deck via the ceiling crane and either changing the position of the scaffolding deck or placing the shaker onto another deck at the new location.

Seven shaker locations were used during the course of the modal test to excite the spacecraft structure. No more than three shakers were used simultaneously to excite any particular mode of the spacecraft. Figure 2 shows the locations of the shakers. Attachments of the shaker armatures to the spacecraft driving points were accomplished with flexures (stingers), devices specially designed by RCA for transmitting pure axial forces to the structure. The flexures reduce the need for precise shaker alignment and eliminate bending moments into the force gages.

Seventy-six accelerometers attached to the spacecraft were used to measure mode shapes. Figure 3 shows the

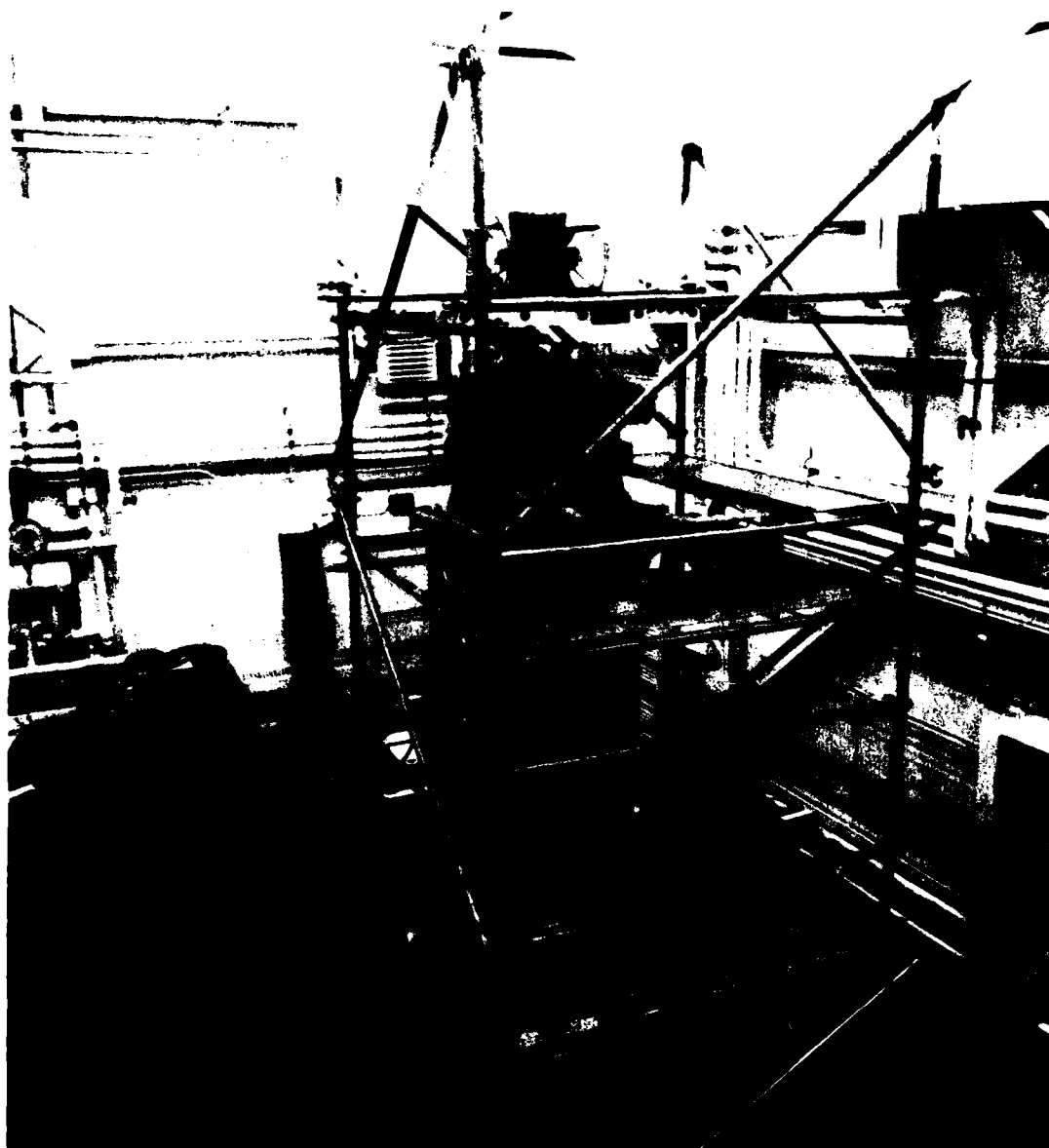


Figure 1. Defense Meteorological Satellite Program Block 5D-2 Spacecraft Mounted and Instrumented for Modal Test

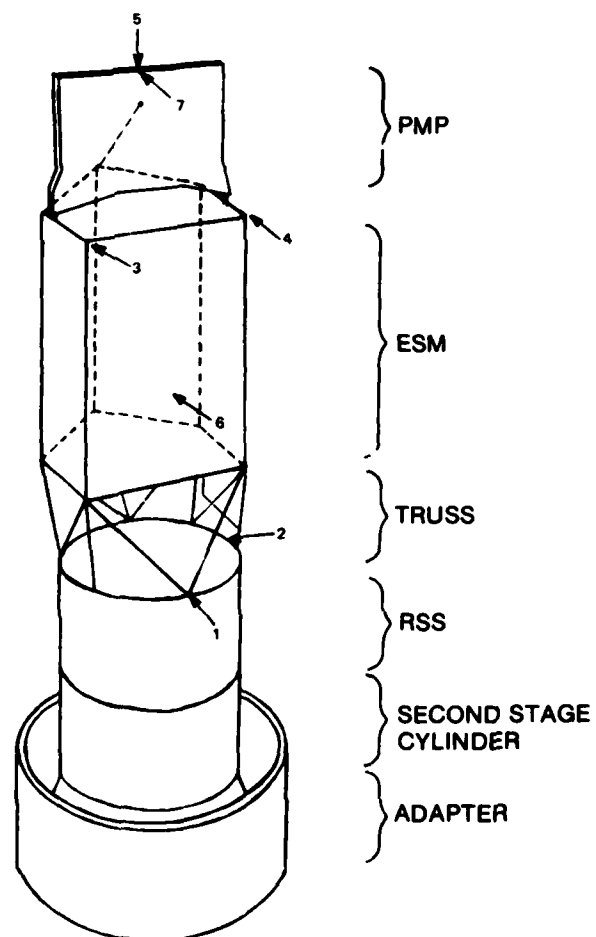


Figure 2. Exciter Locations for the 5D-2 Modal Test

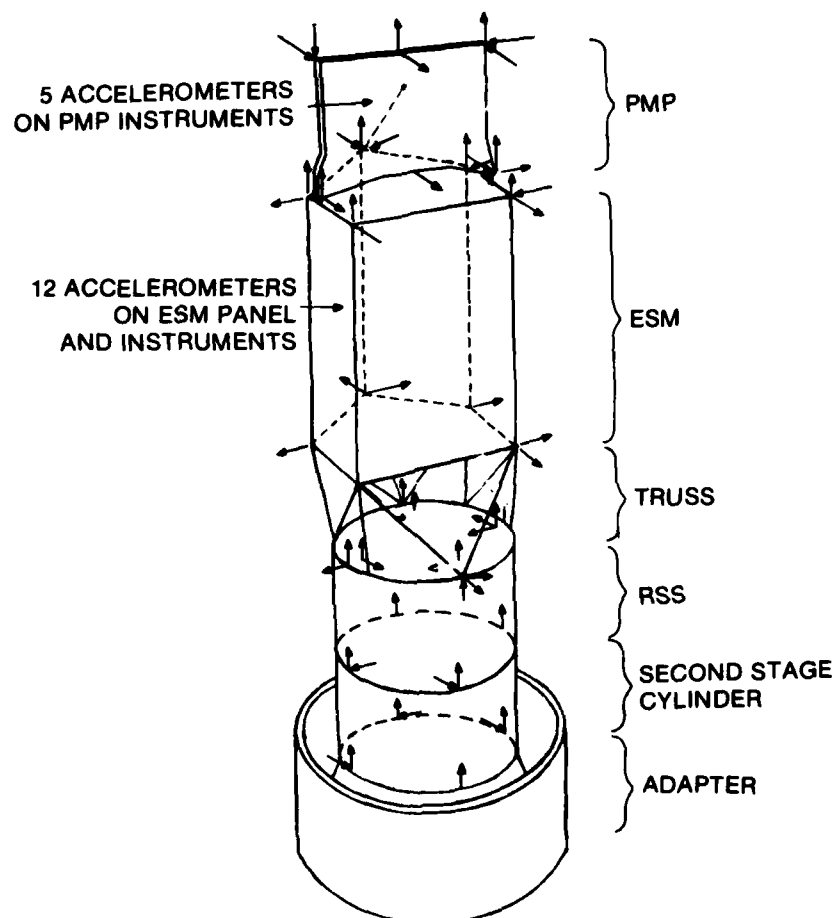


Figure 3. Accelerometer Locations for the 5D-2 Modal Test
(Each Arrow Represents an Accelerometer)

mounting locations of the accelerometers. Data from these transducers was processed by a mini-computer utilizing SDRC software. The electronic gear setup, visible in Figure 1, is shown in detail in Figure 4. A schematic of this equipment is shown in Figure 5.

Five initial exciter locations (i.e., positions 1 to 5 in Figure 2) were used to perform the single exciter sine sweep between 0 and 55 Hz. The frequency response functions (FRF) between the driving point acceleration and force were calculated and the resonant frequencies of the spacecraft were determined from the peaks in the FRF plots. Figure 6 shows the driving point FRF from exciter locations 1 and 2. By inspection of the FRF from all five initial exciter locations, nine modes below 50 Hz were identified to be the structural modes of the spacecraft.

With the frequencies of the modes identified, modes were tuned according to the procedure described in this paper. Once the mode was tuned, the acceleration data for all of the 76 accelerometers was acquired by dwelling at the resonant peak. The proper force amplitudes were set and controlled through a force feedback loop so that resonance occurred under invariant conditions. The frequency response between the master force and each acceleration signal was calculated. The mode coefficients were determined from the quadrature values of the measured acceleration response at the resonant frequency. Once the complete mode shape coefficients were obtained, an animated mode shape was displayed. Figure 7 shows the mode shape display for the first bending mode of the spacecraft, and Figure 8 shows a typical Nyquist plot from that mode.

The modal damping coefficient is derived from the frequencies of the maximum (ω_a) and minimum (ω_b) coincident response at each mode. Assuming equivalent viscous damping, the modal damping coefficient ζ_i for mode i is obtained by:

$$\zeta_i = \frac{1}{2} \frac{(\omega_a/\omega_b)_i^2 - 1}{(\omega_a/\omega_b)_i^2 + 1}$$

The CO plot from the master shaker on each mode is used for the calculation. Figure 9 shows the calculation of the modal damping coefficient for the first mode of the spacecraft.

It is required by the task assignment that the orthogonality check is performed to verify the accuracy of the test results. The test accuracy goal is to achieve off-diagonal terms in the error matrix of magnitude 0.1 or less, where the diagonal terms are normalized to 1. The resulting error matrix, given in Table 1, shows very good modal purity. It is noted from this table that only two terms exceed the 0.1 goal. The two high values lie between 0.1 and 0.2, and are for higher order modes, the eighth and ninth. It is, therefore, believed that the results shown in Table 1 represent very good results which in total are better than required.

One traditional way to verify the purity of the tuned mode and to evaluate the modal damping is the decay check. Due to the limitation on testing time and the fact that the modal damping could be calculated more accurately using the driving point CO plot, the decay check was performed only for the first mode using shaker no. 3. The resulting decay curve is given in Figure 10. The modal damping calculated from this decay curve is equal to 0.0066, as shown in the figure. This number is in close agreement with the value shown in Figure 9. The tuning purity is indicated by the absence of beating in the decay response.

Although the purpose of this test is to create a dynamic model of the spacecraft directly from the experimental measurements, an analytical finite element model was created for the spacecraft in the test configuration. This was necessary for the construction of the mass matrix which is needed in the orthogonality check of modes. This model was also found to be invaluable in guiding the locations and the tuning of shakers and in sorting out discrepancies discovered when initial measurements did not satisfy the criteria for orthogonality between modes. This computer model, as shown in Figure 11, consists of beams and spring elements and 36 mass points with a total of 179 dynamic degrees of freedom. These dynamic degrees of freedom reduce to 120 after Guyan reduction and, hence, the mass matrix [M] for the test has dimension 120 x 120.

The natural frequencies calculated from this computer model are, in general, lower than the frequencies measured from



Figure 4. Electronic Equipment for Controlling the Modal Test and for Data Processing

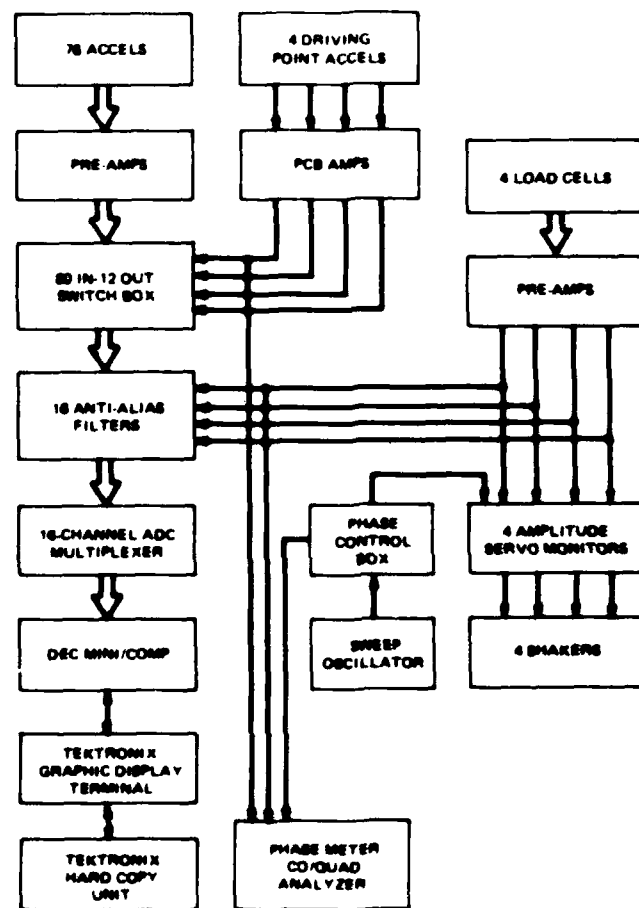


Figure 5. Schematic of Electronic Gear for Modal Test

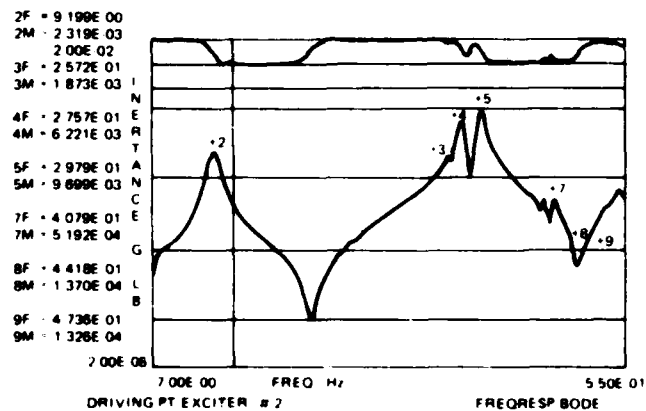
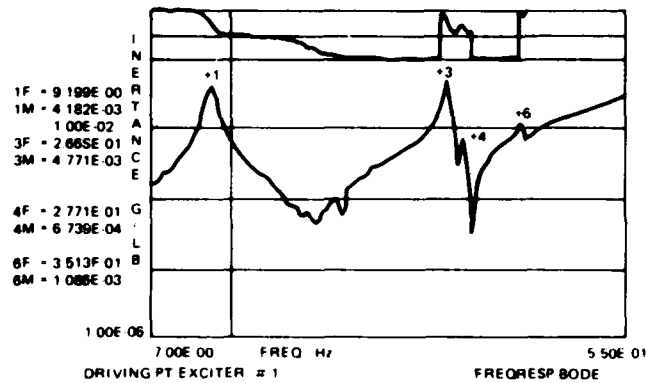
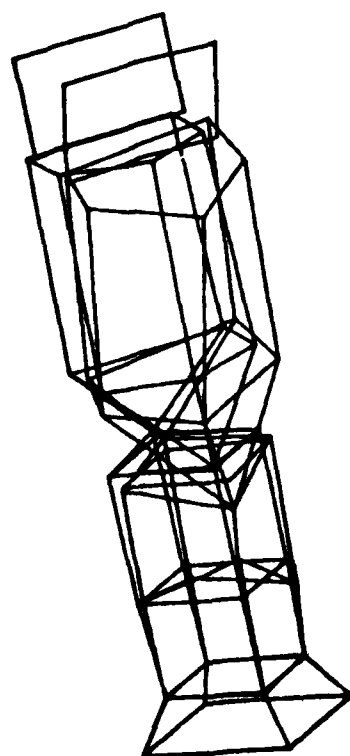


Figure 6. Frequency Response Function Plot for Shakers No. 1 and No. 2



9.165 HZ (1.0, -3.0, 1.0, 60.0)-VIEW

Figure 7. Animated Mode Shape Plot for Mode No. 1

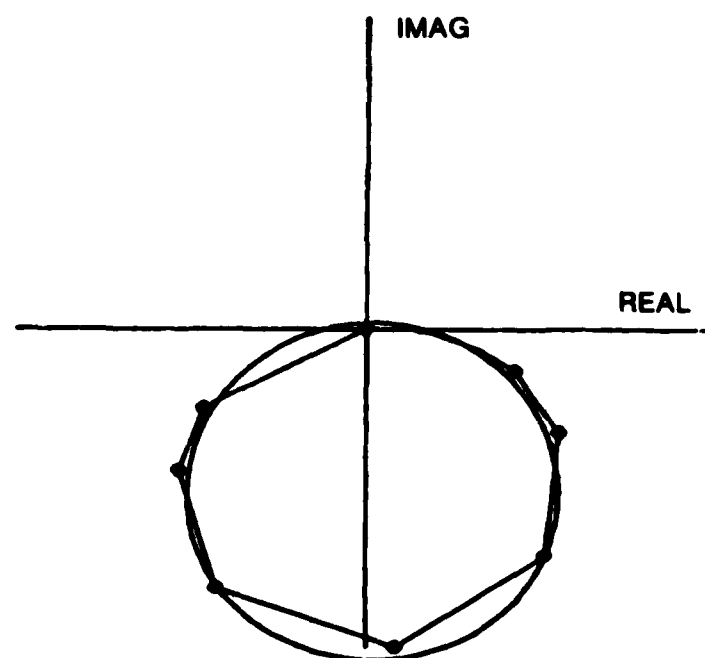


Figure 8. Driving Point Nyquist Plot for Short Sweep of Mode No. 1
($f = 9.0 \text{ Hz} - 9.4 \text{ Hz}$)

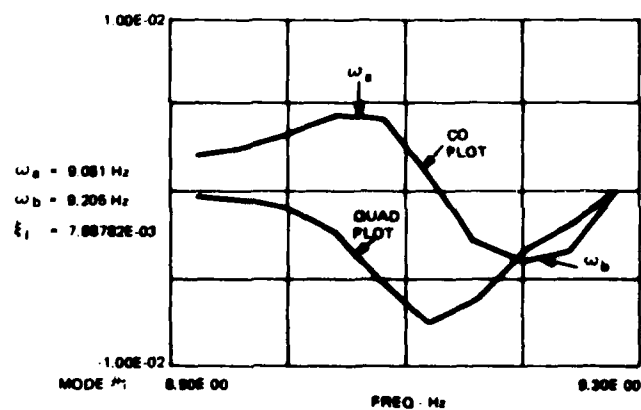


Figure 9. Modal Damping Calculation for Mode No. 1

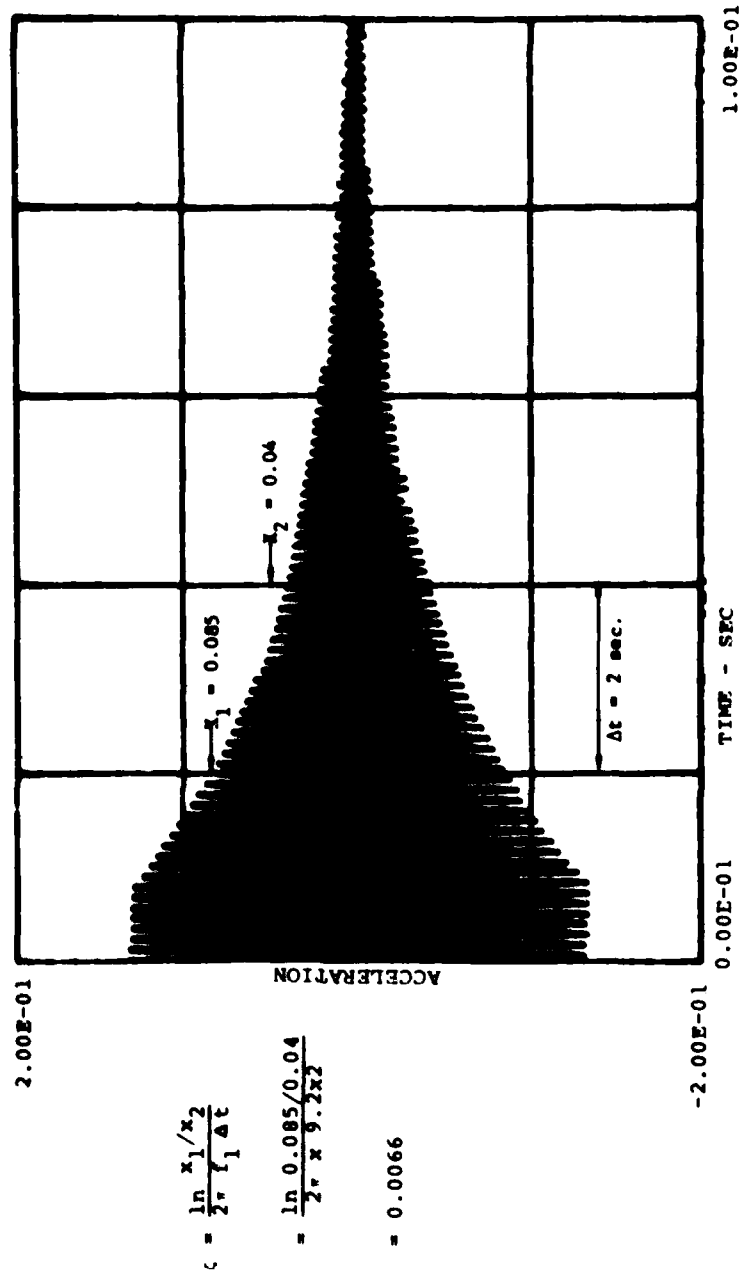


Figure 10. Decay Curve for Mode No. 1

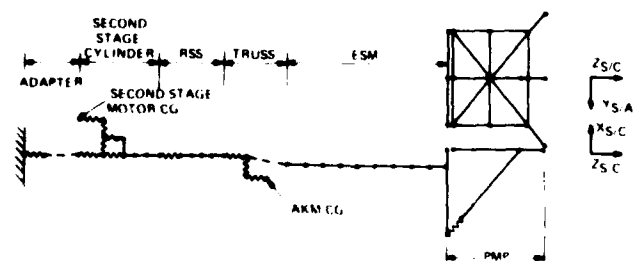


Figure 11. Dynamic Finite Element Model of 5D-2 Spacecraft

TABLE 1
Error Matrix for Orthogonality Check

Mode No.	1	2	3	4	5	6	7	8	9
1	1.0	0.014	0.062	0.001	-0.059	0.082	0.005	0.062	-0.002
2		1.0	-0.051	0.062	0.087	0.042	-0.007	-0.015	-0.016
3			1.0	-0.051	-0.016	0.025	-0.021	-0.018	0.091
4				1.0	0.016	0.087	-0.072	0.049	-0.021
5					1.0	-0.049	-0.002	-0.040	-0.012
6						1.0	0.079	0.149	0.103
7							1.0	-0.045	-0.010
8								1.0	-0.115
9									1.0

TABLE 2
Comparison of Natural Frequencies and Mode Shapes from Test and Analysis

Mode No.	Frequency (Hz)			Mode Shape	
	Test	Pre-Test Model	Post-Test Model	$[\phi]_M^T [M] [\phi]_A$	Description
1	9.13	7.74	9.04	0.98	First Y Bending
2	9.13	7.79	9.09	0.93	First Z Bending
3	25.79	22.92	25.43	0.94	PMP Bending.
4	27.56	25.06	27.20	0.91	PMP Torsion
5	29.76	27.24	29.44	0.90	First Torsion
6	35.51	33.27	36.05	0.92	Second Y Bending
7	40.42	37.59	41.17	0.85	Second Torsion
8	44.59	39.87	45.86	0.79	First Thrust
9	47.27	--	--	--	ESM Panel Mode

the test. Modifications were made to this computer model and the updated model gives the natural frequencies of the spacecraft within 3 percent of the test results. Table 2 gives the comparison of the natural frequencies.

A comparison between the mode shapes from the test measurements and the updated computer model is also given in Table 2. The comparisons of the mode shapes are made based on the criteria $[\phi]_M^T [M] [\phi]_A$ where $[\phi]_M$ is the measured mode shape, $[\phi]_A$ is the analytical mode shape from the computer model. If two mode shapes are identical, the value is 1.

CONCLUSION

A modal test of a Defense Meteorological Satellite developed and built at RCA Astro-Electronics for the USAF was successfully completed in May 1979. The test was performed to create a dynamic model of the spacecraft directly from experimental measurements. This dynamic model is necessary for an accurate loads analysis in order to predict spacecraft and launch vehicle loads during lift-off and boost ascent. The procedure used in the test was the multi-shaker sine-dwell technique required by the task assignment.

This paper presents the test results and the systematic test procedure developed at RCA for this test. Nine modes with resonant frequencies below 50 Hz were measured. Single-exciter sine sweeps were used to locate all these frequencies and to guide the tuning of shakers. Then modes were tuned, one at a time, using the analytical shaker force calculation method. Since the driving points mode shape coefficients are needed to calculate the shaker forces, an iteration procedure is developed to improve the shaker forces using the updated mode shapes from each iteration cycle.

ACKNOWLEDGEMENT

This project was done under the Air Force Contract F04701-75-C-0182 with the supervision of Captain H. Mitchell. Technical guidance was provided by Messrs. J. Anderson and R. Seebach of Aerospace Corporation. SDRC technical consultation was provided by Dr. T. Comstock and Mr. J. Nieb.

REFERENCES

1. G. Morosow, "Exciter Force Apportioning for Modal Vibration Testing Using Incomplete Excitation," Ph.D. Thesis, University of Colorado, Boulder, Colorado, 1977.
2. G. Morosow, R. S. Ayre, "Force Apportioning for Modal Vibration Testing Using Incomplete Excitation," Shock and Vibration Bulletin, Vol. 48, Part 1, pp. 39-48, 1978.

DEVELOPMENT OF A MULTIAXIAL FORCE-PULSE GENERATOR

R. D. Crowson
U. S. Army Engineer Waterways Experiment Station
Vicksburg, Mississippi

F. B. Safford
Agbabian Associates
El Segundo, California

W. J. Schuman, Jr.
U. S. Army Ballistic Research Laboratory
Aberdeen Proving Ground, Maryland

R. Freiberg
U. S. Army Electronic Research Development Command
Fort Monmouth, New Jersey

U. S. Army mobile tactical communication systems, typically housed in shelters on trucks, may be loaded substantially from the airblast produced by high explosive or nuclear weapons. A laboratory simulation device capable of generating specified force-time histories could be used to subject the equipment to loads as might be encountered in a battlefield condition. Such a device has been developed with a capability of producing rectangular force pulses along two axes in excess of 45 kN. Calibration of the force pulser and initial biaxial tests using a simulated mass in lieu of actual radio equipment have been conducted. Such tests clearly demonstrate the feasibility of the system's usefulness in subjecting equipment to force-time histories having both the amplitude and frequency content of those measured in high explosive field tests.

INTRODUCTION

Mobile tactical communication systems used by the U. S. Army are housed in a shelter typically mounted on a 2-1/2-ton truck (Figure 1). Airblast, generated by high explosive or nuclear weapons, loads the shelter, thereby inducing transient vibrations to the communication equipment. Typical acceleration-time histories at the midpoint of the equipment rack, recorded in the DICE THROW high explosive event, are shown in Figure 2. Residual shock spectra for the horizontal data record of Figure 2 are shown in Figure 3, from which can be observed the broad frequency range of response (20 to 5000 Hz). At zero damping this display is equivalent to the Fourier magnitude of the time history.

The transient loadings and resulting motion of the equipment are quite severe. A laboratory simulation device capable of generating specified force-time histories could be used to determine the vulnerability/survivability of individual pieces of equipment. A program was initiated to develop such a simulation device and

subject various components of the communication system to loadings as might be encountered in a battlefield environment. Program management is being provided by the U. S. Army Electronic Research Development Command (ERADCOM) and the U. S. Army Ballistic Research Laboratory (BRL). The simulation system is being developed and implemented jointly by Agbabian Associates (AA) and the U. S. Army Engineer Waterways Experiment Station (WES).

SIMULATOR DEVELOPMENT

A mechanical pulse simulating device provides a means of closely approximating the transient acceleration-time histories on equipment as experienced in high explosive field tests (References 1 and 2). This simulation may be accomplished in one, two, or three orthogonal axes simultaneously. For this program biaxial tests are being used. In addition, single axis tests were tried with the pulse thrust axis placed at angles between the major horizontal and vertical axes. Test acceleration levels of the equipment will be set slightly below, equal

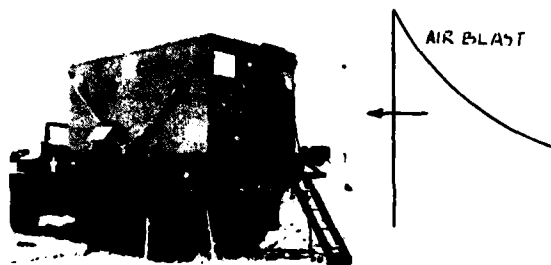


Fig. 1 - Airblast loading of equipment shelter.

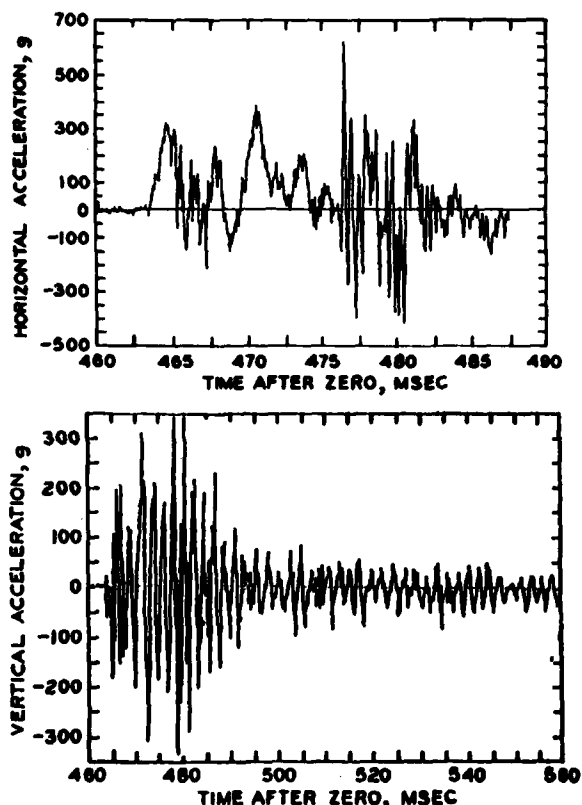


Fig. 2 - Acceleration time-histories as recorded on equipment rack in DICE THROW event.

to, and several factors above high explosive field test records for analysis and evaluation of vulnerability. Additional survivability, or acceptance, tests are planned using specified motion-time histories as criteria.

The recorded data of acceleration-time histories from high explosive tests on the communications equipment is used as an objective function. This is the motion to be matched in both horizontal and vertical direction by the pulse tests on the equipment in a laboratory. The upper half of Figure 4 describes the field test and the lower half describes the

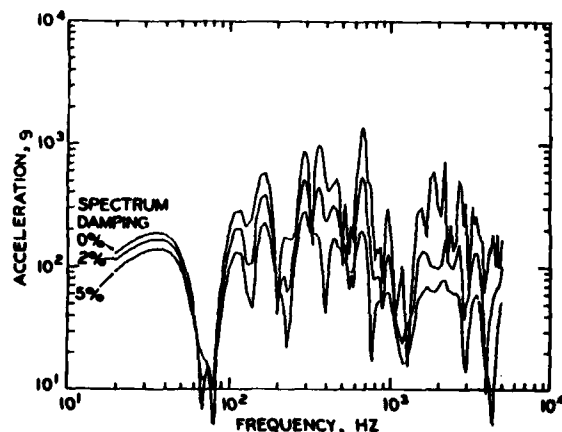


Fig. 3 - Shock spectra of horizontal motion.

computational procedure needed to generate the pulse train. In many situations high explosive field tests data upon equipments are not available, in which case response motions from computer models may be used as the objective function. In this latter case, airblast loads on scale models of the vehicle or shelter from shock tubes should be used with the finite element computer model of the structure.

Impedance measurements between the vertical and horizontal input loading points of the holding fixture and the transducer locations on the equipment are first made. The measurements include vertical and horizontal drive point inertance functions and cross-axis transfer inertance functions. These measurements, when converted to impulse functions, are used in the development of the pulse train. Impedance measurements are in the form of inertance, the complex ratio of output acceleration to input force $\left[\frac{\ddot{x}}{F} (j\omega) \right]$.

Pulse trains are a series of rectangular pulses that vary in amplitude, time duration, and initiation time. An iterative optimization algorithm is to be used to tailor a pulse train by convolution with the impedance measurements to cause the test article to have response accelerations matching specified motions or motions experienced in the high explosive field tests (see Figure 4).

A highly efficient search algorithm is used, which employs an adaptive random search technique. Given a two-axes test for a response motion bandwidth of 20 Hz to 4000 Hz, pulse trains are generated in accordance with the following matrix:

$$\begin{bmatrix} \ddot{x}_H \\ \ddot{x}_V \end{bmatrix}_{OF} \leftrightarrow \begin{bmatrix} \ddot{x}_H \\ \ddot{x}_V \end{bmatrix}_P = \begin{bmatrix} \Gamma_H & \Gamma_{VH} \\ \Gamma_{HV} & \Gamma_V \end{bmatrix} \begin{bmatrix} F_H \\ F_V \end{bmatrix}$$

Objec-	Pulsed	System	Pulse
tive	motion	func-	trains
func-		tions	
tion			

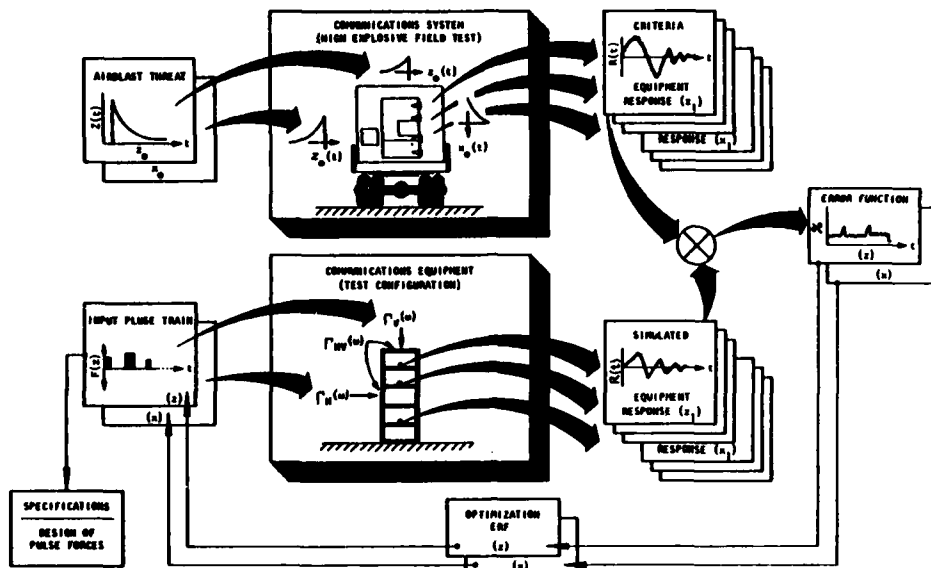


Fig. 4 - Optimum response of communications equipment by pulse excitation to match motions induced by air blast loads.

where

$\begin{bmatrix} \ddot{x}_H \\ \ddot{x}_V \end{bmatrix}_{OF}$ - Response acceleration motion (vertical and horizontal) from field tests (objective function)

$\begin{bmatrix} \ddot{x}_H \\ \ddot{x}_V \end{bmatrix}_P$ - Response acceleration motion (vertical and horizontal) due to force-pulse train inputs

Γ_H - Horizontal transfer inductance impulse function

Γ_V - Vertical transfer inductance impulse function

$\Gamma_{HV} = \Gamma_{VH}$ - Cross-axis transfer inductance impulse function (motions generated orthogonally to input axis)

$\Gamma = F^{-1}[\Gamma(j\omega)]$ - The impulse function, Γ , is the inverse Fourier transform of the complex ratio of output acceleration to input force over the frequency range of interest (inductance function)

$\begin{bmatrix} F_H \\ F_V \end{bmatrix}$ - Force pulse trains

Optimization iterations are continued until error functions, as given below for both vertical and horizontal motions of the equipment to be tested, are equal to or less than 5 percent.

$$erf = \frac{\int_0^t (\ddot{x}_{OF} - \ddot{x}_P)^2 dt}{\int_0^t \ddot{x}_{OF}^2 dt}$$

An adaptive random search method was used to determine the pulse trains for both the horizontal and vertical axes (Reference 4). These pulses were convolved with the impulse function matrix shown above to induce motions in the equipment. Since each individual pulse in the train is characterized by the independent parameters of amplitude, duration, and initiation time, a total of three parameters are needed to define each pulse and each direction. Thus, for example, if eight pulses are required for both

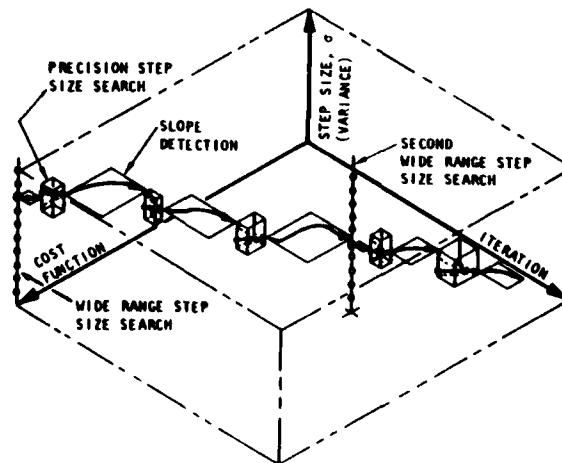
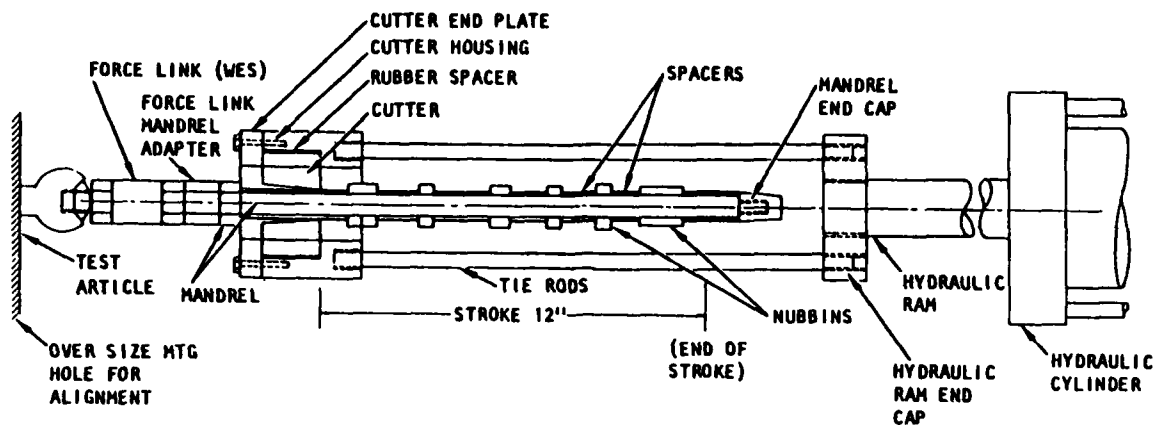
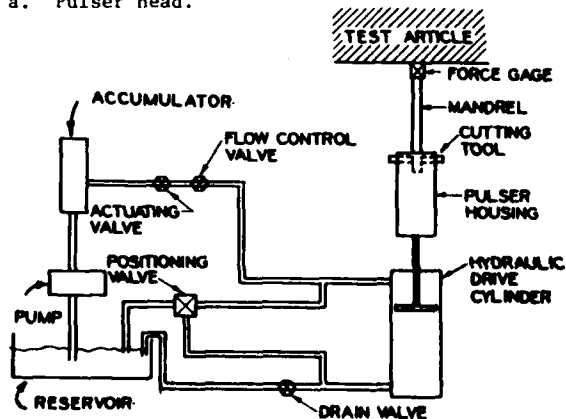


Fig. 5 - Adaptive step size search, both wide range and precision for rapid convergence of cost function.



a. Pulser head.



b. Complete system.

Fig. 6 - Schematic of pulse generator system.

vertical and horizontal direction, 48 parameters would be required.

The algorithm for the adaptive random search consists of alternating sequences of a global random search with a fixed value for the step size variance (σ) followed by searches for the locally optimal σ . Figure 5 illustrates the adaptive algorithm whereby a very wide-range search selects the best standard deviation of step size (σ) for the coarseness of the increments used, followed by a sequential precision search of finer increments. As the rate of convergence decreases, a new precision search is made, but directed towards a smaller step size. At selected iteration intervals, the wide-range search is reintroduced to prevent convergence to local minima.

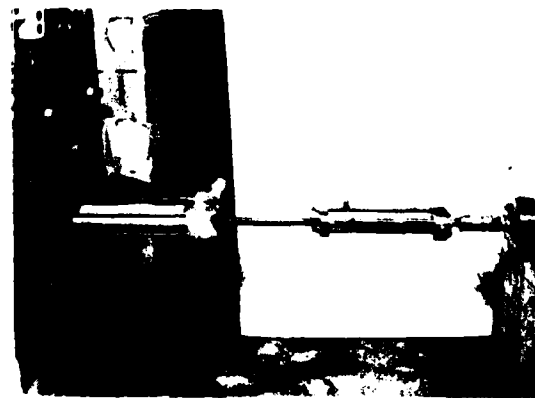


Fig. 7 - Pulse generator as used in calibration test.

PULSER DESIGN

Using the procedures in Figure 4, specifications will be developed for the pulse train, which are then used to establish the physical parameters of the pulse generating device. The pulse units employed are metal cutting devices in which a cutter removes shaped projections from an aluminum mandrel (References 1, 2, and 3). The resulting forces generated by cutting the projections from the mandrel are transmitted directly to the system to be tested. Pulse amplitudes, wave form shapes, and pulse durations are functions of cutter design, projection shapes, cutting velocity, type of metal, and energy source. The pulse generator system including power supply is depicted schematically in Figure 6, and a photograph of the pulser is shown in Figure 7.

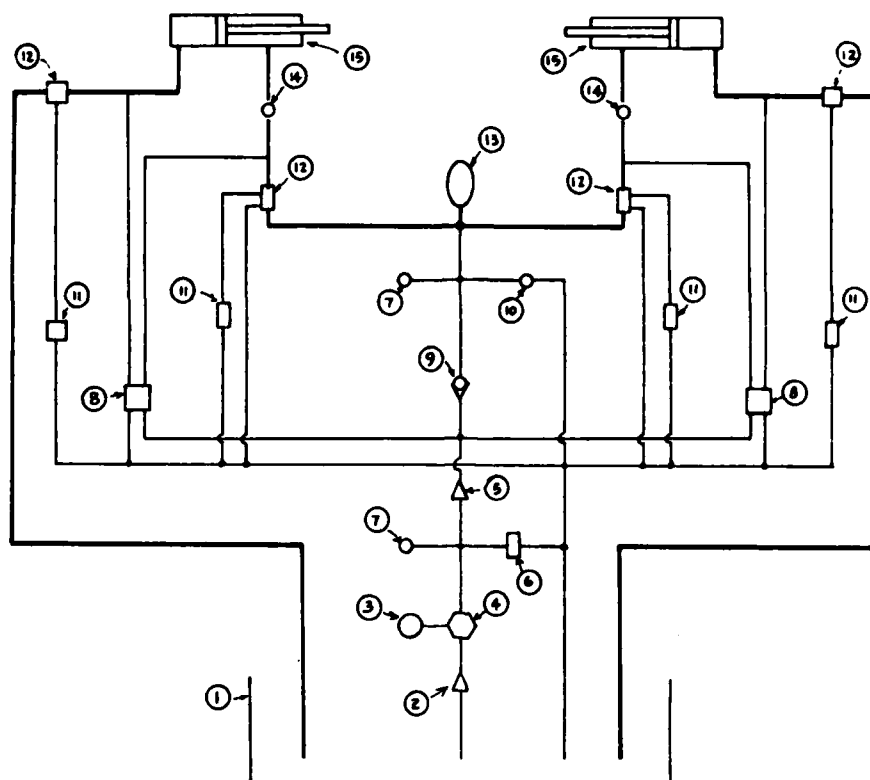


Fig. 8 - Hydraulic power supply circuit.

TABLE 1

Hydraulic Power Supply Component List

ITEM	QTY	DESCRIPTION	ITEM	QTY	DESCRIPTION
1	1	Thirty-gallon reservoir with cover, sight gage, flush drain, and baffles, Activation No. T30L	9	1	Check valve, Gould No. DC 500
2	1	Suction strainer, MFP No. SR45	10	1	Ball valve, Clayton Mark No. 1/2 CSB-790
3	1	Electric motor, 3HP, Lincoln No. 182T	11	4	Directional control valve, 4-way, 2-position, solenoid operated, Double A No. QJ-005-C-10B1
4	1	Pressure compensated pump, Hydura No. PVQ-06-LSAY-CNSN	12	4	Relief valve, Double A No. BT-12-12A2
5	1	High pressure filter, 5 micron, MFP No. HPI-1-G08	13	1	Ten-gallon accumulator, Greer No. 30A-10A
6	1	Relief valve, sun No. RPGC-JAN-CEB	14	2	Flow control valve, Double A No. YB12-10A1
7	2	Pressure gage, 0-3000 psi, UCC No. UC-3907	15	2	Hydraulic cylinder, 2-1/2-in bore, 1-in rod diameter, 13-in stroke, Sheffer Heavy Duty HH Series Model No. 2-1/2 HHRF13CRA
8	2	Directional control valve, 4-way, 3-position, solenoid operated, Double A No. QF-01-C-10F1			

HYDRAULIC POWER SUPPLY

A hydraulic energy source, Activation Model No. 1-1674-1, is used to drive the pulser. The power supply schematic is shown in Figure 8 and Table 1 and a photograph in Figure 9. A bladder accumulator is precharged to a given pressure and an oil pump brings the system to operating pressure. The system was designed to power two pulsers simultaneously or individually. A solenoid control valve releases the oil stored in the accumulator and separate flow control valves are used to regulate flow to each hydraulic cylinder.

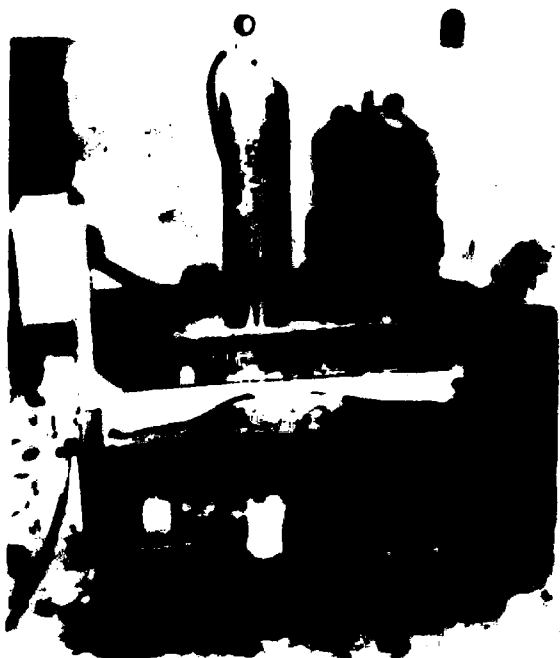


Fig. 9 - Hydraulic power supply.

CALIBRATION TESTS

Calibration tests were conducted with the pulser positioned horizontally between two rigid reaction structures (Figure 7). Tests were made using 2024-T3 aluminum nubbins as well as half-hard, free machining brass alloy 360 (3 percent Pb, 36 percent Zn, 61 percent Cu). The tests were performed to measure the following parameters:

- Output force
- Depth of cut
- Flow rate and flow control settings
- Optimal system operating pressures

All data were recorded on an FM magnetic tape recorder and played back on oscillograph traces.

A typical calibration test nubbin arrangement is shown in Figure 10 and resulting force record in Figure 11. The high frequency damped harmonics are the result of tool chatter as the

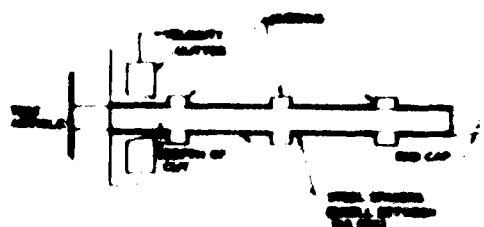


Fig. 10 - Typical nubbin configuration.

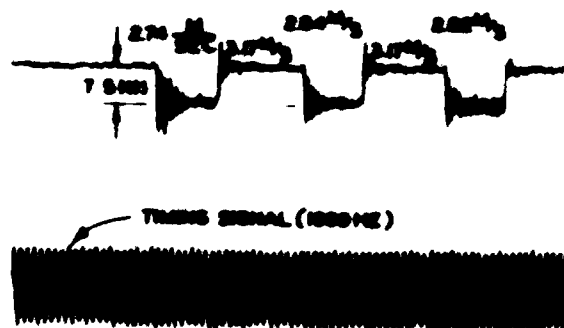


Fig. 11 - Typical calibration test data, 0.15-mm depth of cut, Flow Control No. 6-1/2.

aluminum is cut. A different cutter shape was tried but the chatter has yet to be removed. The various parameters were altered and after repeated tests calibration curves, such as those shown in Figures 12 and 13, were developed. Other curves which were developed but are not shown include various relations of flow rate control, force, cutting velocity, depth of cut, gain and loss of velocity and energy, and dwell velocity between nubbins.

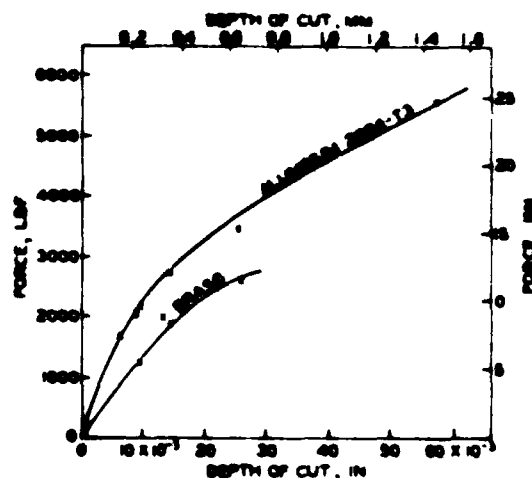


Fig. 12 - Force versus depth of cut calibration curve.

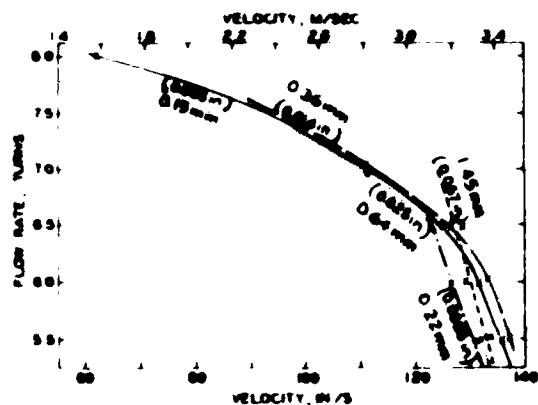


Fig. 13 - Flow control versus velocity versus depth of cut, calibration curve.

EQUIPMENT RACK TESTS

Initial biaxial pulse tests were conducted on the equipment rack using a simulated mass in lieu of a radio component. For this purpose of the study only generic pulse trains were used as work is continuing on developing specific objective functions. Additional parameters will be combined with the measured field test data to generate more meaningful functions to which the pulse train will be optimized. The test configuration, as used for the initial generic tests, is shown in Figure 14. Input forces were measured along with rack acceleration at the radio attachment points. The pulser was designed for, and has a capacity in excess of 45 kN (10,000 lb). However, using the smaller nubbins with 0.2-mm (0.008-in.) depths of cuts, 9.3 kN (2100 lb) was generated (Figure 15). These force levels resulted in peak acceleration levels of 800 g, which are well within the range of interest. The data were recorded unfiltered on an FM magnetic tape recorder. For analysis, some of the data were played back through a tuneable Krohn-Hite analog filter onto oscillograph traces. The data shown in Figure 15 were played back through a 3-kHz low pass filter. In general, the upper limit of the frequency range of interest for the radio equipment will be in the 1000- to 4000-Hz range based on the shock spectra of Figure 3.

SUMMARY

A low cost multi-axis force pulse generator has been developed. The device is capable of generating specified pulse trains in excess of 45 kN. Using previous test data, or arbitrary data, as criteria functions, pulse trains will be developed to simulate equipment motions which might be expected in a battlefield environment. Such laboratory simulation tests can be used to specify performance standards as well as verify hardness levels of communication system components. The pulse generator is portable



Fig. 14 - Test setup for initial biaxial tests.

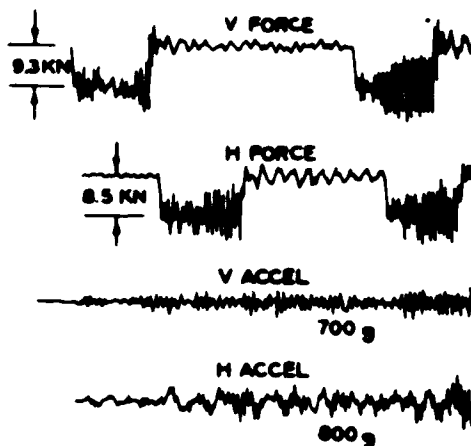


Fig. 15 - Input force and rack acceleration data from biaxial test (3-kHz low pass filtered).

and could be used to test other types of equipment. With some modifications to the hardware, but no change in theory, an additional axis of excitation could also be added.

Work is continuing on pulse train optimizations to match the radio equipment criteria functions. A variety of system components will be tested to failure or to previously specified maximum limits.

REFERENCES

1. Safford, F. B., and Masri, S. F., "Analytical and Experimental Studies of a Mechanical Pulse Generator," Jnl of Eng. for Industry, Trans. ASME, Series B, 96:2, May 1974, pp 459-470.
2. Safford, F. B., Carlson, L. E., Walker, R. E., and Huang, C. C., "Air Blast and Ground Shock Simulation Testing of Massive Equipment by Pulse Techniques," presented at the 5th Int. Symp. on Military Application of Blast Simulation, Stockholm, Sweden, May 23-26, 1977.
3. Shaw, M. C., "Designs for Safety," Mechanical Engineering, 94:4, April 1972, pp 23-29.
4. Masri, S. F., Bekey, G. A., and Safford, F. B., "Adaptive Random Search Method for Identification of Large-Scale Nonlinear Systems," 4th Symp. for Identification and System Parameter Estimating, Int. Federation of Automatic Control, Tbilisi, USSR, September 1976.

DISCUSSION

Mr. Showalter (SVIC): Were the high frequency oscillations possibly longitudinal oscillations of the bars or the holding structure? Could you stiffen them, if that is the cause of it, to eliminate that or do you really care? Does it hurt anything?

Mr. Crowson: Are you speaking of the oscillations as shown on the force pulse?

Mr. Showalter: Yes.

Mr. Crowson: No, those are very obviously due to the cutter. You can look at the nub that it has been cut and actually see the chatter marks. We haven't calculated the longitudinal vibrations but we feel that the high frequency oscillations on the pulse trains are due to the chatter and running it through a 1000 Hz filter completely does away with all of the high frequency noise.

Mr. Showalter: And can you eliminate that chatter by redesigning the cutter?

Mr. Crowson: We tried different types of cutters and different configurations of cutters and the designs we tried, which we thought would eliminate the chatter, actually made it a little bit worse. But we did have less chatter with the softer brass material and using something like teflon, nylon or even a softer material, would probably do away with the chatter.

Mr. Showalter: How long can you use the cutter, do you have to sharpen it every so often?

Mr. Crowson: We haven't had any problem with it yet. We have had it operational now for about six months, I guess, and they are still working fine.

Mr. Silver (Westinghouse): Do you have data to show you are duplicating the real responses at the critical elements within the radio, and along the different axes and to show the degree of coherence between those occurrences in real explosive cases versus the tests?

Mr. Crowson: We have not gone that far yet. We plan to actually do the optimization sequence in the coming year to generate pulses that we are looking for.

Mr. Silver: Yes, we would feel that it would be prudent to be careful of the coherence. You could get a lot of damage due to coherence that might be unrealistic. Also why are you using a square wave? I gather that these racks are fastened to the walls of the hut. Is that correct?

Mr. Crowson: Yes.

Mr. Silver: Is the pulse coming in from both to the side and the top at sort of an angle partly from the side and partly from the top?

Mr. Crowson: Yes.

Mr. Silver: Are you really putting the force in as if it were an air blast pulse? Is that your intent?

Mr. Crowson: Yes.

Mr. Silver: Is it square in nature?

Mr. Crowson: It really doesn't matter what your source of excitation is on these tests. We are simply exciting the rack and then the dynamics of the rack will actually give you some type of motion. We are trying to duplicate the

motion of the rack with the measured motion and it really doesn't matter how you get this rack to move as long as it responds in a way similar to what was measured.

Mr. Silver: That wasn't quite clear to me; so you don't care whether it is square, rectangular or what have you.

Mr. Crowson: Yes. We are just exciting the rack some way.

Mr. Silver: Yes. But you do have measured motions on the rack.

Mr. Crowson: Yes.

Mr. Silver: In what form are they?

Mr. Crowson: Acceleration time histories, and this is what we are trying to duplicate.

Mr. Silver: So having that you could evaluate the coherences, the correlations or the cross spectral densities between those.

Mr. Crowson: Yes. That is what we will do in the coming year. Thus far we have just developed the device and shown that it seems feasible and that it is working properly.

Mr. Silver: Great differences in damage have occurred in pyrotechnic shock tests where coherence has been ignored in some test procedures in the past.

Mr. Frydman:(Harry Diamond Labs): Since you are talking about simulating two degrees of freedom, as far as input is concerned, how do you propose to control your phasing relationship between the inputs?

Mr. Crowson: This will be taken care of in our optimization algorithm. I am not that familiar with that because I have not worked in that area. I have developed the actual pulser. We will control the phasing between the horizontal and the vertical pulsers by actually positioning one a little bit closer to the first nub than the other one, so this is kind of an experimental process. But we do have the capability to control the phasing between the actual hardware pieces.

VIBRATION QUALIFICATION OF EQUIPMENT
MOUNTED IN TURBOPROP AIRCRAFT

L. G. Smith
Hughes Aircraft Company
Fullerton, California

(U) A test program required the derivation and implementation of environmental criteria for qualification of equipment mounted in turboprop aircraft. This paper discusses the vibration portion of the program. Both the criteria and the test control methods are unique and are applicable to other programs for qualifying equipment for the turboprop aircraft vibratory environment.

INTRODUCTION

(U) Testing services, including vibration testing, were performed by Hughes Aircraft Company, Ground Systems Group upon equipment to be mounted in a turboprop aircraft. There was no specific criteria for the vibration testing. The criteria was to be based on existing specifications for turboprop cargo aircraft, if available, or else from existing data for the specific aircraft involved.

(U) A literature search did not determine any existing turboprop criteria, so criteria derivation became a part of the testing scope. The criteria so developed consisted of sinusoidal harmonic components superimposed upon broadband random. This paper discusses derivation of the criteria, the actual criteria used, and the test methods used to achieve the desired environment.

CRITERIA DERIVATION

(U) General

(U) Consideration of the aircraft geometry, the equipment location, and the nature of the available flight test data resulted in the zoning of the aircraft into four zones: Forward cabin floor (six measurements available), aft cabin floor (eight measurements), forward shelf mounted to primary ring structure (six measurements), and mid ship bulkhead mounted (two measurements). Due to configuration changes only two zoning levels were used for test.

(U) Ground and flight (normal rated power) data were available. The levels were similar and criteria was based on the flight level, because of the longer duration of flight

events. Landing shock was not considered, as the cargo aircraft is designed for soft landings.

(U) By mutual agreement with the test customer, testing was conducted in a single lateral axis, the apparently most sensitive axis for each specimen.

SINUSOIDAL DATA

(U) The flight test data report presented the data in power spectral density format. The sinusoidal effective band width of the analysis filter was stated. This allowed accurate calculation of sinusoidal levels. These levels were tabulated within each zone for each significant frequency. These frequencies were described in the data report text as the first several harmonics of the propeller rotation frequency. The resulting amplitude set of all values for each harmonic for each zone were statistically evaluated for average and RMS deviation.

(U) The hardware utilized was flight hardware. In order to avoid unnecessary damage to these specimens, a nominal test level of 2 sigma above average was used as a compromise between achieving a high probability (97 percent) of testing representative of worst location within the zone, and avoiding unreasonably high levels. The resulting amplitudes were 17 to 50 percent above data maxima. To keep the test duration reasonable the levels were doubled such that one hour of testing was typical of one hundred flight hours. The resulting sinusoidal levels are tabulated in Table 'A'.

RANDOM CRITERIA

(U) Because of the broadband nature of the random portion of the environment and practical

TABLE A
Test Criteria (U)

ZONE	SINUSOIDAL CRITERIA		RANDOM CRITERIA	
	Frequency Hz	Peak Gs	Frequency Hz	PSD G ² /Hz
Fwd. cargo floor and mid-ship bulkhead	68	3.0	20	.0063
	136	1.8	150	.0063
	198	1.4	500	.015
	272	1.2	1000	.015
			RMS = 3.48 G	
Fwd. shelf mounted (cantilever from main longitudinal stringers)	68	5.9	20	.0024
	136	2.1	60	.0024
	198	5.1	120	.04
			400	.04
			1000	.004
			RMS = 4.49 G	
Aft cargo floor mounted	68	.34	20	.0008
	136	.54	200	.0008
	198	.48	350	.003
			800	.003
			1000	.0016
			RMS = 1.48 G	

All tests to be conducted using combined random and sinusoidal application.

limitation on point-by-point data analysis for a "one shot" program, an enveloping approach was taken to the problem of deriving representative power spectra. Flight test spectra zone groups were enveloped, but singly occurring sharp peaks were ignored as these are usually a result of local structural and equipment compliance and enveloping a group of them is unrealistically severe.

(U) The enveloping process itself accounted for statistical variation, and a 6 db factor was added to the resulting envelope to account for the test time factor consistently with the sinusoidal portion. The resulting levels are also presented in Table 'A'.

TEST CONDUCT METHODOLOGY

(U) The basic test approach was to combine a computer generated equalized open loop random control signal with an analog taped pre-equalized sinusoidal control signal. The fourier analyzer digital-to-analog output was used to produce the sinusoidal signal. First various phase relationships were tried to find a signal with equal positive and negative peaks. To obtain the desired signal at the exciter the gain and phase lag were found experimentally by driving the exciter system with the desired signal and making a fourier analysis of the return signal from a typical control location. The input signal was adjusted accordingly and

UNCLASSIFIED

the process continued until a control signal giving the desired return characteristics was obtained. For the actual tests, two iterations were required. This process was performed with the appropriate slip fixture, but no specimen was used. It was not necessary to reiterate when the specimens were present. The resulting signal was taped for eighty minutes. Since there was no feedback loop involved, it was not necessary to have excitation while taping.

(U) The problem of obtaining the correct sinusoidal amplitude for the actual test was resolved by using an independent real time analyzer. The analog tape produced as above was played into this analyzer and the lines excited were noted. An oscillator was then tuned to a frequency corresponding to each line one by one and adjusted to an output voltage corresponding to the various sinusoidal test levels. The peak response of the real time analyzer to each component was marked as a test "target" both on a CRT display and on a plotter. These narrow band peaks were many db above broad band test levels, so the eventual

contribution of the random portion is insignificant.

(U) To start the test the tape recorder was connected to the test circuit with the tape running and the tape gain down, as in Figure 1. The purpose of starting in this manner was to avoid switching transients. Random equalization was performed in the normal manner, using the digital control system. When equalization was complete, the random system was open looped, and then the tape gain raised until response peaks approached those marked on the CRT. The reasonably equal occurrence of all harmonics reaching the target level was indicative that readjustment of the sine input was unnecessary. Final verification was to sweep the plotter to obtain a more accurate amplitude readout. A typical plot is shown in Figure 2.

(U) The above process was repeated for arbitrary durations at -12, -9, -6, and -3 db, and at full level for one hour, although the full buildup was not always used at customer on-site representative discretion.

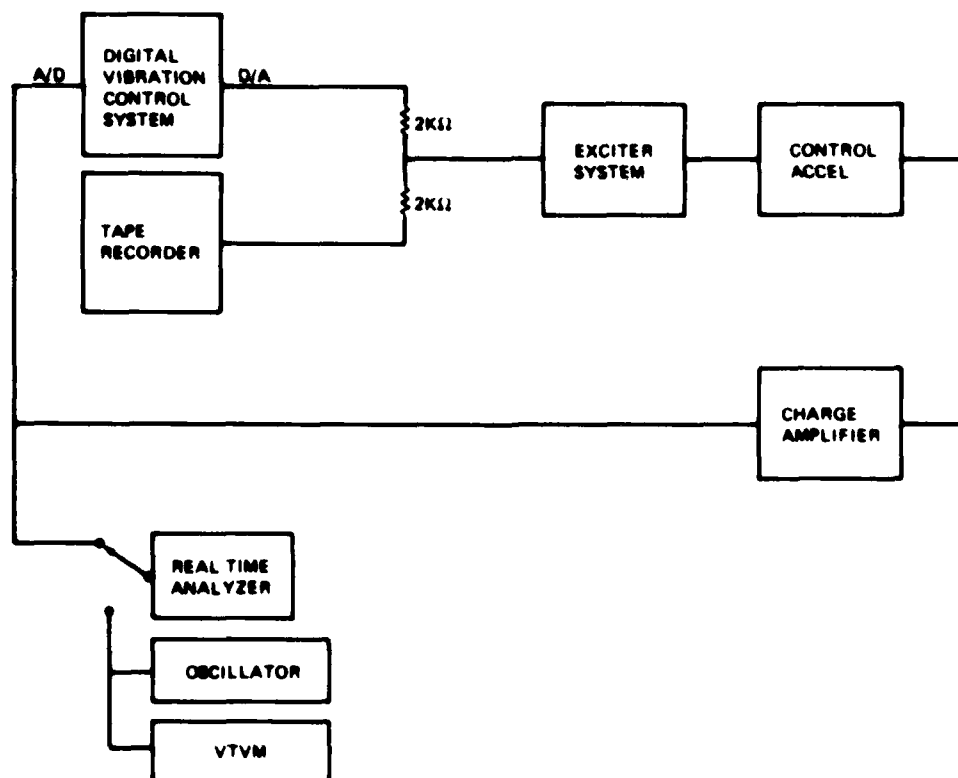
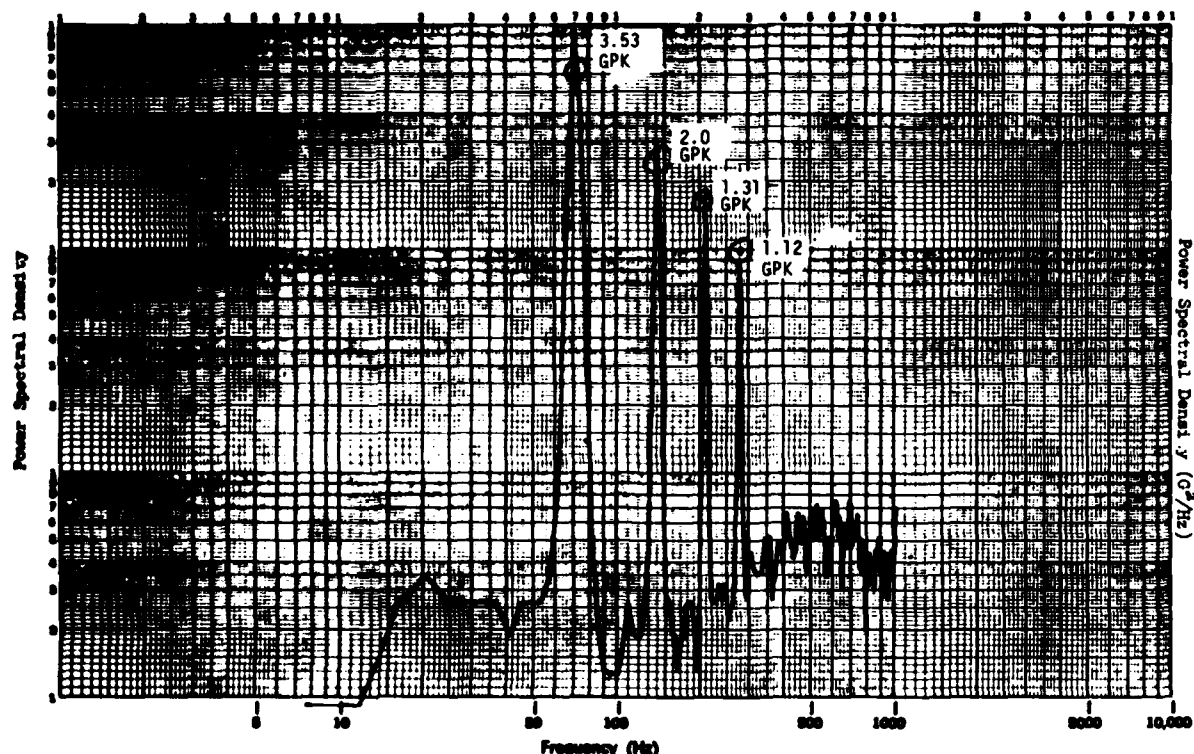


Fig. 1 - Test block diagram



Note: Circled quantities are target values.

Fig. 2 - Typical sinusoidal test data

TEST WORTHINESS

(U) Because of the unique nature of the test, close coordination with the on-site test representative was unusually important. As each test level occurred the apparent severity of the excitation became the final criteria for the worthiness of the test. Both laboratory and customer personnel were in agreement that the severity seemed appropriate, both at -6 db as a reasonable flight simulation, and at 0 db as a test level. It was also noted that the excitation produced a sound similar to a turbo-prop aircraft.

(U) The purpose of the overall program was the delivery of a special aircraft and the testing program came about because the critical equipment had no flight history. The testing

itself convinced the customer of the flight worthiness of the equipment, and no dynamic flight test measurements were made to verify the test program.

CONCLUSIONS:

(U) 1 - This test program established useful guidelines for testing equipment mounted in turboprop aircraft. The criteria developed may not stand up to rigorous statistical scrutiny such as based upon multivehicle measurement programs. It will, however, give a meaningful test based upon both the available data, and upon observation of test witnesses.

(U) 2 - Testing for combined multiharmonic sinusoids and wide band random is feasible using present test methodology.

"QUICK LOOK" ASSESSMENT AND COMPARISON OF VIBRATION SPECIFICATIONS

Jeffrey H. Schmidt
The Marquardt Company
Van Nuys, California 91409

A technique is developed by correlating sine, shock or random to the equations obtained via a response spectrum analysis solution for random vibration. By means of this correlation, which is developed for simple then complex structures, it is shown that only one analysis technique need be used to solve all or any one of the designing dynamic environments for a given structure.

The proposed technique is simpler and more cost effective than standard solution techniques. Applicable assumptions and limitations are discussed.

INTRODUCTION

Often designs must be evaluated for a variety of load environments in order to establish which environment is most severe. In most evaluations, no one environment designs all structural components and therefore leads the engineer into separate analyses such as shock, sine and/or random.

The proposed approach allows an extremely simple means to compare and to evaluate, one to another, the vibration environments or specifications of shock, sine and random vibration specifications. The concept applies equally well to simple as well as complex structures. The approach allows the engineer to evaluate all three environments by a single analysis technique.

GENERAL APPROACH

A. Single Degree of Freedom Structures

The approach is based upon the concept of "Response Spectrum Analysis" (RSA) that was developed and is used extensively for earthquake analyses. The derived equations used in RSA are simplifications from the more general equations developed for structural random analyses. As will be shown, the simplified equations for RSA can be directly correlated to sine or shock vibration analyses. Therefore, by means of this correlation, only one analysis technique need be used to solve all or any one of the designing dynamic environments for a given structure.

The main difficulty in attempting to assess the relative severity of different vibration environments, such as shock, sine, or random, is that all three environments appear to be non-comparable entities prior to detailed dynamic

analyses for each of the environments. Once detailed dynamic analyses is completed, load, deflections and stresses can be compared directly for the analyzed structure. In reality, all three of the environments can be converted to a common basis, for comparison, before structural analyses need be done.

In particular:

1. Random criteria is specified in terms of g^2/Hz . (spectral density) versus frequency.
2. Sine criteria is specified in terms of applied g 's versus frequency, and
3. Shock criteria is specified in terms of shock shape (i.e., sawtooth, rectangular, etc.), magnitude (g 's) versus shock duration (milliseconds).

All of the above may be simplified and plotted on a common graph of response g 's versus frequencies. For example, take a simple one mass degree of freedom system (i.e., a mass on a spring) as shown in Figure 1.

Random criteria are usually specified in terms of g^2/Hz versus frequency as shown in Figure 2A. The power spectral density plot (PSD) of Figure 2A may be converted into a plot of response g_{RMS} (root mean square) versus frequency as shown in Figure 2B. This conversion is accomplished by the expression:

$$g_{RMS} = \sqrt{\frac{\pi}{2} f_n Q g_n} \quad \text{(Absolute acceleration)} \quad (1)$$

where:

f_n = natural frequency (Hz)

Q = amplification factor

$= \frac{1}{2\zeta}$; ζ = ratio of assumed to critical damping

$g_{in} = g^2/\text{Hz}$ value at f_n

Selecting 3 times g_{RMS} as a limit (yield) g load, g 's at various natural frequencies can be computed and plotted as shown in Figure 2B.

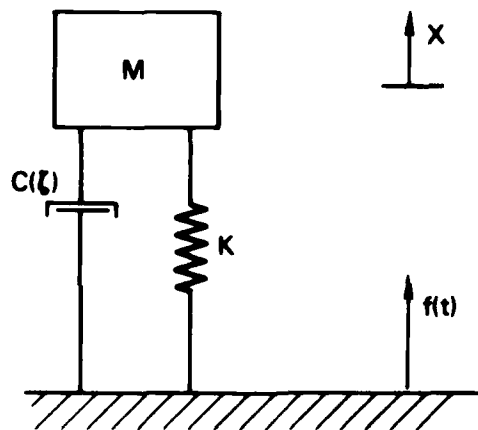


Figure 1. One Degree-of-Freedom Structure

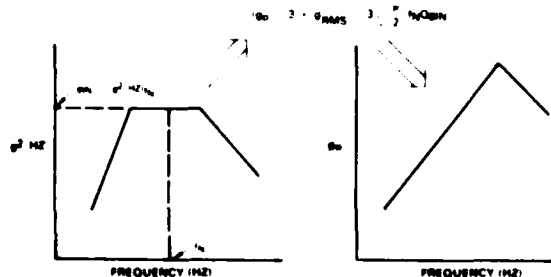


Figure 2.A, 2B. Typical P.S.D. Plot for Random Environment and Random Response Plot

Shock criteria are usually specified in terms of shock input magnitude "g", shock duration in milliseconds and shock shape for example, Figure 3A. From these shock parameters, various references, e.g., Ref. 1 permit

conversion to response "g" versus $t_1 \tau$, where t_1 = shock duration and $\tau = \frac{1}{f_n}$. By se-

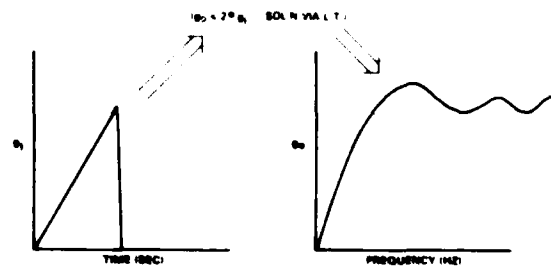
lecting various f_n 's a plot of g 's response versus frequency can be plotted, Figure 3B.

Sine criteria is usually specified in terms of "g" input versus frequency and, in this case, a "g" response curve versus frequency can be generated easily by the expression:

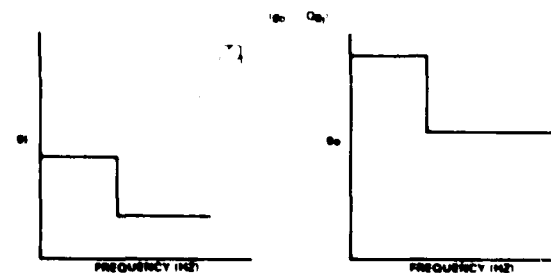
$$g_{response} = g_{input} Q \quad (2)$$

A typical sine input criteria and corresponding g response versus frequency plot are shown in Figures 4A and 4B respectively.

All three response plots, Figures 2A, 3A and 4A can now be combined into one plot as shown in Figure 5. Upon review of Figure 5, all three criteria that, at first, seemed to be non-comparable vibration environments are now easily compared one to another.



Figures 3A, 3B. Typical Shock Environment and Shock Response Plot



Figures 4A, 4B. Typical Sine Environment and Sine Response Plot

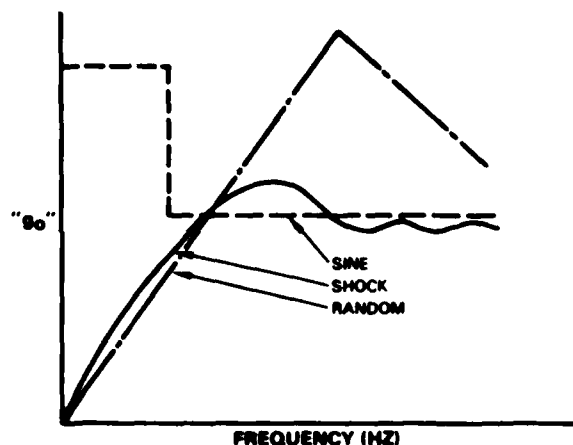


Figure 5. Combined Response Plots

But let us review the assumptions made to arrive at Figure 5, they are as follows:

1. The structural system used to develop Figure 5 is, by definition, a one-degree-of-freedom system as shown in Figure 1.
2. The equations used to convert the given general vibration criteria (the criteria applies equally to one-degree-of-freedom system as well as to many degree-of-freedom systems) apply only to a one-degree-of-freedom system.
3. The plots shown in Figure 5 are 3 response plots corresponding to their respective input plots for a one-degree-of-freedom system. That is, Figure 5 plots are, in reality, solutions to the posed problem of Figure 1 for vibration inputs of shock, sine and random.
4. Figure 5 does show curves rather than a single point, which is what one would expect for a single frequency problem of Figure 1, because we assumed the proposed structure may have any frequency, but only one.

What remains as a logical step is to extend the above concept to include multi-degree-of-freedom structures (i.e. complex structures) and thus allow an initial evaluation of the vibration environments such as shock, sine and random, and to eliminate a detailed separate dynamic analyses for each of the aforementioned environments.

B. Multi Degree of Freedom Structures

In general, consider an n [multi] degree-of-freedom lumped parameter structural system with mass matrix $[m]$, stiffness matrix $[k]$, damping matrix $[c]$ and column matrix

of external forces $\{F(x_j, t)\}$. M_i, k_{ij}, C_{ij} , and F_i are expressed in the w coordinate system. For

$$\{F(x_j, t)\} = \{P_0 p(x_j)\} f(t) \quad (3)$$

The differential equations of motion in the w coordinate system take the matrix form

$$[m] \{\ddot{w}\} + [c] \{\dot{w}\} + [k] \{w\} = P_0 \{p(x_j)\} f(t) \quad (4)$$

Apply a coordinate transformation

$$\{w\} = [\phi] \{\eta\} \quad (5)$$

in which each column of ϕ is a modal column of the system and $\{\eta\}$ represents the normal coordinates.

From Equation (5)

$$\{\dot{w}\} = [\phi] \{\dot{\eta}\} \quad (6)$$

and

$$\{\ddot{w}\} = [\phi] \{\ddot{\eta}\} \quad (7)$$

Substituting Equations (5), (6), (7) into Equation (4) and premultiplying by the transpose of $[\phi]$, Equation (4) becomes

$$[\phi]^T [m] [\phi] \{\ddot{\eta}\} + [\phi]^T [c] [\phi] \{\dot{\eta}\} + [\phi]^T [k] [\phi] \{\eta\} = P_0 [\phi]^T \{p(x_j)\} f(t) \quad (8)$$

From the orthogonality relations of natural modes, it follows that

$$[\phi]^T [m] [\phi] = [M_r] \quad (9)$$

$$[\phi]^T [k] [\phi] = [\omega^2] [M_r] = [K_r] \quad (10)$$

Comparing the triple matrix product

$$[\phi]^T [c] [\phi] \quad (11)$$

with Equations (9) and (10) this product will result in a diagonal matrix only when the damping matrix $[c]$ is proportional to either the mass matrix $[m]$ or the stiffness matrix $[k]$ that is

$$[c] = 2\beta [m] \quad (12)$$

or

$$[c] = \alpha [k] \quad (13)$$

or

$$\beta r = \zeta_r \omega_r \quad (13a)$$

Using Equation (12) in Equation (11) and comparing with Equation (9)

$$[\phi]^T [c] [\phi] = 2\beta [M_r] \quad (14)$$

The substitution of Equations (9), (10), and (14) with Equation (8) results in a set of n decoupled differential equations of motion.

$$[M_r] \{\ddot{\eta}\} + 2\beta[M_r] \{\dot{\eta}\} + [\omega_r^2][M_r] \{\eta\} = [\phi]^T \{p(x_j)\} P_0 f(t) \quad (15)$$

The r th Equation of Equation (15) has the form

$$M_r \ddot{\eta}_r + 2\beta M_r \dot{\eta}_r + \omega_r^2 M_r \eta_r = P_0 \{\phi(r)\} \{p(x_j)\} f(t) \quad (16)$$

Let

$$\{\phi(r)\} \{p(x_j)\} = \Gamma_r \quad (17)$$

= participation factor

Dividing through by M_r in Equation (16) and using Equation (17) results in:

$$\ddot{\eta}_r + 2\beta \dot{\eta}_r + \omega_r^2 \eta_r = \frac{P_0}{M_r} \Gamma_r f(t) \quad (18)$$

A general form of solution to Equation (18) is obtained readily by the use of Laplace Transform (for particulars see References 1,2,3).

For the case of shock spectrum the solution of Equation (18) becomes

$$\eta_r(t) = \frac{P_0 \Gamma_r}{\omega_r^2 M_r} D_r(t) \quad (19)$$

in which

$$D_r(t) = \int_0^t h(t-\tau) f(\tau) d\tau \quad (20)$$

$$= \int_0^t \frac{\omega_r^2}{\sqrt{\omega_r^2 - \beta^2}} e^{-\beta(t-\tau)} \sin \left[\sqrt{\omega_r^2 - \beta^2} (t-\tau) \right] f(\tau) d\tau$$

where $D_r(t)$ is called the dynamic load factor.

The total deflection of the structure, $w(x,t)$, is obtained by inserting Equation (20) into Equation (5). Thus

$$w(x,t) = P_0 \sum_{i=1}^n \frac{\Gamma_i}{\omega_i^2 M_i} \phi_i(x) D_i(t) \quad (21)$$

Starting again from Equation (18) and posing the problem of harmonic or sine excitation,

$$f(t) = e^{i\Omega t} \quad (22)$$

Use of Laplace Transform provides the steady-state solution given by

$$\eta_r(t) = \frac{P_0 \Gamma_r}{\omega_r^2 M_r}$$

$$\frac{1}{1 - \frac{\Omega^2}{\omega_r^2} + i 2\zeta_r \frac{\Omega}{\omega_r}} \frac{\Omega}{\omega_r} f(t) \quad (23)$$

$$= \frac{P_0 \Gamma_r}{\omega_r^2 M_r} H_r(\Omega) f(t) \quad (24)$$

where:

$$r = 1, 2, \dots, n$$

$$H_r(\Omega) = \frac{1}{1 - \left(\frac{\Omega}{\omega_r}\right)^2 + i 2\zeta_r \frac{\Omega}{\omega_r}} \frac{\Omega}{\omega_r} \quad (25)$$

The total deflection of the structure, $w(x,t)$ is obtained by inserting Equation (24) into Equation (24) into Equation (5). Thus

$$w(x,t) = P_0 \sum_{i=1}^n \frac{\Gamma_i}{\omega_i^2 M_i} \phi_i(x) H_i(\Omega) f(t) \quad (26)$$

$$w(x,t) = \sum_{r=1}^n \phi_r(x) \eta_r(t) \quad (27)$$

The mean square of the response is written as

$$\overline{w^2(x,t)} = \lim_{T \rightarrow \infty} \frac{1}{2T} \int_{-T}^T w^2(x,t) dt \quad (28)$$

Substituting in Equation (28) from Equation (27) and then from Equation (24) we have

$$\overline{w^2(x,t)} = \lim_{T \rightarrow \infty} \sum_{r=1}^n \sum_{s=1}^n \phi_r(x) \phi_s(x) \frac{1}{2T} \int_{-T}^T \eta_r(t) \eta_s(t) dt = \sum_{r=1}^n \sum_{s=1}^n$$

$$\frac{P_0^2 \Gamma_r \Gamma_s}{\omega_r^2 \omega_s^2 M_r M_s} \lim_{T \rightarrow \infty} \frac{1}{2T} \int_{-T}^T H_r(\Omega) H_s(\Omega) f^2(t) dt \quad (29)$$

If as an approximation we disregard phase relations which will tend to result in a higher mean square value in Equation (29); then the integral on the right-hand side of this equation can be written as

$$\lim_{T \rightarrow \infty} \frac{1}{2T} \int_{-T}^T H_r(\Omega) H_s(\Omega) f^2(t) dt \quad (30)$$

$$\lim_{T \rightarrow \infty} \frac{1}{2T} \int_{-T}^T H_r(\Omega) H_s(\Omega) f^2(t) dt$$

When the forcing function $f(t)$ is a representative record of an ergodic process, we can transform the limiting process of Equation (30) from the time domain to the frequency domain because the function $f(t)$ is then represented by frequency components in a continuous frequency spectrum $0 < \Omega < \infty$. Thus

$$\overline{f^2(t)} = \lim_{T \rightarrow \infty} \frac{1}{2T} \int_{-T}^T f^2(t) dt \quad (31)$$

$$\frac{1}{2\pi} \int_0^\infty f(\Omega) d\Omega$$

Using this transformation from the time to the frequency domain in Equation (30) we write

$$\lim_{T \rightarrow \infty} \frac{1}{2T} \int_{-T}^T |H_r(\Omega)| |H_s(\Omega)| f^2(t) dt \quad (32)$$

$$\frac{1}{2\pi} \int_0^\infty |H_r(\Omega)| |H_s(\Omega)| f(\Omega) d\Omega$$

Starting from Equation (29) we write for the mean square response of an n degree of freedom system excited by a random forcing function

$$\sum_{r=1}^n \sum_{s=1}^n \phi_r(x) \phi_s(x) \frac{p_0^2 \Gamma_r \Gamma_s}{\omega_r \omega_s M_r M_s} x$$

$$\frac{1}{2\pi} \int_0^\infty |H_r(\Omega)| |H_s(\Omega)| f(\Omega) d\Omega \quad (33)$$

Equation (33) can be simplified by introducing another approximation

approximating the magnification

$$\left[\frac{1}{1 - \left(\frac{\Omega}{\omega_r} \right)^2} + 4\zeta^2 \frac{\Omega^2}{\omega_r^2} \right]^{-1/2} \quad (34)$$

For a lightly damped multi-degree-of-freedom system. The magnification factors $|H_r(\Omega)|$ have regions of pronounced peaks in the neighborhood of the corresponding natural frequencies ω_r . The products $|H_r(\Omega)| |H_s(\Omega)|$ for $r \neq s$ are seen to be small in comparison with the same products for $r = s$. In addition, in Equation (33), terms with $r \neq s$ may be negative as well as positive depending upon the sign of the product $\phi_r(x) \phi_s(x) \Gamma_r \Gamma_s$ while terms with $r = s$ are always positive. The contribution of cross product terms ($r \neq s$) to the mean square response. Equation (33) will therefore be small. Hence, by disregarding the cross product terms corresponding to $r \neq s$, Equation (33) becomes

$$\overline{w^2(x,t)} = \sum_{r=1}^n \phi_r^2(x) \frac{p_0^2 \Gamma_r^2}{\omega_r^4 M_r^2} \quad (35)$$

$$\frac{1}{2\pi} \int_0^\infty |H_r(\Omega)|^2 f(\Omega) d\Omega$$

Equation (35) can be further simplified by approximating the integrals of Equation (35) by replacing $f(\Omega)$ by its discrete values $f(\omega_r)$ at the natural frequencies ω_r (see Figure 6) and using

$$\begin{aligned} \frac{f(\omega_r)}{2\pi} \int_0^\infty \frac{1}{\left[1 - \left(\frac{\Omega}{\omega_r} \right)^2 \right]^2 + 4\zeta^2 \frac{\Omega^2}{\omega_r^2}} d\Omega \\ = \frac{f(\omega_r)}{2\pi} \frac{\pi}{4} \frac{\omega_r}{\zeta_r} = \frac{f(\omega_r) \omega_r}{8\zeta} \end{aligned} \quad (36)$$

By introducing the following definitions

$$f(\omega_r) = g'_{\text{input}} \otimes f_n \quad (37)$$

$$g'_{\text{in}} = g'_{\text{input}} = g^2 / \text{Hz input} \otimes f_n \quad (37a)$$

$$f_n = f_r = 2\pi \omega_r \quad (38)$$

$$Q = \frac{1}{2\zeta} \quad (39)$$

Equation (35) becomes

$$\begin{aligned} \overline{w^2(x,t)} = \sum_{r=1}^n \phi_r^2(x) \frac{p_0^2 \Gamma_r^2}{\omega_r^4 M_r^2} \\ \left(\frac{\pi}{2} g'_{\text{in}} f_n Q \right) \end{aligned} \quad (40)$$

Equation (40) is the equation which forms the basis of the method "Response Spectrum Analysis" (RSA).

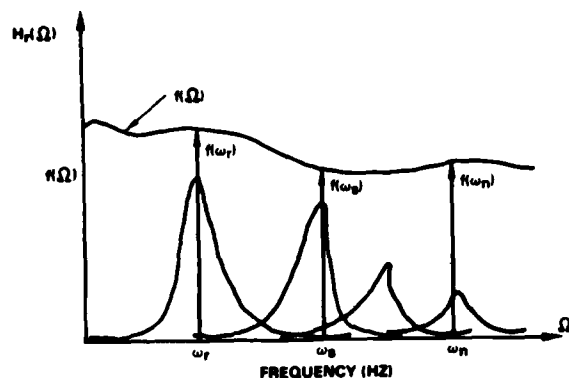


Figure 6, Magnification Factors for a Lightly Damped Multi-Degree-of-Freedom System

Recall the assumptions leading to Equation (40) they are:

1. Ignore phase relations
2. Magnification products at different frequencies are ignored
3. All modes (frequencies) are lightly damped
4. Using discrete values of the input spectrum at the natural frequencies.

At this point, we can summarize and list equations (21), (26) and (40) as follows:

Case 1) Shock

$$w(x,t) = \sum_{r=1}^n \frac{p_0 \Gamma_r}{\omega_r^2 M_r} \phi_r(x) D_r(t) \quad (21)$$

where: $r = i = 1, 2, \dots, n$

or

$$\ddot{w}(x,t) = \sum_{r=1}^n \frac{p_0 \Gamma_r}{\omega_r^2 M_r} \phi_r(x) D'_r(t) \quad (21A)$$

where

$$D'_r(t) = \frac{d^2}{dt^2} (D_r(t))$$

(now in units of acceleration)

Case 2) Sine

$$w(x,t) = \sum_{r=1}^n \frac{p_0 \Gamma_r}{\omega_r^2 M_r} \phi_r(x) H_r(\Omega) f(t) \quad (26)$$

where: $r = i = 1, 2, \dots, n$

or

$$\ddot{w}(x,t) = \sum_{r=1}^n \frac{p_0 \Gamma_r}{\omega_r^2 M_r} \phi_r(x) Q f'(t) \quad (26A)$$

where $f'(t) = \frac{d^2}{dt^2} (f(t))$ (now in units of acceleration)

and

$$Q = \frac{1}{2\zeta_r} \quad (\text{per Equation (34) when } \Omega = \omega_r)$$

Case 3) Random

$$\ddot{w}^2(x,t) = \sum_{r=1}^n \frac{p_0^2 \Gamma_r^2}{\omega_r^4 M_r^2}$$

$$\phi_r^2(x) \left(\frac{\pi}{2} g'_{in} f_n Q \right) \quad (40)$$

where, in all cases, $\ddot{w}(x,t)$ is defined as response acceleration.

In the case of random (case 3), response g_{RMS} is defined as

$$g_{RMS} = \sqrt{\ddot{w}^2(x,t)} = \left[\sum_{r=1}^n \frac{p_0^2 \Gamma_r^2}{\omega_r^4 M_r^2} \phi_r^2(x) \left(\frac{\pi}{2} g'_{in} f_n Q \right) \right]^{1/2} \quad (41)$$

which includes all frequencies (ω_r, f_n) and modes $\phi_r(x)$ of the structural system under consideration. Whereas, g_{RMS} per mode or frequency, which is computed as a first step toward the overall g_{RMS} computation is

$$g_{RMS}^{(r)} = \sqrt{\ddot{w}^2(x,t)}_{\omega_r}$$

$$\frac{p_0 \Gamma_r}{\omega_r^2 M_r} \phi_r(x) \left(\frac{\pi}{2} g'_{in} f_n Q \right)^{1/2} \quad (42)$$

By comparing Equation (42) to Equation (26A) and in turn to (21A) we see that the only difference in the response of a multi-degree-of-freedom structure at a natural frequency, ω_r , are the forcing function terms, that is

Case 1) Shock

$$D'_r(t) \quad (43)$$

Case 2) Sine

$$Q f' (t) \quad (44)$$

and

Case 3) Random

$$\left(\frac{\pi}{2} g'_{in} f_r Q \right)^{1/2} \quad (45)$$

all other terms of the above cases, that is

$$\frac{p_o r}{\omega_r^2 M_r} \phi_r (x) \quad (46)$$

define a multi-degree-of-freedom system (as opposed to a one-degree-of-freedom system) and are common to all $g_{response}$ solutions for shock, sine or random environments.

Equations (43) - (45) are nothing more than the $g_{response}$ terms already discussed for a simple one-degree-of-freedom system. Thus, Figure 5 is again directly applicable, for not only a one-degree-of-freedom system but for multi (complete structures)-degree-of-freedom system as well. However, the interpretation of Figure 5 must be modified. For a one-degree-of-freedom system, Figure 5 presents the "true" $g_{response}$ for shock, sine and random en-

vironments. For a multi-degree-of-freedom system, Figure 5 is not the final or "true" analytical $g_{response}$ but must be modified by Equation (46). Since Equation (46), is common to all three sets of solutions (shock, sine, random), Figure 5 is merely "off" by a constant multiplier that can only be determined by analyzing the structure in detail for all the frequencies, modes $\phi_r (x)$, etc. that define a multi-degree-of-freedom structure.

Using the analysis technique for Response Spectrum Analysis and saving the g_{rms} terms at each natural frequency will then allow the determination of "true" g_{rms} response for each environment (shock, sine, or random), which differ by a g_{input} magnitude difference defined and known via Equations (43) - (45).

CONCLUSIONS

The above approach does provide the benefits of time and cost savings, but is limited by the assumptions required to derive the approach. The application of the approach can be verified early in the design, but requires the capability to solve the dynamic analysis using a program that utilizes both approaches formulated by Equation (29) versus Equation (40) - the program "Stardyne", for example.

Although shock response is little affected by assumed damping, both sine and

random analyses depend heavily on modal damping assumptions for the accuracy of their predictions.

Until that time that damping can be determined accurately, prior to actual vibration testing, the approach will remain useful.

REFERENCES

- W. C. Hurty, and M. F. Rubinstein, "Dynamics of Structures" Prentice-Hall, Inc., Englewood Cliffs, New Jersey, 1964.
- M. F. Gardner, and J. L. Barnes, "Transients in Linear Systems", Vol. I, John Wiley & Sons, Inc., New York 1942.
- W. T. Thomson, Laplace Transforms (2nd ed.) Prentice-Hall, Inc., Englewood Cliffs, New Jersey, 1960.

VIBRATION TEST LEVEL CRITERIA FOR AIRCRAFT EQUIPMENT

Preston S. Hall
Flight Dynamics Laboratory
Air Force Wright Aeronautical Laboratories
Wright-Patterson AFB, Ohio

The Combined Environment Reliability Test (CERT) Evaluation Program, conducted by the Air Force Wright Aeronautical Laboratories (AFWAL), utilized different methodologies to formulate the vibration test conditions. The problems of mission profiling the vibration environmental stresses are varied. Each methodology is examined for ease of vibration test condition formulation, utilization, and resultant reliability of the specimens tested. A recommendation is made on vibration test criteria for CERT based upon five years of experience and test results.

INTRODUCTION

The purpose of the CERT Evaluation Program, conducted by AFWAL, is to evaluate the effectiveness of CERT for early identification of deficiencies and to provide insight into how the equipment will perform in operational service (Ref. 1). In this program, up to ten different equipment items will be exposed to up to three different levels of environmental simulation; namely, Full CERT, CERT Without Altitude, and MIL-STD-781C Appendix B (Ref. 2). This program is to determine the degree of correlation between these three different test sequences and the actual field reliability in terms of failure rates and modes.

Each of these test sequences utilized different methodologies for the establishment of the test conditions. MIL-STD-781C Appendix B was the most completely defined in terms of methodology of determining test conditions, while Full CERT and CERT Without Altitude made use of many readily available tools such as analytical models, measured flight test data, or engineering judgments.

This report focuses on the methodologies used to formulate the vibration conditions used during each test sequence and assess the impact on the resultant reliability statistics.

Section II points out the problems of mission profiling vibration environmental stresses as compared to other environmental stresses. This is followed by a description of the general approach to vibration test condition formulation utilized for each of the three test sequences.

RELIABILITY TESTING VIBRATION CRITERIA BACKGROUND

After considerable concern was expressed regarding the reliability of avionics equipment used in high performance aircraft, an investigation was conducted (Ref. 3) to determine how many avionic field failures were environmentally induced and the significant environmental parameters affecting avionics reliability. The evidence was conclusive that environments are responsible for 52 percent of the avionics field failures, with 90 percent of environment related failures attributed to temperature, altitude, humidity, and vibration.

Traditionally, tests have not exposed avionics equipment to realistic environmental stresses, thus contributing to the poor correlation between field and laboratory failure rates and modes. The AFWAL has conducted a number of reliability tests using the flight profile concept, designed around basic aircraft missions, as a straightforward approach

to identify failure modes and rates on avionics equipment in the laboratory comparable with field experience. During the on-going CERT Evaluation Program, each engineer responsible for a test in the program individually developed the flight profiles. In many cases, flight profiles were developed using measured data, analytical data, or a composite of both. Regardless of the data source used, each engineer attempted to develop profiles that were representative of the flight conditions that a piece of avionics would see in service.

As mentioned previously, the flight profiles representative of aircraft missions (combat, low-altitude bombing, training, reconnaissance, etc.) forms the foundation for the environments to which the avionics will be exposed. The result is a very tailorable test with parameters traceable to characteristic circumstances. The major environmental stresses that are used in the CERT Evaluation Program are temperature, humidity, altitude, and vibration. Each environmental stress, with the exception of vibration, would have a time varying profile that was directly related to the flight profile in time. Due to the capabilities of vibration controllers, vibration profiles had to be structured from multiple vibration spectra representing various phases of the mission flight profile; for example, takeoff, cruise, combat, and landing (Fig. 1). The resulting vibration spectra require two parameters, amplitude and frequency, to define a unique vibration stress (Fig. 2). During the CERT Evaluation Program, each test engineer selected one of the three techniques to generate the vibration spectra.

Since the CERT Evaluation Program was structured to compare the present MIL-STD-781 methods with the AFWAL CERT concept, the conventional means for generating vibration spectra as outlined in MIL-STD-781C Appendix B was one technique used throughout the program. The criteria used in the specification are very straightforward with just two spectra shapes (Fig. 3) and two equations expressing the levels for the spectra. The equations are related to the aerodynamic induced vibrations and the only information required is Mach, altitude, and equipment location (Table I). The Mach and altitude values, obtained from the mission flight profiles, would be related to a specific portion of the profile instead of every instant of time. A maximum of four vibration levels will be determined by: (1) takeoff, (2) maximum aerodynamic pressure (q_{max}), (3) minimum aerody-

amic pressure (q_{min}), and (4) average aerodynamic pressure (q_{avg}) (Ref. 4).

Since the AFWAL CERT concept places explicit emphasis on realism, flight data were often used to generate vibration spectra. Various sources of data are available for obtaining flight time histories of vibration, which can be matched very closely to characteristic mission flight profiles. The disadvantage of flight data is that data may not always be available for a specific equipment location. Also, this technique may not be useful to generate vibration spectra for equipment to be used in new aircraft for which no flight data exists.

Another technique of generating vibration spectra used in the AFWAL CERT program is analytical prediction. The vibration prediction technique most commonly used was a computerized generation of vibration spectra that was developed by AFWAL/FIEE (Ref. 5). The vibration spectra resulting from this technique are a very close approximation of flight data and relates to specific aircraft, maneuvers, and equipment locations. The prediction technique requires the availability of a computer, the prediction software, and aircraft parameters: aerodynamic distance of the avionic specimen from the aircraft nose, distance of specimen from skin, equipment weight, etc., along with specific Mach-altitude combinations and straight-and-level or buffet turn maneuvers. The computer software has the capability to predict levels for only five fighter aircraft. In order for this technique to be used on aircraft other than the five preprogrammed, it is necessary to supplement the program with additional information regarding fuselage bending modes and transfer functions describing the primary and secondary structures of the aircraft in question.

The commonality of all these methods of vibration spectra generation is that all are dependent upon Mach and altitude combinations. The spectra vary in shape and amplitude depending upon which technique is used. The methods used in the AFWAL CERT concept generally resulted in more tailored spectra shapes which seemed to satisfy the desire to achieve a degree of realism. The ability to time vary the spectra in direct relation to the time varying Mach and altitude values of a mission flight profile is at present technically impossible due to the limitation of the state-of-the-art for vibration controllers. With all these considerations kept in mind, the issue of concern is: What is required of test criteria to

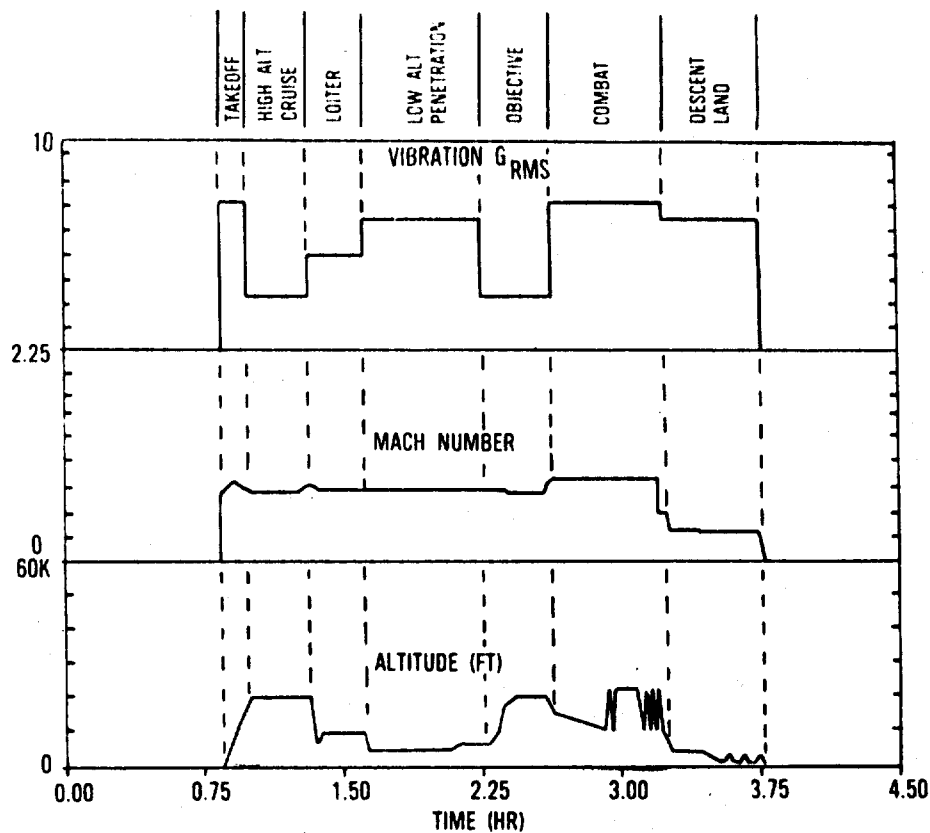


Figure 1 -- Typical Mission Flight Profile

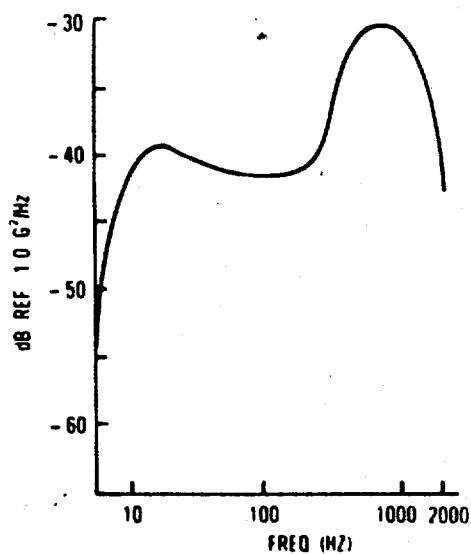


Figure 2 -- Random Vibration Spectrum

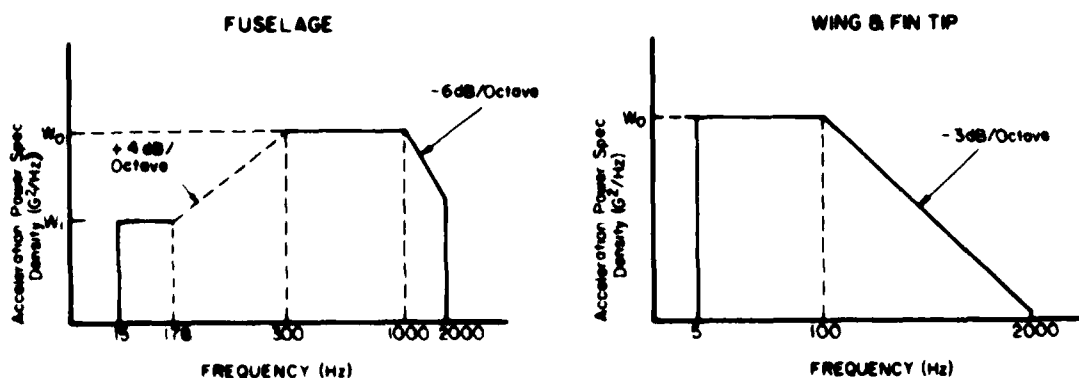


Figure 3 -- Jet Aircraft-Random Vibration Test Envelope

TABLE I -- MIL-STD-781C JET AIRCRAFT-RANDOM VIBRATION TEST CRITERIA

Aerodynamic Induced Vibration	
$W_0 = K(q)^2$	q = Dynamic Pressure (when $q > 1200$ psf use 1200)
$W_1 = W_0 - 3dB$	
K	Equipment Location
$.67 \times 10^{-6}$	Equipment attached to structure adjacent to external surfaces that are smooth, free from discontinuities.
$.34 \times 10^{-6}$	Cockpit equipment and equipment in compartments and on shelves adjacent to external surfaces that are smooth, free from discontinuities.
3.5×10^{-6}	Equipment attached to structure adjacent to or immediately aft of surfaces having discontinuities (i.e., cavities, chins, blade antennas, etc.).
1.75×10^{-6}	Equipment in compartments adjacent to or immediately aft of surfaces having discontinuities (i.e., cavities, chins, speed brakes, etc.).
SPECIAL CASE CONDITIONS	
Fighter Bomber	
Condition/Equipment Location	W_0
Takeoff/attached to or in compartments adjacent to structure directly exposed to engine exhaust Aft of engine exhaust plane (1 minute)	.7
Cruise/(same as above)	.175
Takeoff/in engine compartment or adjacent to engine Forward of engine exhaust plane (1 minute)	.1
Cruise/(same as above)	.025
Takeoff, landing, maneuvers/wing and fin tips deceleration (speed brake) (1 minute)	.1
High q (> 1000 psf)/wing and fin tips	.02
Cruise/wing and fin tips	.01
Takeoff/all other locations (1 minute)	.002

identify realistic failure rates and failure modes in the laboratory?

VIBRATION SPECTRA GENERATION

Before an engineer can determine the vibration spectra to be used for combined environments tests, he must first examine the various mission/environmental profiles that are possible for the aircraft/avionic combination. Figure 4 shows a typical logic flow diagram a test engineer may use in establishing the test profiles for a piece of avionics in a specific aircraft. An individual aircraft type is designed to operate within a specific flight envelope and to fly specifically determined mission profiles. These design flight envelopes and mission profiles should be utilized when formulating the environmental profiles for a test. A number of mission profiles may be possible for one aircraft type, but statistically only two may be representative of the aircraft's major life. After the aircraft mission profiles have been determined for testing, the environmental profiles shall be generated and shall vary according to the aircraft mission profile. As pointed out earlier, the thermal, humidity, and altitude test environment profiles can have a one-to-one time varying relationship with the aircraft mission profile just as in flight. However, aircraft mission profiles must be analyzed by individual flight phases such as takeoff, climb, mission objective, descent, and landing to generate a number of vibration spectra which, when exposed sequentially to the test specimen, would make up the environmental vibration profile. After the test engineer has determined what flight phases significantly impact the test, he must determine the maximum, minimum, or average conditions and Mach/altitude combinations necessary to generate the vibration spectra. The test engineer then makes another judgment as to whether he wants multiple vibration spectra or a composite of several for the aircraft mission profile.

After determining the vibration spectra required to give a representation of vibration stresses, the engineer must give consideration to test equipment limitations. There exists a number of ways to control vibration inputs, all of which have their limitations. The devices to control vibration range from simple audio recording equipment to extensive digital computer controllers (Ref. 6).

The minimum level of a vibration spectrum is of concern for any vibration

controller. With both analog and digital controllers, there exists a noise floor or a level of vibration that is so low that the controller's signal to noise capability is exceeded. The manufacturer establishes a cut-off level for a controller relative to its characteristic noise floor in order to assure good controllability. For some cases in the CERT Evaluation Program, the levels of vibration derived from flight data and analytical methods have been below the cut-off level of the controllers. A judgment must be made to either eliminate vibration exposure during these periods of the vibration profiles or choose some minimum spectrum level that the controller could handle for the total mission.

Economics is another concern if vibration requirements impose the use of more sophisticated vibration control equipment. The developer of a piece of avionics may find it economically impossible to purchase a sophisticated digital system in order to achieve the vibration requirements. The analog controller is fine for vibration spectrum control; however, the major difference between it and digital systems is that only one spectrum shape can be effectively controlled per mission simulation. Considerable time is required to establish a spectrum and there is no convenient method of storing multiple spectra that may be introduced at various times to represent different phases of vibration profile. Early tests during the CERT Evaluation Program used analog systems, as digital controllers were not available. A single vibration spectrum was used throughout the test and the mean time between failures (MTBF) was in good correlation with field MTBF data (Ref. 7).

Under MIL-STD-781 procedures for establishing vibration spectra, a number of the engineering decisions are eliminated and equipment limitations are nonexistent in the majority of cases. By definition, the engineer is still required to give consideration to the various mission/environmental profiles that are possible for the aircraft/avionic combination to be tested. However, when design flight envelopes and specifically designated flight mission profiles are not available, the generalized mission profiles listed in MIL-STD-781C Appendix B are to be used for development of environmental profiles.

With regard to vibration spectra generation, MIL-STD-781C Appendix B has only two spectrum shapes and the level is dependent upon Mach/altitude

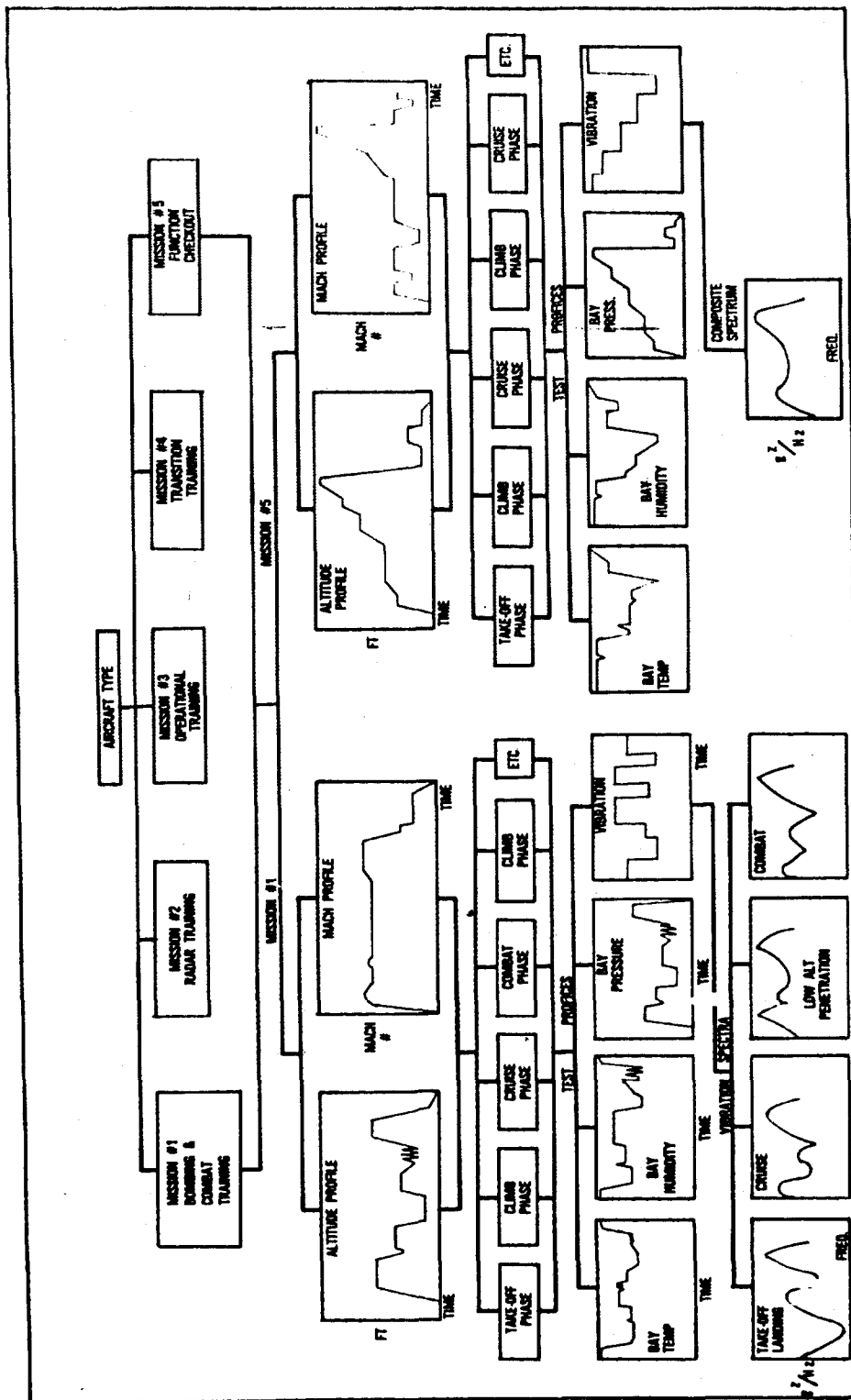


Figure 4 -- 7-st Profile Generation Logic Diagram

combinations obtained from actual profile data or given values in Appendix B (Tables II, III, and IV) (Ref. 4). A constant value also must be determined from a choice of four values relating to equipment location. If the level for a particular phase of the vibration profile is less than $0.001 \text{ g}^2/\text{Hz}$, then vibration exposure is not required.

The criteria in MIL-STD-781C give the test engineer the advantage of determining numbers of missions, flight phases, and vibration spectra for new avionics on new aircraft for which there are no mission/environmental data. The criteria also allow the use of analog equipment to control the vibration spectra, since only one shape exists and levels are easily changed. Problems with control of extremely low levels are eliminated, since the minimum cut-off level in the test criteria is well above the capability of most controllers.

With the introduction of a cut-off level for vibration under MIL-STD-781C criteria, the possibility exists that the test specimen may not be exposed to vibration during considerable portions of the tests. With the AFWAL CERT concept of testing, vibration is continuous during the flight portion of a mission as long as it is within controller capabilities. As previously mentioned, the number, shape, and levels of vibration spectra used in this portion of the evaluation program varied for a number of reasons, but the exposure time is continuous, or nearly so.

The project engineer for the AN/APX-76 IFF Transponder test in the evaluation program examined the differences between MIL-STD-781C and AFWAL CERT vibration in both time and levels (Ref. 8). Figure 5 shows the difference in the two test concepts' spectra. During AFWAL CERT, the straight-and-level vibration spectrum was applied 63 percent of the time to the equipment under test. "No vibration was applied 19 percent of the time due to ground park, and the maneuvering spectrum was applied 18 percent of the time. In a MIL-STD-781C Appendix B test, due to level cut-off limitations and ground park, no vibration would be applied 70 percent of the time, $W_0(\text{max})$ two percent of the time, $W_0(\text{min})$ eight percent of the time, and $W_0(\text{avg})$ 20 percent of the time. Therefore, severe vibration is applied to the equipment for 12 percent more time in MIL-STD-781C Appendix B testing than in AFWAL CERT." (Ref. 8)

After the original three test sequences in the evaluation program had

been completed on the AN/APX-101 IFF Transponder to A-10 mission profile conditions, an additional series of test cycles was to be conducted to Full CERT criteria without the highly stylized computer predicted vibration spectra. The test was to use MIL-STD-781C Appendix B spectra, but the cut-off level exclusion was eliminated, thus combining the best practical advantages of AFWAL and MIL-STD-781C methodologies. This would provide for vibration to be continuous throughout the test, but the levels would never go below $0.001 \text{ g}^2/\text{Hz}$. This level was found to be greater than the predicted tailored levels and measured data. The intent of using the simplistic vibration criteria, along with the other realistic environmental profiles, was an attempt to evaluate the need for stylized vibration profiles and the effect of vibration exposure time.

ANALYSIS

The CERT Evaluation Program, to date, has tested six pieces of avionics. Each test has utilized at least two, and sometimes all three, methods of generating vibration spectra previously mentioned. In every case, the avionics tested has had flight data available to generate flight environmental profiles, were previously tested to MIL-STD-781B or -781C, and field reliability data (AFM 66-1) were available.

From available literature examined (Ref. 9), it was found that the presence of very low amplitude vibration for a long period of time does have a significant impact on equipment life (Fig. 6). Even though these data are for a single environmental condition, which is much less complex than combined environments, they still suggest the importance of vibration-caused failures over a long period of time, even at low amplitudes.

At this time, testing of the APX-101 to A-10 conditions is continuing with over 1000 hours of ON time. Although tests have already been conducted on this equipment to Full CERT and MIL-STD-781C Appendix B, it is now being tested to Full CERT again but with MIL-STD-781C Appendix B vibration spectra in lieu of the highly tailored spectra. In cases where the vibration level was calculated to be below the standard's cut-off level, vibration was to be continuous over that range at the cut-off level. Although the level may be higher than actual field conditions, and the findings in the referenced literature (Ref. 9) is true even in combined environments cases, then the failures may propagate at a faster rate and then level off. It was indeed found in the modified AFWAL

TABLE II -- TYPICAL MISSION PROFILE - AIR SUPERIORITY FIGHTER

Flight Mode	Test Phase*	% Time	Altitude (1000 ft)	Mach Number	q (psf)
Ground Runup (no AB)	A,F	4	0 to 0.5	0	-
(with AB)		1			
Takeoff	B,G	5	0.5 to 1	0 - 0.4	-
Climb (to 40,000 ft)	B,G	8	to 40	0.6	245
Cruise (500 ft)	C,H	6	.5	0.8	900
(20,000 ft)		5	20	0.9	550
(40,000 ft)		40	40	0.9	225
Acceleration	C,H	4	40 to 50	1.7	620
Combat (500 ft)	C,H	1	.5	0.85	900
(5,000 ft)		1	5	0.9	1000
(10,000-40,000 ft)		2	10 to 40	2.0	1800
(50,000 ft)		3	50	2.5	1180
Descent	D,I	8	40 to 3	0.8	445
Loiter	D,I	8	3	0.4	200
Landing	D,I	5	3 to 0.5		

*See Fig. B-3 of MIL-STD-781C Appendix B.

TABLE III -- TYPICAL MISSION PROFILE - INTERDICTION FIGHTER

Flight Mode	Test Phase*	% Time	Altitude (1000 ft)	Mach Number	q (psf)
Ground Runup (no AB)	A,F	4	0.5	0	-
(with AB)		1	0.5	0	-
Takeoff	B,G	4	0.5 to 1	to 0.4	-
Climb (to 35,000 ft)	B,G	5	to 35	.6	245
Cruise (500 ft)	C,H	27	.5	0.8	900
		32	35	0.9	280
Acceleration	C,H	3	35 to 50	1.7	620
Combat (500 ft)	C,H	2	.5	0.85	900
(10,000-35,000 ft)		1	10 to 35	2.0	1800
(50,000 ft)		4	50	2.5	1180
Descent	D,I	6	40 to 3	0.8	445
Loiter	D,I	7	3	0.4	200
Landing	D,I	4	3 to 0.5		

*See Fig. B-3 of MIL-STD-781C Appendix B.

TABLE IV -- TYPICAL MISSION PROFILE - TRANSPORT/CARGO AIRCRAFT

Flight Mode	Test Phase*	% Time	Airspeed Knots**	q (psf)
Ground Runup	A,F	5	-	-
Takeoff/Climb	B,G	5	to 260	200
Cruise High Altitude 36K	C,H	70	240	210
Medium Altitude 22K		5	250	225
Low Altitude 1K		10	350	400
Descent/Land	D,I	5	140	100

*See Fig. B-1 of MIL-STD-781C Appendix B.

**Knots Equivalent Airspeed.

VIBRATION INPUT TO PRIMARY STRUCTURE

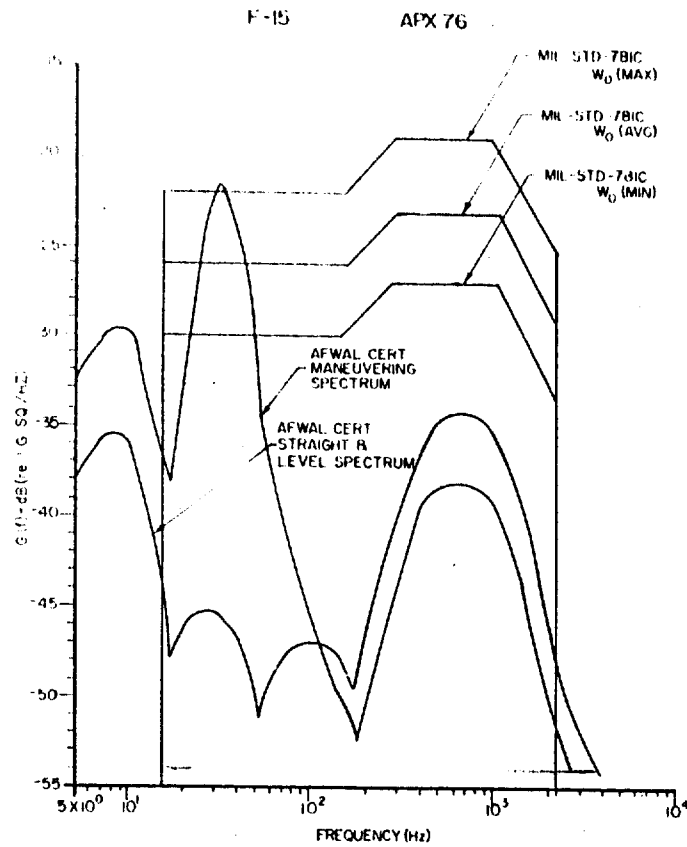


Figure 5 -- Vibration Input to Primary Structure

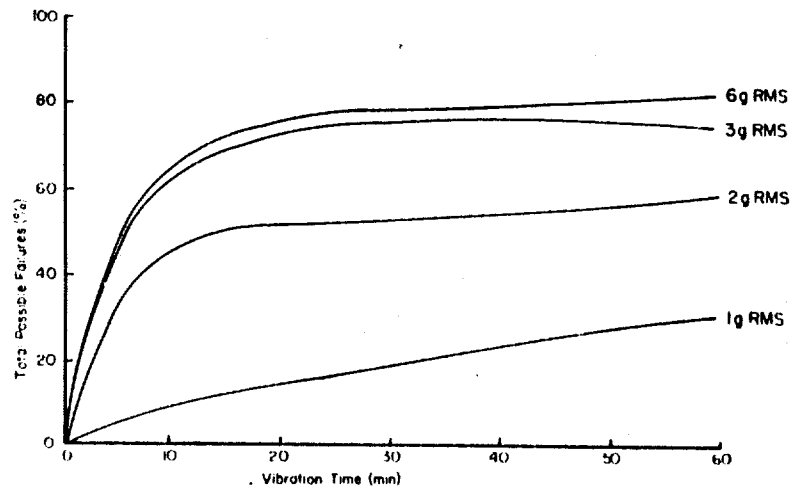


Figure 6 -- Random Vibration Faults

AFWAL CERT test that the only two failures found to date were discovered in the first test cycle.

Although these data are not enough to give overwhelming support to the vibration issue, they also do not refute the claim for simpler test criteria. What is implied, though, is that the payoff from using the MIL-STD-781C vibration spectrum for CERT may be less expensive in testing, increased ease of implementation, and better test results over present MIL-STD-781C criteria. The test results still must have additional data to increase upon confidence of the preliminary results.

Considerable savings in testing would be the result if laboratories and manufacturers did not have to obtain additional peripheral test equipment and software to generate highly sophisticated tailored vibration spectra. Finally, since the random vibration spectra in MIL-STD-781C are commonly used and accepted, then continued use of some form of these spectra may result in less confusion for future test concepts.

CONCLUSIONS AND RECOMMENDATIONS

From the tests run to date for the CERT Evaluation Program, it is apparent that continuous vibration throughout the test mission may contribute to a strong degree the good correlation between field and laboratory MTBF of internally-carried aircraft equipment. With the variance in engineering judgments made in the generation of vibration spectra (numbers, shapes, and levels), it appears that highly tailored vibration spectra are not technically or economically necessary to achieve realistic results. On a limited basis, it has been shown that with continuous vibration to MIL-STD-781C spectra, equally good data correlation exists as did testing to a stylized profile in the AFWAL CERT concept.

If AFWAL CERT vibration testing were performed using the spectral shapes of MIL-STD-781C Appendix B, it is felt that CERT would be more widely accepted for economic and simplicity reasons. The stipulation in MIL-STD-781C Appendix B criteria of no vibration exposure for levels calculated below $0.001 \text{ g}^2/\text{Hz}$ should be eliminated. Instead, vibration exposure should continue at $0.001 \text{ g}^2/\text{Hz}$ until a phase in the mission profile requires a higher level. The need for highly sophisticated vibration controllers, digital computers for spectra generation, and extensive software/programming would not be required to perform the vibration

portion of a reliability test. With a simplistic approach and yet technically correct to generating vibration spectra for a reliability test, the resulting data are trackable and confidence increased for procurement buys of avionics equipment.

REFERENCES

1. "Combined Environment Reliability Test Evaluation Program Plan," Jun 76, plus revision dated 1 Nov 77.
2. Scott, R., Captain, USAF, "Joint ASD/AFWAL Combined Environment Reliability Test (CERT) Evaluation Program," Proceedings of 24th Annual Technical Meeting of the Institute of Environmental Sciences, Fort Worth, Texas, Apr 78, pp 34-37.
3. Dantowitz, A., Hirschberger, G, and Pravidlo, D., "Analysis of Aeronautical Equipment Environmental Failures," AFFDL-TR-71-32, May 71.
4. "Reliability Tests: Exponential Distribution," MIL-STD-781C, 21 Oct 77.
5. Sevy, R., and Haller, M., "Computer Program for Vibration Prediction of Fighter Aircraft Equipment," AFFDL-TR-77-101, Nov 77.
6. Polallus, R., and Hirschberger, G., "Interim Report Utilization of Taped Random Spectra for Vibration Testing," Grumman Aerospace Corporation.
7. Prather, D., and Earls, D., "A Flight Profile Combined Environment Reliability Test of the AN/APQ-146 Terrain Following Radar System," AFFDL-TR-76-20, Mar 76.
8. Stanczak, E., "An Evaluation of the Combined Environment Reliability Testing of the RT868A/APX-76 IFF Interrogator Receiver-Transmitter," AFFDL-TR-77-132, Dec 77.
9. Kobe, F., and Hirschberger, G., "An Investigation to Determine Effective Equipment Environmental Acceptance Test Methods," ADR 14-04-73.2, Apr 73.
10. Prather, D., and Burkhard, A., "Combined Environment Reliability Test of the CN-1260/ASN-90(V) Inertial Measurement Unit," AFFDL-TR-79-3043, Apr 79.
11. Earls, D., "An Experimental Combined Environment Reliability Test of the AN/ARC-164 Radio Set," AFFDL-TR-78-127, Oct 78.
12. Hart, D., "A Test Plan for

Combined Environment Reliability Test
for the APX-101 Radio Receiver-
Transmitter," 25 Jul 78.

CONSERVATISM IN LEAST FAVORABLE RESPONSE ANALYSIS AND TESTING

Thomas L. Paez
The University of New Mexico
Albuquerque, New Mexico 87131

A structural shock test is conservative when it excites a more severe response than the input which it is meant to represent. We can measure shock signals from random sources in the field and use these to generate a shock test. If a structure survives this test then there is some probability that it would survive shocks generated by the random field sources in the future. This probability depends on the random shock sources and the degree of conservatism inherent in the shock test specification technique. In this paper we demonstrate a procedure for computing the probability of shock test conservatism for tests generated using the method of least favorable response. Several numerical examples are presented.

1.0 Introduction

To obtain adequate designs for engineering structures we analyze structural models and test structural prototypes in the laboratory. In order for a design to be optimal, in some sense, it is desirable to test a structure using an input which is conservative, but not a severe overtest. In this study we say that a test is conservative with respect to a field input when it excites a structural response which is more severe than the response excited by the field input. In the course of this investigation four reports (1-4)* have been written dealing with the conservatism in shock testing where tests are specified using the method of shock response spectra. We found that the method of shock response spectra can be expected to provide conservative shock tests when used properly. But the method is certainly not guaranteed to provide conservative shock tests in any sense. Situations can arise where a structure is significantly undertested even though its test has been properly specified using the method of shock response spectra. More commonly, tests specified using the method of shock response spectra are found to overtest structural components(5).

Another method available for the specification of shock tests is the method of least

favorable response(6). This method can be used analytically or in the laboratory and is guaranteed to provide tests which are conservative, at least in one sense. The method is based on analyses by Drenick and Shinozuka given, for example, in References 7 and 8. When the impulse response function, or equivalently the frequency response function, is available between a point of interest on a structure and the input point of the structure, and when we know the real function which envelops the modulus of the Fourier transform of all possible inputs which might excite the structure, then the method of least favorable response can be used to find an upper bound on the response which the point of interest on the structure can realize. We use this in the analysis of structural peak response. In the laboratory the least favorable response is generated experimentally, for example, by testing the structural unit on a shake table. If the structure survives the laboratory test, then we assume that it could survive any input in the class of inputs whose Fourier transform moduli are enveloped by the function used in the analysis. In all the analyses performed in this paper, it is assumed that an accurate estimate of the system frequency response function is available.

The problem with the method of least favorable response arises when we wish to use the technique to prove the capability of a structure to survive loads from a random source which will be applied at some time in the future. In this

*Numbers in brackets refer to a list of references appended to this report.

situation the loads applied in the future are independent of those measured in the past and used to specify the test. The loads generated in the future may be much more severe than those measured in the past. In view of this we depend on the inherent conservatism of the method of least favorable response to assure that a test is conservative with respect to future inputs. It is assumed that the random shock signal sources which will excite a structure in the field have characteristics which can be estimated based on past measurements from the random sources. In this study the expression "random shock signal source", refers to any random process forcing function generating phenomenon whose probabilistic characteristics do not change. For example, the random forcing function inputs which are generated at the base of a mechanical component during first stage separation when a particular type of missile is flown n times, come from one random shock signal source.

The objective of this study was to analyze the inherent conservatism of the method of least favorable response, and in this report we demonstrate a technique that can be used to do this. First, we review the method of least favorable response and show how it is used analytically and experimentally. Next we develop the technique used to measure the conservatism in a least favorable response test. Finally, we apply the method in some numerical examples where we measure the degree of conservatism in the tests of some specific structures.

2.0 The Method of Least Favorable Response

The method of least favorable response (LFR) is a technique that can be used analytically to find an upper bound on the response at a degree of freedom of a linear structure for a class of shock inputs. When the following two items of information are available we can obtain this upper bound. First, we require the impulse function at the point of interest on the structure when excited at its base. For present purposes we require only that an acceleration input impulse response function be specified. In this analysis we will consider only single source base excitations, and we will consider the output at a single structural point. Second, we require a function which envelops the moduli of the Fourier transforms of all inputs which might possibly excite the structure. We use this information in the following way to obtain the LFR. Let $h(t)$ be the impulse response function described above. the response, $Y(t)$, to an acceleration input $\ddot{X}(t)$ can be written using the convolution integral.

$$Y(t) = \int_0^t h(t - \tau) \ddot{X}(\tau) d\tau, \quad t \geq 0. \quad (2-1)$$

The frequency response function, $H(\omega)$, of the system is defined as the Fourier transform of the impulse response function.

$$H(\omega) = \int_{-\infty}^{\infty} h(t) e^{-i\omega t} dt, \quad |\omega| < \infty. \quad (2-2)$$

This can be written in terms of its modulus and phase as

$$H(\omega) = |H(\omega)| e^{i\phi(\omega)}, \quad |\omega| < \infty, \quad (2-2a)$$

where $\phi(\omega)$ is the complex phase of the frequency response function. When both sides of Equation 2-1 are Fourier transformed we obtain

$$Y(\omega) = H(\omega) X(\omega), \quad |\omega| < \infty, \quad (2-3)$$

where

$$Y(\omega) = \int_{-\infty}^{\infty} Y(t) e^{-i\omega t} dt, \quad |\omega| < \infty, \quad (2-3a)$$

$$X(\omega) = \int_{-\infty}^{\infty} \ddot{X}(t) e^{-i\omega t} dt, \quad |\omega| < \infty \quad (2-3b)$$

are the Fourier transforms of the linear system response and the acceleration input, respectively. Through inverse Fourier transformation of Equation 2-3 the system response can be expressed as follows.

$$Y(t) = \frac{1}{2\pi} \int_{-\infty}^{\infty} H(\omega) X(\omega) e^{i\omega t} d\omega, \quad t \geq 0, \quad (2-4)$$

where we have assumed the system initial conditions to be zero. The absolute value of the system response as a function of time is

$$|Y(t)| = \frac{1}{2\pi} \left| \int_{-\infty}^{\infty} H(\omega) X(\omega) e^{i\omega t} d\omega \right|, \quad t \geq 0. \quad (2-4a)$$

The absolute value of the system response is bounded by

$$\max_t |Y(t)| \leq \frac{1}{2\pi} \int_{-\infty}^{\infty} |H(\omega)| |X(\omega)| d\omega = I. \quad (2-5)$$

On the left-hand side we write the expression for peak response since the quantity on the right-hand side is a constant, independent of time. The quantity, I , is known as the least favorable response for the input, $\ddot{X}(t)$. The quantity, I , is a structural response which is as great or greater than the peak response excited by $\ddot{X}(t)$.

If a number of inputs from different sources will be used to excite the structure, and if several realizations of the acceleration input from each source are available, then we can compute a LFR for these signals. To be precise, we denote an acceleration input, $\ddot{X}_j(t)$, $j = 1, \dots, N$, $k = 1, \dots, N$, $t \geq 0$. This is the j th input from the k th source. We compute a function, $X(\omega)$, which is the exact envelope of the complex moduli of the Fourier transforms of all these functions as follows.

$$X_e(\omega) = \max_{j,k} |X_{jk}(\omega)|, \quad |\omega| < \infty, \quad (2-6)$$

where

$$X_{jk}(\omega) = \int_{-\infty}^{\infty} \ddot{x}_{jk}(t) e^{-i\omega t} dt, \\ j = 1, \dots, N_k \\ k = 1, \dots, N \\ |\omega| < \infty \quad (2-6a)$$

Now a bound on the structural response corresponding to all these inputs can be obtained as

$$\max_t |Y(t)| \leq \frac{1}{2\pi} \int_{-\infty}^{\infty} X_e(\omega) |H(\omega)| d\omega = I. \quad (2-7)$$

The quantity, I , is a response which is equal to or greater than the system response which can be excited by any of the individual inputs, $X_{jk}(t)$, $j = 1, \dots, N_k$, $k = 1, \dots, N$. The number, I , is the least favorable response for this collection of inputs.

When shock records from a number of sources are available and when a structure will be subjected to inputs from these sources, then a conservative value of the response can be obtained analytically as shown above. A shock test which is conservative with respect to the inputs, $\ddot{x}_{jk}(t)$, $j = 1, \dots, N_k$, $k = 1, \dots, N$, can be obtained in the following way. Let $\ddot{x}_T(t)$ be the test input, and let $X_T(\omega)$ be its Fourier transform.

$$X_T(\omega) = \int_{-\infty}^{\infty} \ddot{x}_T(t) e^{-i\omega t} dt, \quad |\omega| < \infty. \quad (2-8)$$

The test response excited by the test input is

$$Y_T(t) = \frac{1}{2\pi} \int_{-\infty}^{\infty} X_T(\omega) H(\omega) e^{i\omega t} d\omega, \\ t \geq 0. \quad (2-9)$$

We can force the test response to assume the value, I , from Equation 2-7, at a time, $t = t_0$, if we set

$$Y_T(t_0) = \frac{1}{2\pi} \int_{-\infty}^{\infty} X_T(\omega) H(\omega) e^{i\omega t_0} d\omega = I, \\ t_0 \geq 0. \quad (2-10)$$

The right-hand equation can be satisfied by taking $X_T(\omega)$ as

$$X_T(\omega) = X_e(\omega) e^{-i(\phi(\omega) + \omega t_0)}, \\ |\omega| < \infty, \quad (2-11)$$

where $\phi(\omega)$ is the complex phase of the frequency response function of the system under consideration. When $X_T(\omega)$ assumes the above form the structural response at time, $t = t_0$, will equal I . The complete time domain test input can be obtained by inverse Fourier transformation of Equation 2-11.

$$\ddot{x}_T(t) = \frac{1}{2\pi} \int_{-\infty}^{\infty} X_e(\omega) e^{i(\omega(t-t_0) - \phi(\omega))} d\omega, \\ t \geq 0. \quad (2-12)$$

The procedure outlined above can be used to obtain an input for use in the laboratory. When applied to the structure the input will excite the least favorable response. The test input obtained above is known as the least favorable input.

3.0 Least Favorable Response Test Conservatism

The method of least favorable response (LFR) can be used to obtain a bound on the response of a structure when a collection of measured inputs is available. And it can be used to obtain a test input which, if the structure survives, proves the capacity of the structure to survive those inputs. But the method of LFR does not prove the capacity of a structure to survive inputs which will be generated from a random source in the future. This is clearly impossible since the structural excitations which come from a random source in the future may be much more severe than any which came from that source and were measured in the past. In view of this, there exists only some nonunit probability that a LFR test, which is based on past, measured structural excitations, will be conservative with respect to inputs generated in the future. In this section we define a means for finding the probability of LFR test conservatism under different sets of circumstances.

We analyze the conservatism of a LFR test in two situations. The first situation is relatively simple and specialized. The second situation is very general, and includes, among others, the first situation as a special case. The elementary situation is that in which a single input measured from a single random source is used to specify a LFR test for a structure which will be subjected to one exposure to that source in the field. The second more general case is that in which one or more random signals measured from several sources are used to obtain a single LFR test, and the test will be used to prove a structure which will be subjected to one or more exposures from each random source in the field.

In this investigation we consider two random shock signal sources. Both random sources are characterized in the following way. Let $X(t)$, $|t| < \infty$, denote the continuous parameterized, continuous valued random process to be used in the study. $X(t)$ is defined by

$$\tilde{X}(t) = e(t) X_0(t), \quad |t| < \infty \quad (3-1)$$

where $X_0(t)$, $|t| < \infty$, is a stationary normal random process with zero mean and spectral density

$$S(\omega) = S_0, \quad |\omega| < \infty \quad (3-1a)$$

The function $e(t)$ takes the two forms

$$e_1(t) = H(t) - H(t - T), \quad |t| < \infty, T > 0 \quad (3-2a)$$

and

$$e_2(t) = Ae^{-\alpha t} H(t), \quad |t| < \infty, \alpha > 0 \quad (3-2b)$$

where $H(t)$ is the Heaviside unit step function, and A , α , and T are constants. This is a separable, nonstationary, normal random process.

In the following we develop a methodology for approximately determining the probability that a shock test is conservative when it is specified using the LFR method. When I is a LFR based on a collection of inputs from different random sources, this is simply the probability that I , as computed in Equation 2-7, is greater than each of the peak structural responses excited by a random input from each of the underlying sources. To find this probability we must find the probability distribution of the LFR for each of the situations described previously. Further, we must find the peak response probability distribution for a degree of freedom on a multi-degree-of-freedom (MDF) structure for each of the inputs described in Equations 3-1 and 3-2. The random variables representing the LFR and the peak structural responses are independent since they correspond to shock events occurring at different times. In view of this, the marginal probability density functions (pdf) for these random variables provide sufficient information to compute the probability of test conservatism. Therefore, in the following we will develop approximate probability distributions for the LFR, I , and the peak response of a MDF system to a random input.

We will first show that the LFR has an approximately normal probability distribution. Initially, we consider the single input case. The formula for the LFR given in Equation 2-5 is repeated here.

$$I = \frac{1}{2\pi} \int_{-\infty}^{\infty} |H(\omega)| |X(\omega)| d\omega, \quad (3-3)$$

where $|H(\omega)|$ is the complex modulus of the frequency response function of the structural system, and $|X(\omega)|$ is the complex modulus of the Fourier transform of the input. We can simplify this formula by using an approximation for

$|H(\omega)|$. That is, we let

$$|H(\omega)| = \begin{cases} |H(\omega_l)| = H_l, & \omega_l - \frac{\Delta\omega_l}{2} \leq |\omega| \leq \omega_l + \frac{\Delta\omega_l}{2} \\ 0 & \text{elsewhere} \end{cases} \quad (3-4)$$

where

$$\Delta\omega_l = 4\zeta_l\omega_l \ln(2/\sqrt{\zeta_l}), \quad l = 1, \dots, M \quad (3-4a)$$

and ω_l and ζ_l , $l = 1, \dots, M$ are, respectively, the modal frequencies and damping factors for the modes excited by the input. M is the number of structural modes excited by the input. H_l is the height of the frequency response function curve at the modal frequency, ω_l . The approximation actually provides an upper bound on the value of I when used in Equation 3-3. The derivation of this approximation is given in Appendix A of Reference 13. This approximation takes advantage of the fact that the modulus of the frequency response function of a lightly damped system is relatively large near the system modal frequencies and relatively small elsewhere. Using this approximation, the LFR can be written as

$$I \approx \frac{1}{\pi} \sum_{l=1}^M H_l \int_{\omega_l - \Delta\omega_l/2}^{\omega_l + \Delta\omega_l/2} |X(\omega)| d\omega. \quad (3-5)$$

This shows that the LFR can be approximated as the sum of M random variables, each having the form

$$D_l = H_l \int_{\omega_l - \Delta\omega_l/2}^{\omega_l + \Delta\omega_l/2} |X(\omega)| d\omega, \quad l = 1, \dots, M, \quad (3-6)$$

where H_l is a constant. It is clear that if the collection of random variables, D_l , $l = 1, \dots, M$, is large enough, and if no single random variable dominates over all the others, then the Central Limit Theorem requires that the distribution of I must approach the normal distribution. In practice, even if the sum in Equation 3-6 is composed of very few components, the probability distribution of I will be nearly normal. In this analysis we assume that the probability distribution of I can be taken as normal in all cases, even when $M = 1$. The reason for this is that the random variable

$$D_l^* = \int_{\omega_l - \Delta\omega_l/2}^{\omega_l + \Delta\omega_l/2} |X(\omega)| d\omega, \quad l = 1, \dots, M \quad (3-7)$$

has a nearly normal distribution, itself. This arises from the fact that the integral can be written as a sum of random variables, $|X(\omega)|$, and, again, from the Central Limit Theorem, the distribution of a sum should approach a normal distribution.

In view of the above assumptions we need only to estimate the first two moments of D_l^* , $l = 1, \dots, M$, to completely specify the distribution of the LFR, I . In all cases, the first two moments of D_l^* can be approximately computed. In this section we will write the expressions for the moments of D_l^* , and in Section 4.0 we will derive computational formulas which can be used in a numerical evaluation of the moments. The mean of D_l^* is defined

$$E[D_l^*] = \int_{\omega_l - \Delta\omega_l/2}^{\omega_l + \Delta\omega_l/2} E[|X(\omega)|] d\omega, \quad l = 1, \dots, M, \quad (3-8)$$

where $E[|X(\omega)|]$ is the mean of the modulus of the Fourier transform of the random process, $X(t)$, and usually varies with frequency. The Fourier transform is defined

$$X(\omega) = \int_{-\infty}^{\infty} \tilde{X}(t) e^{-i\omega t} dt, \quad |\omega| < \infty. \quad (3-8a)$$

Once the expression for $E[|X(\omega)|]$ has been specified, the mean of D_l^* can be easily computed, either in closed form or numerically. The analysis where we obtain $E[D_l^*]$ for the random processes defined in Equations 3-1 and 3-2, is deferred till Section 4.0. The variance of D_l^* can be expressed

$$V[D_l^*] = \int_{\omega_l - \Delta\omega_l/2}^{\omega_l + \Delta\omega_l/2} \int_{\omega_l - \Delta\omega_l/2}^{\omega_l + \Delta\omega_l/2} \text{cov}[|X(\omega_1)|, |X(\omega_2)|] d\omega_1 d\omega_2, \quad (3-9)$$

where $\text{cov}[|X(\omega_1)|, |X(\omega_2)|]$ is the autocovariance function of the Fourier transform of the random process, $\tilde{X}(t)$, evaluated at frequencies ω_1 and ω_2 . This can be evaluated once the autocovariance function is given, and a technique for approximating the autocovariance function for the random processes defined in Equations 3-1 and 3-2 will be developed in Section 4.0.

With the information provided above we can find the mean and variance of the random variables D_l , $l = 1, \dots, M$. They are

$$E[D_l] = H_l E[D_l^*], \quad l = 1, \dots, M, \quad (3-10a)$$

$$V[D_l] = H_l^2 V[D_l^*], \quad l = 1, \dots, M. \quad (3-10b)$$

Finally, we assume that the random variables D_l and D_j are uncorrelated for $l \neq j$. This is a reasonable assumption when the structural modes are widely separated, i.e., when there is little or no overlap of modal bandwidths. With this assumption we can write the expressions for the mean and the variance of the LFR, I . These are

$$E[I] = \mu_I = \frac{1}{\pi} \sum_{l=1}^M E[D_l], \quad (3-11a)$$

$$V[I] = \sigma_I^2 = \frac{1}{(\pi)^2} \sum_{l=1}^M V[D_l]. \quad (3-11b)$$

Given the moments of the LFR, I , we can now write the cumulative distribution function (cdf) for I . It is

$$P_I(a) = \Phi\left(\frac{a - \mu_I}{\sigma_I}\right), \quad (3-12)$$

where $\Phi(\cdot)$ is the cdf of a standardized normal random variable. The cdf described in Equation 3-12 characterizes, approximately, the random behavior of the LFR, I , when I is based on one random input.

To determine the probability that a LFR shock test based on one random input is conservative we must determine the probability distribution of the peak structural response excited by a shock signal from the random source used to derive the test. The technique used to do this, approximately, is given in Appendix B of Reference 13. The technique is a standard numerical, Poisson process approach, described, for example, in References 9 and 10. We will denote the peak response random variable, A , and its pdf, $p_A(a)$. The probability that the LFR shock test is conservative, p_c , is the probability that I is equal to or greater than A . This can be computed from

$$p_c = \int_{-\infty}^{\infty} \left[\int_{-\infty}^a P_I(a) p_A(a) da \right] da, \quad (3-13)$$

where $p_I(a)$ is the normal pdf of the LFR random variable, I . The product of the pdf's of the random variables I and A , is used in this expression since the LFR and the peak response excited by different random inputs are independent. As shown in Reference 13, the probability law governing the peak response is not normal. In view of this it is probably only

possible to obtain a good approximation to p_c by using a numerical integration. However, we can also make the assumption that the random variable, A , is approximately normally distributed to compute p_c using a simple formula. When this is done we obtain

$$p_c = \phi \left(\frac{\mu_I - \mu_A}{\sqrt{\sigma_I^2 + \sigma_A^2}} \right), \quad (3-14)$$

where μ_A and σ_A^2 are the mean and variance of the peak response of a structural system to one of the random inputs defined in Equations 3-1 and 3-2. The means for obtaining these parameters is given in Appendix B of Reference 13. In Section 5.0 some numerical examples are worked to show the probability of conservatism in some sample cases when one input is used to derive a shock input. We expect that if p_c is relatively high, say, greater than 0.99, then the degree of conservatism inherent in the method of least favorable response is high.

It is possible to obtain the probability of conservatism of a shock test in a more general situation. For example, we can find the probability of conservatism of a shock test when several excitations measured from one random source are used to derive a shock test for a structure which will be subjected to one input from that random source in the field. Also, in the field a structure may be subjected to multiple exposures from a single random source, and several excitations measured from that source may be used to obtain the test input. We can obtain the probability of conservatism in this case. Most generally, in the field a structure may be subjected to one or more exposures from one or more random sources, and the shock test may be based on one or more measured environments from each of the random sources. We can estimate the probability of conservatism of the test in this case. We use the general development presented in the previous part of this section to compute these probabilities of conservatism. We will consider the most general case first, and then we will discuss specializations of this approach to other cases.

We wish to find the pdf of the LFR, I , when the LFR is based on several random inputs from a number of sources. We denote the j th input from the k th random source as $X_{jk}(t)$, $j = 1, \dots, N_k$, $k = 1, \dots, N$, $|t| < \infty$. As in the previous analysis we are interested in finding the probability distribution of the random variable

$$D_{jkl}^* = \int_{\omega_l - \Delta\omega_l/2}^{\omega_l + \Delta\omega_l/2} |X_{jk}(\omega)| d\omega, \quad \begin{matrix} j = 1, \dots, N_k \\ k = 1, \dots, N \\ l = 1, \dots, M \end{matrix} \quad (3-15)$$

where $|X_{jk}(\omega)|$ is the complex modulus of the Fourier transform of the signal, $\ddot{X}_{jk}(t)$, and ω_l , $l = 1, \dots, M$, are the modal frequencies of the system under consideration. The reason we are interested in finding the probability distribution of each random variable, D_{jkl}^* , is that the LFR is based on these quantities. In fact, from Equation 2-6, it is apparent that the largest of the values, D_{jkl}^* , $j = 1, \dots, N_k$, $k = 1, \dots, N$, governs the component of the LFR integral in the frequency range, $(\omega_l - \Delta\omega_l/2, \omega_l + \Delta\omega_l/2)$.

Let us define the random variables Z_l , $l = 1, \dots, M$, as follows.

$$Z_l = \max_{j,k} D_{jkl}^*, \quad l = 1, \dots, M. \quad (3-16)$$

Then based on Equation 2-7, and using the approximation in Equation 3-4, the LFR is

$$I = \frac{1}{\pi} \sum_{l=1}^M H_l Z_l. \quad (3-17)$$

This is the LFR derived from the inputs $\ddot{X}_{jk}(t)$, $j = 1, \dots, N_k$, $k = 1, \dots, N$, $|t| < \infty$. To find the probability distribution of I we must find the probability distribution of the largest of the values D_{jkl}^* , $j = 1, \dots, N_k$, $k = 1, \dots, N$. This is Z_l . This distribution is an extreme value distribution. We have already established in Equations 3-6 through 3-9 that each random variable, D_{jkl}^* , is normally distributed. Moreover, we will show in Section 4.0 how the moments of D_{jkl}^* can be obtained, in practice. Based on this, we can find the desired extreme value probability distribution. In Appendix C of Reference 13 we derive the formulas for the cdf of the largest value in an arbitrary collection of random variables. By arbitrary, we mean that the collection can contain random variables representing as many different random shock sources as desired, with as many inputs from each source as desired. The results given in Reference 13 can be used to find the pdf of Z_l . We denote this $p_{Z_l}(z)$. This can be used to find the mean and variance of Z_l using the standard formulas.

$$E[Z_l] = \int_0^\infty z p_{Z_l}(z) dz, \quad l = 1, \dots, M, \quad (3-18a)$$

$$V[Z_l] = \int_0^\infty (z - E[Z_l])^2 p_{Z_l}(z) dz, \quad l = 1, \dots, M. \quad (3-18b)$$

We note that the probability distribution of Z is usually nonnormal.

Using Equations 3-17 and 3-18 it is now possible to compute the moments of the LFR, when

the LFR is based on the inputs $\ddot{x}_{jk}(t)$, $j = 1, \dots, N_k$, $k = 1, \dots, N$, $|t| < \infty$. The first two moments of I are

$$E[I] = \mu_I = \frac{1}{N} \sum_{l=1}^M H_l E[Z_l], \quad (3-19a)$$

$$V[I] = \sigma_I^2 = \frac{1}{(N)^2} \sum_{l=1}^M H_l^2 V[Z_l]. \quad (3-19b)$$

As before, we have assumed that the random variables Z_l and Z_j are independent for $j \neq l$.

Since the random variables, Z_l , $l = 1, \dots, M$, are not normally distributed, the LFR, I , is not exactly normally distributed. However, the LFR is the sum of M random variables. If the number of modes, M , is large enough, then the random variable, I , will have a distribution which is approximately normal, if no single mode dominates the sum in Equation 3-17. In this analysis we assume that the LFR, I , is governed by a normal distribution and its moments are given in Equations 3-19a and 3-19b. We write the cdf of I as

$$P_I(a) = \Phi\left(\frac{a - \mu_I}{\sigma_I}\right), \quad -\infty < a < \infty. \quad (3-20)$$

This cdf characterizes the random variability of the LFR which is based on the collection of inputs, $\ddot{x}_{jk}(t)$, $j = 1, \dots, N_k$, $k = 1, \dots, N$, $|t| < \infty$.

To determine the probability that the LFR shock test based on the inputs listed above is conservative, we must know the probability distribution of the largest structural response excited by the collection of inputs. In Appendix B of Reference 13 we derive the probability distribution of the peak response excited by a single random input. We used this to find the moments of the peak response, earlier, and we used these, along with a normal assumption, to find the probability of test conservatism. In the present case we must describe the peak response excited by a collection of inputs applied separately, at different times. To do this we assume that the individual peak response (response excited by a single input) probability distributions are normal. Then we find the extreme value distribution for the greatest response excited by the entire collection of inputs. These analyses are performed using the approaches of Appendix B and Appendix C in Reference 13. Finally, we find the mean and variance of the highest peak response excited by the collection of field inputs, and we assume, as before, that this random variable is normal. We use this information, along with Equations 3-19 and 3-20 to find the probability of test conservatism. Let $E[A] = \mu_A$ and $V[A] = \sigma_A^2$ be the mean and variance of the highest peak response excited by the field inputs. Then the conservatism probability, p_c , of the LFR test

derived from the inputs, $\ddot{x}_{jk}(t)$, $j = 1, \dots, N_k$, $k = 1, \dots, N$, $|t| < \infty$, is

$$p_c = \Phi\left(\frac{\mu_I - \mu_A}{\sqrt{\sigma_I^2 + \sigma_A^2}}\right) \quad (3-21)$$

where μ_I and σ_I^2 come from Equations 3-19a and 3-19b. In Section 5.0 some numerical examples are worked to show the probability of conservatism in some sample cases.

Some special cases arise in the application of the above formulas. Note that the collection of random inputs is given by, $\ddot{x}_{jk}(t)$, $j = 1, \dots, N_k$, $k = 1, \dots, N$, $|t| < \infty$. To consider one input each, from several random sources, we set $N_k = 1$, $k = 1, \dots, N$. When several random inputs from one source are to be considered, we set $N = 1$. Finally, the case considered in Equations 3-3 through 3-12, i.e., the one input-one source case, occurs when $N_k = 1$, $N = 1$.

4.0 Computation of Least Favorable Response Parameters

In the previous section we developed formulas to compute the probability that a LFR test is conservative. The usefulness of the formulas we developed depends on our ability to obtain a complete description of the probabilistic character of a random process which is defined as the Fourier transform of a real random process. In this section we consider the problem of characterizing the probabilistic behavior of the Fourier transform of a real random process. This is important since it supplies the information required to use Equations 3-8 and 3-9 in Section 3.0. We consider the random processes defined in Equations 3-1 and 3-2, and for convenience, we repeat their definitions here. These random processes are denoted, $\ddot{x}(t)$, $|t| < \infty$, and are defined by

$$\ddot{x}(t) = e(t) X_0(t), \quad |t| < \infty, \quad (4-1)$$

where the function $e(t)$ takes the two forms

$$e_1(t) = H(t) - H(t - T), \quad |t| < \infty, \quad T > 0 \quad (4-2a)$$

and

$$e_2(t) = A e^{-\alpha t} H(t), \quad |t| < \infty, \quad \alpha > 0, \quad (4-2b)$$

$X_0(t)$ is a stationary, zero mean, normal random process with spectral density,

$$S(\omega) = S_0, \quad |\omega| < \infty \quad (4-3)$$

$H(t)$ is the Heaviside unit step function, and A , α and T are finite constants. The Fourier

transform of $\ddot{X}(t)$ is defined

$$X(\omega) = \int_{-\infty}^{\infty} \ddot{X}(t) e^{-i\omega t} dt, \quad |\omega| < \infty. \quad (4-4)$$

This function is a complex valued random process, $X(\omega)$, $|\omega| < \infty$, with continuous parameter, ω . This Fourier transform random process will always exist, in a mean square sense, as long as the restrictions on α and T are satisfied. The Fourier transformation converts the real valued random process, $\ddot{X}(t)$, into a complex valued random process, $X(\omega)$.

We can express the random process, $X(\omega)$ in a form which sheds more light on its fundamental character; that is

$$X(\omega) = X_R(\omega) + iX_I(\omega), \quad |\omega| < \infty, \quad (4-5)$$

where

$$X_R(\omega) = \int_{-\infty}^{\infty} \ddot{X}(t) \cos \omega t dt, \quad |\omega| < \infty \quad (4-5a)$$

and

$$X_I(\omega) = - \int_{-\infty}^{\infty} \ddot{X}(t) \sin \omega t dt, \quad |\omega| < \infty. \quad (4-5b)$$

Apparently, the Fourier transform of the random process, $\ddot{X}(t)$, consists of real and imaginary parts, $X_R(\omega)$ and $X_I(\omega)$. Each of these parts is a nonstationary, normal random process with parameters which depend on, and can be derived from, the parameters of the random process, $\ddot{X}(t)$. The complete probabilistic character of the pair of random processes $X_R(\omega)$ and $X_I(\omega)$, $|\omega| < \infty$, can be fully described with the mean and autocorrelation function of each random process, and the cross correlation function between the pair of random processes. The reason for this is that $X_R(\omega)$ and $X_I(\omega)$, $|\omega| < \infty$, are normal random processes since they are defined using linear operations on the normal random process, $\ddot{X}(t)$, $|t| < \infty$. Later in this section we will derive these moment functions for the component random processes, $X_R(\omega)$ and $X_I(\omega)$.

The modulus of the Fourier transform of the underlying random process, $\ddot{X}(t)$, is given by

$$|X(\omega)| = \sqrt{X_R^2(\omega) + X_I^2(\omega)}, \quad |\omega| < \infty. \quad (4-6)$$

This is a continuous valued, continuous parameter random process. We wish to find an expression for the mean and autocovariance function of this random process. Once obtained, these can be used in Equations 3-8 and 3-9 in the previous section. These can be obtained in terms of the moment functions of the random

processes, $X_R(\omega)$ and $X_I(\omega)$. First we obtain the mean of the random process $|X(\omega)|$. For simplicity of notation, we will denote the random process, $X_R(\omega)$, evaluated at frequency, ω , by X_1 , and we will denote the random process, $X_I(\omega)$, evaluated at frequency, ω , by X_2 . X_1 and X_2 are normal random variables with zero mean, identical variances, σ^2 , and correlation coefficient, ρ_{12} . (The values used for the moments will be shown to be reasonable, later in the analysis.) We wish to find the following expected value.

$$E[|X(\omega)|] = E\left[\sqrt{X_1^2 + X_2^2}\right], \quad (4-7)$$

By definition this is

$$\begin{aligned} E[|X(\omega)|] &= \int_{-\infty}^{\infty} dx_1 \int_{-\infty}^{\infty} dx_2 \sqrt{x_1^2 + x_2^2} p(x_1, x_2), \\ &\quad (4-8) \end{aligned}$$

where $p(x_1, x_2)$ is the joint pdf of a pair of normally distributed random variables. $p(x_1, x_2)$ is given by

$$\begin{aligned} p(x_1, x_2) &= \frac{1}{2\pi\sigma^2\sqrt{1-\rho_{12}^2}} \\ &\exp\left[-\frac{1}{2(1-\rho_{12}^2)\sigma^2}(x_1^2 - 2\rho_{12}x_1x_2 + x_2^2)\right], \\ &\quad -\infty < x_1, x_2 < \infty. \quad (4-8a) \end{aligned}$$

We evaluate the integral in Equation 4-8 using the following approach. Write the exponential function in the joint pdf as a function of ρ_{12} ,

$$f(\rho_{12}) = \exp\left[\frac{a}{1-\rho_{12}^2}(b - c\rho_{12})\right], \quad |\rho_{12}| < 1, \quad (4-9)$$

where

$$a = -\frac{1}{2\sigma^2}, \quad b = x_1^2 + x_2^2, \quad c = 2x_1x_2. \quad (4-9a)$$

This function can be approximated using its Taylor series expansion.

$$\begin{aligned} f(\rho_{12}) &= \sum_{j=0}^{\infty} \frac{\rho_{12}^j}{j!} f^{(j)}(\rho_{12}) \Big|_{\rho_{12}=0} \\ &\quad |\rho_{12}| < 1. \quad (4-10) \end{aligned}$$

And when $|\rho_{12}|$ is relatively small this series is accurately approximated by its first three terms.

$$f(\rho_{12}) \approx f(0) + \rho_{12} f'(0) + \frac{\rho_{12}^2}{2} f''(0), \quad |\rho_{12}| < 1. \quad (4-10a)$$

We use this approximation in Equation 4-8 to simplify the expression to

$$E[|X(\omega)|] \approx \int_{-\infty}^{\infty} dx_1 \int_{-\infty}^{\infty} dx_2 \frac{\sqrt{x_1^2 + x_2^2}}{2\pi\sigma^2 \sqrt{1 - \rho_{12}^2}} \left[1 + \frac{x_1 x_2}{\sigma^2} \rho_{12} + \left(-\frac{x_1^2 + x_2^2}{\sigma^2} + \frac{x_1^2 x_2^2}{\sigma^4} \right) \frac{\rho_{12}^2}{2} \right] \exp\left(-\frac{x_1^2 + x_2^2}{2\sigma^2}\right), \quad |\rho_{12}| < 1. \quad (4-11)$$

Now we perform a transformation of variables. Let

$$x_1 = r \cos \theta, \quad x_2 = r \sin \theta. \quad (4-12)$$

Then the mean expression becomes

$$E[|X(\omega)|] \approx \int_{-\pi}^{\pi} d\theta \int_0^{\infty} dr \frac{r^2}{2\pi\sigma^2 \sqrt{1 - \rho_{12}^2}} \left[1 + \frac{r^2 \cos \theta \sin \theta}{\sigma^2} \rho_{12} + \left(-\frac{r^2}{\sigma^2} + \frac{r^4 \cos^2 \theta \sin^2 \theta}{\sigma^4} \right) \frac{\rho_{12}^2}{2} \right] e^{-r^2/2\sigma^2}, \quad |\rho_{12}| < 1. \quad (4-13)$$

This integral can be evaluated to obtain

$$E[|X(\omega)|] \approx \sqrt{\frac{\pi}{2(1 - \rho_{12}^2)}} \left[1 - \frac{9}{16} \rho_{12}^2 \right] \sigma, \quad |\rho_{12}| < 1. \quad (4-14)$$

This is an estimate of the mean of the modulus of the Fourier transform of the nonstationary random process defined in Equations 4-1 and 4-2. Note that this expression is most accurate for

small $|\rho_{12}|$. As ρ_{12} approaches zero this mean approaches the value

$$E[|X(\omega)|] = \sqrt{\frac{\pi}{2}} \sigma \quad (4-15)$$

The mean must approach this limit since this is the expected value of the square root of the sum of the squares of two identically distributed, uncorrelated, normal random variables. This fact verifies the accuracy of the small correlation behavior of this expected value estimate. Later we will derive the expression for σ and ρ_{12} (these vary with ω) in terms of the parameters of the underlying random process, $X(t)$. Then the above expression can be used in Equation 3-8.

Our next task is to estimate the autocovariance function for the modulus of the Fourier transform random process, $|X(\omega)|$. In Reference 13 we propose three methods for obtaining an estimate of the autocovariance function. Two are based on approximate analyses and are very efficient in a computational sense, but less accurate. Another is based on a Monte Carlo analysis and is less efficient, but more accurate. In this paper we present one of the approximate, analytical approaches. By definition the autocovariance function can be obtained from the autocorrelation function, therefore we find a method for estimating the autocorrelation function. The autocorrelation function of the modulus of $X(\omega)$ is by definition

$$E[|X(\omega_1)| |X(\omega_2)|] = E\left[\sqrt{(X_R^2(\omega_1) + X_I^2(\omega_1))(X_R^2(\omega_2) + X_I^2(\omega_2))}\right]. \quad (4-16)$$

We simplify this notation by replacing $X_R(\omega_1)$ with X_1 , $X_I(\omega_1)$ with X_2 , $X_R(\omega_2)$ with X_3 , and $X_I(\omega_2)$ with X_4 . In terms of these random variables we wish to evaluate

$$E[|X(\omega_1)| |X(\omega_2)|] = E\left[\sqrt{(X_1^2 + X_2^2)(X_3^2 + X_4^2)}\right]. \quad (4-17)$$

The random variables, X_j , $j = 1, 2, 3, 4$, are normally distributed; each has zero mean and variance, σ^2 . The correlation coefficient between random variables X_j and X_k is denoted ρ_{jk} , $j \neq k$, $j, k = 1, 2, 3, 4$. The appropriateness of this assignment of moments will be demonstrated later, when the moments of $X_1(\omega_1)$ through $X_4(\omega_2)$ are computed based on the moments of the random process described in Equations 4-1 and 4-2.

The technique which we develop to evaluate the autocorrelation function of the modulus of the Fourier transform random process, $|X(\omega)|$, uses a normality assumption and a Taylor series expansion on the right side of Equation 4-17 to obtain the approximation. We define

$$Y = (X_1^2 + X_2^2), \quad (4-18a)$$

$$Z = (X_3^2 + X_4^2). \quad (4-18b)$$

In terms of Y and Z the desired moment is

$$E[|X(\omega_1)| |X(\omega_2)|] = E[\sqrt{YZ}]. \quad (4-19)$$

The first two moments of the random variables, Y and Z, can be obtained using Price's Theorem [11]. They are

$$E[Y] = \mu_Y = E[Z] = \mu_Z = 2\sigma^2, \quad (4-20a)$$

$$V[Y] = \sigma_Y^2 = 4\sigma^4(1 + \rho_{12}^2), \quad (4-20b)$$

$$V[Z] = \sigma_Z^2 = 4\sigma^4(1 + \rho_{34}^2), \quad (4-20c)$$

$$\begin{aligned} \rho_{YZ} &= \text{cov}[Y, Z] \\ &= 2\sigma^4(\rho_{13}^2 + \rho_{14}^2 + \rho_{23}^2 + \rho_{24}^2). \end{aligned} \quad (4-20d)$$

To make possible a computation in Equation 4-19 we assume that Y and Z are jointly normally distributed, even though they are not. From Equation 4-19 we obtain

$$E[|X(\omega_1)| |X(\omega_2)|] = \int_{-\infty}^{\infty} dy \int_{-\infty}^{\infty} dz \sqrt{yz} p(y, z), \quad (4-21)$$

where

$p(y, z)$

$$\begin{aligned} &= \frac{1}{2\pi\sigma^2\sqrt{1-\rho^2}} \exp \left[-\frac{1}{2\sigma^2(1-\rho^2)} ((y-\mu_Y)^2 \right. \\ &\quad \left. - 2\rho(y-\mu_Y)(z-\mu_Z) + (z-\mu_Z)^2) \right], \\ &= < y, z >. \end{aligned} \quad (4-21a)$$

To evaluate Equation 4-21 we expand the function, \sqrt{yz} , in its Taylor series about the point (μ_Y, μ_Z) , and we retain the six lowest order terms. This yields the approximation

$$\begin{aligned} \sqrt{yz} &= \sqrt{\mu_Y\mu_Z} \left[1 + \frac{1}{2} \frac{y-\mu_Y}{\mu_Y} + \frac{1}{2} \frac{z-\mu_Z}{\mu_Z} \right. \\ &\quad - \frac{1}{8} \left(\frac{y-\mu_Y}{\mu_Y} \right)^2 - \frac{1}{8} \left(\frac{z-\mu_Z}{\mu_Z} \right)^2 \\ &\quad \left. + \frac{1}{4} \left(\frac{y-\mu_Y}{\mu_Y} \right) \left(\frac{z-\mu_Z}{\mu_Z} \right) \right]. \end{aligned} \quad (4-22)$$

By using this expression in Equation 4-21 we are able to approximately evaluate the autocorrelation function of the modulus of the Fourier transform random process, $|X(\omega)|$. It is

$$\begin{aligned} E[|X(\omega_1)| |X(\omega_2)|] \\ &= 2\sigma^2 \left[1 - \frac{1}{8} \left[2 + (\rho_{12}^2 + \rho_{34}^2) - (\rho_{13}^2 + \rho_{14}^2 \right. \right. \\ &\quad \left. \left. + \rho_{23}^2 + \rho_{24}^2) \right] \right]. \end{aligned} \quad (4-23)$$

As stated, this is simply an approximate expression. It is approximate since Y and Z have been assumed jointly normal, and since \sqrt{yz} has been replaced with the lower order terms of its Taylor series. As the interval between ω_1 and ω_2 is increased, and as ω_1 and ω_2 become large in absolute value, all the correlation coefficients approach zero. (This will be shown later.) In this situation $E[|X(\omega_1)| |X(\omega_2)|]$ approaches the value $1.5\sigma^2$. But we showed in Equation 4-16 that as ρ_{12} approaches zero, the mean of the modulus of the Fourier transform random process should approach $\sqrt{\pi/2}\sigma$. If we require that $|X(\omega_1)|$ and $|X(\omega_2)|$ be independent as ω_1 and ω_2 become widely separated, we must adjust Equation 4-23 slightly so that $E[|X(\omega_1)| |X(\omega_2)|]$ approaches $(\pi/2)\sigma^2$ rather than $1.5\sigma^2$ as the correlation coefficients approach zero. We do this to obtain the approximation

$$\begin{aligned} E[|X(\omega_1)| |X(\omega_2)|] &= \frac{2\pi}{3} \sigma^2 \left[1 - \frac{1}{8} \left[2 \right. \right. \\ &\quad \left. \left. + (\rho_{12}^2 + \rho_{34}^2) - (\rho_{13}^2 + \rho_{14}^2 + \rho_{23}^2 + \rho_{24}^2) \right] \right]. \end{aligned} \quad (4-24)$$

If we use Equation 4-15 to obtain $E[|X(\omega_1)|]$ and $E[|X(\omega_2)|]$, then the product of these expressions can be subtracted from $E[|X(\omega_1)| |X(\omega_2)|]$, above, to obtain the autocovariance function for the random process, $|X(\omega)|$.

The final task remaining in this section is to estimate the moments of the underlying random variables used in the analyses of this section. Particularly, using the definitions provided in Equations 4-1 and 4-2, we wish to find the moments of the random variables defined in

Equations 4-5a and 4-5b. Specifically, we require the means and variances of $X_R(\omega)$ and $X_I(\omega)$, the crosscorrelation between $X_R(\omega)$ and $X_I(\omega)$, and the crosscorrelations between $X_R(\omega_1)$ and $X_R(\omega_2)$, $X_I(\omega_1)$ and $X_I(\omega_2)$, and $X_R(\omega_1)$ and $X_I(\omega_2)$. We obtain these moments in the following. We consider first the random process formed by using Equation 4-2a in Equation 4-1. The means are defined

$$E[X_R(\omega)] = E[X_I(\omega)] = 0, \quad |\omega| < \infty. \quad (4-25)$$

The reason for this is that the random process, $\tilde{X}(t)$, has mean zero. The expected value of the product, $X(\omega_1) X^*(\omega_2)$, is defined

$$E[X(\omega_1) X^*(\omega_2)] = \int_{-\infty}^{\infty} dt_1 \int_{-\infty}^{\infty} dt_2 E[\tilde{X}(t_1) \tilde{X}^*(t_2)] e^{-i(\omega_1 t_1 - \omega_2 t_2)}, \quad -\infty < \omega_1, \omega_2 < \infty. \quad (4-26)$$

Since the underlying input is a white noise random process, $E[\tilde{X}(t_1) \tilde{X}^*(t_2)]$ can be written, approximately,

$$E[\tilde{X}(t_1) \tilde{X}^*(t_2)] = \begin{cases} 2\pi S_0 \delta(t_1 - t_2), & 0 < t_1, t_2 < T \\ 0, & \text{otherwise} \end{cases} \quad (4-27)$$

This is the autocorrelation function of the input random process. Use of this expression in Equation 4-26 results in

$$E[X(\omega_1) X^*(\omega_2)] = \frac{4\pi S_0}{\omega_1 - \omega_2} \sin\left(\frac{\omega_1 - \omega_2}{2} T\right) \left[\cos\left(\frac{\omega_1 - \omega_2}{2} T\right) - i \sin\left(\frac{\omega_1 - \omega_2}{2} T\right) \right], \quad -\infty < \omega_1, \omega_2 < \infty. \quad (4-28)$$

Next we evaluate the expected value of the product, $X(\omega_1) X(\omega_2)$. Using Equation 4-27 we obtain

$$E[X(\omega_1) X(\omega_2)] = \frac{4\pi S_0}{\omega_1 + \omega_2} \sin\left(\frac{\omega_1 + \omega_2}{2} T\right) \left[\cos\left(\frac{\omega_1 + \omega_2}{2} T\right) - i \sin\left(\frac{\omega_1 + \omega_2}{2} T\right) \right], \quad -\infty < \omega_1, \omega_2 < \infty. \quad (4-29)$$

We note that the expected values of the products $X(\omega_1) X^*(\omega_2)$, and $X(\omega_1) X(\omega_2)$ can be rewritten in the alternate forms

$$E[X(\omega_1) X^*(\omega_2)] = E[X_R(\omega_1) X_R(\omega_2)] + E[X_I(\omega_1) X_I(\omega_2)] + i\{-E[X_R(\omega_1) X_I(\omega_2)] + E[X_I(\omega_1) X_R(\omega_2)]\}, \quad -\infty < \omega_1, \omega_2 < \infty. \quad (4-30a)$$

and

$$E[X(\omega_1) X(\omega_2)] = E[X_R(\omega_1) X_R(\omega_2)] - E[X_I(\omega_1) X_I(\omega_2)] + i\{E[X_R(\omega_1) X_I(\omega_2)] + E[X_I(\omega_1) X_R(\omega_2)]\}, \quad -\infty < \omega_1, \omega_2 < \infty. \quad (4-30b)$$

Now the real and imaginary parts of the expressions on the right-hand sides of Equations 4-30a and 4-30b can be equated to the real and imaginary parts on the right-hand sides of Equations 4-28 and 4-29. This yields a set of four equations in the four unknowns, $E[X_R(\omega_1) X_R(\omega_2)]$, $E[X_I(\omega_1) X_I(\omega_2)]$, $E[X_R(\omega_1) X_I(\omega_2)]$, and $E[X_I(\omega_1) X_R(\omega_2)]$. These can be solved simultaneously to obtain

$$E[X_R(\omega_1) X_R(\omega_2)] = \frac{\pi S_0}{\omega_1 + \omega_2} \sin(\omega_1 + \omega_2) T + \frac{\pi S_0}{\omega_1 - \omega_2} \sin(\omega_1 - \omega_2) T, \quad (4-31a)$$

$$E[X_I(\omega_1) X_I(\omega_2)] = \frac{\pi S_0}{\omega_1 - \omega_2} \sin(\omega_1 - \omega_2) T - \frac{\pi S_0}{\omega_1 + \omega_2} \sin(\omega_1 + \omega_2) T, \quad (4-31b)$$

$$E[X_R(\omega_1) X_I(\omega_2)] = \frac{\pi S_0}{\omega_1 + \omega_2} [1 - \cos(\omega_1 + \omega_2) T] - \frac{\pi S_0}{\omega_1 - \omega_2} [1 - \cos(\omega_1 - \omega_2) T], \quad (4-31c)$$

$$E[X_I(\omega_1) X_R(\omega_2)] = \frac{\pi S_0}{\omega_1 + \omega_2} [1 - \cos(\omega_1 + \omega_2) T] + \frac{\pi S_0}{\omega_1 - \omega_2} [1 - \cos(\omega_1 - \omega_2) T]. \quad (4-31d)$$

where in all cases, $-\infty < \omega_1, \omega_2 < \infty$. When we evaluate Equation 4-31a at $\omega_1 = \omega_2 = \omega$, we obtain the variance of $X_R(\omega)$. When we evaluate Equation 4-31b at $\omega_1 = \omega_2 = \omega$, we obtain the

variance of $X_I(\omega)$. When we evaluate Equation 3-31c at $\omega_1 = \omega_2 = \omega$, we obtain the crosscorrelation between $X_R(\omega)$ and $X_I(\omega)$. These are

$$V[X_R(\omega)] = \pi S_0 \left(T + \frac{\sin 2\omega T}{2\omega} \right), \quad (4-31e)$$

$$V[X_I(\omega)] = \pi S_0 \left(T - \frac{\sin 2\omega T}{2\omega} \right), \quad (4-31f)$$

$$E[X_R(\omega) X_I(\omega)] = \frac{\pi S_0}{2\omega} (1 - \cos 2\omega T), \quad (4-31g)$$

where in all cases $|\omega| < \infty$. Clearly, when $\omega T \gg 1$, the variances of the real and imaginary components are approximately equal.

$$V[X_R(\omega)] \approx V[X_I(\omega)] \approx \pi S_0 T, \quad |\omega| < \infty. \quad (4-32)$$

Moreover, for large values of frequency and large frequency differences between ω_1 and ω_2 , the correlation coefficients based on Equations 4-31a through 4-31d, and 4-31g become very small. In view of Equations 4-25 and 4-32, the assumed values used for the moments of the random variables X_j , $j = 1, 2, 3, 4$, preceding Equation 4-7 and following Equation 4-15, are shown to be reasonably accurate.

When we use Equation 4-2b in 4-1 to define the decaying exponential input random process, the moments we obtain for $X_R(\omega_1)$ and $X_I(\omega_2)$ will be different from those listed above. However, a technique identical to that presented above can be used to find the moments of $X_R(\omega_1)$ and $X_I(\omega_2)$. The only difference is that the autocorrelation function of the input random process is

$$E[\ddot{x}(t_1) \ddot{x}(t_2)]$$

$$= \begin{cases} 2\pi S_0 \lambda^2 e^{-\alpha(t_1+t_2)} \delta(t_1 - t_2), & t_1, t_2 > 0 \\ 0, & \text{otherwise} \end{cases} \quad (4-33)$$

The moments for the component random processes follow.

$$E[X_R(\omega_1) X_R(\omega_2)] = 2\pi S_0 \alpha \left[\frac{1}{(2\alpha)^2 + (\omega_1 + \omega_2)^2} + \frac{1}{(2\alpha)^2 + (\omega_1 - \omega_2)^2} \right], \quad (4-34a)$$

$$E[X_I(\omega_1) X_I(\omega_2)] = 2\pi S_0 \alpha \left[\frac{1}{(2\alpha)^2 + (\omega_1 - \omega_2)^2} - \frac{1}{(2\alpha)^2 + (\omega_1 + \omega_2)^2} \right], \quad (4-34b)$$

$$E[X_R(\omega_1) X_I(\omega_2)] = \pi S_0 \left[\frac{\omega_1 + \omega_2}{(2\alpha)^2 + (\omega_1 + \omega_2)^2} - \frac{\omega_1 - \omega_2}{(2\alpha)^2 + (\omega_1 - \omega_2)^2} \right], \quad (4-34c)$$

$$E[X_I(\omega_1) X_R(\omega_2)] = \pi S_0 \left[\frac{\omega_1 + \omega_2}{(2\alpha)^2 + (\omega_1 + \omega_2)^2} + \frac{\omega_1 - \omega_2}{(2\alpha)^2 + (\omega_1 - \omega_2)^2} \right], \quad (4-34d)$$

$$V[X_R(\omega)] = \frac{\pi S_0 \alpha}{2} \left[\frac{1}{\alpha^2 + \omega^2} + \frac{1}{\alpha^2} \right], \quad (4-34e)$$

$$V[X_I(\omega)] = \frac{\pi S_0 \alpha}{2} \left[\frac{1}{\alpha^2} - \frac{1}{\alpha^2 + \omega^2} \right], \quad (4-34f)$$

$$E[X_R(\omega) X_I(\omega)] = \frac{\pi S_0 \omega}{2} \left[\frac{1}{\alpha^2 + \omega^2} \right], \quad (4-34g)$$

where in all cases $-\infty < \omega_1, \omega_2 < \infty$, $|\omega| < \infty$. When $\omega \gg \alpha$, we have

$$V[X_R(\omega)] \approx V[X_I(\omega)] \approx \frac{\pi S_0}{2\alpha}, \quad |\omega| < \infty. \quad (4-35)$$

As in the previous case, the correlation coefficients derived from Equations 4-34 approach zero as ω_1 and ω_2 are made large and moved far apart.

5.0 Applications

In this section we present some applications of the methods developed in Sections 3.0 and 4.0. The purpose of these applications is to determine, approximately, what probability of conservatism exists in some simple situations (Examples 1 through 4) and in one practical situation (Example 5). The five numerical examples are described as follows.

1. A single steady shock (a steady shock has the envelope defined in Equation 3-2a) is used to derive a LFR test for a single-degree-of-freedom (SDF) structure where this structure is to be subjected to one input in the field.

2. Two steady shock inputs are used to derive a LFR test for the structure of example one, where the structure will be subjected to one input in the field.

3. One steady shock input is used to derive a test for the SDF system of example one, where the structure will be subjected to two inputs in the field.

4. Two decaying exponential oscillatory random inputs (a decaying exponential random input has the envelope defined in Equation 3-2b) from different sources are used to derive a LFR test for a SDF structure, where the structure will be subjected to one input from each source in the field.

5. Three random inputs from two sources are used to derive a LFR test for a multi-degree-of-freedom (MDF) structure, where the structure will be subjected to three inputs from these two sources in the field.

To execute the analyses described above we have written some programs, and these are listed in Appendix D of Reference 13. Three of the programs, DUMBB, DUMBZ, and DUMBC, are used to evaluate the mean and variance of the LFR, I , using the three different methods presented in Reference 13 to evaluate the variance of I . The results obtained using program DUMBB are presented in this paper. Another program, Y1, is used to find the cdf of the peak response of a SDF or MDF structure, and the moments of the peak response. The fifth program, DUMEXTA, is used to find the pdf and moments of the largest value among N random variables, where the random variables are mutually independent and each is normally distributed.

5.1 Example One

In this example a single steady shock input from a random source is used to derive a LFR shock test for a SDF structure which will be subjected to one input from that source in the field. The parameters of the steady shock input follow. (Refer to Equations 4-2a and 4-3).

Duration $T = 15 \text{ sec}$
Input spectral density $S_0 = 4.13 \text{ cm}^2/\text{sec}^3$

The SDF system parameters follow. (Refer to Equation 3-4).

Natural frequency $\omega_1 = 4\pi \approx 12.57 \text{ rad/sec}$
Damping factor $\zeta_1 = 0.03$

System bandwidth $\Delta\omega_1 = 3.69 \text{ rad/sec}$
Amplification factor $H_1 = 0.105 \text{ sec}^2$

Program DUMBB, which computes the moments of I following the approach presented in this paper, was used to compute the moments of the LFR, I . We obtained

$$\mu_I = 2.156 \text{ cm}$$

$$\sigma_I = 0.403 \text{ cm}$$

The moments completely characterize the LFR of the SDF structure based on the single input. The moments of the actual peak response, A , to the field input were obtained using the program, Y1. The mean and standard deviation of the peak response are

$$\mu_A = 0.976 \text{ cm}$$

$$\sigma_A = 0.134 \text{ cm}$$

Using Equation 3-14 and the estimated moments listed above, we estimate the probability of conservatism of the LFR test to be

$$p_C = 0.99726$$

Roughly, this states that over 99 percent of all structural tests using the LFR method and based on one past, measured input, will be conservative with respect to a future input, for this structure. This result shows that the LFR test possesses a high degree of inherent conservatism, in this particular situation.

5.2 Example Two

This example is identical to Example One except that here, two inputs from the random source are used to find the LFR. As before, the structure will be subjected to only one shock input in the field. To find the probability of shock test conservatism, we must find the distribution of I , where the more severe of the two random inputs governs the value of I . We enter the program, DUMEXTA (Reference 13), with the mean value, $\mu_I = 2.156$, the standard deviation, $\sigma_I = 0.403$, and the fact that two inputs from the same random source are being considered. The mean and standard deviation of the LFR, I , based on the more severe of the two random inputs are obtained from program DUMEXTA. They are

$$\mu_I = 2.397 \text{ cm}$$

$$\sigma_I = 0.352 \text{ cm}$$

Based on these estimates and the moments of A , given in Example One, the probability of LFR test conservatism was found to be

$$p_C = 0.99992$$

We conclude that when two inputs are used to obtain a LFR test and only one input will be

experienced by the structure in the field, the test is almost sure to be conservative. In general, as the number of inputs used to find the LFR test is increased, the probability of conservatism will increase rapidly, if the structure is to be subjected to only one input in the field.

5.3 Example Three

This example is identical to Example One, except that here the structure will be subjected to two exposures from a single random source in the field. As in Example One, only one measured input is used to specify the random shock test. In this case the larger peak structural response excited by the more severe of the two random inputs governs the conservatism of the test. The test input must excite a more severe structural response than the more severe input to be conservative. To find the moments of the response excited by the more severe structural input we enter the program, DUMEXTA, with the mean value, $\mu_A = 0.976$ cm, and the standard deviation, $\sigma_A = 0.134$ cm. We obtain

$$\mu_A = 1.052 \text{ cm},$$

$$\sigma_A = 0.111 \text{ cm}.$$

These are the approximate mean and standard deviation of the higher of the two structural responses excited by two inputs from the source of Example One. Based on these moments and the mean and standard deviation of I, given in Example One, we find the approximate probability of conservatism of the LFR shock test. It is

$$p_C = 0.99587.$$

This shows that the probability of test conservatism diminishes as the number of field exposures increases, if only one test is used to derive the input. In general, this behavior can be anticipated in situations like this. The decrease is slight, though, in this case. The reason for this is that σ_I^2 is much larger than σ_A^2 in Equation 3-14.

5.4 Example Four

In this example two decaying exponential oscillatory shock inputs from different random sources are used to derive the shock test input for a SDF structure which will be subjected to one exposure from each random source in the field. The parameters of the shock sources follow. (Refer to Equations 4-2b and 4-3).

Multipliers

$$A_1 = 1$$

$$A_2 = 1$$

Decay constants

$$\alpha_1 = 7.0 \text{ sec}^{-1}$$

$$\alpha_2 = 4.0 \text{ sec}^{-1}$$

Input spectral density

$$S_1 = 25,000 \text{ cm}^2/\text{sec}^3$$

$$S_2 = 15,000 \text{ cm}^2/\text{sec}^3$$

where the subscripts refer to the different random sources. The SDF system parameters follow. (Refer to Equation 3-4).

$$\begin{aligned} \text{Natural frequency } \omega_1 &= 500(2\pi) = 3142 \text{ rad/sec} \\ \text{Damping factor } \zeta_1 &= 0.01 \\ \text{System bandwidth } \Delta\omega_1 &= 376.5 \text{ rad/sec} \\ \text{Amplification factor } H_1 &= 5.06 \times 10^{-6} \text{ sec}^2 \end{aligned}$$

Program DUMBB was used to compute the moments of the LFR, I, corresponding to each input. We obtained

Input 1

$$\mu_I = 0.0569$$

$$\sigma_I = 0.00741$$

Input 2

$$\mu_I = 0.0583$$

$$\sigma_I = 0.00568$$

From these moments of the LFR caused by each input we determine, using the program DUMEXTA, that the LFR corresponding to the more severe input has the following moments.

$$\mu_I = 0.0614 \text{ cm},$$

$$\sigma_I = 0.00536 \text{ cm}.$$

The peak response excited by each input can be analyzed using the program, Y1. We find the moments of the peak response excited by each random input to be

$$\mu_{A1} = 0.0263 \text{ cm}$$

$$\mu_{A2} = 0.0225 \text{ cm},$$

$$\sigma_{A1} = 0.00348 \text{ cm}$$

$$\sigma_{A2} = 0.00278 \text{ cm},$$

where the numerical subscripts correspond to the inputs. We can use the program DUMEXTA to determine the moments of the response excited by the more severe input. These are

$$\mu_A = 0.0268 \text{ cm},$$

$$\sigma_A = 0.00303 \text{ cm}.$$

Based on the moments for the LFR, I, and the worst field response, A, we determine the probability of test conservatism using Equation 3-21. It is

$$p_C = 1 - 10^{-8}.$$

This result shows that the test is almost certain to be conservative.

5.5 Example Five

Our final example uses two decaying exponential oscillatory inputs from one random source and one steady input from another random source to obtain a test for a MDF structure which will be subjected to three inputs from the two sources in the field. Source number one will excite the structure twice in the field and two records are available from that source. Source number two will excite the structure once, and one record from that source is available. The parameters of the random shock sources follow.

Multipliers

$A_1 = 1$
 Decay constant⁻¹
 $\alpha_1 = 100 \text{ sec}$
 Duration of input $T_2 = 0.015$
 Input spectral density³
 $S_1 = 1.8 \times 10^7 \text{ cm}^2/\text{sec}^3$
 $S_2 = 1.0 \times 10^7 \text{ cm}^2/\text{sec}^3$

Three modes of the structure under consideration will be excited by all the inputs. (Each input could excite a different number of modes.) The system parameters are

Modal frequencies $\omega_1 = 2824 \text{ rad/sec}$
 $\omega_2 = 4809 \text{ rad/sec}$
 $\omega_3 = 10,554 \text{ rad/sec}$

Modal damping $\zeta_1 = 0.02$
 $\zeta_2 = 0.01$
 $\zeta_3 = 0.005$

Modal bandwidth $\Delta\omega_1 = 598 \text{ rad/sec}$
 $\Delta\omega_2 = 576 \text{ rad/sec}$
 $\Delta\omega_3 = 705 \text{ rad/sec}$

Modal amplification $H_1^2 = 8.9 \times 10^{-6} \text{ sec}^2$
 $H_2^2 = 4.7 \times 10^{-7} \text{ sec}^2$
 $H_3^2 = 1.1 \times 10^{-7} \text{ sec}^2$

Mode Shapes (Normal)

Degree of Freedom

Mode No.	1	2	3
1	-0.37	-1.58	-3.94
2	0.59	2.38	5.38
3	1.58	5.32	8.49

Mode No.	4	5	6
1	-8.00	-15.13	-38.46
2	9.06	10.48	35.63
3	4.76	-16.45	2.06

Note that six structural degrees of freedom are considered.

Program DUMBB was used to find the moments of each modal component of the LFR, I. These are

Mode No.	Input 1		Input 2	
	$\mu_I (\text{cm})$	$\sigma_I (\text{cm})$	$\mu_I (\text{cm})$	$\sigma_I (\text{cm})$
1	1.12	0.371	1.45	0.443
2	0.58	0.191	0.74	0.229
3	0.016	0.005	0.21	0.059

This information, and the fact that two records of input one and one record of input two are available, were used to find the moments of the overall LFR. These are

$$\mu_I = 2.48 \text{ cm},$$

$$\sigma_I = 0.180 \text{ cm}.$$

Program Y1 was used to find the moments of the peak response excited by each random source. These are

Input No.	$\mu_A (\text{cm})$	$\sigma_A (\text{cm})$
1	0.941	0.190
2	1.134	0.251

This information, and the fact that the structure will be subjected to two realizations of input one and one realization of input two in the field, were used to find the moments of the higher peak response. These are

$$\mu_A = 1.21 \text{ cm},$$

$$\sigma_A = 0.187 \text{ cm}.$$

Finally, the moments of the LFR and the peak field response were used in Equation 3-21 to obtain the probability of test conservatism. It is

$$P_C = 0.9969.$$

Apparently, the test conservatism in this complicated case is almost certain.

6.0 Summary, Conclusions and Recommendations

In this report we have established an approximate procedure for computing the probability of conservatism of a least favorable response shock test. In the most general case we showed how to find the probability of test conservatism when a structure is subjected to multiple random shocks from several sources in the field, given that one or more shock acceleration records are available from each random source.

We showed that the computations outlined in the text could be performed by working five numerical examples. In these examples we showed, in a limited sense, that when one input record is available from each source and for each input that the structure will be subjected to in the field, and when these are used to obtain a test input, then the probability of test conservatism is high, that is, over ninety-nine percent. When more inputs are used to obtain a test than the structure will be exposed to in the field, then the probability of test conservatism increases rapidly to a point where test conservatism is practically certain. When fewer inputs are used to obtain a test than a structure will be exposed to in the field, then the probability of test conservatism decreases. But we expect that the number of field exposures must be relatively large for the probability of conservatism to decrease below ninety percent. In all the situations considered the probability

of test conservatism was high.

Several approximations were made which were critical to the analyses performed in this report. The three primary approximations were the following.

1. The complex modulus of the frequency response function of a linear system was approximated using a function which is constant in the region of greatest modal amplification and zero everywhere else (Equation 3-4).

2. In the probability of conservatism computation the probability distribution of the peak response of a linear structure was taken to be normal (Equation 3-14 and preceding).

3. The probability distribution of the least favorable response, I , was taken to be normal (Equation 3-12).

The most important of these approximations is the first. In Appendix A of Reference 13 we show that this approximation is based on the assumption that the first few moments of the complex modulus of the Fourier transform of the random process input are slowly varying in the regions of the system modal frequencies. The accuracy of this assumption could be easily checked for various specific inputs using a Monte Carlo analysis. In fact, this assumption could be eliminated, but that would increase the complexity of the computations and increase the computer time for the numerical analyses.

The second assumption listed above is less important than the first. This assumption is probably not very accurate, but it could easily be eliminated by writing a computer program to evaluate Equation 3-13. In view of the existing inaccuracy, the values of probability of test conservatism, p_c , given in the numerical examples can only be taken as indicators of the probability of conservatism, yielding results which are correct in a relative sense.

The third assumption listed is very important, and probably quite accurate. This assumption could be easily checked for specific random sources using a Monte Carlo analysis.

The supplementary analyses discussed above should be performed to improve our ability to accurately predict the probability of conservatism of a structural test specified using the method of least favorable response. More important, though, the results of the present study should be simplified and put into an experimental design framework, so that those who wish to specify a least favorable response test for a laboratory or analytical experiment could do so, and could easily compute the probability of conservatism of that test.

References

1. Paez, T. L., "Conservatism in Shock Analysis and Testing," Report No. CE-43(78)SURP-617-3, Bureau of Engineering Research, University of New Mexico, Albuquerque, NM, Feb. 1978.
2. Paez, T. L., "Conservatism in Shock Analysis and Testing: Peak Response of Randomly Excited Systems," Report No. CE-44(78)SURP-617-3, Bureau of Engineering Research, The University of New Mexico, Albuquerque, NM, July 1978.
3. Paez, T. L., "Conservatism in Shock Analysis and Testing: Probability of Test Conservatism," Report No. CE-46(78)SURP-61703, Bureau of Engineering Research, The University of New Mexico, Albuquerque, NM, October 1979.
4. Paez, T. L., "Shock Response Spectra: Conservatism of Structural Tests," Report No. CE-48(79)SURP-729-3, Bureau of Engineering Research, The University of New Mexico, Albuquerque, NM, June 1979.
5. Witte, A. F. and Wolf, R. J., "Comparison of Shock Spectrum Techniques and the Method of Least Favorable Response," Report No. K-73-623 (R), Kaman Sciences Corporation, Colorado Springs, CO, September 1973.
6. Smallwood, D. O. and Witte, A. F., "A Transient Vibration Test Technique Using Least Favorable Response," Forty-Third Shock and Vibration Symposium, 1972.
7. Drenick, R. F., "Model-Free Design of a Seismic Structure," Journal of the Engineering Mechanics Division, ASCE, Vol. 96, No. EM4, August 1970, pp. 483-493.
8. Shinozuka, M., "Maximum Structural Response to Seismic Excitations," Journal of Engineering Mechanics, ASCE, Vol. 95, 1970, pp. 729-738.
9. Yang, J.-N., "Nonstationary Envelope Process and First Excursion Probability," Journal of Structural Mechanics, Vol. 1, No. 2, 1972, pp. 231-248.
10. Yang, J.-N., "First Excursion Probability in Nonstationary Random Vibration," Journal of Sound and Vibration, Vol. 27, No. 2, 1973.
11. Papoulis, A., Probability Random Variables and Stochastic Processes, McGraw-Hill Book Company, New York, 1965.
12. Shinozuka, M., "Digital Simulation of Random Processes and Its Applications," Journal of Sound and Vibrations, Vol. 25, No. 1, 1972.
13. Paez, T. L., "Conservatism in Least Favorable Response Analysis and Testing," Report No. CE-50(79)SURP-729-3, Bureau of Engineering Research, The University of New Mexico, Albuquerque, NM, October 1979.

Acknowledgement

The work leading to this report was supported by Sandia Laboratories through a Sandia-University-Research Program contract numbered 281-729-3. This support is gratefully acknowledged by the author. Also, Mr. Charoon Rojwithya wrote the program DUMBC. The author thanks Mr. Rojwithya for allowing him to use this program.

SHOCK TESTING

CALCULATING RESPONSES IN HULL MOUNTED ITEMS OF EQUIPMENT IN SUBMARINES COMPARED WITH MEASUREMENTS CARRIED OUT DURING SHOCK TESTS

K. Hellqvist, MScME
Kockums AB, Malmö, Sweden

The paper describes a method developed in Sweden for calculating responses of items and outfits mounted in submarines subjected to underwater explosions. The shock form is described by means of the Fourier transform of the acceleration-versus-time graph. Dynamic properties of hull and items are defined by their inertances. The method enables responses of items and outfits to be calculated using the above quantities whilst taking into account the reaction between units and hull structure. The method has been used on results from measurements on a specially designed structure in the 'Steel Mosquito' and the results obtained are presented in this paper.

GENERAL

In 1972 work on developing methods for calculating stresses in submarine hull and equipment subjected to shocks from underwater explosions was investigated in Sweden. This development work is sub-divided into four different parts: hull design, design of internally mounted outfits, design of externally mounted outfits and design of items pertaining to sea-water piping systems respectively. At the explosion tests with the 'Steel Mosquito' in 1978 measurements were carried out to be used for verifying these methods.

This paper deals with experiences from an attempt to verify the method of designing internally mounted outfits. As the paper is focused on the practical application of the method relevant theory is only dealt with in brief.

PROBLEM APPROACH

The goal is to develop a method for the calculation of stresses due to shocks in outfits under the assumption that the oscillatory movement is known in such parts of the hull where the unit will be mounted. The movement is only known with regard to an unloaded hull structure i.e. the unit is not mounted. The dynamic properties of the unloaded hull structure are known.

For calculating the stresses it is hence necessary to recalculate the movements of the

unloaded hull structure to such where the structure is loaded with the unit. Such movements can subsequently be used for determining stresses in the unit.

REQUIREMENTS FOR THE CALCULATION METHOD

The calculation method requires that the unit interacts on the oscillatory movement of the hull structure. It is also assumed that the oscillatory movement can be described by linear differential equations and that resonant frequency and damping are typical for the complete structure in question. Hull movements are described by the Fourier transform of the acceleration-versus-time sequence as measured at explosion tests. The dynamic properties of unit and hull structure are described by means of inertances, which may be either measured or calculated.

THEORY OUTLINE

The theory for the calculations which is fairly complicated can be found in Ref. (1) and (2). The present paper only describes briefly and in a simplified form the mathematical operation used in the calculation methods.

Outfit and hull are regarded as linear systems characterised by complex point inertances $\bar{Y}_{ii}(\omega)$ and transfer inertances $\bar{Y}_{ij}(\omega)$, see Figure 1. Point movements are described by

the Fourier transforms of the acceleration-versus-time sequences.

When the two systems are separate, i.e. not connected, the following equations apply:

$$V_1(\omega) = \bar{Y}_{11}F_1(\omega) + \bar{Y}_{12}F_2(\omega)$$

$$V_2(\omega) = \bar{Y}_{12}F_1(\omega) + \bar{Y}_{22}F_2(\omega)$$

$$V_3(\omega) = \bar{Y}_{33}F_3(\omega) + \bar{Y}_{34}F_4(\omega)$$

$$V_4(\omega) = \bar{Y}_{34}F_3(\omega) + \bar{Y}_{44}F_4(\omega)$$

When the systems are connected together as in Figure 2, the following equations apply:

$$V_1^*(\omega) = \bar{Y}_{11}F_1(\omega) + \bar{Y}_{12}F_2^*(\omega)$$

$$V_2^*(\omega) = \bar{Y}_{12}F_2(\omega) + \bar{Y}_{22}F_2^*(\omega) = -\bar{Y}_{33}F_2^*(\omega)$$

$$V_4^*(\omega) = -\bar{Y}_{34}F_2^*(\omega)$$

If the acceleration $A_4^*(\omega)$ in point No. 4 in the interconnected system shall be calculated for an acceleration $A_2(\omega)$ in point No. 2 in the separate systems, the following equation holds:

$$A_4^*(\omega) = \frac{\bar{Y}_{34}(\omega) \cdot A_2(\omega)}{\bar{Y}_{22}(\omega) + \bar{Y}_{33}(\omega)}$$

The time sequence can then be obtained by an inverse Fourier transform of $A_4^*(\omega)$.

If the point inertance $\bar{Y}_{22}^*(\omega)$ shall be determined in the interconnected system and if point and transfer inertances for the two systems are known when not interconnected, the following equation holds:

$$\frac{1}{\bar{Y}_{22}^*} = \frac{1}{\bar{Y}_{22}} + \frac{1}{\bar{Y}_{33}}$$

The above equations which concern systems having two points and one degree of freedom in each point can be generalized to systems having several points and several degrees of freedom in each point. In this case the equations will contain matrices instead of single spectra. Matrix elements will consist of complex point and transfer inertances and of Fourier transforms. Matrix size will become a function of No. of points and No. of degrees of freedom in each point.

This calculation method has been tested in two cases in which the unit had two points of attachment and one point of response. In one case there was one degree of freedom and in the other two degrees of freedom.

MEASUREMENTS FOR VERIFYING THE CALCULATION METHOD

Measurements for verifying the calculation method were made on an especially built dummy unit mounted on the pressure hull. The dummy unit had two well-defined points of attachment and a shape reasonably suitable for finite element simulation. Response calculations were based on results from inertance measurements on the dummy resiliently suspended in the laboratory, inertance measurements on board the 'Steel Mosquito' and measurements of hull structure accelerations at explosion tests.

Calculations for two cases have been performed. In the first case the aim was to verify that interaction between dummy and hull can be taken into account by calculating the point inertance in the hull structure with the dummy in situ from inertances of the dummy measured with it resiliently suspended in the laboratory and those of the unloaded 'Steel Mosquito' hull structure. The thus calculated point inertance of the hull structure loaded with the dummy unit was then compared with the measured inertances.

For laboratory inertances the dummy was suspended in rubber ropes, see Figure 3. The resonance frequency of the rigid dummy when suspended is approx. 5 Hz whilst its lowest internal resonant frequency is approx. 150 Hz. The measurements were made using transient excitation of the oscillatory movement and the inertances are the mean of some ten measurements. Modal analysis was performed on the results prior to the calculations.

In the 'Steel Mosquito' the dummy was mounted onto the hull by bolting it to two adjacent frames keeping it parallel with the main axis of the 'Steel Mosquito'. See also Figure 4.

Inertance measurements on the 'Steel Mosquito' were carried out when it was surfaced and moored. Transient excitation was used and the inertances were the mean of some ten measurements. Modal analysis was not performed on the results. Hull inertance measurements were made with and without the dummy unit mounted to the hull structure.

In the second case the aim was to verify that the response can be calculated using inertance measurements on the dummy in the laboratory, inertance measurements on the unloaded hull structure and acceleration measurements in the hull when subjected to shock. Calculated responses are then compared with responses

measured at explosion tests. In this case unloaded hull inertances were measured at a diving depth of 90 m.

CALCULATIONS

Determining the Inertance Matrix for the Hull Attachment Points

Calculations

In the calculations it is assumed that the points of attachment and the response points have two degrees of freedom. The directions of movement lie in the radial and the tangential directions of the hull respectively. Longitudinal movements are disregarded.

The inertance matrix \ddot{Y}_{uu} for the points of attachment in the hull with the dummy unit mounted was calculated using the inertance matrix Y_{uu}^A for the dummy measured when freely suspended in the laboratory and the inertance matrix Y_{uu} for the unloaded points of attachment in the hull.

The following formula was used for the calculation:

$$\ddot{Y}_{uu} = \{ [Y_{uu}]^{-1} + [Y_{uu}^A]^{-1} \}^{-1}$$

The calculations were made with inertances having a block size of 4096 points. Sampling frequency was in this case reduced to 5 kHz and digital filtering was used.

Results

Figure 6 shows that the dummy unit interacts to a certain degree on the hull structure. Figure 7 shows that the calculated inertance is in reasonably close agreement with the measured one.

The calculations include inverting of 4 x 4 matrices with elements consisting of inertances having a block size of 4096 points. For inverting, conventional signal-analysis calculation methods were used. It was found, however, that these were not sufficiently accurate for this type of operations, producing relatively large errors varying randomly with frequency. A great part of the discrepancies between calculated and measured inertances of the hull structure can thus be traced back to the method for inverting this type of matrices not being adequately developed. Some part of the discrepancies may depend on phase-errors that can be derived from bad accuracies in the measurements and inversions of transducer directions.

Determining the Response in Outfits at Explosion Tests

Calculations

In the calculations it is assumed that the points of attachment and the response points have one degree of freedom only and with a direction of movement in the radial direction of the hull.

The response in one point of the unit, see Figure 8, was calculated using the dummy inertance Y^A measured when freely suspended in the laboratory, inertance Y_{uu}^* measured in frames of the hull structure when dived at 90 m and the Fourier transform A_u^O of the acceleration of an unloaded frame when subjected to an explosion test, again with the 'Steel Mosquito' dived at 90 m.

The following formula was used for the calculations:

$$A_r = Y_{ru}^A [Y_{uu}^A + Y_{uu}^*]^{-1} A_u^O$$

Also in this case block size was 4096 points, sampling frequency 5 kHz and digital filtering was used.

Results

Figures 9 and 10 show that the calculated response fairly closely coincides with the measured response. The agreement appears better than in the preceding calculation case in spite of the calculations being more approximate than in the first case owing to a decrease in number of degrees of freedom.

To a certain extent the low amplitude of the measured response-versus-time curve depends on a slightly overloaded signal.

By decreasing the number of degrees of freedom and hence decreasing the matrices, matrix inverting becomes much more improved than in the former case thus enhancing accuracy.

Figure 10 shows that the noise level has increased. Calculation experiences show that the noise level heavily depends on the manner used for signal analysis in the calculations.

EXPERIENCES

In spite of the calculations in the last case employed more approximations than the first one, calculation results were superior. This is supposed to stem from the fact that calculation accuracy quickly deteriorates as matrix inversion becomes less accurate with larger

matrices. An improved program for inverting matrices consisting of spectra would probably alter this.

Experiences from the calculation methods described above show that sophisticated equipment and extensive knowledge in a variety of fields are of vital importance. Measuring movements at shock and dynamic properties of dummy and hull structures require great accuracy.

The results obviously show that the calculation method can be used on equipment internally mounted in a submarine when subjected to shock. The results of calculations hitherto performed indicate that calculation accuracy can be improved using this method as compared to methods based on shock spectra. It is hence considered advantageous to improve signal analysis methods with a view of applying them for anti-shock design work. Work will consequently be directed towards solving application problems with the above described methods and include these in the present submarine projecting work.

Bibliography

- (1) K. Dovstam 'Use of Mechanical Admittances in Connection with Linear Mechanical Systems Subjected to Shocks' (in Swedish) TM 3.480.02, IFM, Stockholm, Sweden
- (2) K. Dovstam 'Mechanical Systems in Submarines when Subjected to Shocks' (in Swedish) TM 3.480.11, IFM, Stockholm, Sweden

Figure 1 Simple systems representing dummy unit and hull structure.

Figure 2 Two interconnected simple systems having one unloaded point.

Figure 3 Dummy suspended in rubber ropes for measurements in the laboratory.

Figure 4 Dummy unit mounted in the 'Steel Mosquito'.

Figure 5 Point inertances measured in freely suspended dummy (1) and in unloaded hull structure (2). (Vertical scale uncorrect)

Figure 6 Measured inertance in a radial direction with (1) and without (2) dummy unit mounted. (Vertical scale incorrect)

Figure 7 Comparison between measured and calculated point inertance in a radial direction in the hull structure with mounted dummy. (Vertical scale incorrect)

Figure 8 Point of response of dummy.

Figure 9 Comparison between Fourier transforms of calculated and measured responses. (Vertical scale incorrect)

Figure 10 Comparison between calculated and measured response-versus-time. (Vertical scales are the same for both graphs but their absolute values are incorrect)

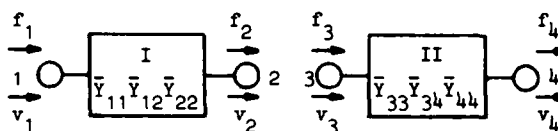


Figure 1. Simple Systems Representing Dummy Unit and Hull Structure

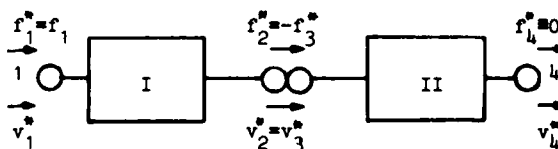


Figure 2. Two Interconnected Simple Systems Having One Unloaded Point

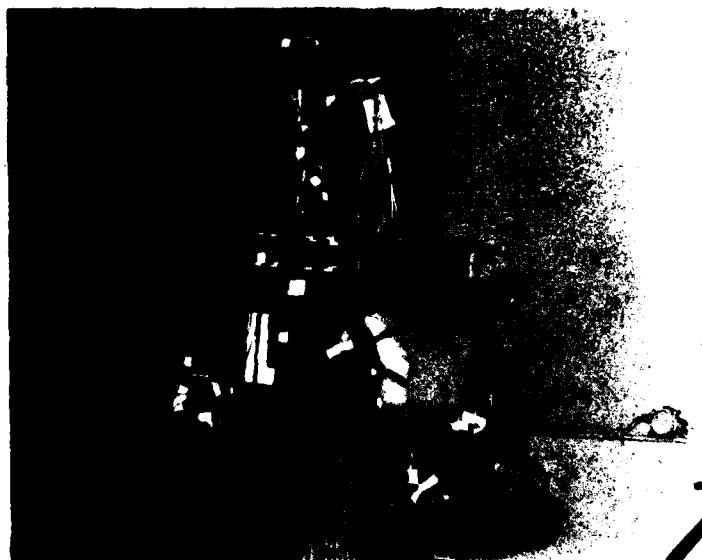


Figure 3. Dummy Suspended in Rubber Ropes for Measurements in the Laboratory



Figure 4. Dummy Unit Mounted in the 'Steel Mosquito'

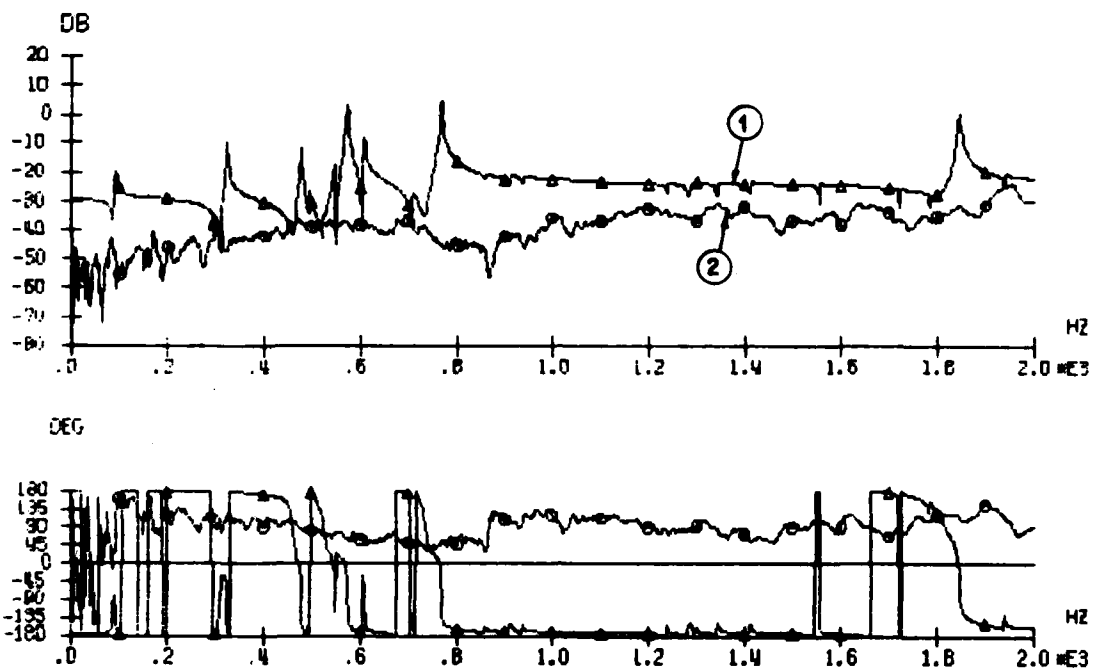


Figure 5. Point Inertances Measured in Freely Suspended Dummy (1) and in Unloaded Hull Structure (2). (Vertical Scale Incorrect.)

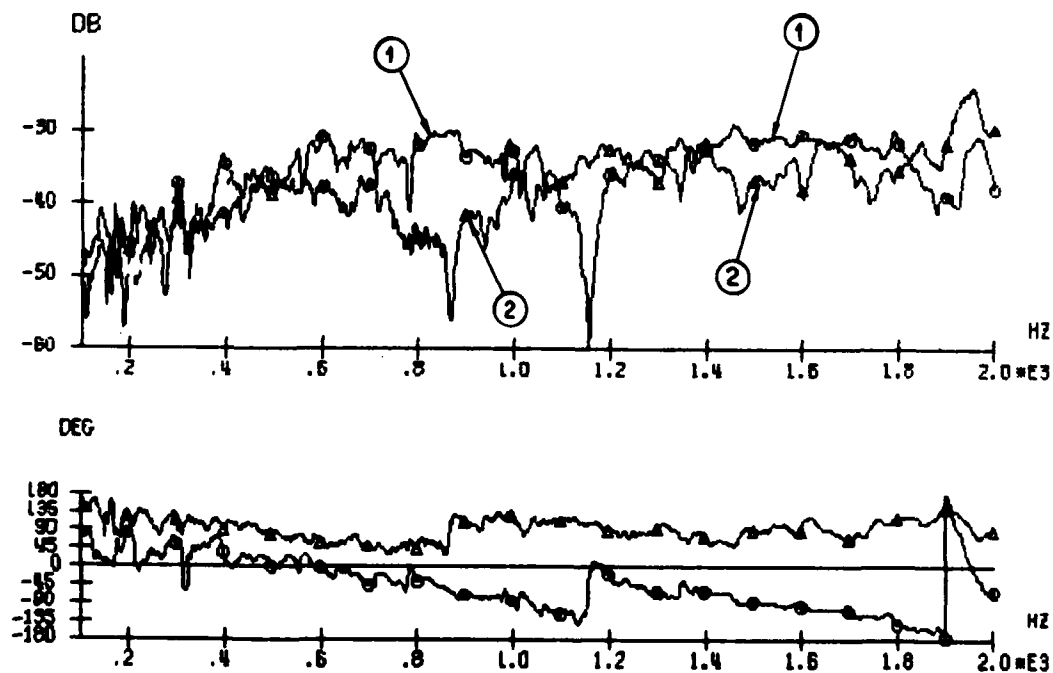


Figure 6. Measured Inertance in a Radial Direction With (1) and Without (2) Dummy Unit Mounted. (Vertical Scale Incorrect.)

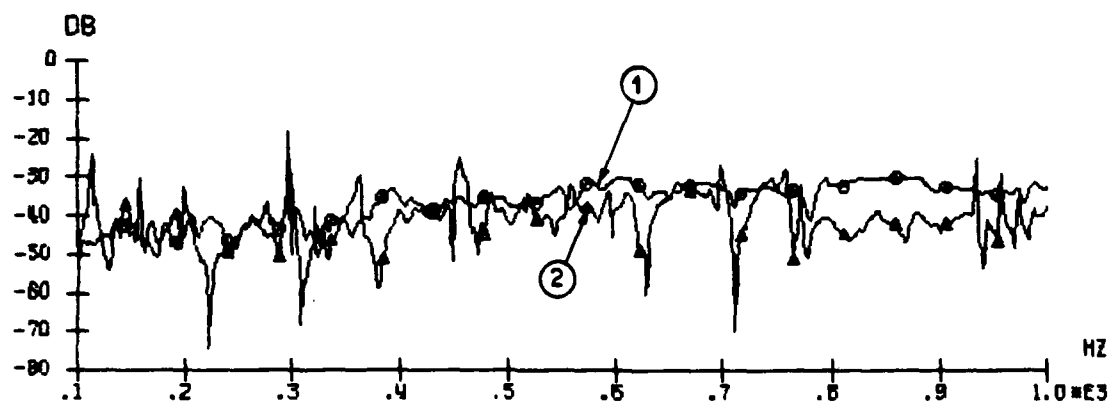


Figure 7. Comparison between Measured (1) and Calculated (2) Point Inertance in a Radial Direction in the Hull Structure with Mounted Dummy. (Vertical Scale Incorrect.)

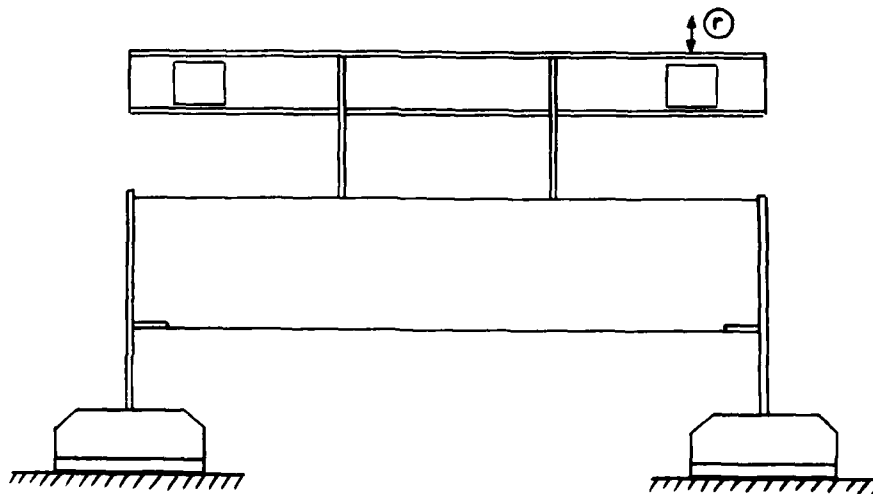


Figure 8. Point of Response of Dummy

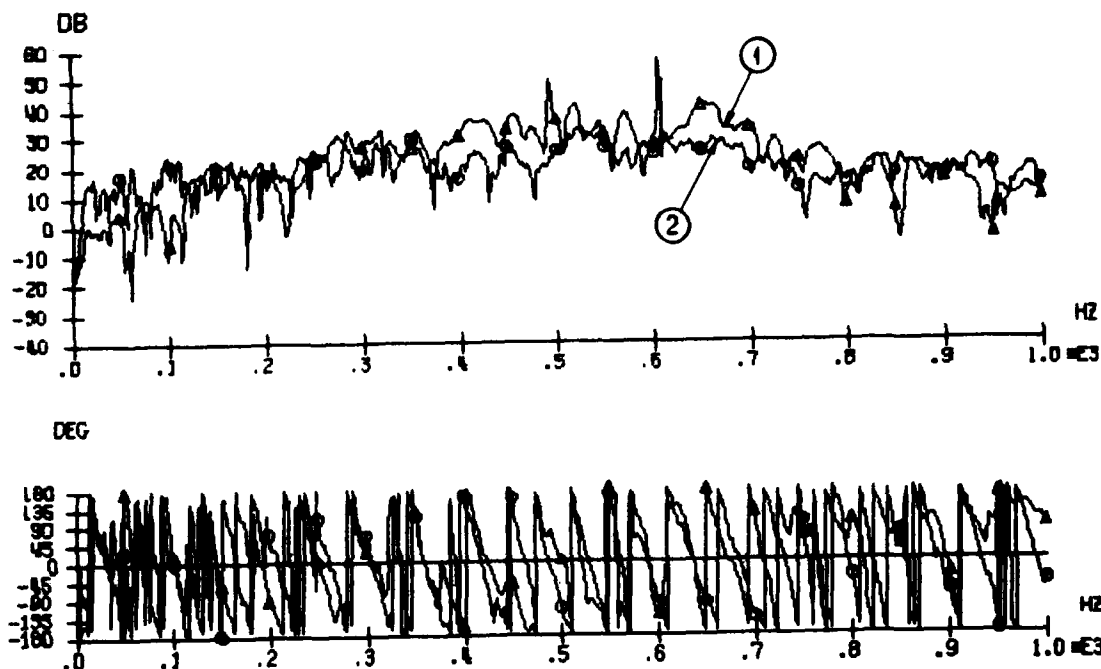


Figure 9. Comparison between Fourier Transforms of Calculated (1) and Measured (2) Responses. (Vertical Scale Incorrect.)

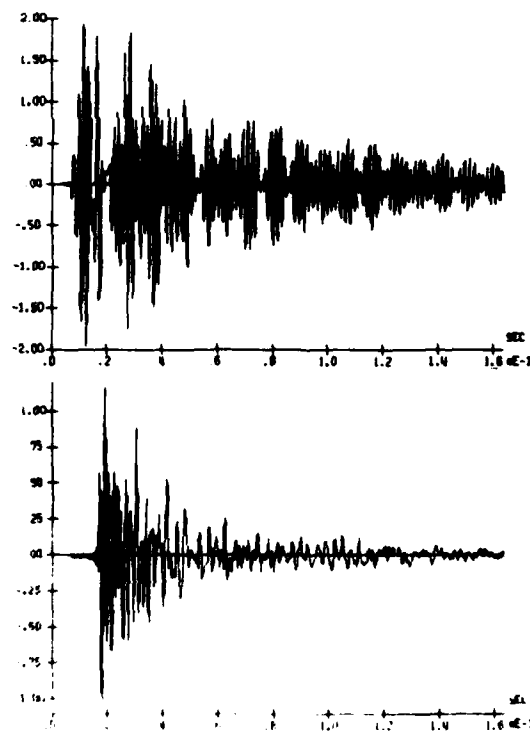


Figure 10. Comparison between Calculated and Measured Response-versus-time. (Vertical Scales are the Same for Both Graphs but Their Absolute Values are Incorrect.)

DISCUSSION

Mr. Huang (Naval Research Laboratory):
Did you measure your hull inertance submerged?

Mr. Hellqvist: Yes.

Voice: How did you protect the instrumentation systems against shock?

Mr. Hellqvist: They were mounted on large isolated platforms.

Voice: So they were well separated from the shock effects?

Mr. Hellqvist: Yes, they were. And a sign of that is the tape recorder ran very well during the shock.

Voice: What was the range of charge sizes?

Mr. Hellqvist: The charge sizes were 137 kilograms.

Voice: Was the closest standoff one charge diameter?

Mr. Hellqvist: No, it is not the diameter, it is the design distance.

A COMPUTER-CONTROLLED MEASURING SYSTEM HAVING 128 ANALOG MEASURING
CHANNELS AND FACILITIES FOR SIGNAL ANALYSIS

K. Hellqvist, MScME
Kockums AB, Malmö, Sweden

When explosion testing the submarine hull section 'Steel Mosquito' in 1978 measurements were carried out using a computer-controlled digital measuring system. The system was chiefly designed for explosion test measurements but it can also be used for various types of vibration measurements. At present the system is capable of handling 128 simultaneous signals but it can be extended to 224 channels. After completed measurements the computer can be used for signal analysis of the measurements. Programs have been worked out for both signal analysis and modal analysis. The paper describes the system as used with the explosion tests in 1978.

GENERAL

For the explosion tests with a submarine hull section called 'Steel Mosquito' in 1978, a new measuring system especially devised for vibration measurements was acquired. The system is a digital multiplexing system using PCM-technique. At present 128 signals can be handled simultaneously but the system can be extended to cope with 224 channels. In order to make the measurements as systematic as possible the system is computer-controlled. After having carried out the measurements, the computer can be used for different types of signal analysis. Table 1 gives salient data for the measuring system.

At the explosion tests against the 'Steel Mosquito' in 1978, the measuring system was used for recording acceleration-versus-time and elongation-versus-time. Pressure-versus-time was recorded using a conventional FM-method owing to the broad-band characteristics of the pressure signals.

Figure 1 shows the measuring system as used for the 'Steel Mosquito' tests. 128 measuring signals are conditioned in 8 encoders consisting of amplifiers, filters and A/D converters. The signals are subsequently recorded using a wide-band tape recorder. The system is monitored and controlled by the computer. The recorded signals are converted from PCM-code to IBM-compatible code by the computer and stored in digital form on tape to be used for various types of signal analysis performed by the computer.

DATA COLLECTING

Sensors

For the explosion tests in 1978 resistive strain gauges were used exclusively and single, angular and rosette gauges were of Type Tokyo Sokki WFLA-6, WFCA-6 and WFLA-6.

Hull accelerations were measured by means of piezo-resistive accelerometers Type Endevco 2261A-10K and Type 2261 M6.

In order to protect the accelerometers against mechanical damages and to limit slightly the bandwidth of the accelerometer signal the accelerometers were mounted on mechanical filters, see Figure 2.

Accelerometers mounted externally were protected together with its mechanical filters in pressure-proof cases. The resonance frequency of the filters was approx. 3,200 Hz.

Filter Characteristics

Owing to the digital measuring system, filtering characteristics were carefully chosen and based on signal analyses of results from earlier explosion tests. For these analyses various types of filtering were tested as well as various ways of connecting the filters in the circuits in order to utilize the amplifier as far as possible consistent with avoiding errors due to overloading. Also the requirements for phase and magnitude compensation in the signal

analyses due to filter action on the signals in the frequency range of interest has been duly regarded.

It was found that steep Bessel filters fully satisfied our requirements. The amplifiers were designed so that their characteristics corresponded to those of a Bessel filter having 9 poles. At the cut-off frequency of 2 kHz the attenuation was 6 dB. It is, however, possible to alter the filter steepness from filters having 6 poles to such with 9 poles for other than explosion test uses.

In order to utilize the dynamic range of the amplifier to its full extent, filtering should be made as early as possible in the amplifier chain. In front of the pre-amplifier there is a passive filter having the characteristics of a 2-pole Bessel filter. As the noise level in the filters became too high if the steepness of the passive filter was made to resemble that of a 3-pole filter, a single-pole filter was inserted between pre-amplifier and main amplifier. After the amplifier there is a 6-pole Bessel filter to minimize aliasing.

The amplifier characteristics can be changed by by-passing either or both of the two first filters. The cut-off frequency can also be altered by changing a resistor assembly on the amplifier printed circuit board.

Amplifier

Since the A/D converter uses 12 bit words, amplifier accuracy is of prime importance. So as to enable the A/D converter to have a measuring range corresponding to 0.5 of the maximum output signal from the amplifier, the signal-to-noise ratio must be better than 78 dB.

The amplifiers have 8 measuring ranges from 5 mV to 1 V. Amplification factor accuracy is 0.025 % and the output voltage from the amplifier is plus or minus 5 V.

A/D Converter

The A/D converter has two ranges, plus or minus 2.5 V and plus or minus 5 V. This enables the A/D converter to utilize half the amplifier working range which is likely to reduce the danger of slew rate effects somewhat. As the measuring system manufacturer has designed the amplifier with due regard to this, measuring accuracy is not appreciably lowered by halving the A/D converter range.

Each A/D converter normally digitizes 16 measuring signals sequentially, making every 16th sample of the output signal represent one specific signal. Each such signal is then recorded on tape and 8 converters are required for handling 128 measurement signals.

The A/D converter sampling frequency is 160 kHz max., i.e. 10 kHz per channel. By decreasing the number of signals per A/D converter, sampling rate for these signals may be increased. Lowest sampling rate for the A/D converter is 4 kHz, i.e. 250 Hz per channel.

One of the A/D converters acts master for synchronizing the other 7 converters providing for simultaneous sampling of related signals.

COMPUTER

The computer is used for several different purposes. Immediately before making measurements the computer can set and check the amplification factor of each amplifier, balance each gauge, check that the system as a whole is ready and produce a 'Ready' signal.

After the measurements the computer can be used for converting PCM-data to data using an IBM-compatible code and make a simple test of measured data. It can also be used for recording information regarding measurement procedures. Such information can be tabulated, see Table 2. The information is recorded on digital tape together with measurement data. At a later signal analysis the information is read out into the computer, automatically securing correct units for measured data with regard to amplification factor, sensor sensitivity etc.

SIGNAL ANALYSIS

The computer is provided with software for signal analysis. Such analyses can be carried out either interactively or automatically in a batch mode.

Owing to analyses being carried out entirely in terms of software they are fairly slow. Thus a 1,000 point Fourier transform will be performed in slightly less than 1 sec. To a certain degree this delay is compensated for by the program being specially designed for analysing great amounts of data by specific orders and that signal analysis can be carried out in batch mode.

Signal analysis programs enable Fourier transforms, digital filtering, sampling reduction, shock spectrum analysis, transfer functions, power density spectra etc. to be carried out. Analysis block size is 4096 points max. There are also programs for modal analysis of up to 256 transfer functions with 62 modes.

Modal analysis is carried out as multiple curve fitting. In this analysis it is assumed that resonant frequency and damping attenuation are the same throughout the complete structure. Figure 4 gives an example of results from a test. Figures in brackets show theoretically

calculated resonant frequencies of each mode shape.

EXPERIENCES

Experiences with the measuring system are most satisfactory. At the very first measurements, the explosion tests with the 'Steel Mosquito' in 1978, some 2,500 measurements were made at 21 tests during 21 days. Measurements were carried out in 13 entirely different measuring planes requiring the sensors to be moved prior to each explosion. Only three persons were required for these measurements, showing that the system is time-saving and requires a minimum of staff and an appreciable cost reduction for such elaborate tests.

Also the measured signal quality is quite acceptable. Figure 5 shows a comparison between measurements made at two identical tests at two different occasions. The figure shows a reasonably good agreement between the measurements. Figure 6 shows the results of inertance measurements on the hull when dived to 90 m. The inertances have been determined from the mean value of 10 measurements using transient excitation. It can also be seen that coherences are reasonably good within the greater part of the frequency range. This is of course no measure of system quality but such a good coherence would be difficult to obtain if the quality of the measured signals were poor.

From the above it is evident that we have acquired a flexible system for advanced vibration measurements capable of systematic and fast handling of vast amounts of data as well as high signal recording quality.

Table 1 Salient data for the measuring system used with the explosion tests against the 'Steel Mosquito' in 1978.

Figure 1 System for vibration measurements.

Figure 2 Mechanical filter for accelerometers.

Figure 3 'Steel Mosquito' measuring system.

Table 2 Example of measurement documentation.

Figure 4 Measured modes of a simple steel plate.

Figure 5 Acceleration measurements in the same point at different explosions using the same detonation distance and the same charge.

Figure 6 Measured hull inertance when dived at 90 m.

Table 1 Salient Data for the Measuring System used with the Explosion Tests against the 'Steel Mosquito' in 1978

No. of Channels	128 max.
Frequency Range	2 kHz max.
Filter Characteristics	Bessel filter, 9 poles max.
Sampling Frequency	10 kHz/channel max.
ADC	12 bits
Ranges	5, 10, 20, 50, 100, 200, 500, 1,000 mV
Max. Output	± 5 V; ± 2.5 V
Recording Speeds	3 3/4, 7 1/2, 15, 30, 60, 120 ips
Minicomputer Nova 3/12	120 kbyte
Hardware Multiply/Divide	
Disc Memory	2 x 5 Mbyte
Digital Tape Recorder	



Figure 1. System for Vibration Measurements.

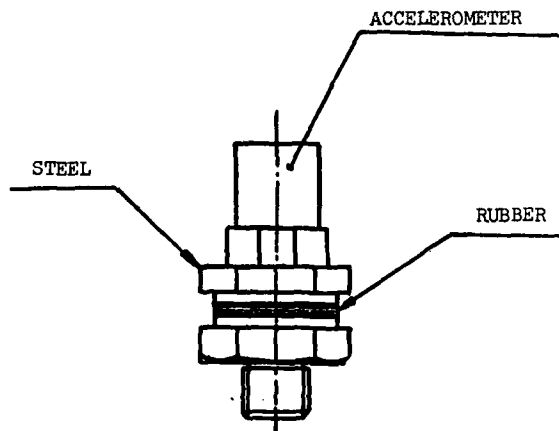


Figure 2. Mechanical Filter for Accelerometers

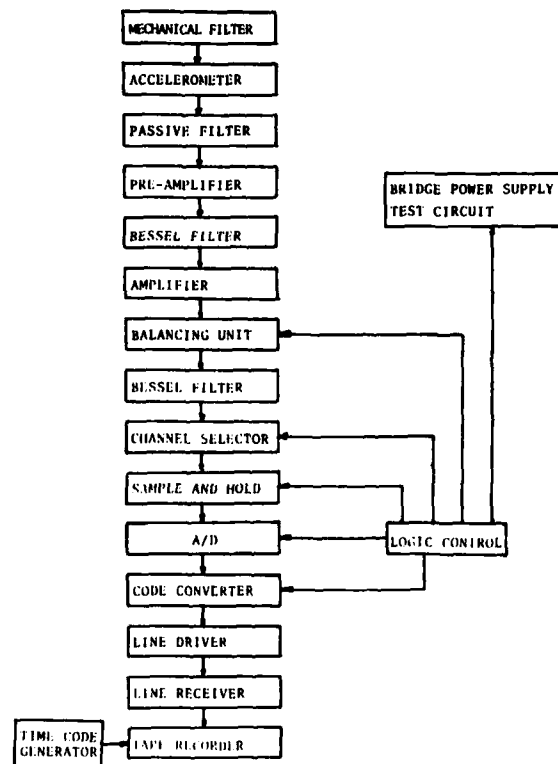


Figure 3. 'Steel Mosquito' Measuring System. Block Diagram.

ACTUAL INSTRUMENT DATA LIST FOR DEVICE # 1												
TEST#	22											
YEAR OF MEASUREMENT	78											
MONTH/DAY OF MEASUREMENT	427											
MEASUREMENT OBJECT DESCR.	EXPLOSION # 11 MP: 2 EXPLO. 12											
TRIGGER DEV. /CHA. /LEVEL	8/ 9/ 0											
TAPE RECORDING SPEED	12000											
TAPE REPRODUCTION SPEED	750											
BRIDGE-RESISTOR DEV. # 1	120	120	120	120	120	120	120	120	120	120	120	120
DEV. # 1	120	120	120	120	120	120	120	120	120	120	120	120
ACTIVE/PASSIVE LIST DEV. # 1	ACT.	ACT.	ACT.	ACT.	ACT.	ACT.	ACT.	ACT.	ACT.	ACT.	ACT.	ACT.
DEV. # 1	ACT.	ACT.	ACT.	ACT.	ACT.	ACT.	ACT.	ACT.	ACT.	ACT.	ACT.	ACT.
NUMBER OF CHANNELS/FILE	16											
SAMPLING PERIOD	.10											
MEASUREMENT POINT# DEV. # 1	16	17	18	19	23	24	59	59				
DEV. # 1	99	60	60	60	79	79	79	121				
SIGN/DIR. OF TRANSD DEV. # 1	-Y	-Y	-Y	-Y	-Z	-Y	-Z	-Y	-Z	-Z	-Z	-Z
PHYS. UNIT CODE DEV. # 1	4	4	4	4	4	4	4	4	4	4	4	4
DEV. # 1	4	4	4	4	4	4	4	4	4	4	4	4
TRANSDUCER SEQU. # DEV. # 1	0	0	0	0	0	0	0	0	0	0	0	0
DEV. # 1	0	0	0	0	0	0	0	0	0	0	0	0
MECH. FILTER SEQU. # DEV. # 1	0	0	0	0	0	0	0	0	0	0	0	0
DEV. # 1	0	0	0	0	0	0	0	0	0	0	0	0
ELEC. FILTER SEQU. # DEV. # 1	1	2	3	4	5	6	7	8				
DEV. # 1	9	10	11	12	13	14	15	16				
AMPLIFIER SEQU. # DEV. # 1	1	2	3	4	5	6	7	8				
DEV. # 1	9	10	11	12	13	14	15	16				
AA-CUTOFF FREQU. DEV. # 1	2000	2000	2000	2000	2000	2000	2000	2000	2000	2000	2000	2000
DEV. # 1	2000	2000	2000	2000	2000	2000	2000	2000	2000	2000	2000	2000
FIRST/SECOND FILTER DEV. # 1	ON/	ON	ON/	ON	ON/	ON	ON/	ON				
DEV. # 1	ON/	ON	ON/	ON	ON/	ON	ON/	ON				
DEV. # 1	ON/	ON	ON/	ON	ON/	ON	ON/	ON				
DEV. # 1	ON/	ON	ON/	ON	ON/	ON	ON/	ON				
AC/DC COUPLING CODE DEV. # 1	DC	DC	DC	DC	DC	DC	DC	DC	DC	DC	DC	DC
TRANSDUC. SENSITIV. DEV. # 1	1870.0	1870.0	1870.0	1870.0	1870.0	1870.0	1870.0	1870.0	1870.0	1870.0	1870.0	1870.0
DEV. # 1	1870.0	1870.0	1870.0	1870.0	1870.0	1870.0	1870.0	1870.0	1870.0	1870.0	1870.0	1870.0
INPUTRANGE DEV. # 1	50	25	50	50	25	50	25	25				
DEV. # 1	25	25	25	25	25	25	25	25				
ADC MAX. VALUE DEV. # 1	OFF	OFF	OFF	OFF	OFF	OFF	OFF	OFF				
DEV. # 1	OFF	OFF	OFF	OFF	OFF	OFF	OFF	OFF				
EXP. SIGNAL MAXVALUE DEV. # 1	0	0	0	0	0	0	0	0				
DEV. # 1	0	0	0	0	0	0	0	0				
BRIDGE SUPPLY DEV. # 1	30MA	30MA	30MA	30MA	30MA	30MA	30MA	30MA				
DEV. # 1	30MA	30MA	30MA	30MA	30MA	30MA	30MA	30MA				

Table 2. Example of Measurement Documentation

RIGID BODY

MODE NO. 1 51.7 HZ (51.8 HZ)

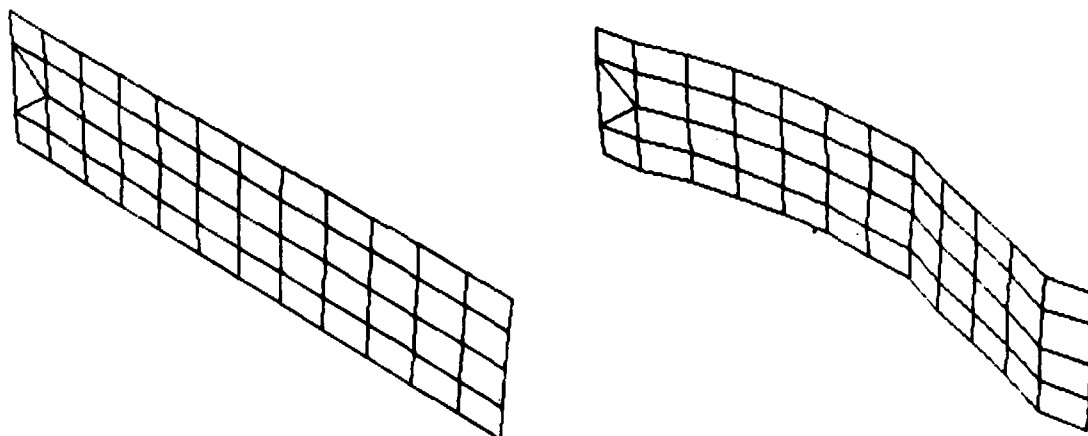


Figure 4. Measured Modes of a Simple Steel Plate

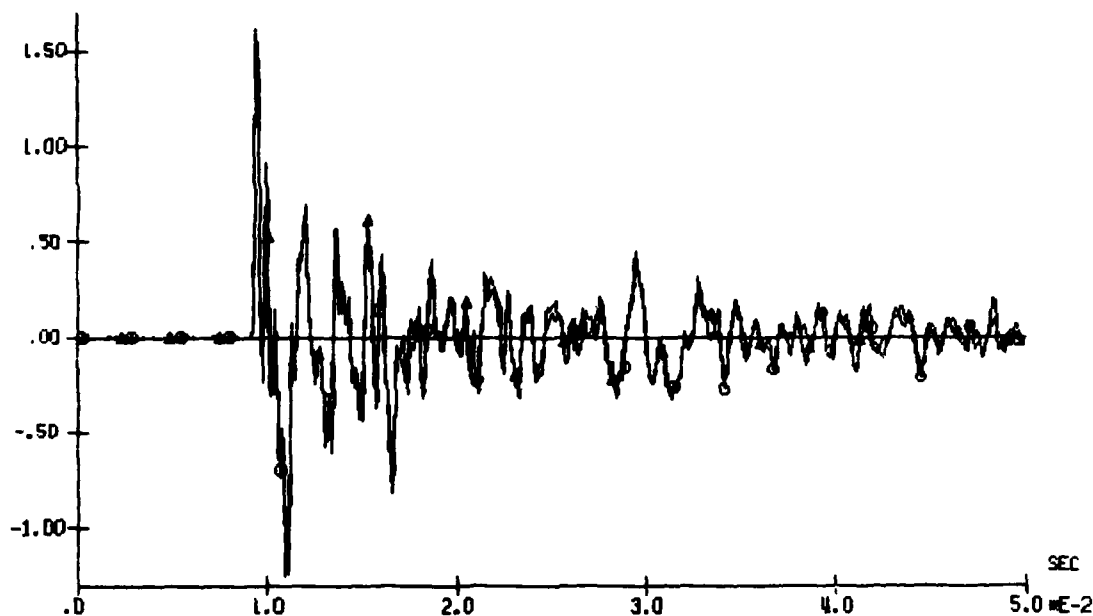


Figure 5 A. Acceleration Measurements in the Same Point at Different Explosions Using the Same Detonation Distance and the Same Charge

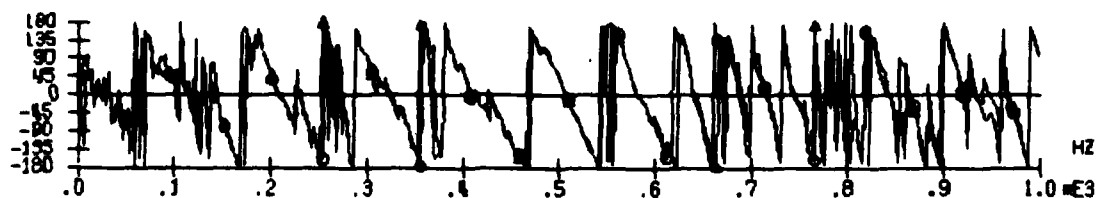
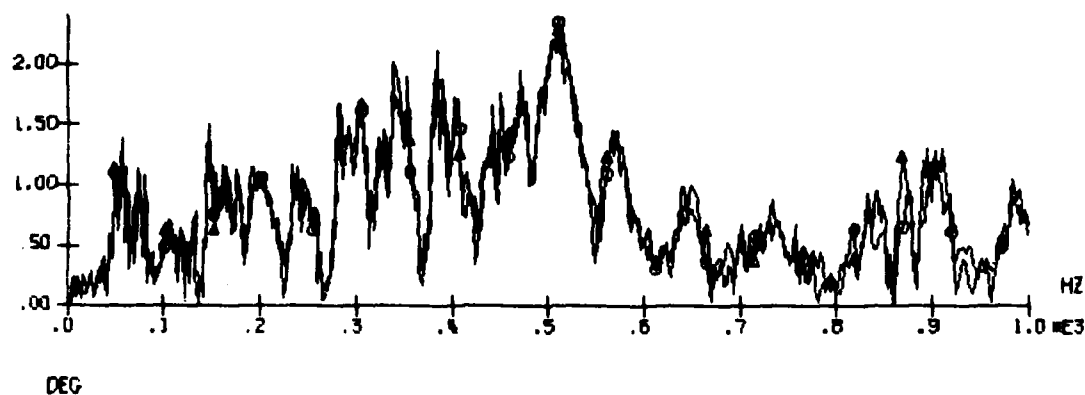


Figure 5 B. Acceleration Measurements in the Same Point at Different Explosions Using the Same Detonation Distance and the Same Charge

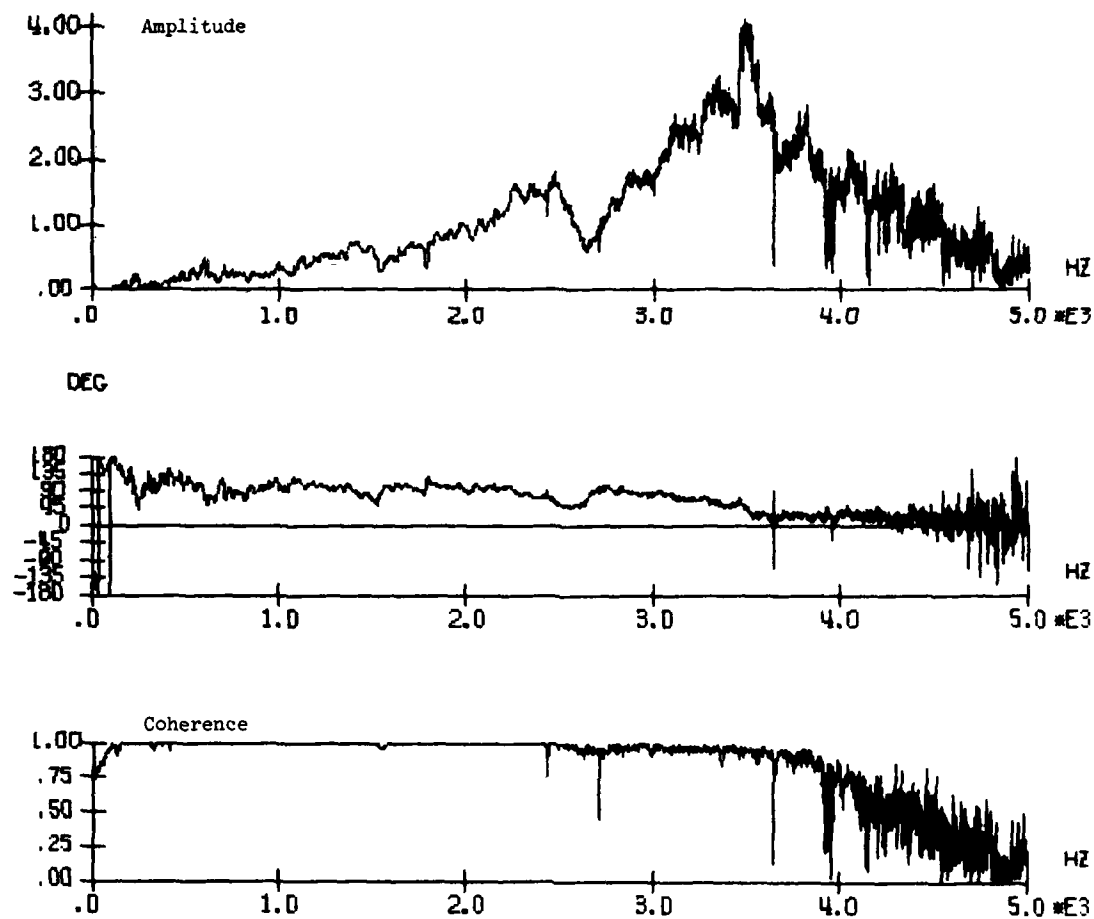


Figure 6. Measured Hull Inertance when Dived at 90 m
(Vertical Scales Incorrect.)

DISCUSSION

Voice: I must say this is not the most complicated measuring system I've ever seen in my life. I've done something similar in the past of course but it seems to me that the breakdown usually is at the transducers; if there is going to be problems - the transducer is going to give it to you. I assume you have made some simple tests on these things. In the past we have done simple tests. For example, we use to have a ballistic pendulum device which simply gave a step velocity to the transducers under test. Have you done any such tests yourself so that for example you know the motion that's going into the thing and you can process your records and come up with that motion?

Mr. Hellqvist: Yes we have made some of them and they have been made by the SAAB Aircraft Company. They have tested lots of different kinds of accelerometers and they have found that the Model 2261 accelerometers made by Endevco are relatively good as we can see from these pictures here. There are two different gauges and two different locations with two different charges that are exploded at the same standoff. As you can see, the measurement is made at the same measuring point in the steel mosquito so it should be exactly the same.

Voice: Right! This shows that they are repeatable. They do the same thing. But my question is, is that what really happens?

Mr. Hellqvist: Nobody knows.

Voice: You mentioned you were trying to find out if the effect of a large charge and a great distance as the same as a small charge and lesser distance.

Mr. Hellqvist: We are trying to investigate if it is possible. Yes we have run different charge weights and different distances and they should give us the same shock factor. They should give the same reaction in the steel mosquito but we haven't had the time to check that out yet.

Voice: How about a simple peak pressure comparison?

Mr. Hellqvist: The peak pressure is as far as I know, the peak pressure is the same, always the same.

Voice: Would you care to comment on he signal to noise ratio you believe you got out of that system?

Mr. Hellqvist: We have made measurements in order to check the manufacturer but we don't have instruments that are good enough to measure the noise. We could measure down to 80 db and we cannot find any noise at that level so we don't know it, however the manufacturer has specified that it should be better than 78 db and we have found that it is better than that.

Voice: How did you decide on the resonant frequency for the mechanical filter?

Mr. Hellqvist: That was a very difficult choice; because the system is digital, we would have to be aware of aliasing so the resonant frequency must be as low as possible in order to not amplify the acceleration signal from the sensor at above half the sampling frequency. The sampling frequency was 10 kHz so the resonance must be a bit lower than 5 kHz in order to avoid aliasing with the Bessel filters that we chose, the damping at 5 kHz won't do it. When the cutoff frequency is 2 kHz the damping is not very high. So we wanted the resonant frequency for the mechanical filter to be as low as possible so we accepted the same amplification of the signal in the mechanical filter as in the electrical filter, which damped the signal up to 2 kHz, and that was 6 db. And if we are using that criteria the resonant frequency of mechanical filter would be about 3,200 Hz. It is also difficult to choose the rubber for the mechanical filter because you have to choose the right rubber to have the right damping in the mechanical system. If you have high damping material the peak will be very broad.

A LARGE-SCALE SUBMARINE SHOCK TEST CARRIED OUT AS PART OF THE SWEDISH
SHOCK DESIGN DEVELOPMENT PROGRAM

K. Hellqvist, MScME
Kockums AB, Malmö, Sweden

The paper describes the detonation tests carried out in 1978 with a test body called the 'Steel Mosquito', a full scale section of a submarine hull. A test site was arranged in the Stockholm Archipelago and the test body was moored at a depth of approx. 90 m (300 ft).

The purpose of the tests were to investigate various outfits for submarines and to obtain data to be used when designing outfits and equipment for submarines as well as for further development work.

GENERAL

In Sweden explosion tests against submarine hull sections and submarines are carried out about every fifth year. The latest explosion tests were performed in 1978 using a submarine hull section called 'Steel Mosquito'. The tests which were carried out in the Stockholm Archipelago form a basis for the development of new methods for calculating shock stresses in submarine equipment and for the development of new types of submarines.

PURPOSE

Range of measurements and test body were selected with regard to needs for developing new submarines as well as developing methods for calculation of stresses due to shocks, a work which is being carried out in Sweden.

Determining Hull Deformations at Explosions at Great Depths

For explosions at design detonation distances minor plastic hull deformations are acceptable. Previous tests were made with the 'Steel Mosquito' dived at quite a small depth, some 15 m. To find out if plastic deformations would increase with increased diving depth it was decided to carry out the tests at a fairly appreciable depth which in this case became the maximum diving depth of 90 m.

By altering the diving depth of the test body at different explosions, variations of the

shock movements in the hull due to diving depth could be studied.

Comparison between Small and Large Charges

Present directives for designing a submarine hull are based on explosion charges having a specified weight. Experiences from earlier tests show that it is difficult to calculate results from other charge weights. It is also interesting to ascertain if heavy charges at great explosion distances can be simulated by small charges at short distances. Hence one goal was to establish shock action on submarine hull and equipment as a function of charge weight.

Testing Heavy Shock-mounted Systems

In Swedish submarines equipment is frequently mounted direct on large platforms that are resiliently mounted onto the hull. The weight of such a complete platform amounts to some 30 ton (metric). Prior to the 'Steel Mosquito' tests no results from shock-testing such assemblies were available and it was thus important to confirm the assumptions on which the design of resiliently mounted heavy assemblies are based.

Testing a Submarine Storage Battery

One important test object was a new type of cells for a submarine storage battery since it was intended to fit the battery without resilient mountings in the battery compartment.

The cells had previously been tested in a drop test machine under laboratory conditions. As such tests could only produce stresses in the vertical direction, the explosion tests were aimed at verifying the laboratory results. It was also important to confirm that cell resistance to horizontal shocks was sufficient and that plastic deformations of the storage battery compartment would not be so great that the cells became crushed by athwartship explosions. Finally it was also important to ascertain how the battery with accessory equipment could take explosions for instance from straight underneath the battery compartment.

Data Collection for Design Directives

Since only a small number of submarines of each type are built in Sweden, design of submarine hull and equipment must be based mainly on theoretical calculations and only to a small degree on full scale tests. Design directives have hence been developed during a number of years and an important aim with the tests was the collection of data for up-dating design directives.

Verifying Design Directives

Design methods which are being developed since 1972 must be tested in practice before applying them to submarine equipment. Thus the explosion tests were aimed at providing data for testing the new calculation methods.

Equipment Testing

In certain cases it is preferable to shock-test equipment than to design it theoretically. Equipment which is vital to submarine safety or submarine functioning must obviously exhibit a sufficient resistance to shocks. Such equipment was therefore also included in the tests.

TEST BODY

The 'Steel Mosquito' is a full-scale section of a submarine hull. Its length is 11 m and its diameter 5.7 m. Ballast tanks are fitted fore and aft which can be filled or discharged by remote-control from ashore. Surface displacement is 226 ton and submerged displacement is 283 ton.

The 'Steel Mosquito' was fitted with several systems and outfits. As mentioned above there was a storage battery compartment having 18 passive and 22 active cells. The cells were connected to form an operational storage battery. Battery functioning was checked by measuring battery capacity and discharge. Storage battery accessories, such as outfits for ventilation, cooling, leakage indication,

cell voltage measurement, electrolyte level measurement etc. were shock-tested. Prior to a test the battery was fully charged and the accessory systems running.

In a special torpedo tube a torpedo Type 42 was tested. Torpedo stresses were measured both with a dry and a water-filled tube.

Also a complete modern periscope was fitted in the 'Steel Mosquito'. The 'fin' supporting the periscope externally was designed so that its dynamic properties as far as possible corresponded to those of the fin on the latest Swedish submarines.

The 'Steel Mosquito' also contained a resiliently mounted platform having a weight of approx. 30 ton including various dummy outfits. Its construction was identical with those in present type Swedish submarines.

In addition the following component items were fitted:

- (a) Hull-mounted valves,
- (b) Hull seatings,
- (c) Compressed-air bottles,
- (d) Hydraulic piping,
- (e) Several types of hatches with covers.

In the hull part proper various types of welds having certain defined weld faults were tested.

TEST SITE ARRANGEMENTS

Figure 4 shows the mooring arrangements on the test site. When dived the 'Steel Mosquito' was suspended from buoys. The diving depth could be set by altering the length of the wire ropes between buoys and the 'Steel Mosquito'. The actual diving depth was sensed by means of a depth gauge on board having an indicator at the shore station which also was fitted with indicating instruments showing bilge water level and hydrogen content of the atmosphere in a few places.

Electrical power was supplied from ashore for normal running of various outfits and DC power for storage battery charging was obtained from an auxiliary craft which also could replenish the air bottles in the 'Steel Mosquito' as required.

EXPLOSION PLAN

Charges were detonated in all directions around the 'Steel Mosquito' which was thoroughly inspected after each explosion. In all twenty-one charges were detonated. Also the distance between charge and test body was altered but only after charges had been detonated in every direction around the 'Steel Mosquito'.

MEASUREMENTS

At the tests were measured: elongation-, acceleration- and pressure-versus-time. Maximum relative displacement between hull and resiliently mounted outfits as well as persistent plastic deformations in the hull were measured mechanically.

Before mounting in the 'Steel Mosquito' inertances of a number of outfits were measured in a laboratory with the outfits suspended freely. At the test site external and internal hull inertances were measured by employing transient excitation of the oscillatory movement. Such measurements were made both when surfaced and when dived to a depth of 90 m.

At each detonation 128 signals from strain gauges and accelerometers were measured together with 13 pressure-versus-time sequences. As charges were detonated in various directions from the 'Steel Mosquito' the program had to be altered between each detonation. In all there were mounted 600 strain gauges, 300 accelerometers and 50 pressure gauges. A total of some 2,700 signals were recorded.

MEASURING SYSTEM

At the explosion tests two measuring systems were used in parallel. Figure 6 shows a block diagram for the systems. Signals from accelerometers and strain gauges were measured using a 128 channel PCM system and for pressure signals a conventional FM system was used. Both systems were controlled by a computer at the shore station and the arrangement was such that full synchronism between the two systems was obtained.

The measuring systems each consisted of two parts, one in the 'Steel Mosquito' and one ashore. In the 'Steel Mosquito' were mounted FM tape recorder, amplifiers, filters and PCM encoders, see Figure 6. Ashore were found PCM tape recorder, time code generator and computer.

RESULTS

The goals aimed at with the explosion tests have generally speaking been achieved and the results are now being used for developing a new series of Swedish submarines. At present they are not used for improving the shock resistance of the submarine but for decreasing construction costs. A preliminary cost calculation shows that savings in building costs are appreciably higher than costs incurred by the explosion tests. Furthermore Kockums' know-how has been much improved and a vast amount of data have been acquired for later use in our design work.

One example of the results is shown in Figure 8. Here the response in one of the cell terminal bolts as measured in a laboratory is compared with the measured maximum response in the terminal bolts of the storage battery cells mounted in the 'Steel Mosquito'. Maximum amplitude was obtained in one terminal bolt in the centre of the battery compartment.

Testing welded joints shows that building costs can be reduced as it has become evident that welded joints in the skin can be simplified, thus decreasing costs for hull construction by between 5 and 10 percent.

Results obtained at the tests are extensive and they are at present being used for the new submarine projecting work.

- Figure 1 'Steel Mosquito' surfacing after an explosion test.
- Figure 2 Launching the 'Steel Mosquito'.
- Figure 3 'Steel Mosquito' and various outfits to be tested.
- Figure 4 'Steel Mosquito' mooring arrangement.
- Figure 5 Explosion plan.
- Figure 6 Block diagram showing measuring system.
- Figure 7 Measuring equipment inside the 'Steel Mosquito'.
- Figure 8 Comparison between acceleration responses from laboratory and explosion tests respectively.

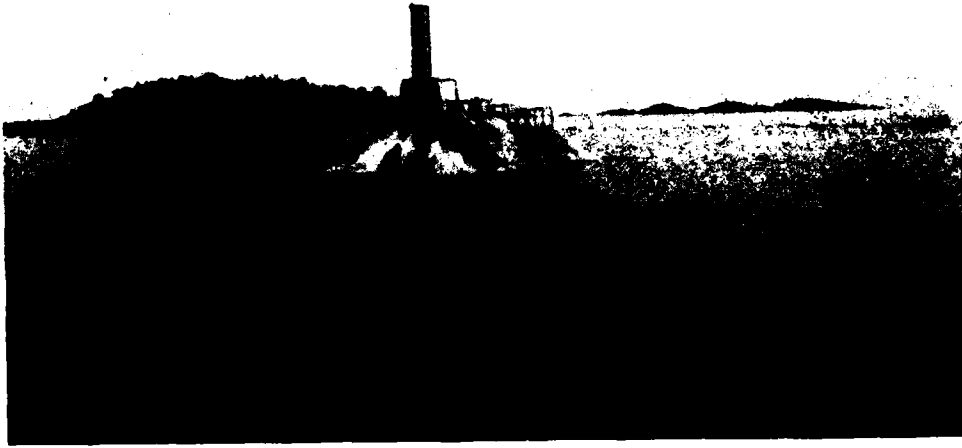


Figure 1. 'Steel Mosquito' Surfacing after an Explosion Test



Figure 2. Launching the 'Steel Mosquito'

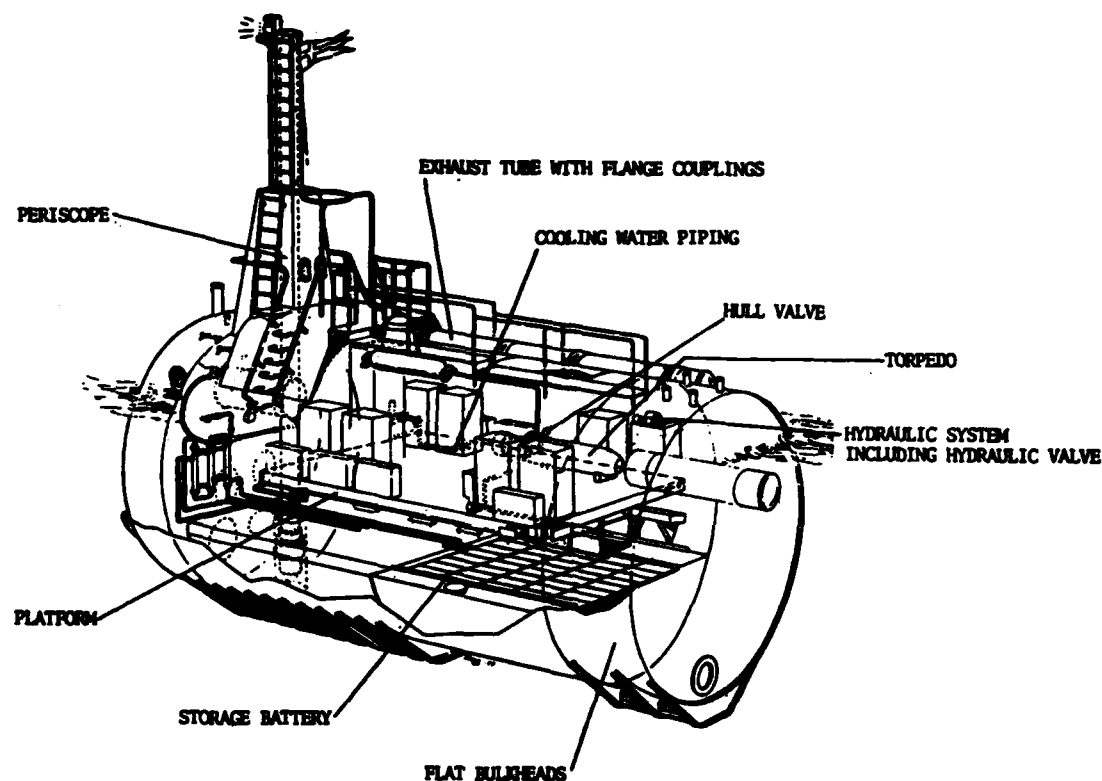


Figure 3. 'Steel Mosquito' and Various Outfits to be Tested

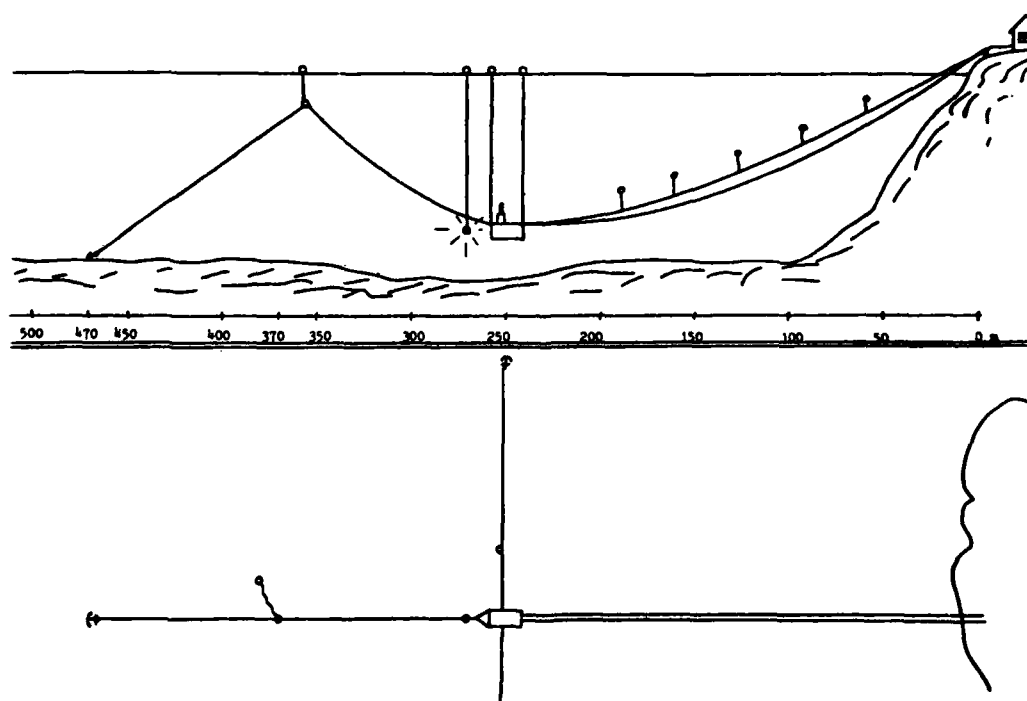


Figure 4. 'Steel Mosquito' Mooring Arrangements

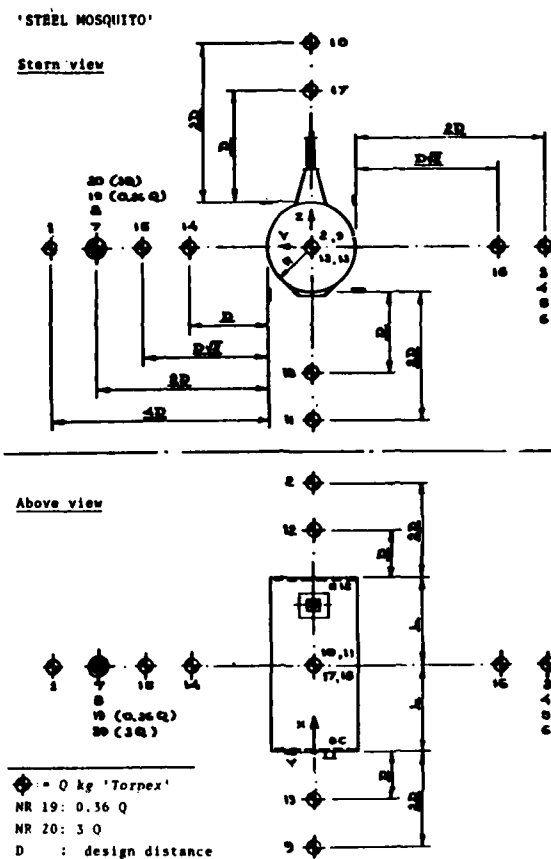


Figure 5. Explosion Plan

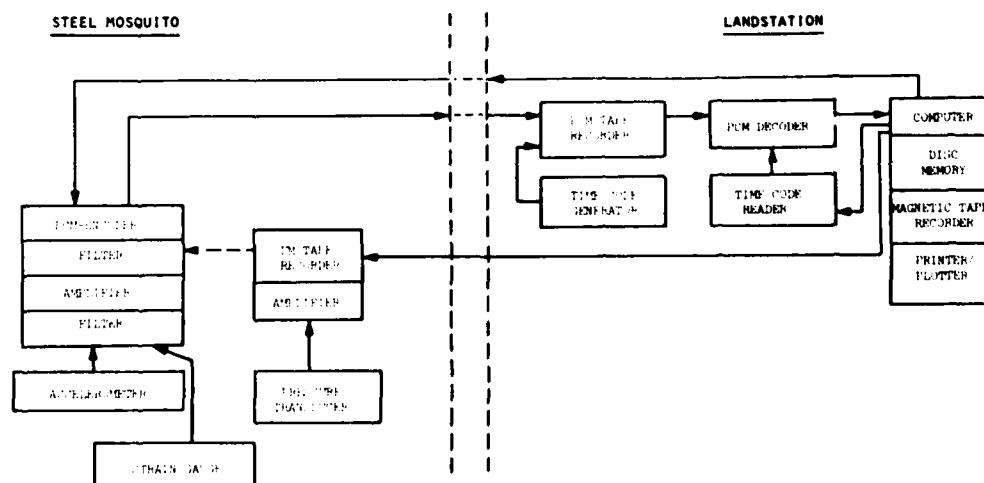


Figure 6. Block Diagram Showing Measuring System

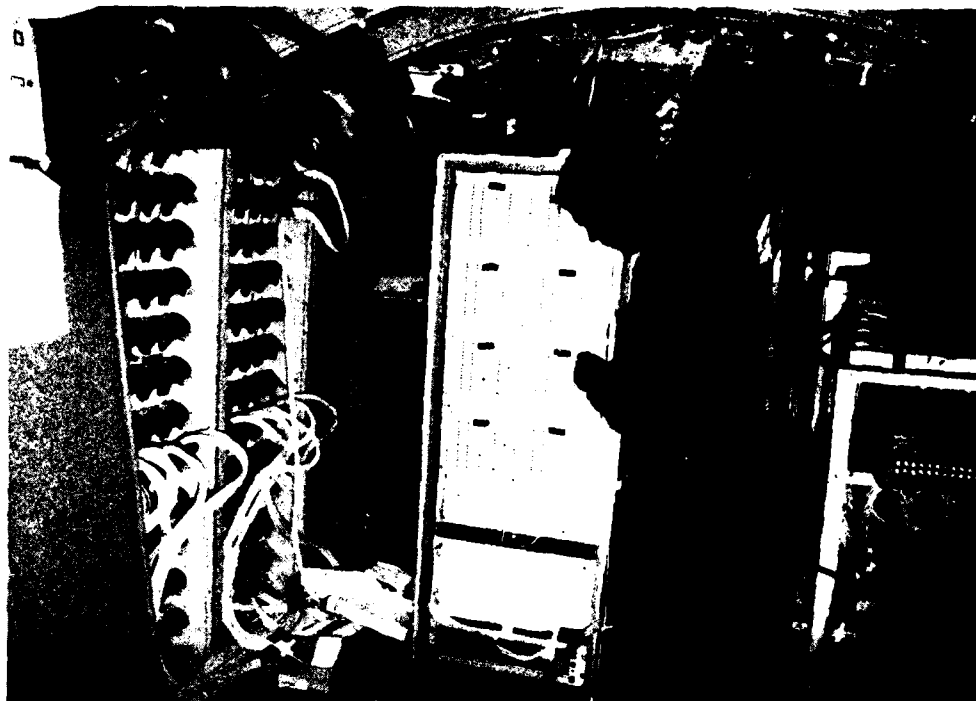


Figure 7. Measurement Equipment Inside the 'Steel Mosquito'

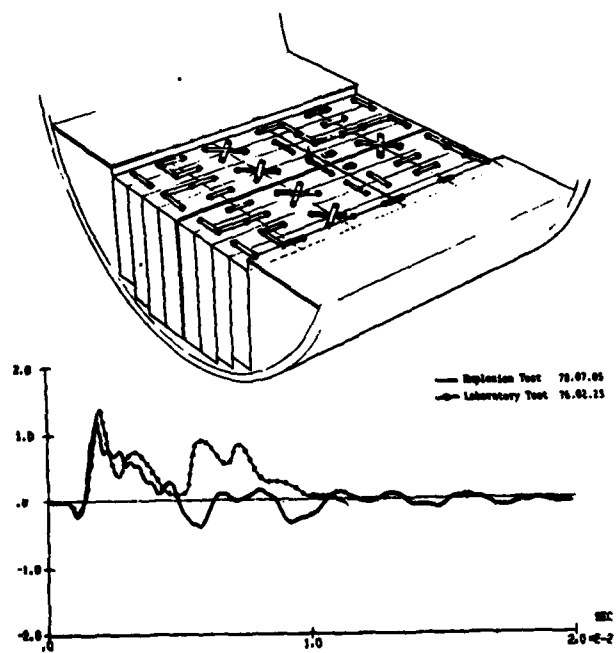


Figure 8. Comparison between Acceleration Responses from Laboratory and Explosion Tests Respectively

DISCUSSION

Voice: Did you get much plastic deformation?

Mr. Hellqvist: Not very much. As you see we can use the test section from other tests too. Then you can understand that the plastic deformation was not very large. It was not as large as we expected and it didn't increase with the diving depth.

Voice: What sort of velocity transducers were used?

Mr. Hellqvist: We didn't use velocity meters. We only used accelerometers.

Voice: How did you predict how much plastic deformation would occur? Did you consider strain rate effects?

Mr. Hellqvist: Many years ago we calculated what the plastic deformations could be and in that case we didn't take strain rate effects into account. Otherwise we have run lots of laboratory tests on strain rate effects and, as far as we can see, the strain rate effect is very low with the velocities we are working with. The strain hardening effect is much more important because the steel becomes harder the more it is deformed and that is much more important in this case than the strain rate effect as far as we can find.

UNCLASSIFIED

EDESS: AN ELECTROMAGNETICALLY-DRIVEN EXPLOSIVE-SHOCK SIMULATOR*

F. J. Sazama and J. B. Whitt
Naval Surface Weapons Center
White Oak, Silver Spring, Maryland 20910

Abstract

A new series of electromagnetically-driven shock generators called EDESS is being evaluated at the Naval Surface Weapons Center for generating explosive-like shocks. A prototype generator, EDESS-1, has been built and its performance has been evaluated using 1.0 and 2.0 metric ton payloads. Its shock output and overall performance are close to design expectations as predicted from computer-aided analysis of a simple electromechanical model. Presently, a larger generator, EDESS-2, is being built to extend the payload capability to 5.0 metric tons and a homopolar-driven generator, EDESS-3, is being contemplated for 15.0 metric ton payloads. This paper presents the electromagnetic shock-generation concept and reviews the progress made in developing these heavy payload shock generators.

INTRODUCTION

The strong need to improve the combat survivability of surface ship and submarine equipment without the burdens of excessive testing cost or explosive damage to the surrounding environment has prompted a search for alternatives to present-day shock testing methods. Present day methods commonly employ conventional impact shock machines [1, 2] and, for a range of larger-scale naval equipment, floating shock platforms [3] with underwater explosives as the driver. A new electromagnetic shock-generation concept has been proposed and is being studied by means of a series of prototype shock generators EDESS-1, 2 and 3 each capable of impulse-shocking larger payloads. The acronym EDESS arises from electromagnetically-driver explosive shock simulator.

An electromagnetically-driven shock platform offers the attractive possibility of producing a range of shock environments that are electrically tailored to represent the in-place dynamic environment actually seen by the equipment when shipboard. Additional advantages such as shot-to-shot reproducibility, reasonable cost and minimal impact to the surrounding environment also appear to be inherent in the concept. This paper describes the concept and the generators that have been designed and built to demonstrate these features. The primary objective of the effort however is to establish the engineering practicality of using electrical

pulse-power for generating explosive-like shocks in sizeable payloads. This objective has been accomplished for 2.0 metric ton (2.0 Mg) payloads with completion of EDESS-1. EDESS-2 is presently being assembled.

THE SHOCK GENERATION CONCEPT

The concept consists of generating explosive like shocks in shipboard equipment by means of the magnetic repulsive force between pairs of spiral-pancake magnet coils that are sandwiched between a large reaction mass and the payload under test. The concept is illustrated in Figure 1 which shows a section view of the two single-layered, spirally-wound coils connected

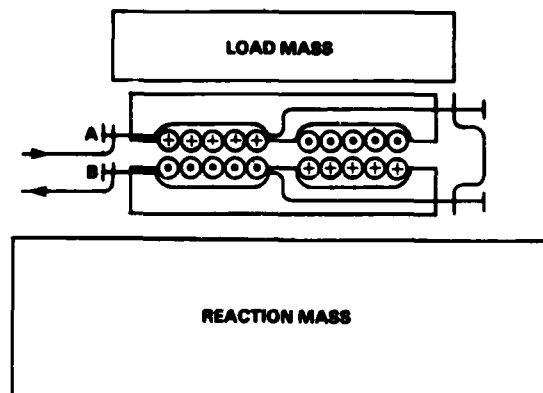


Figure 1. Shock-generation concept: repulsive coil-pairs.

* Paper presented at the 51st Shock & Vibration Symposium, 20-24 Oct 80, San Diego and at 2nd Electromagnetic Guns & Launchers Conf., 4-6 Nov 80, San Diego, CA.

in series opposition. When a pulsed current is made to flow into connector A and around the spiral paths of both top and bottom coils to connector B, a large repulsive force is developed between the pair. It is repulsive because the current has been made to flow oppositely in the nearly-touching circular pancakes (+ refers to current flow into the plane of the paper and to flow out). The driving energy is supplied by the electrostatic energy stored in a capacitor bank, C, shown in Figure 2. When S1 is closed the bank rapidly pulse-discharges into the driving-coil pair. L_A and L_B are the self-inductances respectively of top and bottom coils. The coils are also mutually coupled as measured by the electrical coupling coefficient K. The total resistance of the coil-pair circuit, R, is kept small to achieve high energy transfer efficiency to the inductive pair. As a result the inductive-capacitive circuit current is slowly-damped and oscillatory. The crowbar switch S2 is commanded to close when the current in the coil-pair reaches its first maximum, thus producing a single output shock pulse by trapping, in the coil-pair, most of the originally-stored capacitive energy. The top profile in Figure 3 shows the single output shock pulse predicted for EDESS-1 by the NET-2 code under these conditions. If S2 is commanded to close later, on the second maximum of current, then the double-peaked shock pulse shown in the middle curve of Figure 3 results. The lower curve is obtained when S2 is not closed and the original energy in the capacitor bank rings back and forth between the capacitor bank and driving coils, producing a multiple-peaked shock output.

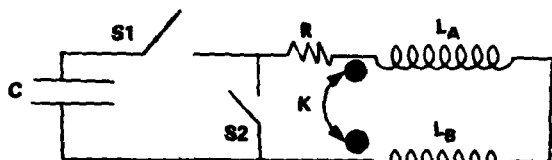


Figure 2. Shock-generator electrical equivalent circuit.

The design of a generator to produce a single shock-pulse of desired duration and shock level is particularly straightforward. It is achieved for a given capacitor bank by a suitable choice of driving-coil inductance in the resulting simple inductive-capacitive electrical circuit. Because shipboard and submarine equipment is generally heavy, their centers of mass often are not displaced significantly during the duration of the shock pulse. Under this condition the choice of coil-pair inductance can be based on the simple ringing frequency formula for an underdamped RLC circuit, namely $f = 1/2\pi\sqrt{LC}$. The single shock-pulse duration, T, is then given approximately by $1/f$ or by,

$$T = 2\pi\sqrt{LC} \quad (1)$$

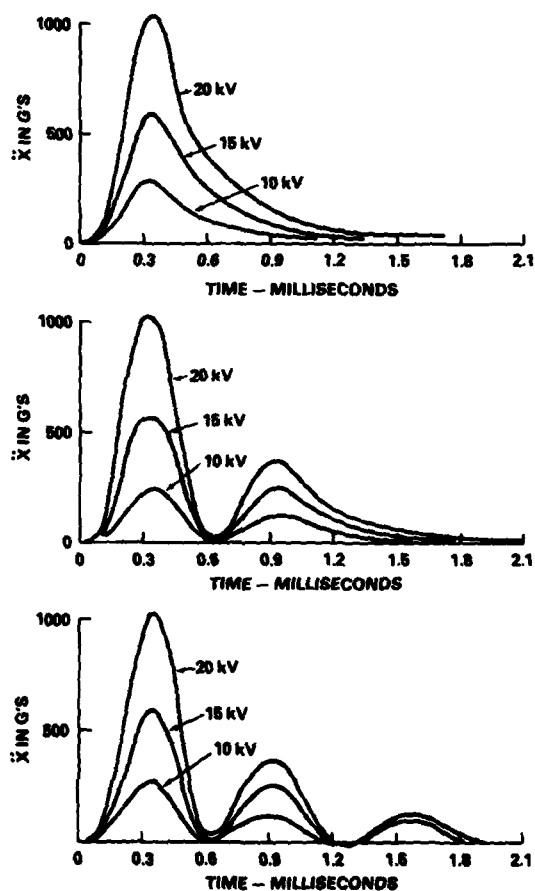


Figure 3. Predicted shock profiles for EDESS-1

The shock pulse risetime is furthermore roughly $T/4$ as verified by subsequent computer calculations. Formula (1) represents the single output shock-pulse width that is produced by the shock generator because once the crowbar, S2, in Figure 2 is thrown, the pulse width is made up of the sum of the current pulse rise time in the RLC circuit and the current pulse decay time in the resulting RL circuit. The pulse risetime is $\sim T/4$ and the decay time is $\sim L/R$ where L is the coil-pair inductance and R is the coil-pair resistance. The decay time for the range of practical coil-pair designs considered was found to equal $\sim 3T/4$ hence the single pulse width is just $T/4 + 3T/4$ or approximately T given by formula (1). When $L = 54\mu H$ and $C = 600\mu F$, evaluation of formula (1) gives $T = 1.13 \times 10^{-3}$ seconds which compares favorably with the complete coupled differential-equations result shown in Figure 3 (top). The above single-pulse formula is coincidentally identical to the expression for the period of oscillation of the current in an LC circuit during which two shock pulses would be produced if no crowbar (S2 in Figure 2) were used at the first current peak.

This situation does indeed transpire when no crowbar is used, for example as shown in Figure 3 (bottom), where two shock pulses are produced in approximately 1.2×10^{-3} seconds, or $\sim T$ as calculated above. Two shock pulses are produced because no crowbar was used and because the output force is in the same direction regardless of the direction of current flow through the coil-pair which is connected in series opposition.

The above inductance, L , is the total circuit inductance which is dominated by the inductance of the coil-pair at launch i.e. before the two coils have separated due to the repulsive force acting between them. As the pancake coils separate this inductance increases until a maximum is reached at a coil separation of about one coil diameter. This spatial inductance variation can be expressed in terms of the separate self-inductances of each pancake coil, L_A and L_B and the electrical coupling coefficient, K , between the coils, or equivalently, in terms of the mutual inductance, M , as follows:

$$L = L_A + L_B - 2K\sqrt{L_A L_B} = L_A + L_B - 2M. \quad (2)$$

For pancake coils, M varies almost exponentially with plate separation, x . For example, the measured total coil-pair inductance for EDESS-1 is shown in Figure 4. Thus the mutual inductance can be expressed as,

$$M = M_0 e^{-x/\alpha}, \quad (3)$$

where M_0 and α are constants for a given coil-pair.

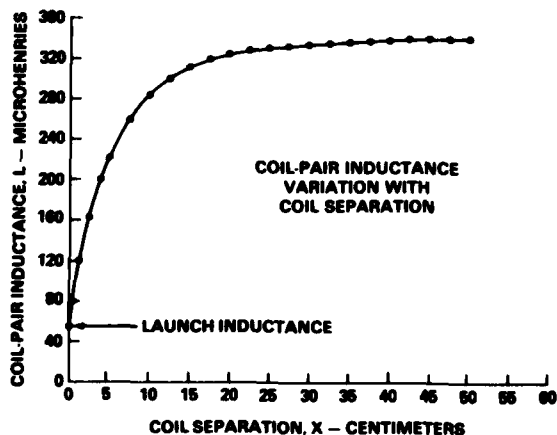


Figure 4. EDESS-1 coil-pair inductance.

To achieve a given shock level, expressions (2) and (3) are important because they allow the governing shock equation to be derived. The instantaneous force, F , exerted by the coil-pair on the payload (and on the reaction mass) is given by,

$$F = -\frac{\partial}{\partial x} (1/2 LI^2) = -\frac{I^2}{2} \frac{\partial L}{\partial x} = LI \frac{\partial I}{\partial x}, \quad (4)$$

where I is the instantaneous current flowing in the coil-pair and $\frac{\partial I}{\partial x}$ is the local spatial derivative of the plate separation. The second term in equation (4) can be expressed as

$\partial I / \partial x = (\partial I / \partial L) (\partial L / \partial x)$ and $\partial I / \partial L$ can be shown to be very nearly equal to $-I/L$. Using equation (2) in (4) and evaluating the derivative, the instantaneous driving force takes on the form,

$$F = -I^2 \frac{\partial M}{\partial x}. \quad (5)$$

This force, F , is distributed uniformly over the area of the coil-face, thus offering the possibility of easy alignment between the applied force-center and payload mass-center, a problem sometimes not easily avoided with conventional shock machines. The mechanical equation of motion for the instantaneous shock, \ddot{x} , exerted during vertical boost on a payload of mass m in a 1.0-g downward gravitational field, thus becomes,

$$\ddot{x} = \frac{I^2 K_0 L_a}{m} e^{-x/\alpha} - g. \quad (6)$$

K_0 is the coupling coefficient between the coil-pairs when the coil-pair separation, x , equals its minimum, i.e. when the coil pairs are resting on top of one another. L_a is the separate self-inductance of one of the two identical pancake coils. Since the instantaneous electrical current in an underdamped RLC circuit has the simple analytic form,

$$I(t) = \frac{V}{2\pi fL} e^{-\frac{rt}{2L}} \sin(2\pi ft), \quad (7)$$

the peak shock level for a generator can be estimated quickly by a hand calculation. The peak instantaneous current occurs when $t \sim T/4$, and can be calculated from equation (7). Hence equation (6) can be used to estimate the peak g-force level that can be applied to the payload from the given generator under consideration. The NET-2 computer code was adapted to handle the complete problem namely that of the coupled electrical and mechanical equations of motion describing the rigid payload model of the generator. The results given by equations (1), (6) and (7) embody the essence of the design concept and were generally confirmed by the NET-2 code results. Of course the NET-2 code, in addition to predicting shock-pulse risetime and peak shock level, also calculated the instantaneous payload acceleration, velocity and position, and the overall conversion efficiency under a range of conditions including appreciable center of mass motion. The code describing the rigid payload model was used extensively in the design of EDESS-1 and 2.

EDESS-1 SHOCK GENERATOR

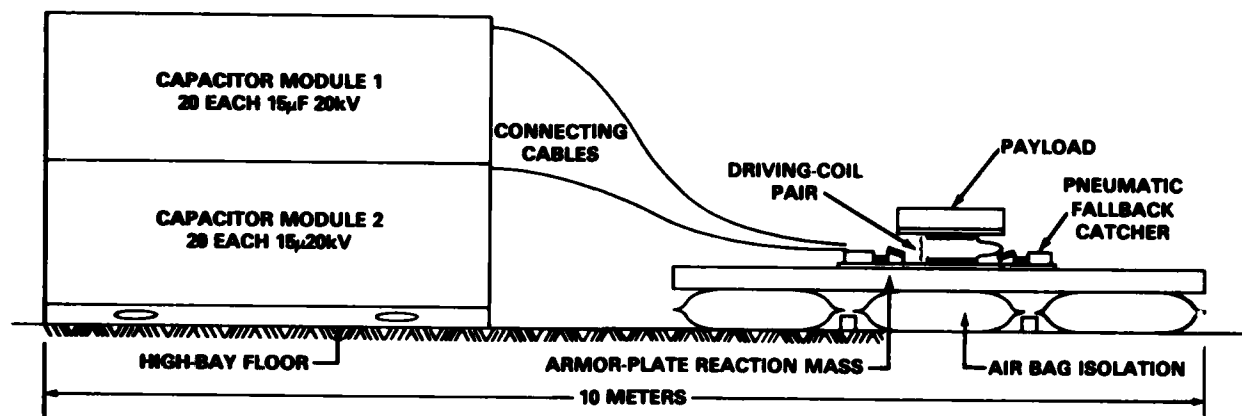


Figure 5. The EDESS-1 generator

EDESS-1 System Description

The EDESS-1 generator is shown in Figure 5. It consists of two capacitor modules, a set of capacitor-to-driving-coil connecting cables, one pair of 380 mm diameter driving coils, a pneumatically-actuated fallback catcher and a 13.3 metric ton reaction mass. The complete generator including power supply and controls occupies a floor area of 6 x 10 meters. The reaction mass is air-floated to shock isolate the driving coils from the concrete laboratory floor. Each of the capacitor modules contain twenty 15 μ F, 20 kV, MLI 33280 capacitors each being capable of pulse-discharge and oscillatory service with high energy-density storage (70 kJ/m³). The capacitor modules also contain eighty GE GL-37248 ignitrons which serve as triggered switches: forty to discharge the capacitors (functioning as S1 of Figure 2) and forty as electronic crowbars (functioning as S2 of Figure 2) to trap the energy in the driving-coil pair. The capacitors in the bank are connected in parallel by means of separate low-inductance coaxial cables, one per capacitor, to a common connector block located close to the driving coils. Two flexible welding cables each about two meters long complete the circuit from connector block to driving coils (points A and B of Figure 1). For the driving coil tests, payload ballast was readily available in the form of naval armor plate, however the effects of ballast fallback could easily invalidate the tests. A simple pneumatic-actuated catcher for the armor plate was built which consists of two steel bars each about one meter long that are top-padded with 10 mm thick polyurethane. Before launch the weight of the payload ballast rests completely on the two driving coils and the reaction mass. When the bank is discharged

the coils repel, the ballast is driven inward between the ballast and reaction mass, thus preventing fallback on the coils.

The heart of the EDESS-1 system is the driving coil pair. The first experimental driving coil design was based on an electrical scale-up of a proof-of-principle model [4] and on the desired output shock-risetime of 300 μ s. The required self-inductance of the coil-pair at launch was then established and several spiral coils of different diameters ranging from 150 to 910 mm were evaluated. Mechanical strength and integrity were predominant considerations in view of the 200-g, 2.0 ms shocks that were desired. These factors resulted in the first coil (Figure 6) being a 380 mm diameter pancake consisting of 37.25 turns of #6AWG formvar-coated copper coil-wire wound in a single layer. The coil was hand-wound into a 410 mm square coil form of G-10 fiberglass-resin, 25.4 mm thick and then epoxied in place using Epon-815.

The self-inductance of a single coil was calculated using Grover's inductance formula [5] for a radially-thick coils,

$$L_A = 0.00254 N^2 a P \quad (8)$$

The calculated inductance was then verified by measurement after the coils were fabricated. The factor P is about 16 for the coils here and is the product of two factors. The first applies to a coil of zero axial dimensions and is a function of the radial proportions of the coil cross-section. The second accounts for the reduction in inductance due to separating the turns in the axial direction. The number of spiral turns, N, which enters quadratically and the mean radius, a, in inches when multi-

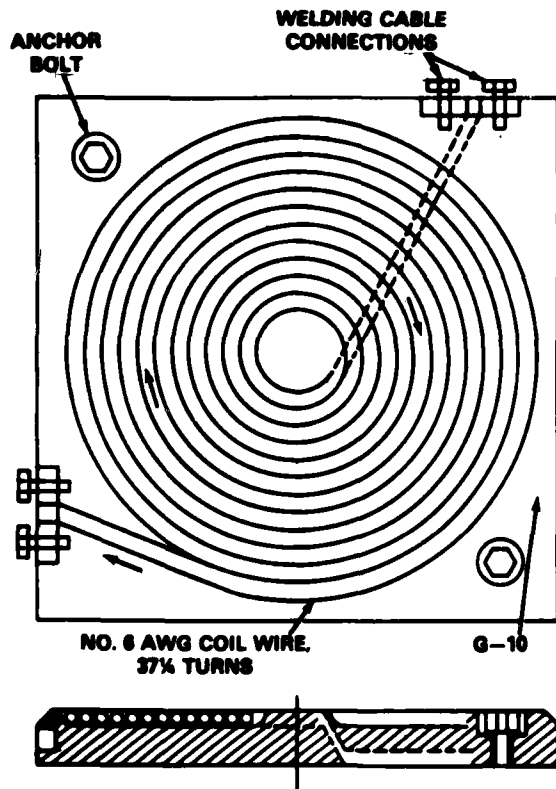


Figure 6. The EDESS-1 driving coil pair.

plied times P , give the self-inductance, L_A , in microhenries. For a single EDESS-1 coil, L_A was calculated to be $238 \mu\text{H}$ using equation (8) and subsequently measured to be $235 \mu\text{H}$ after fabrication. For the coil-pair the total inductance at launch was measured to be $54 \mu\text{H}$ with a total resistance including the welding cables of $76 \text{ m}\Omega$. The coils thus have a mutual inductance of $208 \mu\text{H}$ and an electrical coupling coefficient of $K = 0.89$ at launch.

OPERATIONAL RESULTS

The performance of EDESS-1 and of the originally designed coil-pair has been surprisingly close to optimistic expectations. The first driving coil-pair in which the turns were epoxied into a coil form remains operational after 80 test firings although considerable surface cracking of the mating front faces of the coils has occurred. The primary cause for this cracking is believed to be mechanical fly-back of the copper coil wire which releases deformation energy which is stored while the shock pulse is being delivered to the payload. A second contributor to the cracking was the lack of anchoring of either coil of the pair to the ballast or reaction mass during the early tests. High-speed photography of the unanchored coil pair showed violent motions of each coil after

the boost was completed. The second problem revealed in the tests was that the soft-solder connections to the coils exploded on several occasions. This problem was readily solved by using silver-soldered, bolted connections to the welding cables. A second coil was fabricated using a polyurethane impregnant, Conap EN-7, to avoid the surface cracking problem and to employ a new coil-winding technique to avoid the time-consuming hand-winding used previously. This second coil-pair has performed well without problem for 20 test firings.

The typical output shock response produced by EDESS-1 on armor plate payloads is shown in Figure 7. This response was measured with an Endevco #2262-2000 accelerometer mounted in the center of the 1.0 metric ton, 152 mm thick, 914 mm square armor plate by the 380 mm diameter driving pair. The velocity and displacement curves (middle and lower of Figure 7) were obtained electronically by taking the first and second integrals of the accelerometer output. New rack-mounted electronics [6] was designed specifically for this purpose. This data shows that the thick armor plate is responding with drumhead-like vibrational bending, upward center-of-mass motion and to a lesser extent, by internal stress-wave reflections within the thickness of the plate. Analysis of data like the above indicates that the total energy imparted by EDESS-1 to the plate is partitioned 40% to vibrational bending, 50% to center-of-mass motion and 10% or less to internal shock waves. Vibrational energy is large because the driving coil diameter is only about one-third the width of the ballast weight. Subtracting the vibrational and internal wave energy, center-of-mass shock levels of 300 G's (peak) for the 1.0 metric ton plate and 150 G's (peak) for the 2.0 metric ton load are indicated. The shock pulse duration applied to the center-of-mass based on the smoothed instantaneous velocity profile is less than 4 ms with the indicated risetime being consistent with the intended design value of 300 μs . By varying the capacitor bank charging voltage the peak center of mass displacement can be varied. These results are shown in Figure 8. Fluctuations in these heights are caused by the large vibrational component in the plate responses. Center-of-mass throw heights of 250 mm were observed at the maximum capacitor bank charging voltage of 20 kV with the 1.0 metric ton payload. The output shock-pulse capability and the electrical parameters for EDESS-1 are summarized in Table I.

The center-of-mass shock levels as indicated in Table I from accelerometer measurements fall within a factor of 2 of the original computer-aided predictions which do not take into account the multi-component dynamic response of the armor plate. Four coil-pairs, identical to the one-pair used on EDESS-1, will be built and tested in the future on EDESS-2. These four coil-pairs can be placed to cover the entire 0.81 m^2 area of the armor plate with an

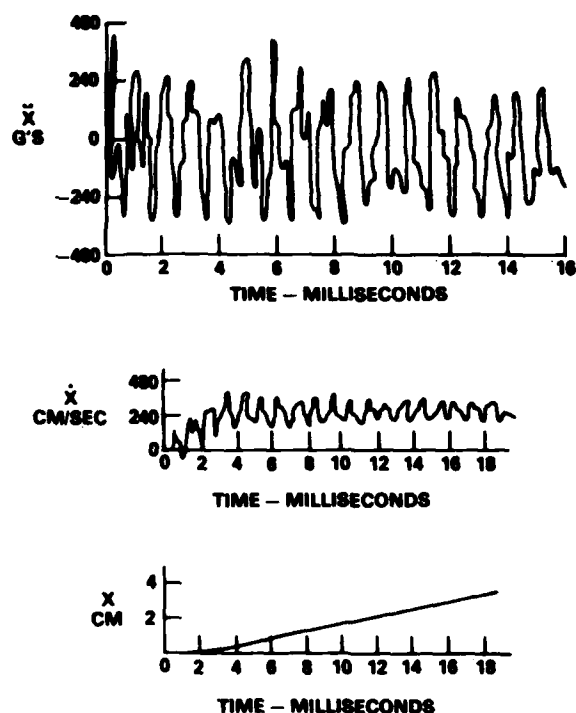


Figure 7. Shock response of a 1.0 metric ton armor plate to a 18.8 kV EDESS-1 pulse.

almost uniformly distributed force. Consequently the vibrational component should be significantly reduced. Also several obvious refinements in the computer model of EDESS-1 will further improve its predictive accuracy. These refinements include introduction of electrical resistance into the capacitor bank equivalent circuit which was not previously included, the use of measured rather than extrapolated values for the mutual inductance curve of the coils and accounting for the effects of the finite-sized reaction mass.

Table I. EDESS-1 Shock-Pulse Capability & Parameters

Shock pulse (peak)	150 g's
Payload mass	2000 kg
Shock duration (base width)	<4 ms
Shock pulse risetime	300 μ s
Payload velocity change (max)	1.3 m/s
Payload displacement (max)	80 mm
Capacitor bank: 40 ea 15 μ F@ 20 kV	120 kJ
Driving coils: 380 mm dia 2 ea	54 μ H

FUTURE EFFORT

Effort is now underway to assemble EDESS-2 which will have a 5 metric ton payload capability. The top and side views of the driving platform are shown in Figure 9. Generally the system will look very similar to EDESS-1. The number of capacitor modules (not shown) will be doubled to store 240 kJ although a tripling in size would have been desirable. Additional

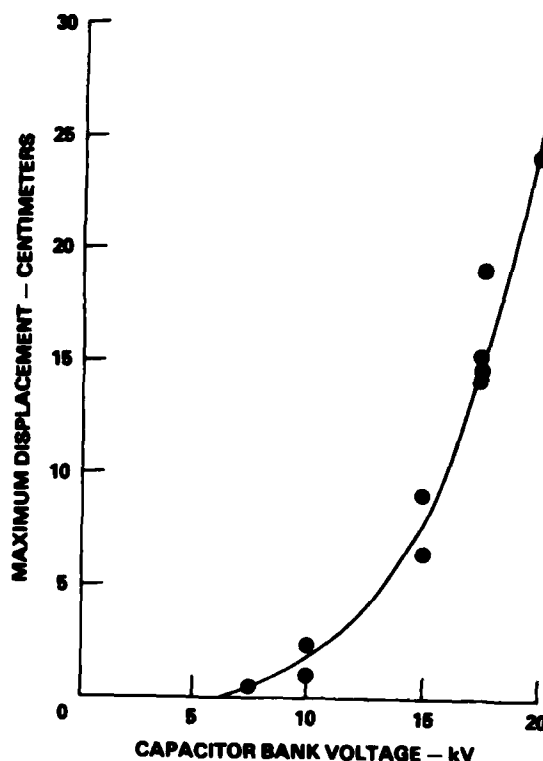


Figure 8. Maximum displacement of a 1.0 metric ton armor plate versus voltage on EDESS-1.

capacitor banks are available but competition for their use is keen. The reaction mass will be tripled to around 30 metric tons and the number of 380 mm diameter driving pairs, which were used successfully on EDESS-1, will be increased to 4. The four-pair shock platform and fall back catcher is shown in Figure 10. Computer-aided analysis shows that extending the number of driving pairs to 4 will keep the overall energy transfer efficiency nearly the same as in EDESS-1. The 4 coil-pair system will also provide some shock-pulse risetime adaptability by allowing coils to be connected in various series/parallel ways. Computer analysis also predicts that a range of shock pulse capabilities are possible. These results are given in Table II. η is the efficiency expressed in percent and defined by the ratio of the center-of-mass kinetic energy to the total stored energy originally in the capacitor banks. Particularly interesting is the prediction in the rightmost column of Table II that a single large 910 mm diameter coil-pair will be more efficient than 380 mm diameter coil-pairs. Consequently a large diameter coil pair has been designed and will be fabricated and tested in our facility.

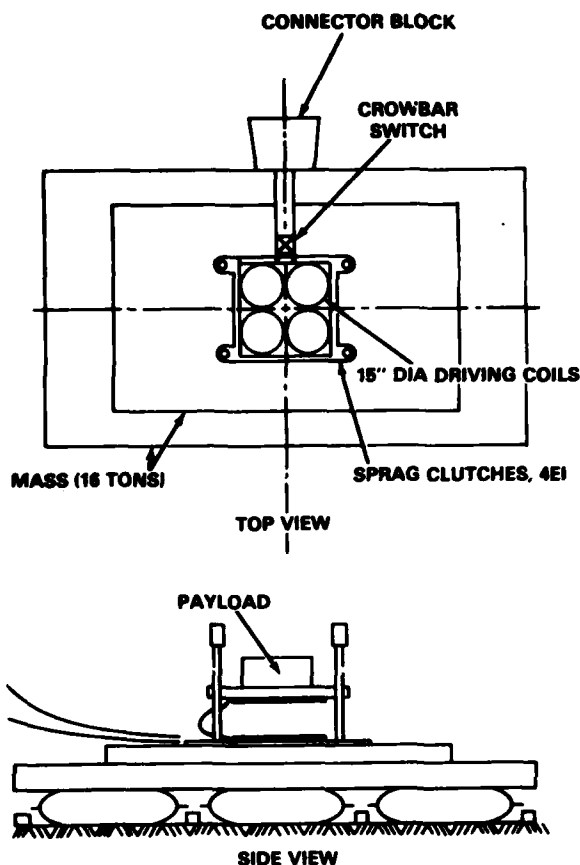


Figure 9. The EDESS-2 generator.

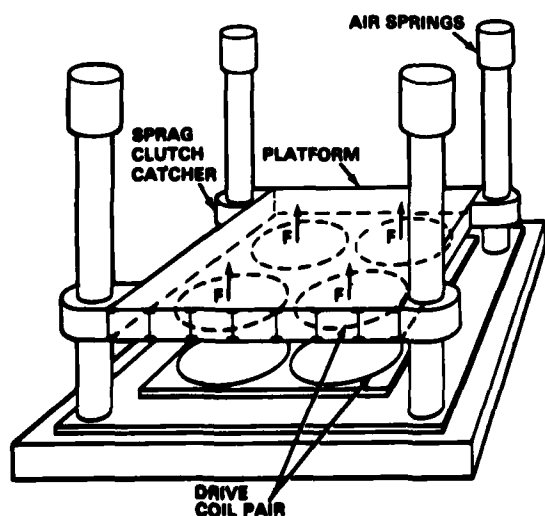


Figure 10. The shock platform for EDESS-2

To extend the payload capability of an electromagnetically-driven shock platform into the 15 to 30 metric ton range requires a departure from the use of capacitor banks as primary energy sources. This is primarily because the capacitor banks required would occupy very large spatial volumes and consequently not be practical for transport. Homopolar generators exhibit high energy-density storage (350 kJ/m^3) and are capable of storing 10 to 20 MJ. Machines like this are being considered as replacements for capacitor banks in EDESS-3 to achieve the larger payload capability. A demonstration experiment to shock-pulse a 15 metric-ton armor-plate payload using Weldon's 5 MJ homopolar generator [7, 8, 9] at the University of Texas is being planned for early next year.

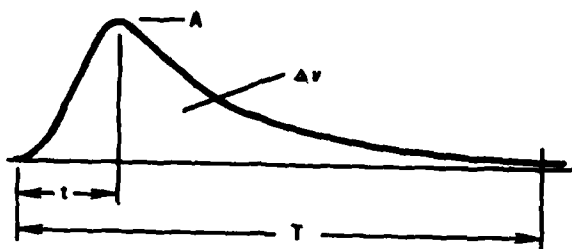
The operating principle of a homopolar generator is illustrated in Figure 11. It consists of a massive, conducting flywheel that is immersed in a uniform magnetic field, ϕ , perpendicular to the plane of the flywheel. After the flywheel is spun-up to a stable angular speed ω , the switch S, in the external circuit is closed, completing the circuit between the wheel rim and shaft through the load. A large decelerating torque is produced, given by,

$$T = -\frac{\phi i_a}{2\pi} \quad (9)$$

where i_a is the large current generated in the external circuit. This decelerating torque results from the circumferential Lorentz force between the current flow in the wheel and the applied magnetic field. Kinetic energy of the rotating flywheel is thus rapidly converted into a single, high-current, low-voltage pulse. All points on the outer circumference of the flywheel have the same polarity potential with respect to points on the shaft hence the name homopolar generator. The entire process can be run in reverse thus creating a homopolar motor by simply supplying motoring current from an external power supply. The load, in Figure 11, for shock generation purposes, becomes the electromagnetically-driven shock platform. An EDESS-3 system is sketched in Figure 12 using the University of Texas homopolar generator as the primary energy store.

Several important mechanical and shock control advantages accrue from this approach. The driving coils of EDESS-1 and 2 can be replaced by simple flat driving plates because the equivalent electrical capacitance of the homopolar generator is so large (5600 farads for the 5 megajoule homopolar). Also the risetime of the output shock profile can be varied easily by simply changing the applied magnetic field across the rotor. That this is true can be readily seen by noting that the voltage developed across the terminals of a homopolar generator is proportional to the applied magnetic field, ϕ . For a constant stored energy in the

TABLE II. Shock pulse capabilities, using electromagnetically-driven platforms with a 360 kJ capacitor bank.



PAYLOAD	2.27 to 13.59 METRIC TONS				0.453 to 4.53 metric tons
COIL	6-PAIR 380 mm DIA SERIES/PARA	8-PAIR 380 mm DIA IN SERIES	16-PAIR 380 mm DIA IN SERIES	16-PAIR 380 mm DIA IN SERIES W/BALLAST	ONE PAIR 910 mm DIA
t (ms)	0.4-0.6	1.2-1.4	2.0	8.0-9.5	1.4-1.6
T (ms)	1.3-1.0	4.0-3.3	7.5-6.0	19.5-16.5	5.0
A (G's)	3000 to 350	400 to 100	300 to 70	33 to 7	1670 to 240
Δv (m/s)	5.33-1.04	4.18-0.85	4.08-0.73	2.19-0.40	8.66-1.71
η %	18.0-4.0	11.0-2.7	10.5-2.0	3.0-0.6	47-11

homopolar of $\frac{1}{2} C_H V^2$, the equivalent homopolar capacitance, C_H , varies as $1/V^2$ and thus as $1/\phi^2$. Since the shock pulse risetime, τ , from equation (1) varies roughly as $T/4$,

$$\tau \sim \sqrt{LC_H} \sim \frac{\sqrt{L}}{\phi} \quad (10)$$

This means that the shock pulse risetime can be controlled by varying ϕ , i.e. the greater ϕ , the sharper the shock onset. This appears to be an important control advantage which has heretofore not been possible on EDESS-1 and 2. Peak shock levels can also be controlled without changing the relative shape of the output shock profile by simply changing the angular speed, ω , to which the homopolar generator is originally spun. These features are currently being studied in the design of the EDESS-3 generator.

CONCLUSIONS

The present experiments with the EDESS-1 prototype clearly demonstrate the feasibility of using electrical pulse-power for generating explosive-like shocks in 1.0 and 2.0 metric ton payloads. The key to obtaining reliable shock performance lies in developing reliable and efficient driving-coil pairs. A considerable range of output shock profiles and payloads appears possible using capacitor banks as primary energy storage devices, as will be tested with EDESS-2. Homopolar-powered systems appear promising for larger payload shock-testing applications where high efficiency, simplicity and compactness are important aspects.

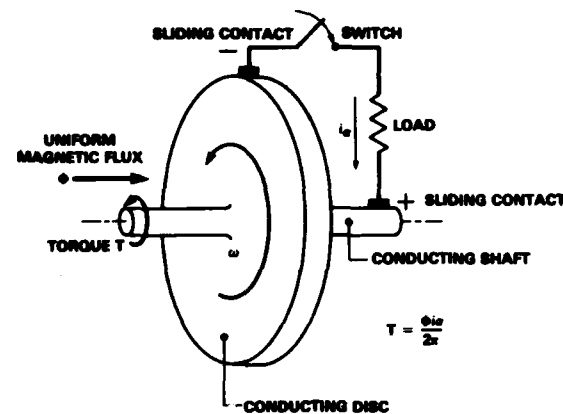


Figure 11. Operating principle of a homopolar generator.

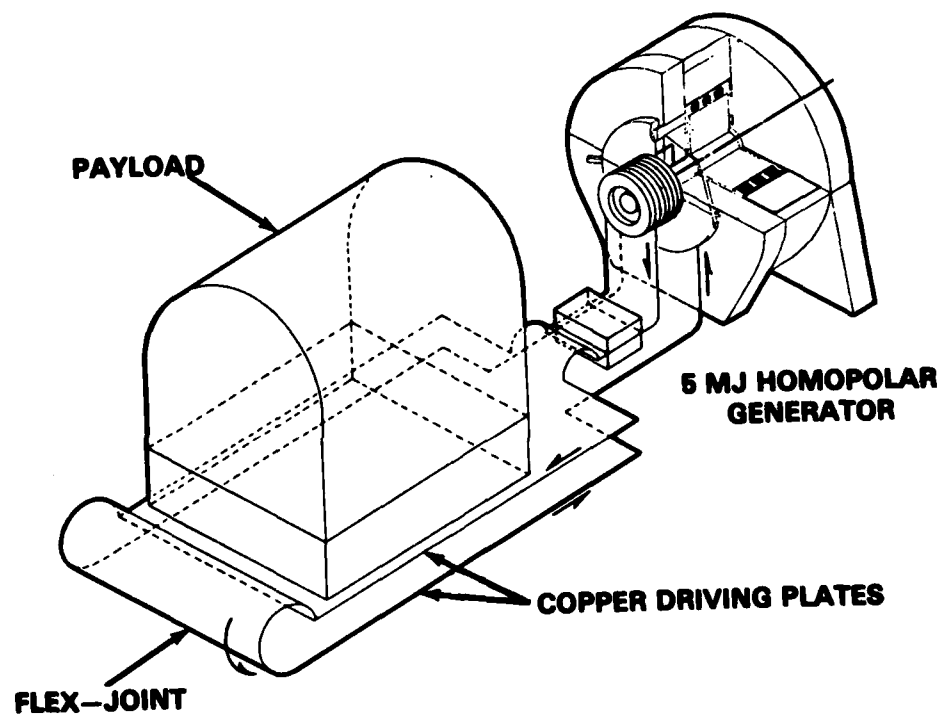


Figure 12. EDISS-3: 15.0 metric ton payloads.

ACKNOWLEDGMENTS

This effort is sponsored by the Naval Surface Weapons Center, the Naval Sea Systems Command, and by the Defense Nuclear Agency. Without the direct help of Dr. T. R. McKnight, Mr. J. R. Sullivan and CDR T. Deevy, USN, respectively from these agencies this program would not be possible. The authors wish to thank Mr. V. F. DeVost for his valuable catalytic effect and for his continued advice and encouragement; Dr. W. F. Weldon for suggesting the use of spiral pancake coils; Mr. V. L. Kenyon, III, Mr. E. K. Pritchard, Dr. E. E. Nolting, and Mr. R. A. Smith for many practical ideas and suggestions; and the research technicians whose assistance was invaluable: Mr. M. Ruppalt, Mr. W. Spicer, Ms. J. Via, Mr. J. King, Ms. G. Glowacki and Mr. P. Jilinski.

REFERENCES

1. Clements, E.W., "Shipboard Shock and Navy Devices for Its Simulation", Naval Research Laboratory Report 7396, July 1972.
2. DeVost, V. F., "WOX-7B Shock Testor", Naval Ordnance Laboratory Technical Report 70-196, September 1970; DeVost, V. F., "VHG Impact Test Set", Naval Ordnance Laboratory Technical Report 68-158, September 1968;; DeVost, V. F., "WOX-7A (Subroc Shipboard Shock Tests)", Naval Ordnance Laboratory Technical Report 65-210 CONF, December 1965.
3. "The Floating Shock Platform for Shock Testing Equipment up to 30,000 Pounds", Report 7-61, Underwater Explosions Research Division, David Taylor Model Basin, Portsmouth, Virginia, May 1961.
4. Sazama, F. J., and Nolting, E. E., "Scale Model of a New Concept Magnetically-Driven Shock Simulator", Naval Surface Weapons Center Technical Report (in press).
5. Grover, F. W., Inductance Calculations, Working Formulas and Tables, Dover Publications, 1946 page 105.
6. Pritchard, E. K., Ruppalt, M. H., and Via, J., Naval Surface Weapons Center Technical Note (in press).
7. Weldon, W. F., Rylander, H. G., and Woodson, H. H., "Homopolar Generator Development at the University of Texas", Proceedings of the Australian-United States Seminar on Energy Storage, Compression and Switching, 15-21 November 1977, page 86.
8. Gully, J. H. et al., "Rebuilding the Five Megajoule Homopolar Machine at the University of Texas", Proceedings of the IEEE International Conference on Pulse-Power, Lubbock, Texas 12-14 July 1979.
9. Weldon, W. F., et al, "The Design of Homopolar Motor-Generators for Pulsed-Power Applications", 6th Symposium on Engineering Problems of Fusion Research, San Diego, California, 18-21 November 1975.

DISCUSSION

Mr. Misovec (Weidlinger Associates):
Could you comment on the control you might have over pulse shape?

Mr. Sazama: We will explore that in the EDESS 2 generator. There the major control can be achieved by placing the driving coils in series or in parallel and that is the easy alternative. The other alternative is to design other coil-pair sets that have different resonant frequencies for a particular shock application. That would be the direct way of doing it. Another possible alternative with the capacitively driven system is to change the capacitance of the driving bank; and of course you can always vary the charge voltage on the capacitor bank to vary the level. We have not run extensive tests on the adaptability of the system but we have run computer studies which show us that the range of possibilities is very promising.

Mr. Wise (Watts, Inc.): Can you improve the rise time and is it possible to conceive of an anvil in a water tight package so you can simulate a shock wave in the water?

Mr. Sazama: We have thought of that. Mr. DeVost has sketched a concept of generating underwater shocks using this as the driver. As far as improving the rise time, in the capacitively driven system it is very easy to go to a very fast pulse. In fact, we could go down to microseconds as Sandia can testify. The flyer plate technology is a hundred to maybe fifty microseconds in response so it is very easy to go to a faster pulse. We have problems in the capacitively driven system with the opposite, which is to go to a five or a ten millisecond problem. We can easily go to very fast pulses. Very fast pulses are not of interest for our purposes because we are interested in the big payload capabilities but we can usually do that.

ANALYSIS OF ENERGY-ABSORBING SHOCK MOUNTS

V. H. Neubert
The Pennsylvania State University
University Park, PA 16802

The behavior of nonlinear energy-absorbing shock mounts or shock snubbers was measured in a standard test machine and in a drop table shock machine. Configurations tested were an aluminum honeycomb and low carbon steel end-loaded tubes, side-loaded tubes and double reverse corrugated metal.

Some configurations deform by buckling, with associated positive and negative stiffnesses, while others yield without buckling and exhibit primarily positive stiffness. Analysis was carried out, guided by the experimental results, of energy-absorbing mounts in series and in parallel with linear mounts. The mechanical fuse effect of the energy-absorbing mounts is demonstrated in the series arrangement. In the parallel arrangement the energy-absorbing mount helps reduce deflection.

INTRODUCTION

The present paper summarizes material presented in references [1] and [2].

The problem considered is the protection of equipment during ground shock through the use of energy-absorbing shock mounts. A one-degree-of-freedom representation of one system is shown in Figure 1. The machine or equipment to be protected is represented by the mass. Sometimes there is a vibration mounting for small amplitudes, possibly representable by the linear spring and dashpot. For large amplitude shock, the shock mount, or snubber, is depicted here as $L(t)$, which here is taken as a nonlinear, energy-absorbing component. This nonlinear shock mount is the subject of the present study.

The free-body diagram in Figure 1(b) emphasizes the forces that act on the body during a specified ground motion y_0 . A primary goal is to limit the maximum absolute acceleration y felt by the mass; an equivalent goal is to limit the maximum resultant force acting on the mass.

An alternate arrangement is shown in Figure 2(a) where the energy-absorbing mount $L(t)$ is in series with the linear mount. Here the force acting on the mass is always the same as that transmitted by the mount $L(t)$, and the mount could be designed to act as a mechanical fuse so the force transmitted would never exceed a certain value.

Several configurations were studied to de-

termine load-deformation behavior taking into account deformation rate where applicable. The configurations are: aluminum honeycomb, axially-loaded tubing, a double reverse corrugated metal (DRCM), and side-loaded tubes, with more emphasis on the last two. At the beginning it was decided that, for practical purposes, the thickness and stroke of the mounts should be less than 3 inches.*

The aluminum honeycomb and axially-loaded tubing were tested in only one direction. Initially they behave elastically, but for higher loads they deform by plastic buckling with the load-deformation curve showing regions of alternately positive and negative stiffness. The honeycomb behaves in a similar manner. The unconstrained DRCM and the side-loaded tubing yield without buckling and present a smoother load-deformation curve. While the DRCM is loaded in only one direction, mounts made of side-loaded tubing were loaded in three orthogonal directions. In addition, the side-loaded tubing may be straightened for re-use, and load vs. deformation curves are presented for straightening tubes with various initial deformations.

Data for a set of elastic Aeroflex Corporation twisted wire cable mounts is presented for comparison.

Finally, results of analysis are presented in which the attenuations provided by several mount combinations are compared. As expected, *See Table 6 for conversion to SI Units.

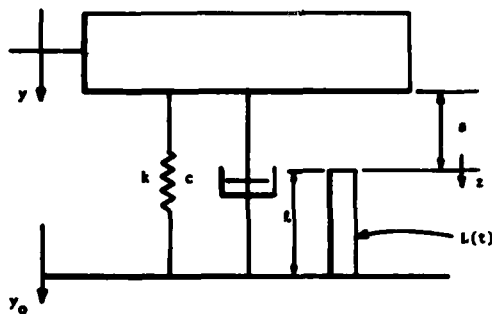


Figure 1(a). Parallel shock mount system.

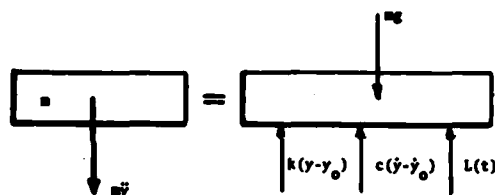


Figure 1(b). Inertia force and free-body diagrams for Figure 1(a).

reducing acceleration by using a soft mounting system results in larger deflections, but predicted deflections are less than the specified stroke of the mount.

MATERIAL BEHAVIOR AND RATE EFFECTS

The important material properties are elasticity, yield stress, ductility, rate sensitivity, post-yield stiffness, and ultimate strength.

The metals of interest are steel and aluminum. The strain rates are associated with gross structural motions of equipment on their foundations and range up to about 30/sec. The elastic modulus is practically insensitive to such loading rates. A primary effect of rate is the increase in yield strength. Hecker [4], in Reference [3], recently summarized experimental studies of yield phenomena in biaxially loaded metals, giving 277 references. Lindholm [5] reviewed methods for conducting tests over the range of strain rates. Structural steel is typically very strain rate sensitive, while

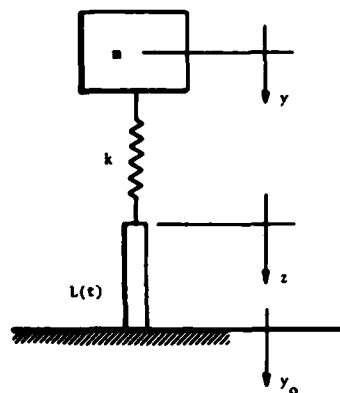


Figure 2(a). Series shock mount system.

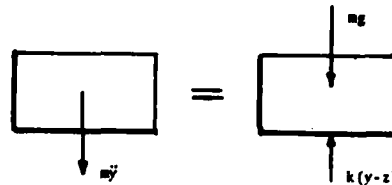


Figure 2(b). Inertia force and free-body diagrams for Figure 2(a).

aluminum is much less so. The dependence of the dynamic lower yield stress $\sigma(\dot{\epsilon})$ on the plastic strain rate $\dot{\epsilon}$, for strain rates up to 1000/sec, was represented by Cowper and Symonds [6] as the following empirical expression,

$$\frac{\sigma(\dot{\epsilon})}{\sigma_0} = 1 + \left(\frac{\dot{\epsilon}}{D}\right)^{\frac{1}{p}} \quad (1)$$

where σ_0 is the static yield stress, D and p are material constants and p may be taken as an integer. The values $D = 40/\text{sec}$ and $p = 5$ were deduced from data from tension impact tests of steel of Manjoine [7]. For aluminum [8] the values were in the range of $D = 6500/\text{sec}$ and $p = 4$. Belshheim [9] discussed dynamic yield stress as related to strain rate and Vigness [10] summarized data relating dynamic yield to "delayed-yield time." The time delay between applied dynamic stress and resulting strain is another important effect which is accounted for to some extent in the constitutive equation

proposed by Malvern [11].

$$\dot{\epsilon} = \frac{\dot{\sigma}}{E} + K(\sigma - \sigma_{st})^{\frac{1}{n}} \quad (2)$$

Here ϵ and σ are functions of time, E is Young's modulus, σ_{st} is the static stress for the same strain, and K and n are material parameters. Cristescu [12] and others have discussed more general forms of constitutive equations.

Plass [14] developed a constitutive equation for beam bending by assuming plane sections remain plane after bending and integrating (2) over the beam cross-section, with the result

$$\dot{k} = \frac{\dot{M}}{EI} + R(M - M_{st})^{\frac{1}{n}} \quad (3)$$

Here \dot{k} is curvature rate, M is dynamic moment, EI is bending stiffness, and M_{st} is moment obtained from the static moment-curvature curve.

Some surveys and extended reference lists related to dynamic plastic behavior of structures are given in references [33] thru [44].

The type of law in equation (1) applies best to perfectly plastic materials since it relates only to increased yield stress. Perrone [13] suggested a flow law in Equation (4) which accounts for the strain hardening aspects as well as increased yield:

$$\frac{\sigma}{\sigma_0} = [1 + (\frac{\dot{\epsilon}}{D})^{\frac{1}{n}}] [1 + c\epsilon] \quad (4)$$

$$c = f(\dot{\epsilon}) \quad (5)$$

If the strain hardening is a function of strain rate, then equation (6) could be used with (5). For the present study, equation (5) was used for fitting curves to dynamic stress-strain data, with c a constant. However, in predicting timewise behavior for beams or other structures an equation of the form of (2) has also been used [1].

TESTING AND INSTRUMENTATION

The tests were performed on a Tinius-Olsen test machine and on a drop table shock test machine.

The Tinius-Olsen is a controlled deformation machine on which specimens were tested at a constant deformation rate. Load versus deformation is read out on an x-y plotter.

The drop table shock machine is an IMPAC 1818 from Monterey Research Laboratory, Inc., now part of MTS Systems Corp. The elastomer programmer used produces approximately a half-sine acceleration pulse at the table. In Figure 3, an arrangement is shown of a simulated

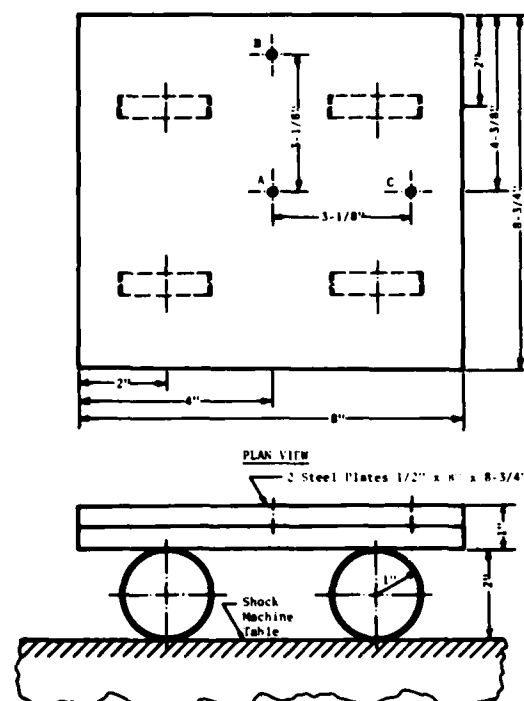


Figure 3. Simulated machine-snubber configuration using steel plates and side-loaded rings.

machine and shock mount on the shock machine table. Here the machine is represented by two rigidly connected steel plates and the four side-loaded rings are the shock mounts. Accelerometers were located on the shock machine table, to measure \ddot{y}_0 , and at locations A, B, and C on the top of the plate, to sense \ddot{y} as well as rigid body rotation about two axes.

The displacements y and y_0 were obtained by integrating the accelerations twice. The deformation of the nonlinear mounts is then $y_r = y - y_0$.

CONFIGURATION CHARACTERISTICS

Aluminum Honeycomb

Honeycomb has received considerable attention as an energy-absorbing, cushioning material for protection during air drops of equipment, moon landing of space craft and for many other applications. An excellent tutorial paper on cushioning for aerial delivery was given by Thompson and Ripperger [15].

The materials which have been tested most are paper and aluminum honeycombs. For air drops, the ideal load-deformation curve is flat. One measure of the efficiency for energy absorption is

$$\text{Efficiency} = \frac{U}{\sigma_m d} \times 100\% \quad (6)$$

where U = area under stress-deformation curve, σ_m = maximum stress and d is maximum deformation. Thus a rectangular stress-deformation curve would represent the ideal efficiency of 100%. Paper honeycomb has a nearly ideal stress-strain curve up to about 70% strain, above which it stiffens as it begins to bottom out.

Aluminum honeycomb stress-strain curves typically show an initial sharp stress peak, called the compressive strength, at which buckling begins. As the strain increases further, the stress drops to a nearly constant level, called the crush strength, which is usually 65 to 70 percent of the compressive strength. Data sheets are available which list compressive strength, crush strength, shear strength in two directions, and beam shear modulus. A typical aluminum honeycomb may be specified as 3.7 - 3/8 - .0025 which means successively: density in pounds/ft.³, cell size in inches, and metal gage in inches.

With regard to analysis, McFarland [16] discussed two possible modes of failure for honeycomb, a crushing mode and a gross shear failure mode. For the crushing mode the energy U_c and force F_c are

$$U_c = \frac{D \sigma_o t^2}{4} \left(2.057 + 12.396 \frac{P_w}{D} \right) \quad (7)$$

$$F_c = \frac{D \sigma_o t^2}{P_w S^2} \left(4.750 + 28.628 \frac{P_w}{D} \right) \quad (8)$$

where

t = cell wall thickness
 S = cell minor diameter
 $D = [S/3]^{1/2}$ = width of cell wall
 P_w = width of basic panel element
 $(D/4 \leq P_w \leq D/2)$

The deformation occurs in an accordian-like pattern, with P_w the length of one pleat, measured along the slope, from peak to valley. For shear deformation, using q_o as yield stress for shear,

$$U_s = 0.433 q_o t D P_w \quad (9)$$

$$F_s = \frac{1.155 q_o t}{S} \quad (10)$$

The total energy U and total force F are

$$\begin{aligned} U &= U_c + U_s \\ F &= F_c + F_s \end{aligned} \quad (11)$$

In addition it is noted in [16] that if the ratio $t/S > 0.004$, the gross shear mode failure will occur, rather than the crushing mode. This is undesirable since the energy absorption in the shear mode is less than in the crushing mode for the same t/S ratio.

As part of the present investigation, experiments were performed on aluminum 5052 alloy honeycomb donated by American Cyanamid Corporation. The honeycomb was military grade, density 3.7 lb./ft.³, 3/8" core, 0.0025 metal gage, and 5/8" deep. The crush strength is published as 290 psi and compressive strength as 200 psi. A quasi-static load-deformation curve from the Tinius-Olsen machine of a 2" x 2" specimen is shown in Figure 4. There were thirty complete cells. A photograph of a typical deformed specimen is shown in Figure 5(d). The inner cells deformed by the formation of successive pleats, much as the axially crushed tube shown in Figure 5(c). Three pleats can be seen in Figure 5(d). The outer walls buckle in a mode involving the total depth of the specimen. The initial peak or crush strength is higher than 4 in² x 290 psi expected from the advertised value but the advertised compressive strength of 4 in² x 200 psi is close to the average after the first peak.

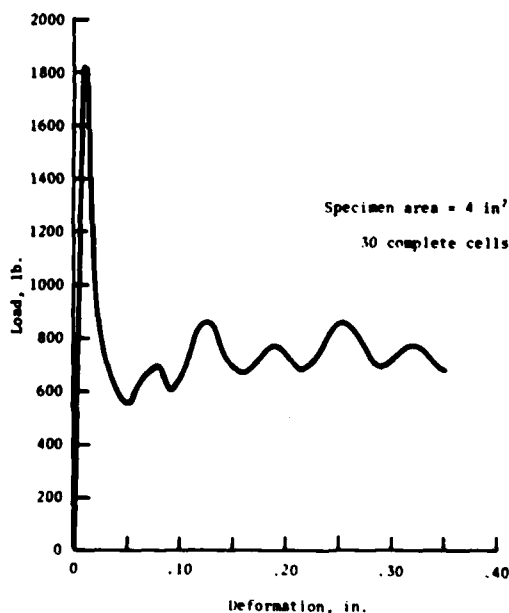
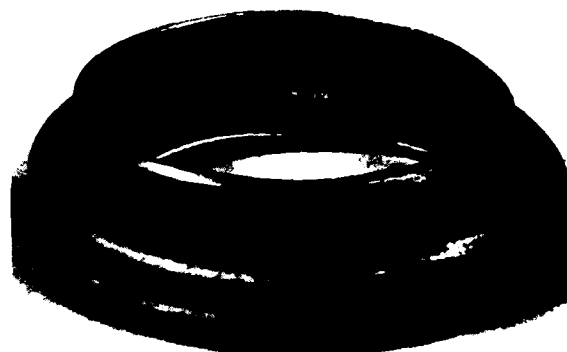


Figure 4. Experimental load versus deformation for aluminum honeycomb.



(a) Side-loaded as-received tube



(c) Axially loaded crushed tube



(b) Side-loaded annealed tube



(d) Axially loaded honeycomb

Figure 5. Photographs of deformed specimens.

The initial high peak in the load-deformation curve is undesirable in a shock snubber, since it leads to a high transmitted acceleration. To avoid this peak the honeycomb may be pre-crushed or pre-dimpled [17]. Further data on honeycomb is given in [17], [18] and [19].

Axially Loaded Crushed Tubes

Axially loaded tubing has been investigated in a crushing mode [20,21] a "frangible" mode [22,23,24], and an inverting mode [25].

The axially loaded tubing in a crushing mode deforms in an accordion-like fashion. The load-deformation curve has a large initial peak and then oscillates about a fairly flat average. The oscillations are due to the successive formation and bottoming out of new pleats.

Shaw [26] studied this type of deformation and attempted to predict the length h of the tube involved in one pleat. An Euler instability is assumed to be involved. The buckling load for a slender column of height h with hinged ends constrained to remain vertically aligned is

$$P = \frac{\pi^2 EI}{h^2} \quad (12)$$

If, further, the instability occurs when the tube just becomes plastic, then

$$P = \pi d t \sigma_0 \quad (13)$$

Then, using $I = \frac{1}{12} d t^3$, eliminating P gives

$$\frac{h}{t} = \sqrt{\frac{\pi^2 E}{12 \sigma_0}} \quad (14)$$

Shaw said this agreed well with the observed pattern with a mandrel in place, which aided in stabilizing the formation of the pleats. The load was related to deformation x by

$$P = \pi d t \sigma_0 \left(\frac{\pi t}{2h} + \frac{h}{2d} \sqrt{\frac{2h}{x} - 1} \right) \quad (15)$$

The minimum value of x for which this equation holds is x_0 , the displacement at which the plastic hinge first develops. The value of x_0 is

$$\frac{x_0}{h} = \frac{2}{1 + 4 \left(\frac{d}{h} \right)^2 \left(1 - \frac{\pi t}{2h} \right)^2} \quad (16)$$

The approximate outside diameter of the flange formed in one pleat is

$$D = d + h - t \quad (17)$$

The predicted value from these equations agreed well with static test results, but not with dynamic.

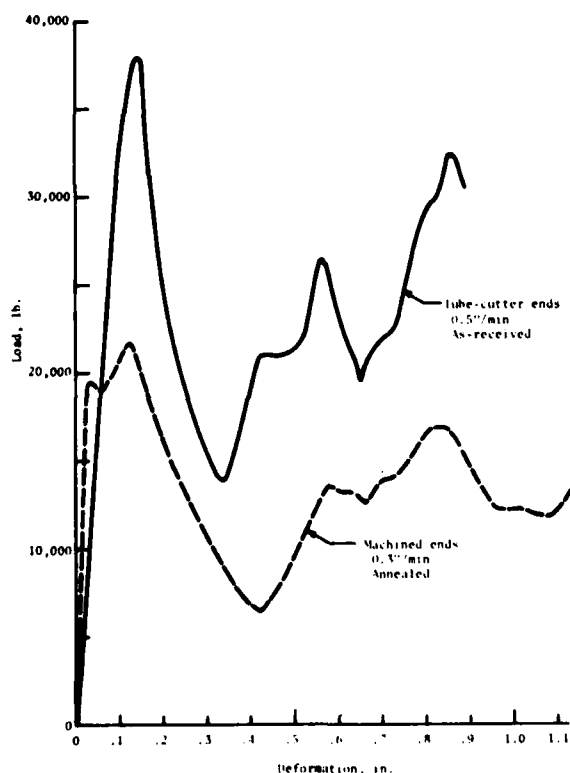


Figure 6. Experimental load versus deformation for as-received and annealed tubes loaded axially.

For the present study, several tests were run at moderate loading rates in the Tinius-Olsen machine of the 2" diameter steel tubing 0.065" thick under axial loading. A typical load-deformation curve for an as-received, 2" long tube is shown in Figure 6, in comparison with that for an annealed tube of the same size. The ends of the as-received tube were cut with a tube-cutter, while those of the annealed tube were machined square. The end conditions affect the initial shape of the curve, until the end starts to curl in and the first pleat begins to form. The deformed, annealed tube is shown in Figure 5(c), showing two well-formed pleats. The pleats develop successively and the rise and fall of the load-deformation curve is associated with the formation of successive peaks.

Double Reverse Corrugated Metal

Double Reverse Corrugated Metal (DRCM) is manufactured by Transpo-Safety, Inc.[†] and is often used as a wind screen, a snow drift barrier, or a headlight glare screen between highway lanes. It is a plain carbon steel with carbon less than 0.25%. The flat galvanized steel, with measured thickness of 0.0335 in. and steel thickness of 0.026 in., is pierced by short slits 1/2" apart in an alternating pattern as shown in Figure 7. Every other section is bent

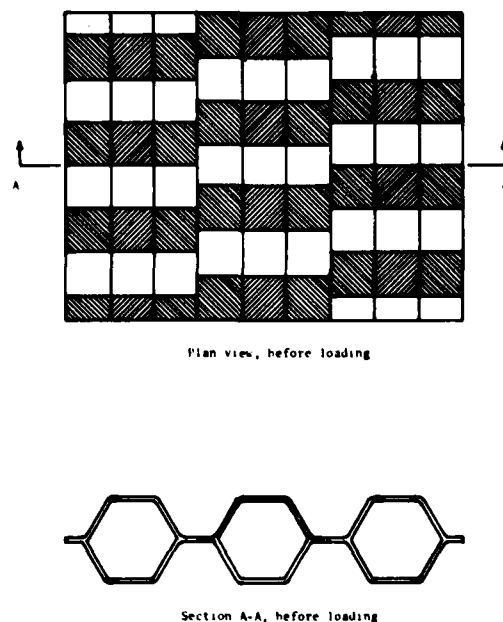
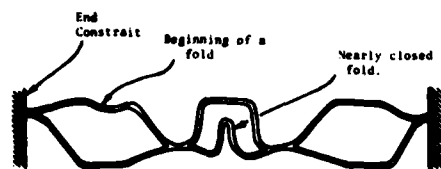


Figure 7. DRCM before loading.

[†]111 Cedar Street, New Rochell, NY 10801.



Section after 0.25" deformation with ends constrained.

Figure 8(a). Section after 0.25" deformation with ends constrained.



Section after 0.68" deformation with ends free.

Figure 8(b). DRCM section after 0.68" deformation with ends free.

up into half-hexagon shape, while the intermediate sections are bent down into a similar shape. The overall thickness of the resulting corrugated sheet metal as received was 1.02 in.

The DRCM was tested in compression only. All specimens were cut from the same sheet. Test results of seven specimens are given in Figure 9 and 10, with information about each specimen given in Table 1. As the material is compressed the arches are bent down and the specimen tends to lengthen as shown in Figure 8(b), if the ends are unconstrained. The first five specimens were tested with unconstrained ends. Results for four specimens are shown in Figure 9. The ordinate is pressure, equal to applied force divided by initial planview area. The abscissa is deformation.

The specimens were tested to varying maximum deformations primarily to be able to study the deformation pattern for various percentages of deformation. The specimen behavior was fairly repeatable except that the load for BB was about 17% higher than for the others and the recovery of load-carrying capacity occurred sooner for BB, at about 42% deformation. The reason for the difference between BB and the others may be due partly to variation in behavior of the edges of the specimen, but it was also observed that the deformation pattern of the internal corrugations for BB was different

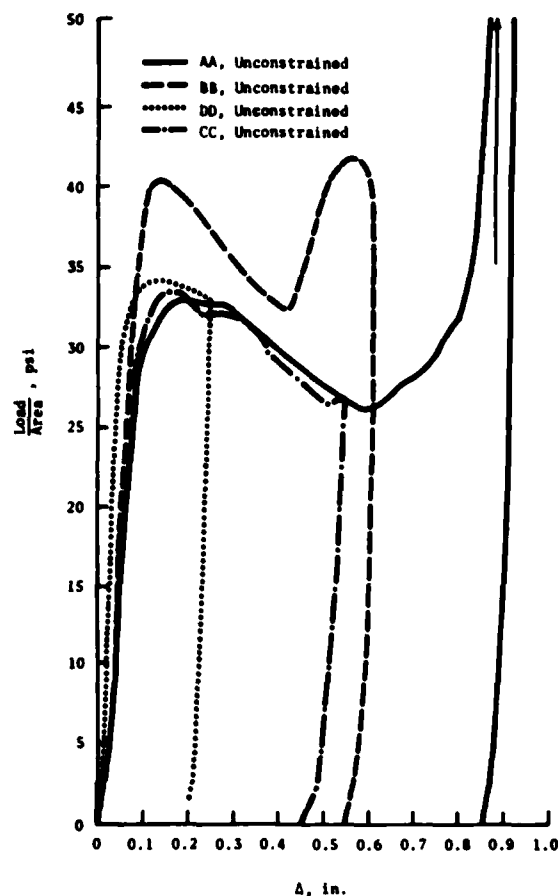


Figure 9. Pressure-deformation for unconstrained DRCM.

from that of the others.

At 82% deformation the typical DRCM specimen with ends free has absorbed about 670 in. lb/in.³ of energy.

In Figure 10, pressure-deformation curves for two specimens with constrained ends are presented, in comparison with a curve for specimen EE which had unconstrained, or free, ends. Considerable pressure is required to initiate plastic deformation in the constrained specimen because folding must occur, as shown in Figure 8(a). Note that the constraint is only in the horizontal direction. The flat portions of the arches start to curve up or down as folds form progressively. The steepest pressure decrease occurs after a fold has developed on every downward arch on the centerline of the specimen. The stiffening at the 0.35 inches deformation began as the folds began to be flattened.

Some of the irregularities in the curves are due to edge effects which would be less prominent in larger specimens.

Specimen	Boundary	Initial $l \times W$ (in. x in.)	Δ_{max}	Final Length (in.)
AA	Unconstrained	3 x 2-1/2	0.92	3-3/4
BB	"	3 x 2-1/2	0.61	3-5/8
CC	"	3 x 2-1/2	0.55	3-1/2
DD	"	3 x 2-3/4	0.25	3-1/4
EE	"	4-1/2 x 3-1/2	0.85	5-5/8
FF	Constrained	4-1/2 x 3-1/2	0.72	4-1/2
GG	"	4-1/2 x 3-1/2	0.40	4-1/2

Table 1. Summary of DRCM specimens tested.

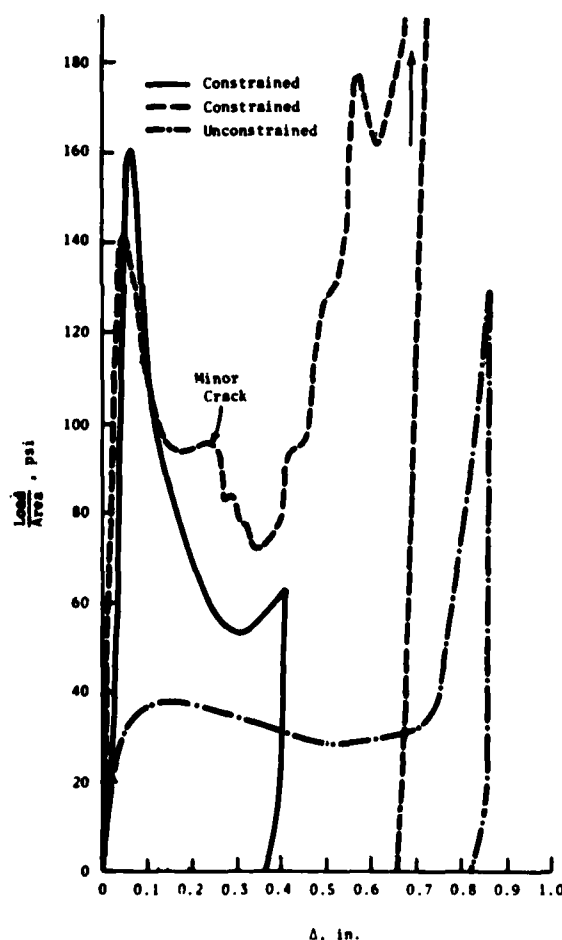


Figure 10. Pressure-deformation for constrained DRCM.

Constrained specimens absorb more than twice the energy absorbed by the unconstrained, but the high initial peak and sudden drop-off is undesirable in shock mounts. This could be overcome by pre-compressing the material about 0.1 in. The stiffening at 0.35 inches is also undesirable for the constrained specimens. In general the unconstrained material displays a load-deformation curve better suited for shock mounting.

SIDE-LOADED TUBES

Equations for Side-loaded Tube in Compression

The large plastic response of side-loaded tubes under static loading between two rigid plates has been studied analytically and experimentally [27,28]. The deformation Δ is related to load P and tube average diameter d by

$$P = \frac{P_0}{\sqrt{1 - \left(\frac{\Delta}{d}\right)^2}} \quad 0 \leq \Delta \leq \frac{d}{\sqrt{2}} \quad (18)$$

The solution ceases to be valid for $\Delta > \frac{d}{\sqrt{2}}$.

The load P_0 is the load at which the tube begins to deform as a mechanism after formation of plastic hinges at the quarter-points. The load P_0 is related to the fully plastic moment M_0 , the mean radius r , the tube thickness t , and the tube width W by

$$P_0 = \frac{4M_0}{r} = \frac{\sigma_0 t^2 W}{r} \quad (19)$$

For the dynamic behavior of material under uniaxial, impulsive loading Perrone [29] suggested a simplification in the analysis, namely that the initial strain rate could be assumed to be constant throughout the entire flow process. For a pulse-loaded structure, it is necessary to estimate the peak strain rate and assume the associated stress to be constant.

For an application of side-loaded rings to highway impact data, Perrone [30] presented stress versus strain rate data for $10^{-2} < \dot{\epsilon} < 400/\text{sec}$ and static load versus deflection curves for tubes of three different types of steel. These tubes were 18 inches in diameter.

With regard to energy absorption, Perrone assumed that the load-deformation curve rose linearly from P_0 at zero deflection to $2P_0$ at deflection equal to $2r$, so that the energy U absorbed is approximately

$$U = 3P_0 r = 12M_0 = 3\sigma_0 t^2 W \quad (20)$$

The result is surprising, since the energy absorbed does not depend on radius of the tube. Rate of loading effects may be taken into account by increasing the yield stress according to equation (1).

It should be noted that in reference [28] it was assumed that the tube was being crushed between parallel plates so that the contact point would separate into two points which move out as the characteristic peanut shape develops for the tube. In reference [30], the loading appears to be more centrally applied, which results in a softer load-deformation curve for large deformation.

The maximum load carried should occur at maximum deformation, unless the tube fails before that. Failure could occur at the plastic hinges for brittle metals. The suitability of the material can best be determined by tests of the tubing itself.

Test Results for Side-Loaded Tubes in Compression

The tubes tested were all obtained from one piece of round seamless mechanical tubing of cold drawn carbon steel, with 0.10 - 0.25% carbon. The wall thickness was 16 gauge or 0.065 inches, and the outside diameter was 2 inches. Some of the tubing was annealed, after it was found that the as-received tended to crack at the plastic hinges at large deformations (see Figure 5(a)).

Small tensile specimens were cut from the tubing with the axis of the specimens in the direction of the axis of the tubing. The specimens had a slight curvature and the ends were flattened in the grips, but this was thought to have little effect on the tensile properties. The annealed material had a definite yield at 44,000 psi. Tubes were annealed at 1200°F for 140 minutes and then oven cooled for 24 hours. The as-received exhibit strain hardening and had a 0.2% offset yield of 65,000 psi.

Specimens 2" long were cut from the as-received tubing in a non-ideal, but practical, way by using a plumber's tube-cutter. This produced a v-shaped groove. The tubing was tested in the Tinius-Olsen machine at varying

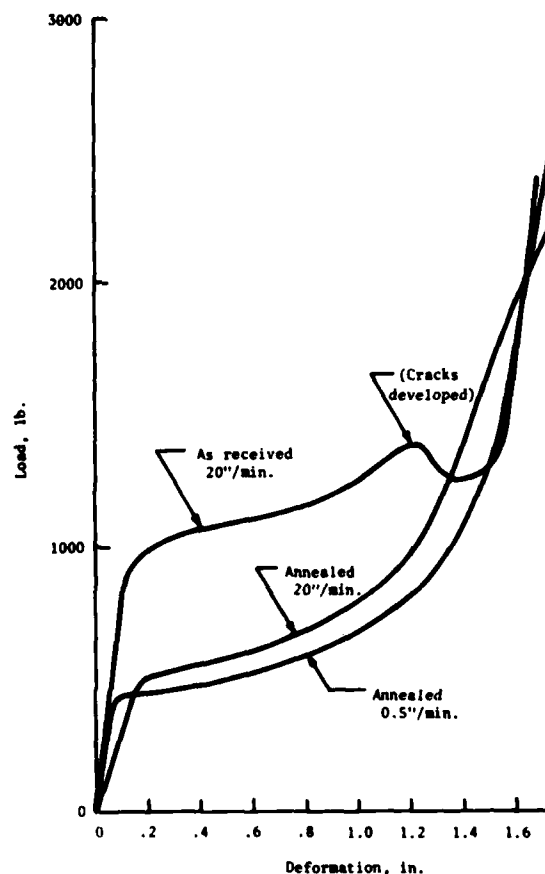


Figure 11. Load vs. deformation for a 2" long, side-loaded tube, using Tinius-Olsen machine. (Tube edges cut by tube cutter.)

rates. Plastic hinges tend to develop, first on the top and bottom and then on the sides of the tubing, so finally there are four hinges located at 90° intervals around the tube circumference (see Figure 5(b)). All the as-received tubes developed cracks at about one inch deformation. On Figure 11, a load-deformation curve is shown at a loading rate of 20"/min. A sudden, temporary, loss of stiffness occurred when the cracks developed. This tubing was judged to be unacceptable in the as-received state and all subsequent tests were done on annealed tubing. Test results for annealed tubing at two rates are shown in Figure 11. The varying slopes of the initial elastic portion of the curves were due in part to the raised edges produced by the tube-cutter. Specimens for later tests were cut and had edges machined on a lathe.

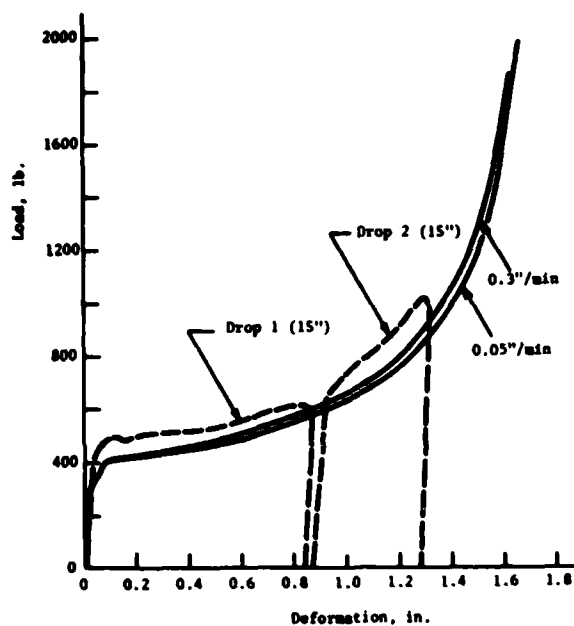


Figure 12. Load vs. deformation for annealed, side-loaded tubes using Tinius-Olsen and shock machines.

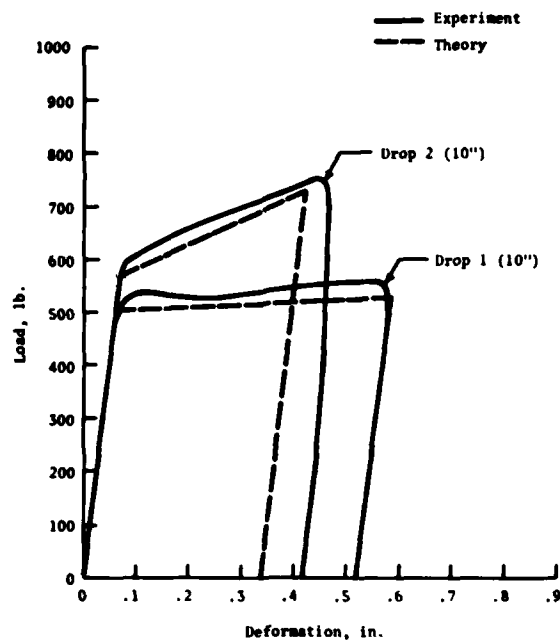


Figure 14. Theoretical and experimental load-deformation curves for 10" drops 1 and 2, for side-loaded tubes.

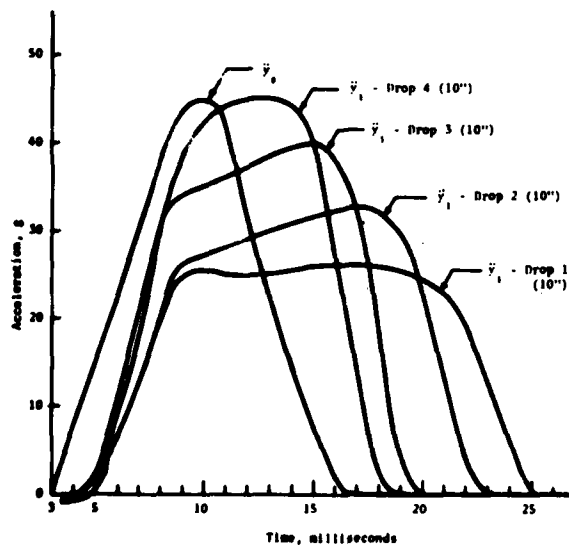


Figure 13. Input acceleration \ddot{y}_0 and transmitted acceleration \ddot{y}_1 versus time, drops 1, 2, 3, and 4 using side-loaded tubes.

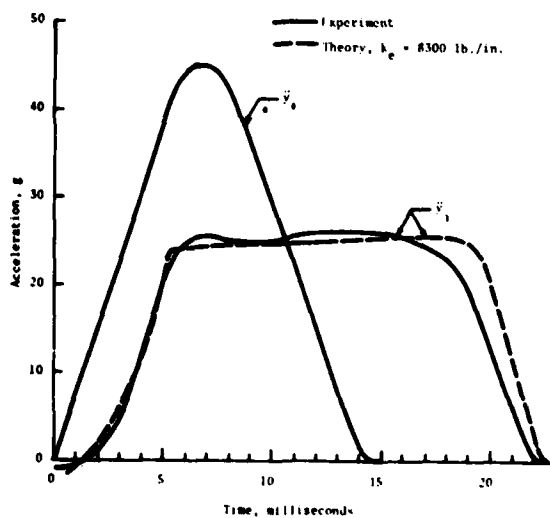


Figure 15. Theoretical and experimental acceleration vs. time; \ddot{y}_1 , for 10" drop 1, for side-loaded tubes.

In the shock machine, four 1/2" long tubes were used, rather than one 2" long tube. In static compression tests, the load-deformation curve for four 1/2" long tubes was practically identical to that of one 2" long tube, at the same loading rate.

In one set of shock machine tests, a set of four 1/2" long annealed tubes was submitted to eight successive 10" drops and then a 15" drop. Resulting load-deformation curves for Drops 1 through 4 and Drop 9 are shown in Figure 12 and compared with a curve at 0.05"/min. deformation rate on the Tinius-Olsen. The higher rate of loading in the shock machine produces a higher yield stress. Note that less energy is absorbed on each successive drop.

Transmitted acceleration is compared with base acceleration in Figure 13 for the first four 10" drops. For the first drop the maximum transmitted acceleration, \ddot{y} , is about 26 g compared to a peak base acceleration, \ddot{y}_0 , of 45 g. However, by the fourth drop, the tubes furnished no attenuation.

For analysis of data, several non-dimensional quantities were used. A non-dimensional deformation is $\bar{\Delta}$, given by

$$\bar{\Delta} = \frac{\Delta}{2r} \quad (21)$$

The theoretical maximum deformation is

$$\Delta_{\max} = d_1 = d_0 - 2t = 2r - t \quad (22)$$

and the non-dimensional maximum is

$$\bar{\Delta}_{\max} = 1 - \frac{1}{2} \frac{t}{r} \quad (23)$$

A non-dimensional load is achieved using Equation (19) as

$$\bar{P} = \frac{Pr}{\sigma_0 t^2 W} \quad (24)$$

In plots, a reference yield stress value $\sigma_0 = 45,000$ psi was used. If that value is also the yield load, then obviously at yield,

$$\bar{P}_0 = \frac{P_0 r}{\sigma_0 t^2 W} = 1 \quad (25)$$

Theoretical Results for Side-loaded Tubes in Compression

In Figure 14, predicted load-deformation curves are compared with those from measurements. To predict the results, an equation based on Figure (1) was used, with $y_r = y_1 - y_0$, $c = 0$ and $k = 0$:

$$\begin{aligned} m\ddot{y} + L(t) &= -mg \\ \text{or } m\ddot{y}_r + L(t) &= -mg - m\ddot{y}_0 \end{aligned} \quad (26)$$

The $L(t)$ curve was a bi-linear curve which was estimated from test data from the Tinius-Olsen machine, but with the yield increased to account for rate effects. The input was measured \ddot{y}_0 . Agreement is good except for the unloading curve and the residual deformation for Drop 2.

Predicted acceleration versus time is given in Figure 15 for 10" Drop 1 and in Figure 16 for 10" Drop 2. In Figure 16, the effect is studied of doubling the theoretical elastic stiffness k_e of the tubing. The $k_e = 8300$ lb./in. produces the better fit.

In general, predictions are good for side-loaded tubing, but could be improved by incorporating a constitutive equation of the form of equation (2).

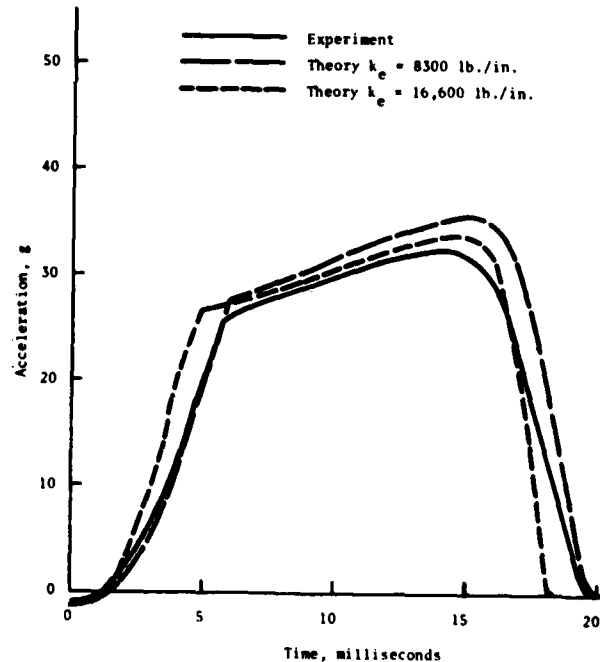


Figure 16. Theoretical and experimental acceleration vs. time; y_1 , for 10" drop 2, for side-loaded tubes.

Tubing	$\dot{\epsilon} \left(\frac{\text{in.}}{\text{in.s.}} \right)$	$\left(1 + \frac{\dot{\epsilon}}{D} \right)^{\frac{1}{5}}$	Predicted σ_o'	Experimental σ_o'
$d_o = 2.00"$ $t = 0.125"$	2.3×10^{-5}	1.056	34,800	35,000
	1.6×10^{-4}	1.083	35,700	36,000
	1.6×10^{-3}	1.13	37,290	39,600
$d_o = 3.06"$ $t = 0.073"$	1.66×10^{-5}	1.053	34,700 (Experimental)	34,700
	1.2×10^{-4}	1.078	35,600	35,500
	1.2×10^{-3}	1.124	37,000	37,800

Table 2. Predicted and measured value of dynamic yield stress.

Rate Effects for Side-loaded Tubes in Compression

Annealed tubes of 2" and 3" diameter were tested in compression in the Tinius-Olsen machine at three different deformation rates: 0.016, 0.114, and 1.16 in./min. The resulting load-deformation curves are given in reference [2]. In order to predict increased yield, equation (1) was used, with $D = 40.4/s$ and $n = 5$.

$$\frac{\sigma_o'}{\sigma_o} = 1 + \left(\frac{\dot{\epsilon}}{D} \right)^{\frac{1}{n}} \quad (1)$$

Strain rates were not measured during the experiments, but they were estimated from experimental data as follows. The smallest radius of curvature after a loading interval Δt was approximately

$$r_f = \frac{d_o - \alpha \Delta t}{4} \quad (27)$$

The curvature rate was obtained from

$$\dot{\epsilon} = \frac{t}{2\Delta t} \left(\frac{1}{r_f} - \frac{1}{r} \right) \quad (28)$$

Here α is the deformation rate. The time interval Δt was taken as 5 minutes.

The measured values of P_o were taken from data. The experimental σ_o' was then obtained from equation (25), assuming $\sigma_o = \sigma_o'$ for the lowest deformation rate.

The theoretical value of σ_o was then estimated from the lowest strain rate for the 3" tubing by:

$$34,700 = 1.053 (\sigma_o)$$

$$\text{or } \sigma_o = 33,000 \text{ psi}$$

This value of σ_o was used to calculate the other five values of predicted σ_o' in Table 2.

The Table 2 shows only that if σ_o is estimated from the data obtained at the lowest rate of loading, then Equation (1) gives a good estimate of the yield stress at the two higher rates of loading.

The shape and parallel nature of the load-deflection curves after yield indicate that the dynamic behavior of the rings can be represented by the curve shape obtained from static tests if the yield stress is modified according to Equation (1).

Straightening of Deformed Tubes

Experiments were performed to straighten side-loaded tubes which had been deformed previously in compression. Under first loading the circular cross-section is deformed into the typical peanut shape. The method used to straighten the tubes was to simply rotate the deformed tubes 90° and compress them again in the Tinius-Olsen machine.

Some typical shapes are shown in Figures 17 and 18. Tube A is undeformed initially and then compressed under first loading to a final outer thickness of 1.49". The corresponding maximum width was 2.48", so the final dimensions of the tube A are given as 1.49" x 2.48".

Tubes B, C, and D were already deformed, as indicated by their initial dimensions in Figures 17 and 18. They are shown after a 90° rotation. They were then compressed to try to return them to the original circular shape. The initial deformations of tubes B, C, and D were $\bar{\Delta} = 0.55, 0.68$ and 0.83 respectively. The final shapes in Figures 17 and 18 show that B returned to a nearly circular shape, but tube D was almost square after straightening. The effect of several cycles of deforming and straightening was not studied.

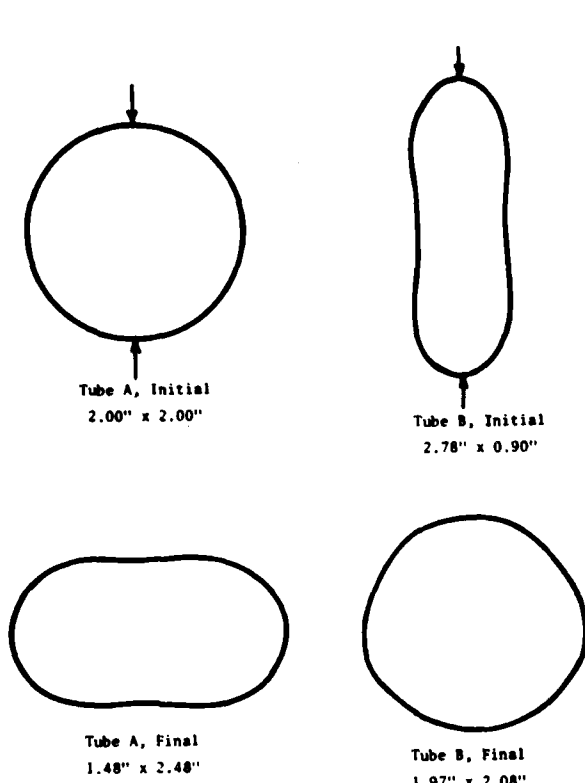


Figure 17. Tube A before and after first loading. Tube B before and after straightening.

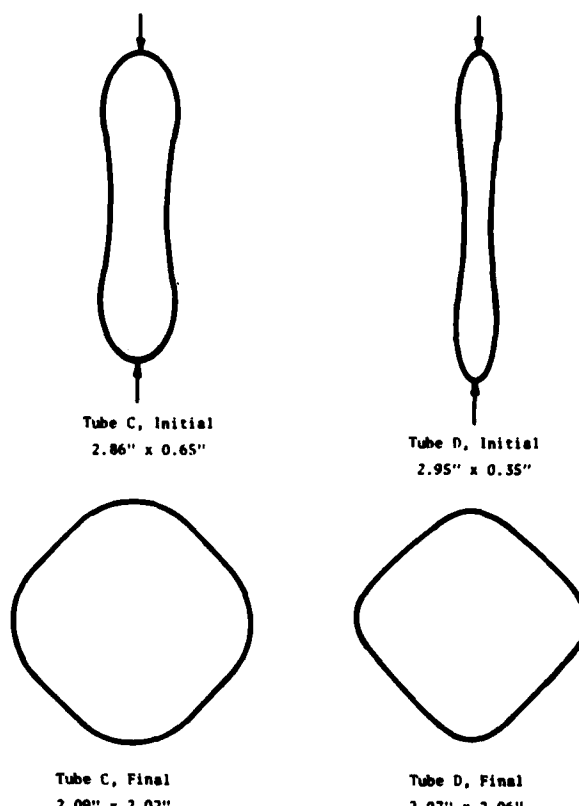


Figure 18. Tubes C and D before and after straightening.

The load versus deformation curve associated with the initial loading of the annealed tube A, with $d_o = 2"$, $W = 2"$, and $t = 0.065"$, is shown in Figure 19. The measured yield stress for this tubing is $\sigma_o = 44,000$ psi. The loads required to straighten tubes B, C, and D, which had the same W and t , are also shown. The curves rise to a large initial load and then show a negative stiffness until they are straightened to the nearly circular (or square) cross-section.

Directional Properties of Side-loaded Tubes

In addition to the compression tests of side-loaded tubing, tests were conducted in the shear and roll directions.

For the shear and roll tests, a jig was used as shown in Figure 20, using eight rings, each $1/2"$ wide, in parallel. Shear corresponds to the x-direction, roll, to the y-direction. Rings were clamped at the outer edges. The inner edges were attached to a push plate, onto which the load was applied.

Resulting load-deformation curves are shown in Figure 21 for four annealed rings having $d_o = 2"$ and $t = 0.065"$. It is seen that the rings sustained considerable deformation in each direction. The stiffening for large Δ was due to the constrained boundaries, which lead to development of tension in the rings at large deformation.

Burns [31] summarized the properties of certain yielding, cylindrical mounts as follows. Numerical values are for the 2" diameter rings.

$$\text{Shear} \quad P_{ox} = \frac{3}{2} \frac{n \sigma_o W^2 \left[1 - \left(\frac{r_o - t}{r_o} \right)^2 \right]^{1/2}}{3(r_o - t)/r_o} = 8350 \text{ lb.} \quad (30)$$

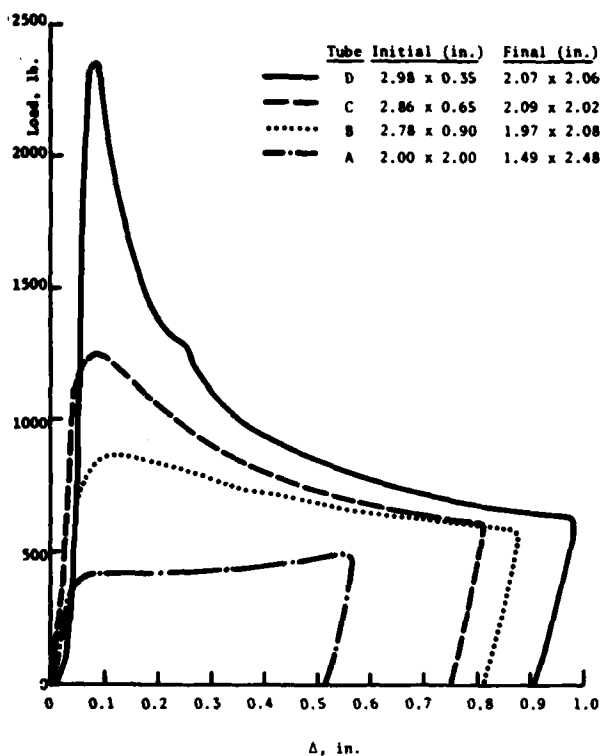


Figure 19. Load-deformation for tubes A,B,C, and D.

Roll

$$P_{oy} = \frac{n\sigma_o W t^2}{d_o} = 186 \text{ lb.} \quad (31)$$

Compression

$$P_{oz} = \frac{\pi}{2} \frac{n\sigma_o W t^2}{d_o} = 292 \text{ lb.} \quad (32)$$

Here $t = 0.065''$, $r = .4675''$, $W = 1/2''$, $d_o = 2$, $r_o = 1''$, $\sigma_o = 44,000 \text{ psi}$ and $n = \text{number of tubes} = 4$.

The elastic stiffnesses are given in [31] as

Shear

$$k_x = \frac{nEW^3 t}{3\pi r_o^3} = 103,400 \text{ \#/in.} \quad (33)$$

Roll

$$k_y = \frac{nEWt^3}{3\pi r_o^3} = 1748 \text{ \#/in.} \quad (34)$$

Compression

$$k_z = \frac{nEWt^3}{1.79r_o^3} = 9203 \text{ \#/in.} \quad (35)$$

Comparison with the curves of Figure 21 indicates fair agreement between predicted and measured values for roll and compression, but an order of magnitude error in predicting the values for shear. The reason for this discrepancy is not entirely clear, but two reasons are suggested: (1) the rings deformed also in torsion and the theory includes only bending and (2) the ring clamps and supporting jig were not a perfectly rigid support.

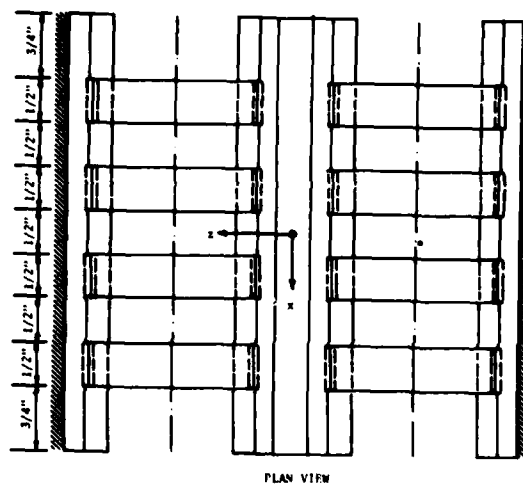


Figure 20. Apparatus for shear and roll tests.

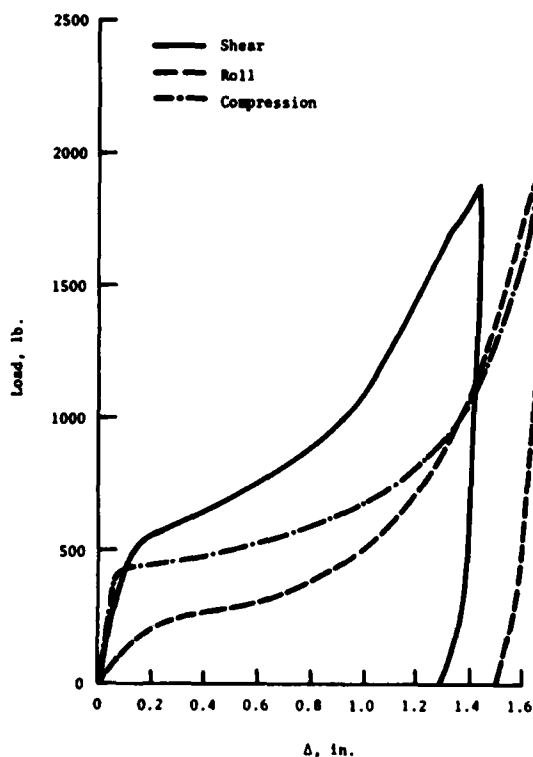


Figure 21. Load-deformation for three directions for tubing, $d_o = 2"$, $t = 0.065"$.

CONVENTIONAL SHOCK MOUNTS

Commercial shock mounts were purchased from Aeroflex Laboratories, Inc.[†] They are made of stranded stainless steel wire rope in a helical pattern and are advertised to provide 15 to 20% of critical damping. The mounts tested were Number C1260-39 with outside dimensions of 5.66" long, 2.19" high, and 3.19" wide. Some of the characteristics as summarized from the catalog are given in Table 3.

The load mode 45° CR means the mount is oriented 45° from the vertical and that the deformation has both a compression component and a roll component.

[†] South Service Road, Plainview, Long Island, NY 11803.

Load Mode	Average K (lb./in.)	Maximum Rated	
		Shock Load (lb.)	Dynamic Travel (in.)
Compression	208	250	1.2
Shear	139	250	1.8
45° CR	54	125	2.3

Table 3. Catalog characteristics of Aeroflex C1260-39 shock mounts.

The mounts were tested separately, first in direct compression in the Tinius-Olsen machine. Then they were attached to the jig shown in Figure 20 for tests in the shear and roll directions. In compression the average stiffness is approximately as advertised. In shear and roll the stiffness is less than 278 lb./in. for small deflections, but then displays a hardening curve. The load-deformation curves in roll and shear are similar. The stiffening, or hardening, above 1.2 in. deflection is due to the type of support, which requires the cable to stretch at large deformations of the mount in both roll and shear.

COMBINATION OF MOUNTS

A practical arrangement would be to have a linear shock or vibration mounts in series with a load-limiting mount, such as DRCM.

Some idealized theoretical curves are given in Figure 22. A linear average curve for two Aeroflex mounts in compression is shown as well as a bilinear curve to approximate the behavior of DRCM. Then the theoretical stiffness curves of the two in parallel and in series are shown.

THEORETICAL RESPONSE OF A MACHINE-FOUNDATION-SNUBBER ARRANGEMENT.

The theoretical load-deflection curves of Figure 22 were used in the computer analysis associated with the system of Figures 1 and 2 to compare theoretical behavior of the various shock mounting systems. The following data was used:

- $k = 335$ lb./in. (Two Aeroflex mounts in compression)
- $k_e = 4300$ lb./in. (Elastic stiffness of DRCM)
- $k_p = 10$ lb./in. (Plastic stiffness of DRCM)
- $c = 0$
- $m = 20\#/g$

The base acceleration was that measured in table of the shock machine, with a maximum $y_o = -29g$. The resulting acceleration-time curves are shown in Figure 23 for the series and parallel arrangement of Figure 22.

A summary of maximum accelerations and deformations is given in Table 4.

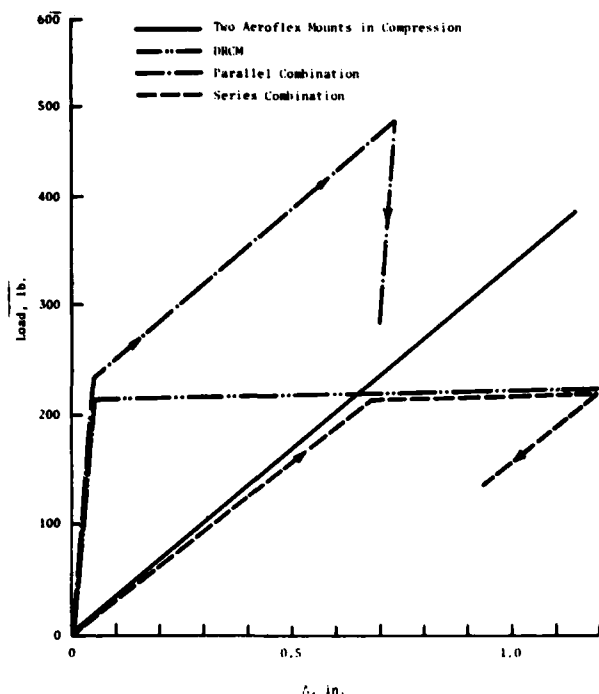


Figure 22. Theoretical load-deformation for various mounting systems.

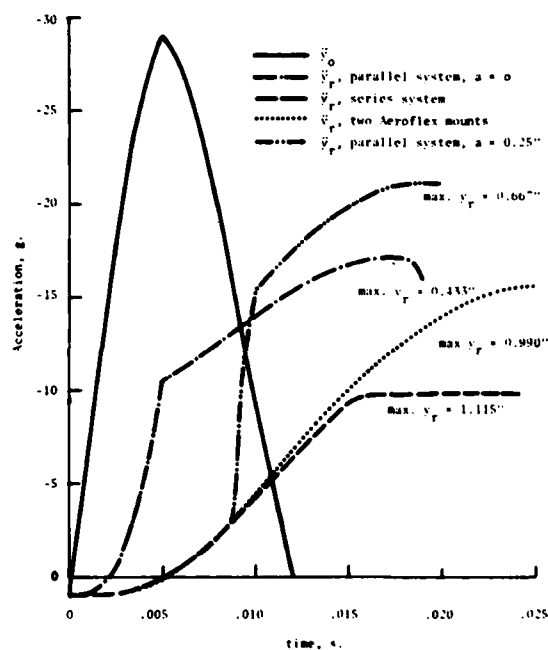


Figure 23. Theoretical acceleration-time for machine-foundation-snubber with $(\ddot{y}_o)_{\max} = -29$ g.

Mount System	$(\ddot{y})_{\max} (g)$	$(y_r)_{\max} (in.)$
Parallel, $a = 0.25''$	-21.0	0.667 (including a)
Parallel, $a = 0$	-17.2	0.433
Linear (Two Aeroflex Mounts)	-15.6	0.990
Series	-10.0	1.115

Table 4. Maximum transmitted acceleration and relative displacement for various mounting systems.

The best system for limiting transmitted acceleration is clearly the arrangement of the linear mount (Aeroflex) in series with the load-limiting mount (DRCM), but the deflection is maximum.

SUMMARY AND CONCLUSIONS

This study is concerned with the development of analytical methods for design of energy-absorbing foundations for protection of equipment from shock induced by base motion or ground shock, with particular emphasis on gaining more information on side-loaded tubes and DRCM.

Some of the energy-absorbing systems studied in the present report are compared with other systems in Table 5.

Axially crushed, frangible, and inverting tubes have high specific energies, but axial alignment is very important and they may be difficult to use in a 3 inch space. Honeycomb is a very efficient energy absorber. Cost may be a factor in some applications.

System	Specific Energy $\frac{\text{ft. lb.}}{\text{lb.}} \times 10^3$	Comments
Inverting tube [25]	2 to 4	Aluminum, $d_o = 3"$, $t = 0.035"$
Aluminum honeycomb [32]	1 to 8	Strain dependent, up to 70% strain
Side-loaded tube	0.5 to 1.5	$\frac{r}{t} > 5$
Frangible tube [22]	38.5	AISI 4130 steel, cold water quenched
Axially crushed tube [1]	10.0	$d_o = 2"$, $t = 0.065"$
DRCM, unconstrained	0.2	
DRCM, constrained	0.6	
Side-loaded tube (shear)	0.6	$d_o = 2"$, $t = 0.065"$
Side-loaded tube (roll)	0.3	$d_o = 2"$, $t = 0.065"$

Table 5. Energy absorbing systems

The double reverse corrugated metal (DRCM) with constrained ends compares favorably with side-loaded tubes with regard to energy absorbed per pound. However, the load-deformation curve has a high initial peak, which is undesirable in shock mount. The unconstrained DRCM has a better load-deformation curve, but it absorbs less energy per pound.

The side-loaded tubes might be used as snubbers, or shock absorbing bumpers, so they would be loaded only in compression. However, the shear and roll tests show that they have significant stiffness and energy-absorbing capability in those directions also. The design formulas in the literature for the shear direction do not appear adequate and require further development.

The tests of side-loaded annealed steel tubing in compression at three different deformation rates show that the primary rate effect is increased yield stress. The increase in yield stress is predicted satisfactorily by the equation of reference [6].

With regard to the tests of tubes of different diameters and thicknesses, the effect of thickness and radius appears to be correctly represented by the expression

$$P_o = \frac{\sigma_o W t^2}{r}$$

for the thin tubes, with $r/t > 5$. Also, converting Equation (20) to non-dimensional quantities gives

$$\bar{P} = \frac{\bar{P}_o}{\sqrt{1-\bar{d}^2}}$$

indicating that the curves should have the same shape above the yield load. This is confirmed in Figure 5, Reference [2] for 1" and 2" tubes, but not for the 3" diameter tube tested.

The straightening of tubing that had been deformed under compression side loading is readily accomplished in a load machine or with a set of jacks. An estimate of the load required may be made from Equation (19), using r as the smallest radius of the peanut-shaped tube, but a more precise equation for this shape should be developed.

It is demonstrated by analysis of the machine-foundation-snubber arrangement that use of a load-limiting shock mount or snubber such as a side-loaded tube or DRCM in series with a conventional mount is helpful in reducing transmitted acceleration, but there is a penalty because of increased deflection. The problem is one of optimization: once a maximum allowable displacement has been set, to minimize transmitted acceleration. Optimization should be studied further to produce design curves.

ACKNOWLEDGEMENTS

The work was supported by Defense Nuclear Agency directly under contracts DNA 001-78-C-0036 and then through the Office of Naval Research Contract N 00014-79-C-1049. The benefit of discussions with Dr. N. Perrone and Lts. R. Wade and R. Elsbernd is gratefully acknowledged. Mr. R. Volin, Shock and Vibration Information Center, assisted with the literature search. Computer programming for the series and parallel mount combinations was done by Mr. K. Kasraie, graduate student at The Pennsylvania State University.

REFERENCES

1. Neubert, V.H. and Yin, S.J., "Analysis of Energy Absorbing Foundations" Report No. DNA 4800F, Contract No. DNA 001-78-C-0036, Defense Nuclear Agency Washington, D.C.,

20305, 15 December 1978.

2. Neubert, V.H., "Analysis of Energy-Absorbing Foundations," Contract No. N00014-79-C-0149, Office of Naval Research, October 1979.
3. Stricklin, J.A. and Saczalski, K.J., Constitutive Equations in Visco-plasticity: Computational and Engineering Aspects, ASME Applied Mechanics Division, Vol. 20, 1976.
4. Hecker, S.S., Experimental Studies of Yield Phenomena in Biaxially Loaded Metals," Reference [1], pp. 1-33.
5. Lindholm, U.S., "High Strain Rate Testing," in Techniques of Metals Research, Vol. V, Bunshah, R.F., Ed., Interscience, N.Y., pp. 199-271, 1971.
6. Cowper, G.R. and Symonds, P.S., "Strain Hardening and Strain Rate Effects in the Impact Loading of Cantilever Beams," Technical Report No. 28, Brown University, 1957.
7. Manjoine, M.J., "Influence of Rate of Strain and Temperature on Yield Stress of Mild Steel," J. Appl. Mech., 11, 211, 1944.
8. Parkes, E.W., "The Permanent Deformation of an Encastrate Beam Struck Transversely at Any Point in its Span," Proc. of the Inst. of Civil Eng., Vol. 10, pp. 277-304, 1958.
9. Belsheim, R.O., "Delayed Yield Time Effects in Mild Steel Under Oscillatory Axial Loads," Trans. ASME, 1957.
10. Vigness, I., Krafft, J.M., and Smith, R. C., "Effect of Loading History Upon the Yield Strength of a Plain Carbon Steel," Proc. Inst. Mech. Engrs., 1975.
11. Malvern, L.E., "The Propagation of Longitudinal Waves of Plastic Deformation in a Bar Exhibiting a Strain Rate Effect," J. Appl. Mech., 18, 203, 1951.
12. Cristescu, N., Bul. Acad. Pol. Sci., XI, 129, 163. See also "A Procedure for Determining the Constitutive Equations for Materials. Both Time-Dependent and Time-Independent Plasticity," Int. J. Solids and Structures, Vol. 8, pp. 511-531, 1972.
13. Perrone, Nicholas, "A Mathematically Tractable Model of Strain Hardening, Rate Sensitive Plastic Flow," J. Appl. Mech., 33, 210-211, 1966.
14. Plass, H.J., Jr., "Theory of Plastic Bending Waves in a Bar of Strain Rate Material," Second Midwestern Conference on Solid Mechanics, pp. 109-134, 1955.
15. Thompson, J.N. and Ripperger, E.A., "Cushioning for Aerial Delivery," Shock and Vibration Bulletin No. 30, Part 3, pp. 261-275, Feb. 1962.
16. McFarland, R.K., Jr., "Hexagonal Cell Structures under Post-Buckling Axial Load," AIAA Journal, Vol. 1, No. 4, pp. 1380-1385, 1963.
17. Lewallen, J.M. and Ripperger, E.A., "Energy-Dissipating Characteristics of Truss-grid Aluminum Honeycomb," Structural Materials Research Lab. Report SMRL RM-5, University of Texas, March 1962.
18. Daigle, D.L. and Longborg, J.O., "Evaluation of Certain Crushable Materials," Tech Report No. 32-120 (Contract No. NASW-6), Jet Propulsion Lab., C.I.T., January 13, 1961.
19. Lipson, S., "Cellular Aluminum for Use in Energy Dissipation Systems," NASA CR-93, 1964.
20. Alexander, J.M., "An Approximate Analysis of the Collapse of Thin Cylindrical Shells under Axial Loading," Quart. J. Mech. & Appl. Math. XIII, 10-14, 1960.
21. Pugsley, A. and Macaulay, M., "The Large-scale Crumpling of Thin Cylindrical Columns," Quart. J. Mech. and Appl. Math. VIII, 1-9, 1960.
22. McGehee, J.R., "Experimental Investigation of Parameters and Materials for Fragmenting Tube Energy Absorbing Process," NASA TN D-3268, 1966.
23. McGehee, John R., "A Preliminary Experimental Investigation of an Energy-Absorption Process Employing Frangible Metal Tubing," NASA TN D-1477, October 1962.
24. McGehee, John R., "Experimental Investigation of Parameters and Materials for Fragmenting-Tube Energy-Absorption Process," NASA TN D-3268, February 1966.
25. Kroell, C.K., "A Simple, Efficient, One Shot Energy Absorber," Shock and Vibration Bulletin No. 30, Part III, pp. 331-338, February 1962.
26. Shaw, Milton C., "Design for Safety: The Mechanical Fuse," Mechanical Engineering, pp. 23-29, April, 1972.
27. Hwang, Chintsun, "Plastic Collapse of Thin Rings," Int. of Aero. Sci., pp. 819-826, December 1953.
28. De Runtz, J.A., Jr. and Hodge, P.G., Jr., "Crushing of a Tube Between Rigid Plates," Int. of Appl. Mech., pp. 391-395, September 1963.
29. Perrone, N., "On A Simplified Method for Solving Impulsively Loaded Structures of Rate-Sensitive Materials," J. Appl. Mech.,

- 33, 489-493, 1965.
30. Perrone, N., "Thick-Walled Rings for Energy-Absorbing Bridge Rail Systems," Final report No. FHWRD-73-49, for Federal Highway Administration Offices of Research and Development, Washington, D.C., 20590, December 1972.
 31. Burns, A.B., Guide for the Selection & Application of Shock Mounts for Shipboard Equipment, Contract No. Nobs-78963, Bu Ships Code 423, September 1, 1961.
 32. Perrone, N., "Crashworthiness and Biomechanics of Vehicle Impact," in Dynamic Response of Biomechanical Systems, ASME, New York, N.Y., 1970.
 33. Baker, W.E., "Approximate Techniques for Plastic Deformation of Structures under Impulsive Loading," Shock and Vibration Digest, Vol. 7, No. 7, pp. 107-117, 1975.
 34. Jones, N., "A Literature Review of the Dynamic Plastic Response of Structures," Shock and Vibration Digest, Vol. 7, No. 8, pp. 88-105, 1975.
 35. Goldsmith, W., Impact, Arnold, 1960.
 36. Rawlings, B., "Recent Progress in the Study of Steel Structures Submitted to Impulsive Overload," Dynamic Waves in Civil Engineering, (eds.) D.A. Howells, J.P. Haigh and C. Taylor, Wiley Interscience, p. 543-565, 1971.
 37. Symonds, P.S., "Survey of Methods of Analysis of Plastic Deformation of Structures Under Dynamic Loadings," Brown University, Rept. BU/NSRDC/1-67, 1967.
 38. Johnson, W., Impact Strength of Materials, Arnold, London and Crane Russak, (U.S.), 1972.
 39. Jones, N., Dumas, J.W., Giannotti, J.G., and Grassit, K.E., "The Dynamic Plastic Behavior of Shells," Dynamic Response of Structures, (eds.) G. Herrmann and N. Perrone, Pergamon Press, pp. 1-29, 1972.
 40. Lee, L.H.N., "Dynamic Plasticity," Hud. Engr. Des. 27, pp. 386-398, 1974.
 41. Krajcinovic, D., "Dynamic Response of Rigid-Ideally Plastic Structures," Shock and Vibration Digest, Vol. 5, No. 2, pp. 1-8, February 1973.
 42. Witmer, E.A., Balmer, H.A., Leech, J.W., and Pian T.H.H., "Large Dynamic Deformations of Beams, Rings, Plates, and Shells," AIAA Jnl., Vol. 1, No. 8, pp. 1848-1857, 1963.
 43. Jones, N., "On the Collision Protection of Ships," Nuclear Engineering and Design, Vol. 38, pp. 229-240, 1976.
 44. Yim, S.J., "Large Deflection Response of Elastic/Viscoplastic Beams under Combined Tension and Bending," Doctoral Thesis, The Pennsylvania State University, November 1978 (contains extensive Supplemental Bibliography).

To Convert From	To	Multiply by
foot	meter (m)	3.048000 X E - 1
foot-pound-force	joule (J)	1.355818
inch	meter (m)	2.540000 X E - 2
kip (1000 lbf)	newton (N)	4.448222 X E + 3
kip/inch ² (ksi)	kilo pascal (kPa)	6.894757 X E + 3
pound-force	newton (N)	4.448222
pound-force inch	newton-meter (N·m)	1.129848 X E - 1
pound-force/inch	newton/meter (N/m)	1.751268 X E + 2
pound-force/foot ²	kilo pascal (kPa)	4.788026 X E - 2
pound-force/inch ² (psi)	kilo pascal (kPa)	6.894757
pound-mass	kilogram (kg)	4.535924 X E - 1

Table 6. Conversion factors for U.S. customary to metric (SI) units of measurement.

ANALYSIS OF THE EFFECTS OF EXPLOSIVE FUEL IGNITION ON AN AIRCRAFT NOISE SUPPRESSOR SYSTEM

V. R. Miller, E. R. Hotz, D. L. Brown
Flight Dynamics Laboratory
Wright-Patterson Air Force Base, Ohio

This paper presents the results from a test in which the door acceleration and the pressure environment were measured in an aircraft noise suppressor system, following the delayed ignition of the augmenter fuel of a turbofan engine such that an explosion of this fuel occurred. The system was instrumented with hydrophones, as well as accelerometers and a high temperature microphone. The resulting data were used to define the effects of the augmenter fuel explosion pressure on the noise suppressor system and its components.

INTRODUCTION

Stalls of turbofan engines are caused by afterburner hard starts caused by a missed or late light-off or blow-out. This is followed by an explosive auto-ignition of the fuel mixture a few seconds later by the hot exhaust gases. Augmenter blowouts result in an unburned fuel mixture being ignited explosively inside the augmenter section of the engine. A pressure wave propagates forward up the fan duct, and the resulting backpressure causes the fan and/or high pressure compressor to stall. In turn, the afterburner can be blown out again due to the fluctuation in flow caused by the repeated sequence of stall, hard start and stall of the fan and/or high pressure compressor. This chain of events can continue until the engine core does not have enough energy to accelerate. In the meantime, the combustor continues to pump hot gases into the turbine section which can overheat and suffer an overtemperature condition. This can result in turbine blade damage.

Stalls caused by augmenter blowouts have occurred during ground run-ups when snapping an aircraft engine throttle from idle to maximum afterburner. These blowouts have resulted in damage to noise suppressor systems. For example, bolts have been sheared, stiffeners broken, and welds cracked. A test program was performed by the Flight Dynamics Laboratory to determine the magnitude of the pressure at various locations within the secondary enclosure of a noise suppressor system (NSS) following delayed ignition of augmenter fuel.

DESCRIPTION OF TEST ARTICLE

The NSS used during the testing is shown in Figure 1. The aircraft was positioned in the NSS such that the aft portion of the aircraft is inside of the secondary enclosure (see Figure 2). The primary air intake mufflers (PAIM) were positioned in front of the aircraft engine inlets. The PAIM reduces the noise produced by the engine compressor, which is medium to high frequency and requires minimal acoustic treatment to achieve the required noise reduction. The secondary air intake seals around the aft portion of the aircraft and provides an acoustically treated path for the cooling air which mixes with the engine exhaust in the augmenter. The augmenter, in conjunction with the engine, acts as an eductor, causing the ambient air to flow through the secondary air intake and mix with the engine exhaust. The augmenter is sized to bring in sufficient cooling air and cause adequate mixing prior to being discharged in the exhaust muffler. The exhaust muffler directs the exhaust vertically to obtain noise attenuation by spherical dispersion and includes acoustical baffles for additional noise reduction. In the forward part of the augmenter are cooling tubes which spray water into the exhaust to limit the temperatures in the exhaust muffler to 800°F during afterburner operation of the engine. The water and water tubes also break up the engine exhaust which reduces the formation of low frequency noise which is otherwise difficult to attenuate.

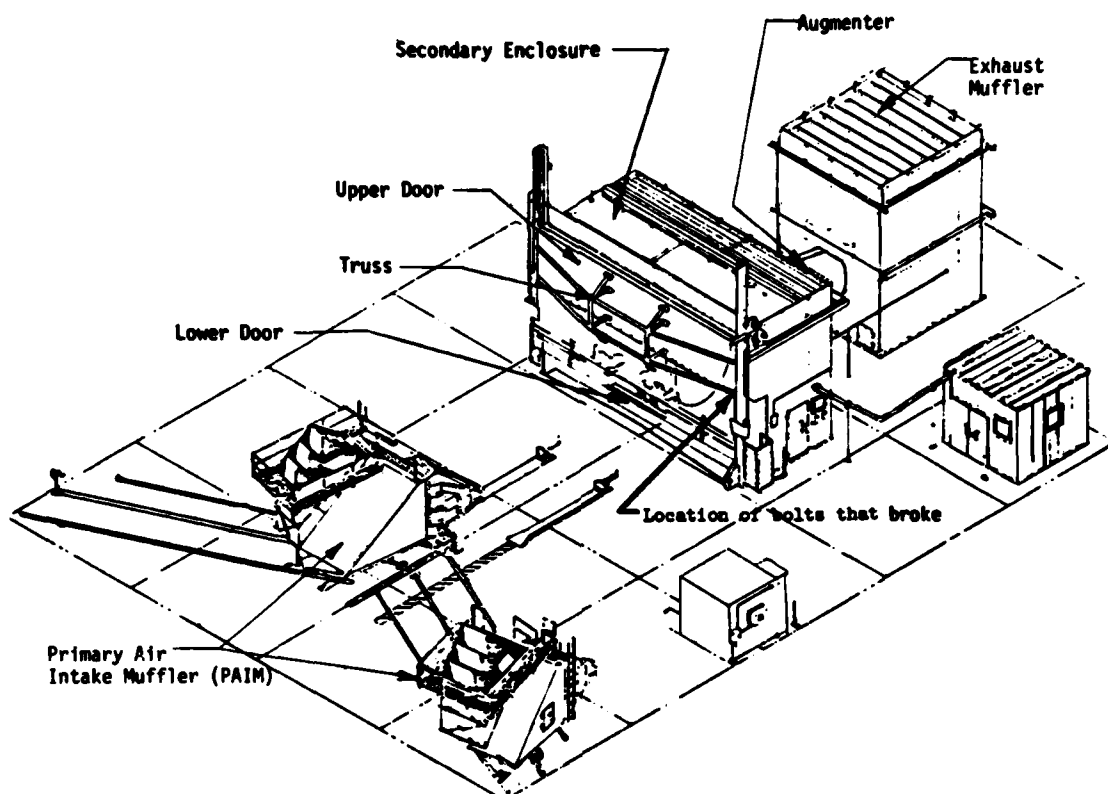


FIGURE 1 Location of Bolts Broken on Upper Door of Noise Suppressor System

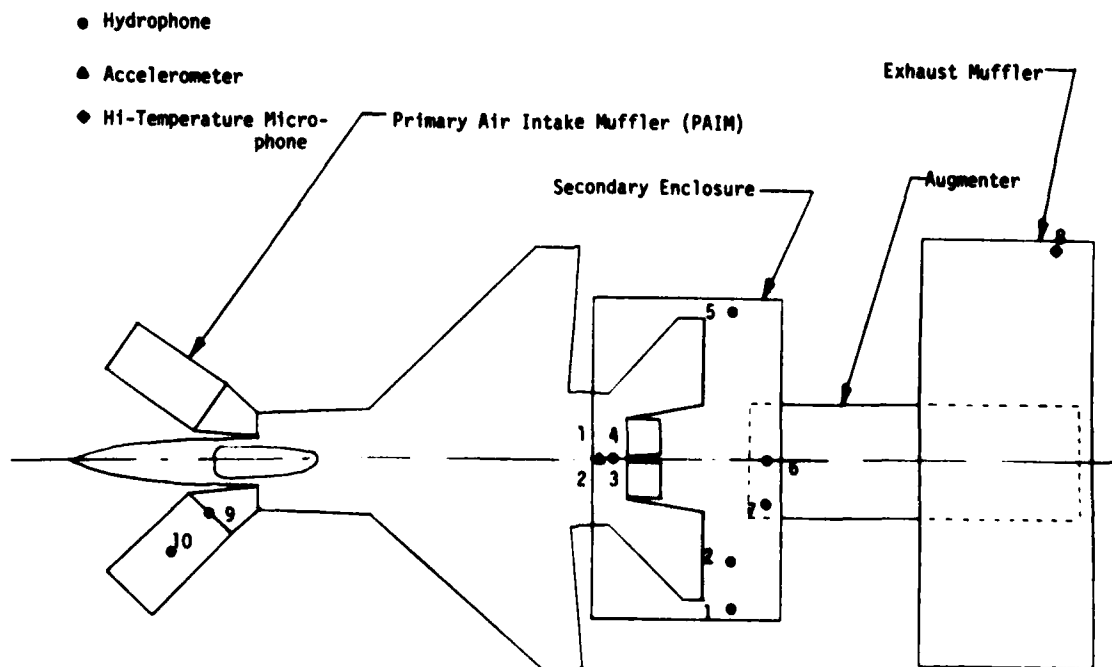


FIGURE 2 Location of Instrumentation in Noise Suppressor System

INSTRUMENTATION AND DATA REDUCTION PROCEDURES

The NSS was instrumented with nine 3/8 inch diameter hydrophones, one high temperature microphone, and two accelerometers. Hydrophones were used because of their excellent frequency response characteristics and are typically used in blast and shock measurements. The location of the instrumentation is shown in Figure 2. A complete description of the data acquisition instrumentation is given in Reference 1. All data were continuously recorded on one fourteen channel tape recorder. The magnetic data tapes, recorded during testing, were analyzed on a General Radio Analyzer and Raytheon computer. Overall pressure levels were measured with one-third octave band and narrowband analyses performed for selected transducers and test conditions. Further details concerning calibration and data reduction procedures are given in Reference 1.

TEST PROCEDURES

Data were obtained by the surveys, identified in Table I as Runs 1 through 10, which include the conditions at which the aircraft was operated. All the runs were conducted without an engine shutdown. Run number 1 included running the engine in all stages of augmentor to establish baseline data. Runs 2 through 10 attempted to simulate augmentor blowouts and auto ignitions by delaying augmentor ignition. Throttle advances to each zone of augmentor power were conducted with a

one second igniter delay. Runs 2 through 6 did not result in an explosion. With the igniter set for a 3 second delay, the throttle was advanced from military power to zone 2, with no explosion (Run number 7). The throttle was then snapped from idle to zone 3 (Run number 8) and then from idle to zone 5 (Runs number 9 and 10) to prevent the augmentor fuel from being ignited. Only Runs 9 and 10 resulted in an explosion (the desired simulation). During Run 10, the bolts at the lower left end of the upper door stiffener truss were broken (Figure 1).

TEST RESULTS

Two successful augmentor blowouts were achieved by snapping the engine throttle from idle to zone 5 afterburner with a 3 second augmentor igniter delay (Runs 9 and 10, see Table I). Figure 3 through 5 present pressure versus time plots from Run 10. These data indicate that at least two fan stalls and two compressor stalls occurred before the engine throttle was backed off. This sequence of stalls could have been repeated many more times [2], but were stopped for the purposes of this test program. These stalls had a duration of approximately 100 milliseconds at locations in the secondary enclosure (Figures 3 and 4). The predominant stall cycle's duration is shorter at locations in the PAIM than in the secondary enclosure (40 milliseconds, Figure 5). This is significant because there is more energy in a waveform which has a longer duration when compared to another

TABLE I Summary of Test Runs

Run No.	Throttle Setting	Subsequent Throttle Movement	Augmentor Igniter
1	Military	All five augmentor zones	Normal
2	Military	To Zone 1 Augmentor	One Second Delay
3	Military	To Zone 2 Augmentor	
4	Military	To Zone 3 Augmentor	
5	Military	To Zone 4 Augmentor	
6	Military	To Zone 5 Augmentor	One Second Delay
7	Military	To Zone 2 Augmentor	Three Second Delay
8	Idle	To Zone 3 Augmentor	
9*	Idle	To Zone 5 Augmentor	
10*	Idle	To Zone 5 Augmentor	Three Second Delay

*Cases for which explosions occurred

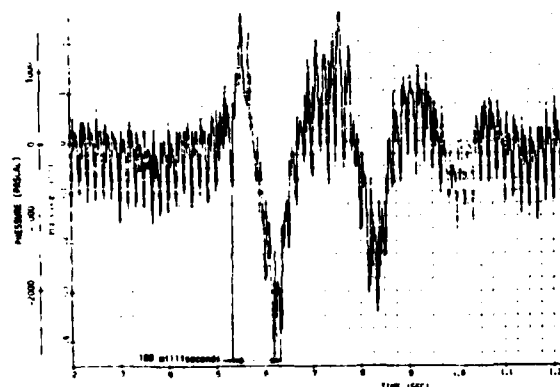


FIGURE 3 Pressure-Time Curve for Throttle Snap from Idle to A/B 5 with 3 sec- and Augmenter Igniter Delay (Run 10) - Hydrophone 1

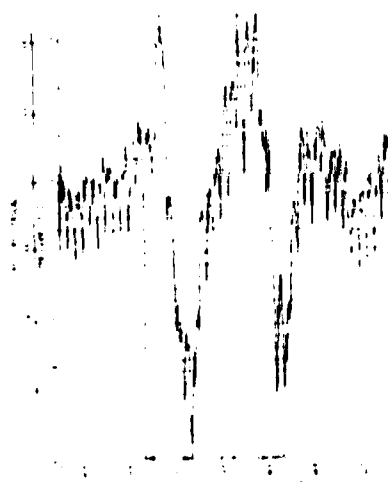


FIGURE 4 Pressure-Time Curve for Throttle Snap from Idle to A/B 5 with 3 sec- and Augmenter Igniter Delay (Run 10) - Hydrophone 4

waveform of the same pressure rise but smaller duration. A wave of longer duration will show stronger low frequency components that are important with regard to structural response and integrity. This will be shown later. These data and other unpublished data [2] show that the propagation velocity of the overpressure pulses is approximately equal to the ambient speed of sound

Large differences in pressure and waveform were seen in comparisons between plots for which an augmentor blowout was achieved to plots where a blowout was not achieved [1]. Data from Reference 3 with engine operation in

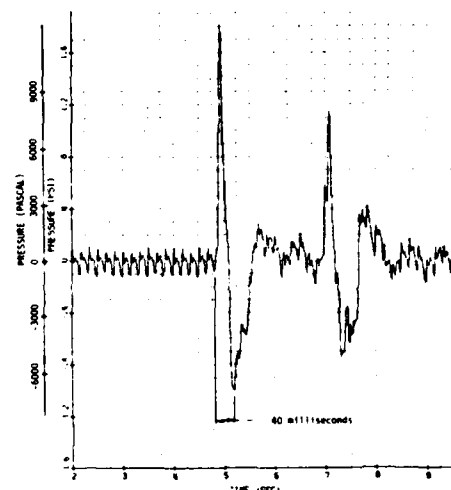


FIGURE 5 Pressure-Time Curve for Throttle Snap from Idle to A/B 5 with 3 sec- and Augmenter Igniter Delay (Run 10) - Hydrophone 10

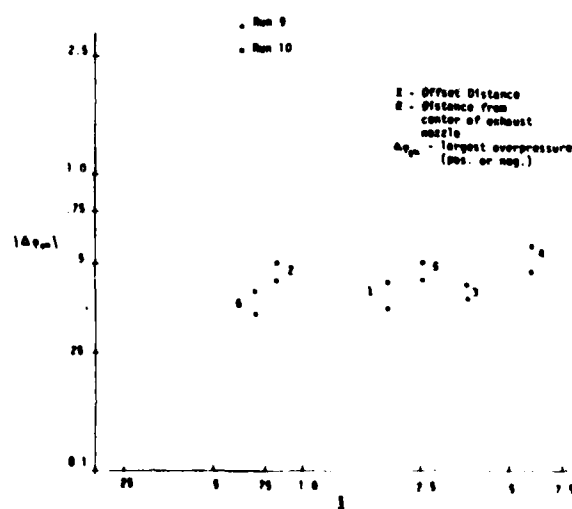
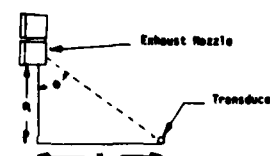


FIGURE 6 Nondimensionalized Nozzle-to-Transducer Distance as a Function of Absolute Value Of Maximum Overpressure for Hydrophones 1 through 7 from Runs 9 and 10

a normal zone 5 afterburner mode are very similar to data obtained when the engine throttle

had been snapped from idle to zone 5 afterburner. This indicates that the pressure environment in the NSS is not increased by a snap throttle movement and igniter delay unless an augmentor blowout takes place.

The absolute value of the largest overpressure is plotted against a ratio of offset distance to the distance from transducer to the engine exhaust nozzle ($\frac{X}{R}$) in Figure 6 for the hydrophones located in the secondary enclosure. This figure shows that the overpressures are reasonably constant for the range of $\frac{X}{R}$ ratios measured. Based on this, it is reasonable to assume that the pressure over the upper door is uniformly distributed.

While it is important to know how the pressure waveform varies with time, it is equally important to know how the structure of

factor ξ is equal to 0.085. This factor is important because the resultant motion of the upper door depends on the amount of damping existing in the door and surrounding structure. The period of oscillation T is the time required for the door to repeat its motion. The spacing of peaks t_0, t_1, t_2 shows that the period (equal intervals of time) was approximately 0.65 seconds, which corresponds to a response frequency (f_d) of 1.5 hertz ($T = \frac{1}{f_d}$).

This was the upper door's response frequency after the stiffener bolts had been broken. Because the breaking of these bolts detached the stiffener at one end, the upper door's stiffness and natural frequency were reduced. Therefore, it was necessary to calculate the natural frequency of the upper door before the bolts broke.

Using the peaks identified in Figure 7 as

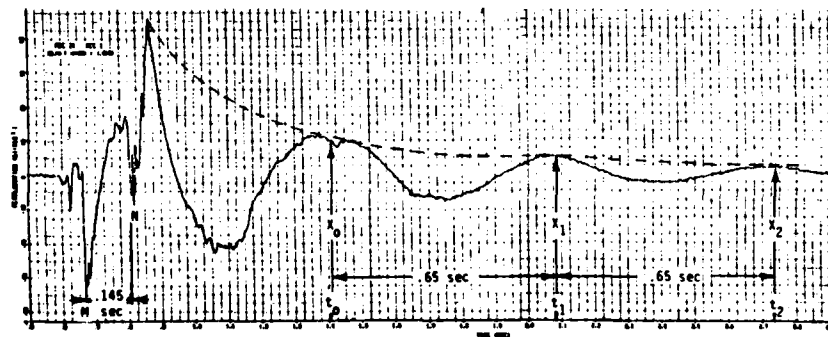


FIGURE 7 Acceleration-Time Curve for Throttle Snap from Idle to A/B 5 with 3 Second Augmentor Igniter Delay (Run 10) for Accelerometer 1 Located on Upper Door

the NSS is affected by the overpressure. Figure 7 shows an acceleration versus time plot from Run 10 of the accelerometer located on the upper door. Note that the door experiences several very large amplitude peaks. Also note the large decrease in amplitude between the first, second, and successive positive peaks. This decay is related to the damping by the concept of energy dissipation per cycle of vibration. The acceleration is approximately a damped sinusoid and can be described by exponential and sine terms of the

form $e^{-\xi f_d t} \sin(f_p t + \phi)$ where f_d is the damped natural response frequency, ξ is the ratio of equivalent viscous damping to critical damping (damping factor), f_p is the forcing (excitation) frequency, and ϕ is an arbitrary constant.

Working with the peaks identified in Figure 7, it can be shown [1] that the damping

M and N suggests that the upper door's natural frequency before the pressure pulse broke the bolts was approximately 7 hertz ($\frac{1}{0.145}$). An analysis performed in Reference 1 verified that this frequency of 7 hertz was, in fact, the upper door's natural frequency before the bolts were broken. For this analysis, the upper door was modeled as a rectangular plate consisting of two freely-supported edges and two free edges. The approximate frequency expressions of Warburton were used [4].

Figure 8 through 10 show the power spectral density (1 hertz bandwidth) for three hydrophones from Run 10. Consideration of an envelope for the PSD's in Figures 8 and 9 reveals two distinct regions. At the very low frequencies, the spectrum varies as f^2 , so that the spectrum rises at 6 dB per octave up to a maximum frequency of $\frac{\sqrt{3}}{\pi \Delta t}$ hertz

as given in Reference 5. Above this maximum frequency comes a range over which the spectrum is inversely proportional to f^2 and its value falls at 6 dB per octave. The duration of the pulse Δt for the hydrophones located in the secondary enclosure (1 through 7) was found to be approximately 100 milliseconds (Figures 3 and 4) which should yield a maxi-

mum frequency of 5 to 6 hertz ($\frac{\sqrt{3}}{\pi(.100)}$). Figures 8 and 9 do show peaks in this frequency region. Frequency peaks in this region are important for structural response, this being the region where significant resonance amplification might be expected from fundamental modes of the NSS. Since it is the low frequencies that have been increased, it is expected that the stress levels produced by the peak overpressures in the structural elements of the NSS will also be increased.

Figure 9 shows that the peak in the frequency spectrum of the pressure pulse measured on the upper door was between 4 and 6 hertz. The dynamic effects of the upper door to the pressure pulse must be considered since the excitation frequency (4 to 6 hertz, f_p) was approximately 1/3 to 1/2 of the upper door's resonant frequency (7 hertz, f_d). This means that the deflection (or acceleration) which was caused by the pressure pulse must be multiplied by a factor to obtain the dynamic response of the upper door. This ratio of maximum amplitude (or maximum acceleration) divided by the amplitude (or acceleration) caused

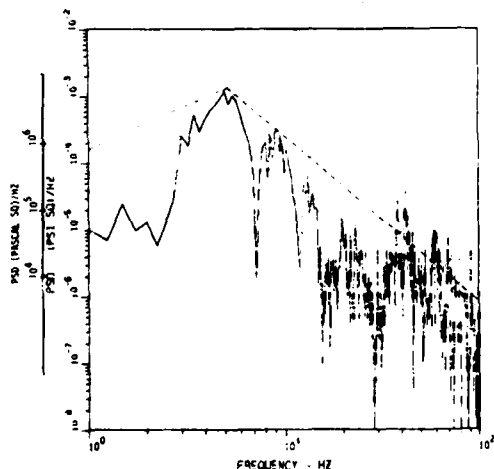


FIGURE 8 Acoustic Power Spectral Density Distribution Obtained from Throttle Snap from Idle to A/B 5 with 3 second Augmenter Igniter Delay (Run 10) - Hydrophone 1

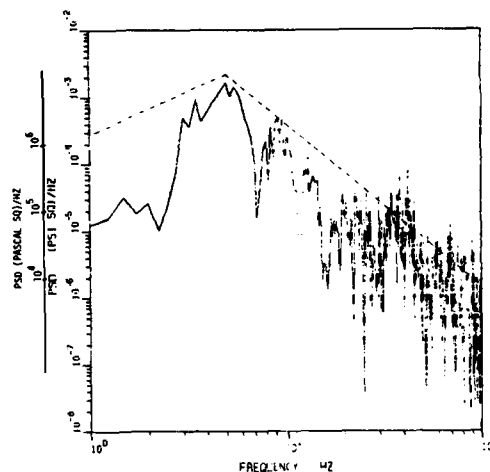


FIGURE 9 Acoustic Power Spectral Density Distribution Obtained from Throttle Snap from Idle to A/B 5 with 3 second Augmenter Igniter Delay (Run 10) - Hydrophone 4

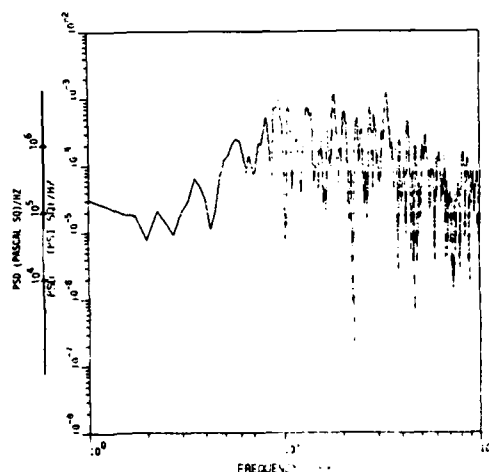


FIGURE 10 Acoustic Power Spectral Density Distribution Obtained from Throttle Snap from Idle to A/B 5 with 3 second Augmenter Igniter Delay (Run 10) - Hydrophone 10

by the pressure pulse equal to the disturbing pressure pulse was equal to:

$$K = \frac{1}{\left(\left[1 - \left(\frac{f_p}{f_d} \right)^2 \right]^2 + \left[2\zeta \frac{f_p}{f_d} \right]^2 \right)^{0.5}}$$

This term normally is referred to as the magnification factor or frequency response function.

The magnification factor for the fundamental mode has been plotted in Figure 11 with the upper door modeled as a single degree of freedom system. This figure shows the effects of various frequency ratios on the amplitude for a damping factor ζ of 0.085 when the door is subjected to a uniformly distributed pressure. For comparison, the damping factor of 0.3 was also plotted. Note that, as the frequency ratio is increased to one, the magnification factor increases. Also note that the lower the damping factor the higher the magnification factor. For the present case two frequency ratios can be considered ($\frac{4}{7} = 0.57$ and $\frac{6}{7} = 0.86$) at the damping factor of 0.085.

Figure 11 shows that the magnification factor for these two frequency ratios are approximately 2 and 4.5. This means that the dynamic response of the upper door was 2 to 4.5 times the static response. If the pressure pulse had been applied statically to the upper door, it would be deflected. However, since the excitation frequency was close to the door's natural frequency, the actual deflection was increased in proportion to this magnification factor.

An alternative analysis based on modeling the excitation as a single sinusoidal pulse and ignoring damping predicts the magnification factor for the two frequency ratios given above to be approximately 1.2 and 3 [6]. However, since the excitation in the form of stalls during the testing could have been allowed to continue many more times, the magnification factors, as predicted above by the steady-state analysis, are considered to be more appropriate.

It appeared that, based on the preceding discussion, the stiffening truss on the upper door increased the door's natural frequency in such a way that it was in the same general frequency region as the overpressure pulse. As a result, the door has greater response with stiffener attached than if it were unattached. The addition of more stiffening would change the door's natural frequency. However, it is estimated that it would require more than four times the present amount of stiffening to raise the door's natural frequency to at least twice excitation frequency region of the overpressure pulse. Damping could also be added to the door in the form of shear bars, shock absorbers, constrained layer treatment, etc., to be used in conjunction with the existing stiffener truss to lower the door's deflection when excited by an overpressure pulse. Another approach to designing the door would be to remove the present stiffening truss and use damping treatments, exclusively to lower the door's response. The actual fix which was used consisted of placing two rigid bars from the door to the back wall of the secondary enclosure so as to raise the door's natural frequency out of the excitation fre-

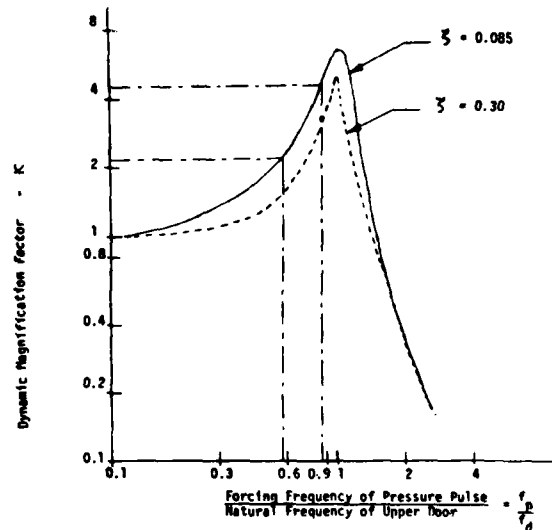


FIGURE 11 Dynamic Magnification Factor with Respect to Ratio of Forcing Frequency and Natural Frequency of Upper Door

quency region. These bars were located at the 1/3 points of the door.

CONCLUDING REMARKS

The experimental investigation reported herein indicates the following conclusions:

1. A fundamental mode (7 hertz) of the noise suppressor system's (NSS's) secondary enclosure upper door was excited by an augments blowout in which the engine throttle was snapped from idle to maximum afterburner with a three second augments igniter delay. This resulted in the failure of the bolts holding a stiffener truss on the upper door.
2. The maximum overpressure occurred in the primary air intake muffler.
3. The dynamic effects of the upper door must be considered since the excitation frequency of blowout (4 to 6 hertz) was close to the NSS upper door fundamental resonance (7 hertz). Considering these dynamic effects showed that the dynamic response of the upper door was 2 to 4.5 times the static pressure.

REFERENCES

1. Miller, et al, "Noise Suppressor Overpressurization Test," AFFDL-TM-78-114-FBE, December 1978.

2. Private communication with M. Schmidt of the Aero-Propulsion Laboratory, Turbine Engine Division, Wright-Patterson Air Force Base, Ohio.
3. Miller, et al, "Acoustic and Vibration Survey of an Engine Operating in a Test Cell," AFFDL-TM-76-99-FBE, September 1976.
4. Warburton, "The Vibration of Rectangular Plates," Proceedings of the Institute of Mechanical Engineers, Serial A, Vol. 168, No. 12, pp. 371-384, 1954.
5. Johnson and Robinson, "Loudness of Sonic Bangs," Acustica, Vol. 21, pp. 307-317. 1969.
6. Harris, C.M., and Crede, C.E., ed, Shock and Vibration Handbook, 2nd ed., p. 8-40, McGraw - Hill, New York, 1976.

FEASIBILITY STUDY FOR THE SURFACE IMPULSE LOADING
OF STRUCTURES USING MILD DETONATING FUZE

D. L. Shirey and F. H. Mathews
Sandia National Laboratories
Explosives Testing Organization 1533
Albuquerque, NM 87185

The possibility of impulsively loading the surface of large structures at relatively low impulse levels by using Mild Detonating Fuze (MDF) has been studied. The impulse is obtained when a metal spray driven by detonation of the MDF explosive core strikes an adjacent target resulting in momentum transfer to the target surface. The performance of two common types of MDF has been measured. Possible interactions between two parallel, detonating strands of MDF have been observed and found to be insignificant. Experimental results are compared. The impulse imparted to flat plate targets was observed using a pulse radiographic technique. Then these results were compared to a computational model which treats the target-spray interaction as an inelastic impact, reasonable agreement was obtained for the normal component of impulse.

INTRODUCTION

The surface loading of large structures at impulse levels of less than 200 Pa.s (2000 Taps) is of interest during weapon system development. Existing impulse loading techniques, such as light-initiated explosive [1-5] and magnetically driven flyer plates [6], have not been utilized for structures exceeding 75 cm in diameter and/or 200 cm in length. British workers of the Atomic Weapons Research Establishment have employed Mild Detonating Fuze (MDF) in small structural loading experiments conducted in a vacuum chamber. Lindberg [7,8], of Stanford Research Institute, has proposed using explosions of MDF as a possible means of delivering the desired impulse to these larger structures. The results of subsequent investigations made at Sandia National Laboratories are presented in this paper.

The experimental portion of this feasibility study includes measurements of explosive propagation rate and expanding sheath velocity for two

types of lead MDF; 1.06 g/m (5 grain/ft) RDX core and 0.43 g/m (2 grain/ft) PETN core. Interactions between the expanding spray from two adjacent MDF strands detonated simultaneously were observed, as well as particle patterns on witness planes parallel to the strands. Position and thickness of the expanding lead spray was measured at radii of interest allowing an estimate of the mean pressure delivered to target surface. Amplitude and distribution of impulse imparted to small area targets were determined and compared to a computational model. All data were collected by making accurately timed single and multiple exposure shadowgraphs using a pulsed x-ray source.

ANALYSIS

In order to develop a mathematical model of the reaction of a target surface oriented parallel to exploding strands of MDF, appropriate initial assumptions are made. First, after the explosive detonation, the expanding lead sheath is considered to be a uniform cylindrical cloud of mass m

moving outward at a constant velocity v . Then, the metal spray which strikes the target surface transfers its momentum inelastically. Finally, the component of momentum acting normal to the surface creates a net normal impulse on the target while tangential momentum components are resisted by tensile forces in the structure and produce no net tangential momentum. A schematic of geometry and designations is given in Fig. 1.

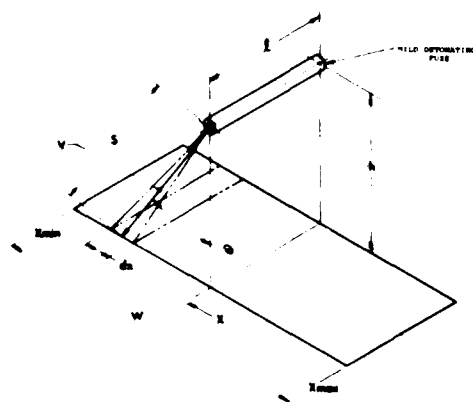


Figure 1
Problem Geometry for a Flat Surface

The radial velocity of the MDF sheath is given in terms of the core explosive's characteristic Gurney [9,10] velocity ($\sqrt{2E}$), by:

$$v = \frac{\sqrt{2E}}{\sqrt{\frac{m}{C} + 0.5}} \quad (1)$$

where m is the MDF sheath mass and C is the mass of the explosive core.

Assuming an inelastic impact, the local normal impulse transferred to a flat target is given by:

$$I_n = \frac{mv \cos^2 \theta}{2\pi l S} \quad (2)$$

where m is the mass of the expanding metal sheath, h is the target plane's separation from the MDF rod, θ is the angular orientation, l is the target length, and S is the radial distance to the point of interest. The tangential component of impulse is given by:

$$I_t = \frac{mv \sin \theta \cos \theta}{2\pi l S} \quad (3)$$

The total momentum M_n imparted to a target of width w where:

$$W = x_{\min} - x_{\max}$$

is:

$$M_n = \frac{mv}{2\pi} \left[\frac{x_{\max}}{\sqrt{x_{\max}^2 + h^2}} - \frac{x_{\min}}{\sqrt{x_{\min}^2 + h^2}} \right] \quad (4)$$

A plot of calculated impulse versus surface position and strand-to-surface spacing is shown in Fig. 2.

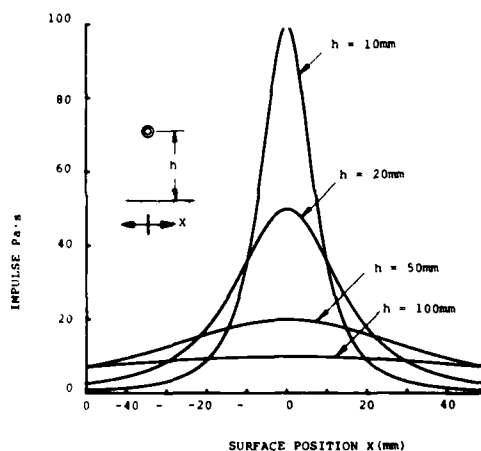


Figure 2
Computed Normal Impulse
Distribution from One MDF Rod

For this example, the PETN explosive loading (C) is 0.43 g/m (2 grain/ft), the lead sheath mass (m) is 11 g/m, and the Gurney velocity ($\sqrt{2E}$) is 2938 m/s giving a spray velocity of 570 m/s. Impulses from multiple rods may be calculated by super position of Eqs. 2 or 3. This requires an additional assumption that the fragment clouds from adjacent strands of MDF do not interact. Experiments which will be described later show that this assumption is valid. A plot of calculated impulse for two rods spaced 12.7 mm apart is shown in Fig. 3. MDF properties are the same as in Fig. 2.

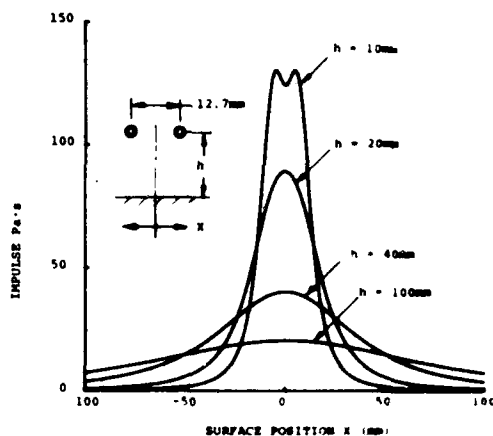


Figure 3
Computed Normal Impulse
Distribution for Two MDF Rods
Spaced 12.7 mm Apart

When a large array of evenly spaced MDF strands are used, some minimum relationship between spacing and target-to-strand separation is required in order to produce a reasonably uniform impulse. The impulse distribution calculated near the edge of a 20 rod array is shown in Fig. 4.

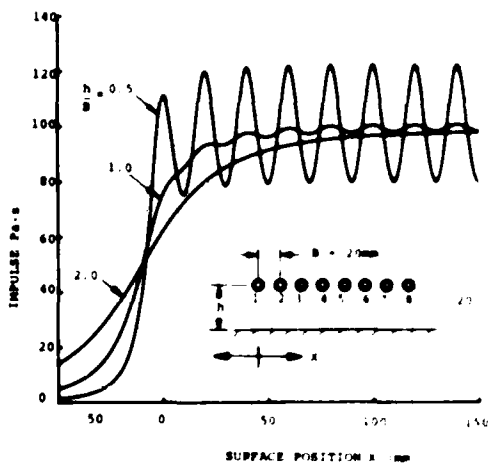


Figure 4
Computed Impulse Distribution
Near the Edge of a 20 Rod Array
at Various Separations From
the Target Surface

Rod properties are the same as before. Whenever the relative spacing

$$\frac{h}{B} \approx 1 \quad \left(\text{where } B \text{ equals the space between two adjacent rods} \right)$$

this figure indicates an insignificant ripple in the impulse. However, a relative spacing near one is desirable since this produces the most rapid rise to a nearly uniform impulse value.

When a large number of rods are placed in a uniform array, the average impulse is given in terms of the space between the rods by

$$I = \frac{V}{B} \left(\frac{m}{L} \right)$$

The term (vm/L) is a specific performance property of the MDF which measures the momentum transferred to a unit length of a flat target by a single strand of explosive. Computed values for the momentum per unit length of the two sizes of lead sheathed MDF employed in our experimental program were 43.3 Pa.s/mm for 5 grain/ft RDX core, and 20 Pa.s/mm for 2 grain/ft PETN core.

Since the experiments were carried out under atmospheric conditions, possible aerodynamic effects were investigated by considering the drag acting upon individual spray particles as they move through the air. For this calculation, it was assumed that a typical lead particle is a cube with one-fourth the original case thickness moving independently of other particles through the air. Thus, the cube has dimensions of 0.85 mm, a mass of 6.9 mg, and is moving initially at 570 m/s. Our calculations indicate that this particle will penetrate through 120 mm of air before losing 10 percent of its initial velocity.

Another possible model of drag effects considers that all air surrounding the MDF must be displaced by the lead spray. This model yields a much higher estimate of air drag. Experiments to be discussed later support the individual particle drag model and show that, for the maximum

target-to-rod spacing of interest (120 mm), air drag does not have an important effect upon momentum transfer to a target surface.

Since the MDF impulse loading technique would eventually be employed during testing of a cylindrical surface, an effort was made to design a realistic explosive assembly. The normal impulse on a cylindrical surface is given by

$$I_n = I \cos \theta$$

when the geometry is designed in Fig. 5 whenever the spacing between MDF



Figure 5
Problem Geometry for a Cylinder

strands and the cylinder is much less than the cylinder radius, the contribution due to the angle θ is insignificant and Eq. 2 is a good approximation. In the case of a cylindrical target, no single measure may be given similar to the specific performance property of Eq. 5. Since some of the metal spray which would strike a flat surface instead misses the curved surface, the impulse delivered by a single rod decreases with smaller cylinder radius.

Two cylinder diameters were chosen for the design study: 610 and 2400 mm with a desired maximum impulse of 70 Pa.s distributed as a cosine θ over half the surface. The minimum MDF-to-surface spacing was varied from 20 to 100 mm. Results are shown in Figs. 6 through 9. These plots indicate that a relatively large rod-to-surface spacing produces the most uniform loading. A ripple in the impulse loading is expected even at relatively

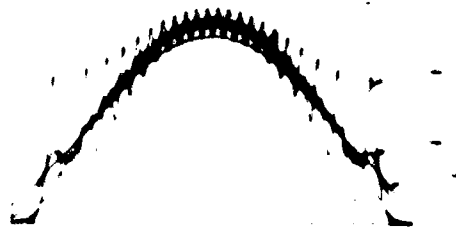


Figure 6
Impulse Distribution for Various Standoffs When a 610 mm Diameter Cylinder is Loaded by 22 Strands of 2 grain MDF



Figure 7
Impulse Distribution for Various Standoffs When a 610 mm Diameter Cylinder is Loaded by 10 Strands of 5 grain MDF

large spacing near the plus or minus 90 degree positions. When 50 mm or larger spacing is used with the 2 grain MDF, the loading is nearly free of ripple over the surface between plus and minus 60 degrees. A spacing of 100 mm is required to produce a uniform load over the same surface when 5 grain MDF is used.

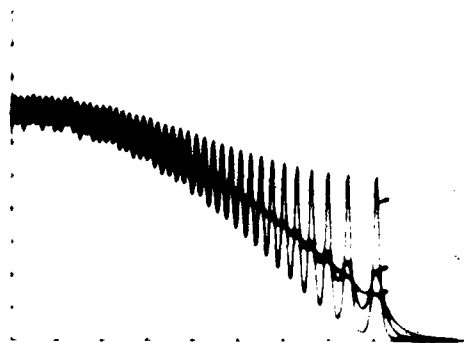


Figure 8
Impulse Distribution for Various
Standoffs When a 2400 mm Diameter
Cylinder is Loaded by 84 Strands
of 2 grain MDF

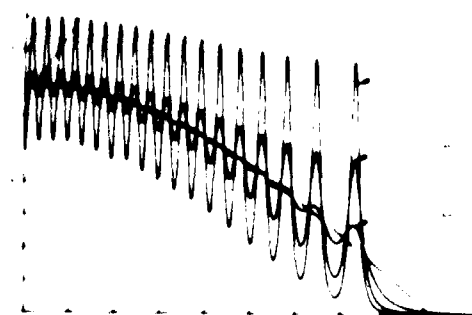


Figure 9
Impulse Distribution for Various
Standoffs When a 2400 mm Diameter
Cylinder is Loaded by 36 Strands
of 5 grain MDF

For the impulse level studied, a minimum rod-to-target spacing of 20 mm is judged acceptable [11] when 2 grain MDF is used to excite membrane response in a cylindrical structure. A minimum rod spacing of 50 mm is required when 5 grain MDF is used. Load uniformity would improve at higher impulse levels and smaller minimum spacings would be acceptable. A consequence of large spacing is a reduction in mean pressure since the

metal spray will strike the target over a longer time interval.

EXPERIMENT

Experimental verification of computed or published parameters for mild detonating fuze was obtained by performing 38 small-scale tests. Two types of MDF were readily available for study: 2 grain/ft lead sheathed with a PETN core, and 5 grain/ft lead sheathed with an RDX core. Test objectives were twofold; specific properties of each type of MDF were determined and impulses imparted to two types of target materials were measured.

All dynamic measurements were obtained by making x-ray shadowgraphs of the event using a 150 kV, multi-channel pulse x-ray source. By controlling the time intervals between pulses and making direct measurement of object positions on x-ray film, velocities of interest were determined. Masses of the lead sheathing materials were measured by weighing known lengths of each type of MDF. Measured MDF properties are given in Table 1.

Table 1
Properties of Mild Detonating Fuze

A fundamental property of the MDF is the detonation wave velocity. Our measurements yielded 7340 m/s for the 5 grain RDX core and 6700 m/s for the 2 grain PETN core.

Since the analytical model for adjacent strands of MDF assumes no interaction between the expanding lead sheaths, experiments were performed in an effort to determine if interaction actually occurs and, if so, to determine the influence on the calculational and experimental results. Several tests were performed using both 2 and 5 grain MDF. Both side and end views of adjacent strands being detonated simultaneously were taken. Typical radiographs are shown in Figs. 10 and 11. Two observations made while studying these radiographs indicate that both the collision of lead particles and possible subsequent jetting effects are minimal. The

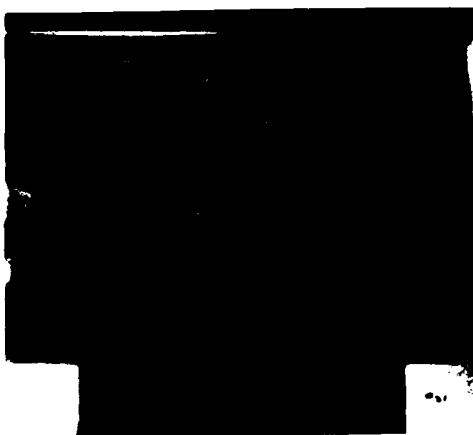


Figure 10
Interaction Study, 2 grain MDF
Strands 50.8 mm Apart, Side View

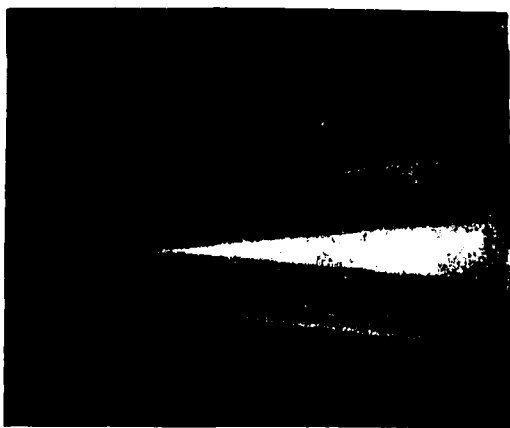


Figure 11
Interaction Study, 5 grain MDF
Strands 50.8 mm Apart, Side View

angle formed by the outer boundary of the conical cloud should change after the clouds meet if significant interaction exists. Also, the apparent

density of the clouds should change after the clouds meet. Neither of these conditions appears important in any of the several radiographs studied. In all cases, these interactions were judged to be insignificant.

For all end view experiments in which the MDF was oriented parallel to the x-ray beam and normal to the film, the strands were supported on a 6.35-mm thick steel plate containing a 12.7-mm wide slot positioned normal to the strands (see Fig. 12). Detonation

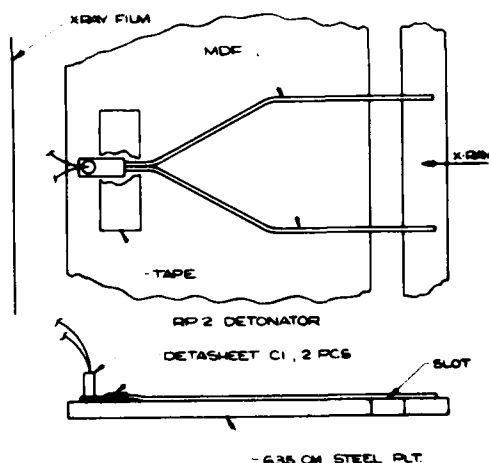


Figure 12
Typical Test Setup, 2 Strand End View

of the MDF produced a clean, 12.7-mm long conically expanding spray on the opposite side of the plate. Thus, in the x-ray image, the observed radial spray dispersion was almost entirely due to a radial velocity gradient. Without the slot, both radial dispersion and effects due to axial dispersion would have been superimposed.

An effort was made to predict the mean pressure anticipated at a target surface 100 mm away from the detonating MDF. An end view radiograph was made of the expanding lead particle cloud. A single exposure was timed to occur at the desired cloud radius and a spray thickness measurement was made (see Fig. 13). From this data:

$$\text{Pressure} = \frac{\text{Impulse} \times \text{Spray Velocity}}{\text{Thickness}}$$

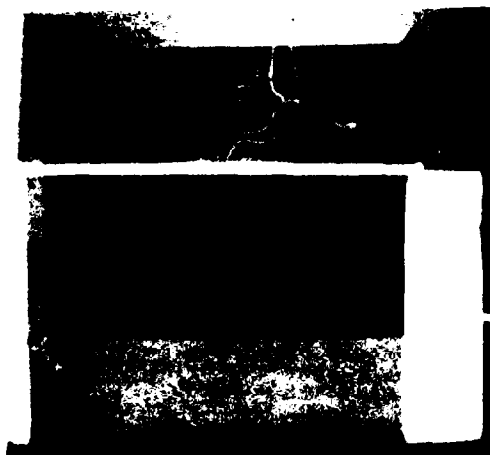


Figure 13
End View 5 grain MDF, Sheath
Expanded to 101 mm Radius

For an impulse of 70 Pa.s and a cloud thickness of 6.6 mm, a mean pressure of 7.5 MPa (74 bar) was calculated.

For all experiments, a sheet of white display board was used to protect the x-ray film holder from lead fragments. The display board also served to record the fragment spray pattern at a distance of approximately 75 mm (see Fig. 14).

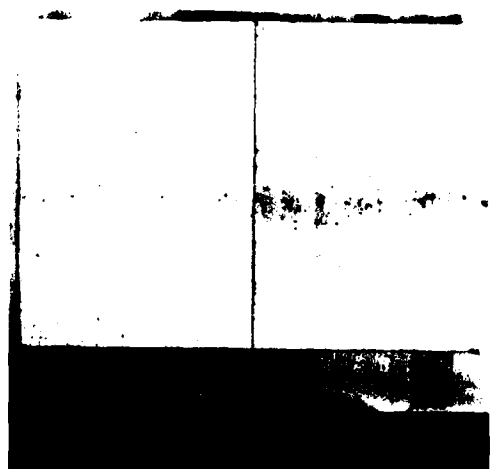


Figure 14
Passive Witness of Lead Sheath
Pattern, 75 mm Strand to Surface

Based upon the fragment pattern, it was concluded that the 5 grain MDF was superior to 2 grain since it yielded a finer, more-evenly dispersed cloud of particles.

Of the 38 tests conducted, 17 involved loading target surfaces and measuring the impulse imparted by the lead spray. A typical test setup is shown in Fig. 15. In all cases, an



Figure 15
Typical Test Setup for Target Impact

attempt was made to measure impulse imparted to individual, symmetrically located target areas. The initial 8 experiments employed 12 aluminum wedges, each with a surface area of 0.806 cm^2 and a mass of 0.775 g (see Fig. 16). Wedge centers were evenly

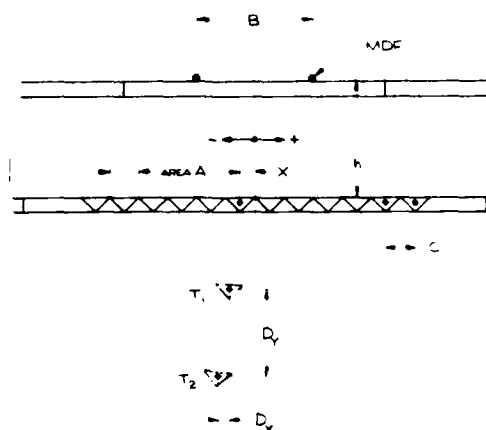


Figure 16
Schematic of Typical Test Setup
with Computational Terms

spaced 12.7 mm apart. A double-exposure radiograph was taken with timing set to obtain images in which target coupons were displaced significantly. A radiograph of a typical test is shown in Fig. 17. Setup parameters are summarized in Table II. Wedge displacements were



Figure 17
Radiograph of Test 19; Two Exposures
Single Strand MDF; 2.54 cm from
Target Surface

TABLE II. TEST PARAMETERS

Test No.	Strand	Strand No.	Strand Size (mm)	Strand Weight (g)	Strand Length (cm)	Strand Thickness (mm)	Strand Width (mm)	Strand Height (mm)	Strand Depth (mm)	Strand Volume (cm ³)	Strand Density (g/cm ³)	Strand Material
17	101	1	12.7	1.0	10.0	1.0	1.0	1.0	1.0	1.0	1.0	Brass
18	101	1	12.7	1.0	10.0	1.0	1.0	1.0	1.0	1.0	1.0	Brass
19	101	1	12.7	1.0	10.0	1.0	1.0	1.0	1.0	1.0	1.0	Brass
20	101	1	12.7	1.0	10.0	1.0	1.0	1.0	1.0	1.0	1.0	Brass
21	101	1	12.7	1.0	10.0	1.0	1.0	1.0	1.0	1.0	1.0	Brass
22	101	1	12.7	1.0	10.0	1.0	1.0	1.0	1.0	1.0	1.0	Brass
23	101	1	12.7	1.0	10.0	1.0	1.0	1.0	1.0	1.0	1.0	Brass
24	101	1	12.7	1.0	10.0	1.0	1.0	1.0	1.0	1.0	1.0	Brass
25	101	1	12.7	1.0	10.0	1.0	1.0	1.0	1.0	1.0	1.0	Brass
26	101	1	12.7	1.0	10.0	1.0	1.0	1.0	1.0	1.0	1.0	Brass
27	101	1	12.7	1.0	10.0	1.0	1.0	1.0	1.0	1.0	1.0	Brass
28	101	1	12.7	1.0	10.0	1.0	1.0	1.0	1.0	1.0	1.0	Brass
29	101	1	12.7	1.0	10.0	1.0	1.0	1.0	1.0	1.0	1.0	Brass
30	101	1	12.7	1.0	10.0	1.0	1.0	1.0	1.0	1.0	1.0	Brass
31	101	1	12.7	1.0	10.0	1.0	1.0	1.0	1.0	1.0	1.0	Brass
32	101	1	12.7	1.0	10.0	1.0	1.0	1.0	1.0	1.0	1.0	Brass
33	101	1	12.7	1.0	10.0	1.0	1.0	1.0	1.0	1.0	1.0	Brass
34	101	1	12.7	1.0	10.0	1.0	1.0	1.0	1.0	1.0	1.0	Brass
35	101	1	12.7	1.0	10.0	1.0	1.0	1.0	1.0	1.0	1.0	Brass
36	101	1	12.7	1.0	10.0	1.0	1.0	1.0	1.0	1.0	1.0	Brass
37	101	1	12.7	1.0	10.0	1.0	1.0	1.0	1.0	1.0	1.0	Brass
38	101	1	12.7	1.0	10.0	1.0	1.0	1.0	1.0	1.0	1.0	Brass
39	101	1	12.7	1.0	10.0	1.0	1.0	1.0	1.0	1.0	1.0	Brass
40	101	1	12.7	1.0	10.0	1.0	1.0	1.0	1.0	1.0	1.0	Brass
41	101	1	12.7	1.0	10.0	1.0	1.0	1.0	1.0	1.0	1.0	Brass
42	101	1	12.7	1.0	10.0	1.0	1.0	1.0	1.0	1.0	1.0	Brass
43	101	1	12.7	1.0	10.0	1.0	1.0	1.0	1.0	1.0	1.0	Brass
44	101	1	12.7	1.0	10.0	1.0	1.0	1.0	1.0	1.0	1.0	Brass
45	101	1	12.7	1.0	10.0	1.0	1.0	1.0	1.0	1.0	1.0	Brass
46	101	1	12.7	1.0	10.0	1.0	1.0	1.0	1.0	1.0	1.0	Brass
47	101	1	12.7	1.0	10.0	1.0	1.0	1.0	1.0	1.0	1.0	Brass
48	101	1	12.7	1.0	10.0	1.0	1.0	1.0	1.0	1.0	1.0	Brass
49	101	1	12.7	1.0	10.0	1.0	1.0	1.0	1.0	1.0	1.0	Brass
50	101	1	12.7	1.0	10.0	1.0	1.0	1.0	1.0	1.0	1.0	Brass
51	101	1	12.7	1.0	10.0	1.0	1.0	1.0	1.0	1.0	1.0	Brass
52	101	1	12.7	1.0	10.0	1.0	1.0	1.0	1.0	1.0	1.0	Brass
53	101	1	12.7	1.0	10.0	1.0	1.0	1.0	1.0	1.0	1.0	Brass
54	101	1	12.7	1.0	10.0	1.0	1.0	1.0	1.0	1.0	1.0	Brass
55	101	1	12.7	1.0	10.0	1.0	1.0	1.0	1.0	1.0	1.0	Brass
56	101	1	12.7	1.0	10.0	1.0	1.0	1.0	1.0	1.0	1.0	Brass
57	101	1	12.7	1.0	10.0	1.0	1.0	1.0	1.0	1.0	1.0	Brass
58	101	1	12.7	1.0	10.0	1.0	1.0	1.0	1.0	1.0	1.0	Brass
59	101	1	12.7	1.0	10.0	1.0	1.0	1.0	1.0	1.0	1.0	Brass
60	101	1	12.7	1.0	10.0	1.0	1.0	1.0	1.0	1.0	1.0	Brass
61	101	1	12.7	1.0	10.0	1.0	1.0	1.0	1.0	1.0	1.0	Brass
62	101	1	12.7	1.0	10.0	1.0	1.0	1.0	1.0	1.0	1.0	Brass
63	101	1	12.7	1.0	10.0	1.0	1.0	1.0	1.0	1.0	1.0	Brass
64	101	1	12.7	1.0	10.0	1.0	1.0	1.0	1.0	1.0	1.0	Brass
65	101	1	12.7	1.0	10.0	1.0	1.0	1.0	1.0	1.0	1.0	Brass
66	101	1	12.7	1.0	10.0	1.0	1.0	1.0	1.0	1.0	1.0	Brass
67	101	1	12.7	1.0	10.0	1.0	1.0	1.0	1.0	1.0	1.0	Brass
68	101	1	12.7	1.0	10.0	1.0	1.0	1.0	1.0	1.0	1.0	Brass
69	101	1	12.7	1.0	10.0	1.0	1.0	1.0	1.0	1.0	1.0	Brass
70	101	1	12.7	1.0	10.0	1.0	1.0	1.0	1.0	1.0	1.0	Brass
71	101	1	12.7	1.0	10.0	1.0	1.0	1.0	1.0	1.0	1.0	Brass
72	101	1	12.7	1.0	10.0	1.0	1.0	1.0	1.0	1.0	1.0	Brass
73	101	1	12.7	1.0	10.0	1.0	1.0	1.0	1.0	1.0	1.0	Brass
74	101	1	12.7	1.0	10.0	1.0	1.0	1.0	1.0	1.0	1.0	Brass
75	101	1	12.7	1.0	10.0	1.0	1.0	1.0	1.0	1.0	1.0	Brass
76	101	1	12.7	1.0	10.0	1.0	1.0	1.0	1.0	1.0	1.0	Brass
77	101	1	12.7	1.0	10.0	1.0	1.0	1.0	1.0	1.0	1.0	Brass
78	101	1	12.7	1.0	10.0	1.0	1.0	1.0	1.0	1.0	1.0	Brass
79	101	1	12.7	1.0	10.0	1.0	1.0	1.0	1.0	1.0	1.0	Brass
80	101	1	12.7	1.0	10.0	1.0	1.0	1.0	1.0	1.0	1.0	Brass
81	101	1	12.7	1.0	10.0	1.0	1.0	1.0	1.0	1.0	1.0	Brass
82	101	1	12.7	1.0	10.0	1.0	1.0	1.0	1.0	1.0	1.0	Brass
83	101	1	12.7	1.0	10.0	1.0	1.0	1.0	1.0	1.0	1.0	Brass
84	101	1	12.7	1.0	10.0	1.0	1.0	1.0	1.0	1.0	1.0	Brass
85	101	1	12.7	1.0	10.0	1.0	1.0	1.0	1.0	1.0	1.0	Brass
86	101	1	12.7	1.0	10.0	1.0	1.0	1.0	1.0	1.0	1.0	Brass
87	101	1	12.7	1.0	10.0	1.0	1.0	1.0	1.0	1.0	1.0	Brass
88	101	1	12.7	1.0	10.0	1.0	1.0	1.0	1.0	1.0	1.0	Brass
89	101	1	12.7	1.0	10.0	1.0	1.0	1.0	1.0	1.0	1.0	Brass
90	101	1	12.7	1.0	10.0	1.0	1.0	1.0	1.0	1.0	1.0	Brass
91	101	1	12.7	1.0	10.0	1.0	1.0	1.0	1.0	1.0	1.0	Brass
92	101	1	12.7	1.0	10.0	1.0	1.0	1.0	1.0	1.0	1.0	Brass
93	101	1	12.7	1.0	10.0	1.0	1.0	1.0	1.0	1.0	1.0	Brass
94	101	1	12.7	1.0	10.0	1.0	1.0	1.0	1.0	1.0	1.0	Brass
95	101	1	12.7	1.0	10.0	1.0	1.0	1.0	1.0	1.0	1.0	Brass
96	101	1	12.7	1.0	10.0	1.0	1.0	1.0	1.0	1.0	1.0	Brass
97	101	1	12.7	1.0	10.0	1.0	1.0	1.0	1.0	1.0	1.0	Brass
98	101	1	12.7	1.0	10.0	1.0	1.0	1.0	1.0	1.0	1.0	Brass
99	101	1	12.7	1.0	10.0	1.0	1.0	1.0	1.0	1.0	1.0	Brass
100	101	1	12.7	1.0	10.0	1.0	1.0	1.0	1.0	1.0	1.0	Brass

101. See Figure 14 for dimensions.
102. One strand only; all other strands used the same.
103. Targets spaced 12.7 mm apart.

Table II
Impulse Experiments (1)

measured in two directions: normal and parallel to the initial position of the impacted surface. Then the normal and tangential impulses were calculated using an average velocity approximation.

In an effort to achieve better correlation to theory, several other target configurations were tried. The most satisfactory targets were brass

squares measuring 9.53 mm x 0.89 mm thick. The brass target centers were much easier to locate on the x-ray exposures and yielded more consistent impulse results in the direction normal to the impacted surface. It should be noted that Test No. 32 differed significantly from the other experiments in that the brass targets were turned 90 degrees. This was done in an effort to achieve correlation with the tangential theory for the impulse delivered to the targets in the "X" direction. The total error due to setup variations and data interpretation was estimated to be plus or minus 7 percent.

An important by-product of the experiments was the development of a reliable initiation scheme for the multiple MDF strand configurations. Since possible applications of these configurations might involve many closely spaced strands, an explosive train utilizing one detonator was developed. The most successful version is illustrated in Fig. 12. This basic idea could be employed with, perhaps, one detonator for each 10 strands.

Since the theoretical analysis depends upon an inelastic collision between the lead particles and the target surface, the posttest surface condition of both the brass and aluminum surfaces was of interest. No attempt was made to measure the exact quantity of lead that remained on the target; however, it appeared that nearly all of the sheath material that struck the target at close-to-normal incidence remained embedded in the surface. As the angle of incidence became smaller, less impacting material remained embedded, especially in the brass target.

COMPARISON - ANALYSIS AND EXPERIMENT

An accurate value of the lead sheath velocity is crucial to predicting impulse delivered to a target surface. Calculations using 2930 m/s for the Gurney velocity [10] and Eq. 1 yield a velocity normal to the MDF strand axes of 570 m/s for 2 grain/ft and 660 m/s for 5 grain/ft. Side view radiographs of the expanding lead sheaths (see Figs. 10 and 11), along with the measured propagation velocities, yielded spray velocities of 580 m/s and 700 m/s, respectively. These values compare to the computed values well within experimental error.

The final portion of our experiments was an attempt to measure impulses imparted to target surfaces and compare them with computed plots similar to Figs. 3 and 4. Figure 19 compares impulse values derived from the radiograph of a single strand test in Fig. 17 with calculated values. Figure 20 makes the same comparison with values derived from a double strand test using the radiograph shown in Fig. 18. In Fig. 21, results of three repeated experiments sharing common test parameters are plotted against theory to illustrate repeatability.

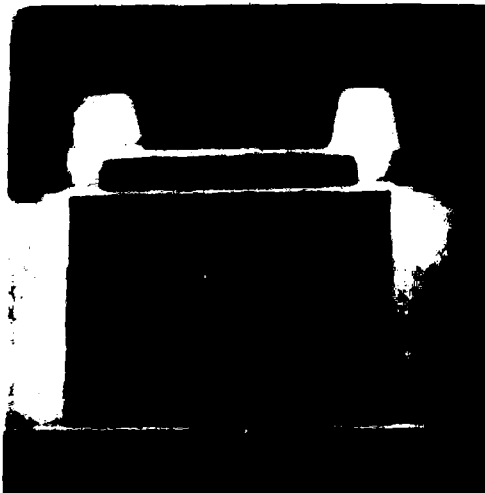


Figure 18
Radiograph of Test 30, 2 Exposures
2 Strands MDF, 5.08 cm Apart,
2.54 cm from Target Surface

Tangential impulse values were also measured and compared in all cases; the experimental values were significantly below (30 to 50 percent) the values predicted. No attempt was made to analyze the disagreement since, for the structural experiments anticipated, the desired component of impulse would be normal only and membrane forces in the structure would resist the tangential component of impulse. Also, with multiple MDF rods, tangential impulse would tend to be cancelled by overlapping sprays having plus and minus components.

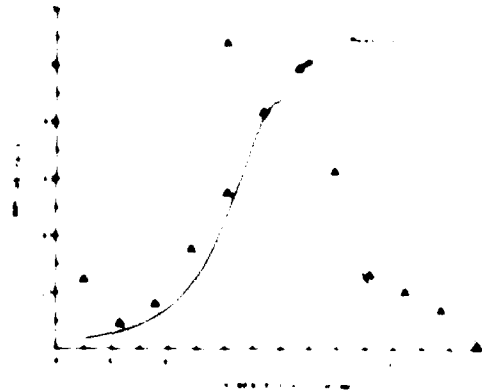


Figure 19
Comparison of Calculated and
Measured Impulse for Test 19

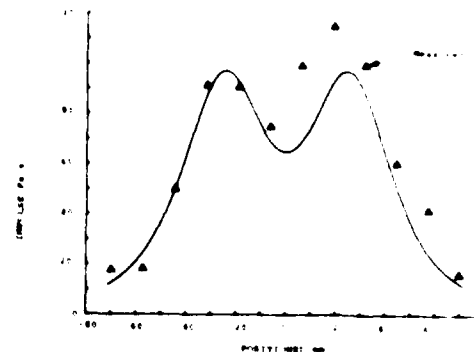


Figure 20
Comparison of Computed and Measured
Impulse for Test 30

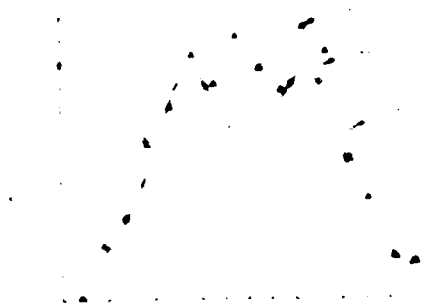


Figure 21
Comparison of Computed and Measured
Impulse for Three Identical Tests

CONCLUSIONS

Several conclusions should be drawn from the experiments and observations made. The 5 grain/ft RDX core MDF is a more attractive surface loading material than 2 grain/ft PETN core MDF. The lead spray from the 5 grain/ft is more uniform and finely dispersed while many of the 2 grain/ft particles are long strings. Also, the large number of strands of 2 grain/ft MDF required to build a test charge would result in higher fabrication costs. Only when relatively small

structures are to be loaded should 2 grain/ft MDF be considered since it would allow for closer rod spacing resulting in a more uniform loading.

Mean pressure estimations obtained by finding the loading duration and assuming a rectangular pulse indicate that the MDF loading technique would produce relatively low-average pressures of less than 1 Kbar.

The computational model used in this work should be useful for designing explosive charges suitable for loading large cylindrical structures at low impulse levels. Impulses delivered normal to the target surface may be predicted within usable accuracy limits. Tangential components are more difficult to forecast since they were significantly lower than predicted when the target surface was brass or aluminum.

When utilizing MDF under atmospheric conditions, aerodynamic effects should be considered. Preliminary calculations and experimental observations indicate little reduction in particle impact velocity at stand-to-surface distances of 100 mm or less.

The feasibility of employing the detonation of parallel strands of mild detonating fuze for impulse loading of structures has been investigated for use at relatively low impulse levels with favorable results. It is concluded that the technique should be considered for use in structural experimentation. This method, because of its simplicity, appears suitable for use in impulse testing of very large cylindrical structures.

REFERENCES

1. F. O. Hoese, C. G. Langhner, and W. E. Baker, "Simultaneous Initiation over Large Areas of a Spray Deposited Explosive," Experimental Mechanics, Vol. 8, September 1968.
2. A. B. Menzel and W. E. Baker, "The Use of Light-Initiated Explosives for Impulsive Loading of Structures," Proc. 16th Annual Meeting of the Institute of Environmental Sciences, Boston, Mass., April 1970.
3. R. A. Benham, and F. H. Mathews, "X-Ray Simulation with Light-Initiated Explosive," The Shock and Vibration Bulletin, No. 45, Part 4, June 1975.
4. R. A. Benham, "Simulation of X-Ray Blowoff Impulse Loading on a Reentry Vehicle Aft End Using Light-Initiated High Explosive," The Shock and Vibration Bulletin, No. 46, Part 1, August 3, 1976.
5. R. A. Benham, F. H. Mathews, and P. B. Higgins, "Application of Light-Initiated Explosive for Simulating X-Ray Blowoff Impulse Effects on a Full-Scale Reentry Vehicle," The Shock and Vibration Bulletin, No. 47, 1978, Supplement.
6. M. J. Forrestal, W. K. Tucker, and W. A. Von Riesenmann, "Impulse Loading of Finite Cylindrical Shells," AIAA, Vol. 13, No. 10, October 1975, pp. 1396-98.
7. Personnel communication: H. E. Lindburg, Stanford Research Institute, January 1980.
8. G. R. Abrahamson, Explosively Induced Impulses, Stanford Research Institute, Poulter Laboratories, PLTR 009-62.
9. R. W. Gurney, The Initial Velocities of Fragments from Bombs, Shells, and Grenades, BRL Report 405, 1943.
10. J. E. Kennedy, "Explosive Output for Driving Metal," Behavior and Utilization of Explosives in Engineering Design, 12th Annual Symposium ASME, published by the New Mexico Section ASME, March 2-3, 1972.
11. C. L. Julian, Acceptable Imperfections in Impulsive Loads for Simulation Tests on Circular Cylindrical Shells, Sandia Laboratories Research Report No. SC-RR-70-600, September 1970.

A THEORY FOR THE CALCULATION OF EXPLOSIVE DEPOSITION
PROFILES FROM THE SPRAY PAINTING OF
LIGHT INITIATED EXPLOSIVE

Floyd H. Mathews
Sandia National Laboratories
Albuquerque, New Mexico

When a weapon structure is exposed to X-rays, the energy deposited in the surface material may result in an impulsive pressure loading on the surface. Laboratory nuclear effects experimentation allows the study of structural response during simulation tests. Spray painted coatings of Silver Acetylide-Silver Nitrate explosive when surface initiated by an intense flash of light provide a suitable test loading. Safety considerations dictated by the initiation sensitivity of this primary explosive require that the spray process be carried out by remote control. The ability to predict deposition during design of the spray procedure is therefore important in developing an efficient and safe technique.

The processes occurring during spray painting of the explosive layer on the target surface were studied and an empirical theory of spray deposition developed. Important parameters which include explosive concentration in the atomized spray, the deposition profiles for a single pass, with deposition efficiency as a function of spacing, position and incident angle are incorporated into a numerical theory describing the space dependent explosive deposition for a single pass of the spray apparatus. When implemented into a computation of multiple overlapping passes, a reasonably complete prediction is obtained. Several geometries including flats, cylinders and cones are described. This work suggests methods for improving the spray process. Consequences of positioning inaccuracies are also studied.

INTRODUCTION

When a weapon structure is exposed to X-rays originating from a nuclear burst, sufficient energy may be deposited in the surface material causing its vaporization and subsequent blowoff. This blowoff imparts an impulsive pressure loading on the remaining surface lasting for a period of a few microseconds. During development of a weapon, vulnerability studies are conducted to assure survival at appropriate intensity of the X-ray environment.

Laboratory nuclear effects experimentation allows the study of structural response during simulation tests. Spray painted coatings of Silver Acetylide-Silver Nitrate (SASN) explosive, when surface initiated by an intense flash of light, provide a suitable test loading.

Desirable features of this laboratory technique include the ability to produce simultaneously applied impulses with intensity varying either gradually or discontinuously over complex curved surfaces. Details of experimentation employing Light Initiated Explosives have been reported at several previous Shock and Vibration Symposia and elsewhere [1-11].

Safety considerations dictated by the initiation sensitivity of this primary explosive require that the spray painting process be carried out by remote control. The ability to predict the aerial density of the explosive deposition during design of the spray procedure is therefore important in developing an efficient and safe technique.

SPRAY PROCESS

The impulse distribution desired on a test object is a function derived specifically for the particular X-ray encounter and materials involved. Typically impulse values decrease approximately as the cosine of the angle between the surface normal and the line of sight to the X-ray source. Different materials exposed to identical X-ray fluences will generally experience different impulse loadings. This situation is illustrated schematically in Figure 1 where the impulse loading is plotted for a ring composed of two materials illuminated from the side by a distant source. The objective is to design a spray painting process to apply an explosive layer which when detonated will impart an acceptable approximation of the desired impulse function.

The impulse imparted by explosive detonation on each small surface element is directly related to the local value of SASN areal density. This function has been determined from numerous tests of target samples and is given by

$$I = 0.00086 \left(\frac{M}{A} \right)^2 + 0.3795 \left(\frac{M}{A} \right); \quad 0 \leq I \leq 225$$

$$I = 0.763 \left(\frac{M}{A} \right) - 42.7; \quad 225 \leq I \quad (1)$$

where M is the explosive mass (g), A the area (M^2) and I the impulse (Pa.s). This equation applies only for the conditions of SASN formulation, spray deposition, and initiation which have become standard practice at the Sandia facility.

The machinery employed in the spray process involves using many overlapping and superimposed passes of a spray gun accomplished by either moving the gun along the surface or by moving the surface past the gun. In this respect, the process is similar to conventional painting. Removable masks placed over the surface may be used to intercept unneeded portions of the spray. Thus, the impulse function of Figure 1 could be obtained by masking material b, spraying a portion of the load on material a, and then removing the mask and completing the spray.

A cross section representing the geometry of a spray pass over a curved surface is illustrated in Figure 2. The purpose of the theory is to predict the explosive areal density M/A as a function of the parameters describing the geometry of the spray setup. These parameters include, V the spray gun traverse rate, N the number of repeated spray passes,

dM/dt the explosive mass flow rate through the spray nozzle, S the distance separating the surface point and spray gun, W the spray fan half width at S , X the surface position of the point being considered, and β the angle of the surface normal relative to the spray gun location.

Generally the atomizing air pressure and atomizing nozzle are specifically designed to disperse material over a wide strip on either side of the spray gun motion with a narrow dispersal along the Z direction, the path of the gun motion. During each spray pass a complete segment along the Z axis passes over each surface point, therefore a simplified treatment which considers only dispersal in the width direction is justified.

The explosive mass flow rate from the nozzle is given by

$$\frac{dM}{dt} = QC \quad (2)$$

where C is the explosive concentration (g/l) in the acetone carrier fluid and Q is the fluid discharge rate (l/s).

The explosive is manufactured for each application using a carefully repeated formulation and is continually stirred and pumped thru the spray gun to prevent explosive particles from settling. Mixture concentration therefore does not change from batch to batch nor during the individual spray processes. The fluid flow rate, Q , is set at a constant value by adjusting the static head at the spray gun for each spray operation.

The total mass emitted from the spray gun per unit length (l) in the traverse (Z) direction is given by

$$\frac{M}{l} = \frac{NQC}{V} \quad (3)$$

Emitted material must be either deposited somewhere on the target surface within the area described by the width of the spray fan ($2W$) and its length or the material is blown away by the atomizing air in the form of overspray. The theory assumes that material lost to overspray does not adhere elsewhere on the target surface. This assumption is correct in most cases of convex surface curvature. Concave curvatures, and in particular barriers in the form of surface bumps and ridges would require special attention not afforded by the present treatment.

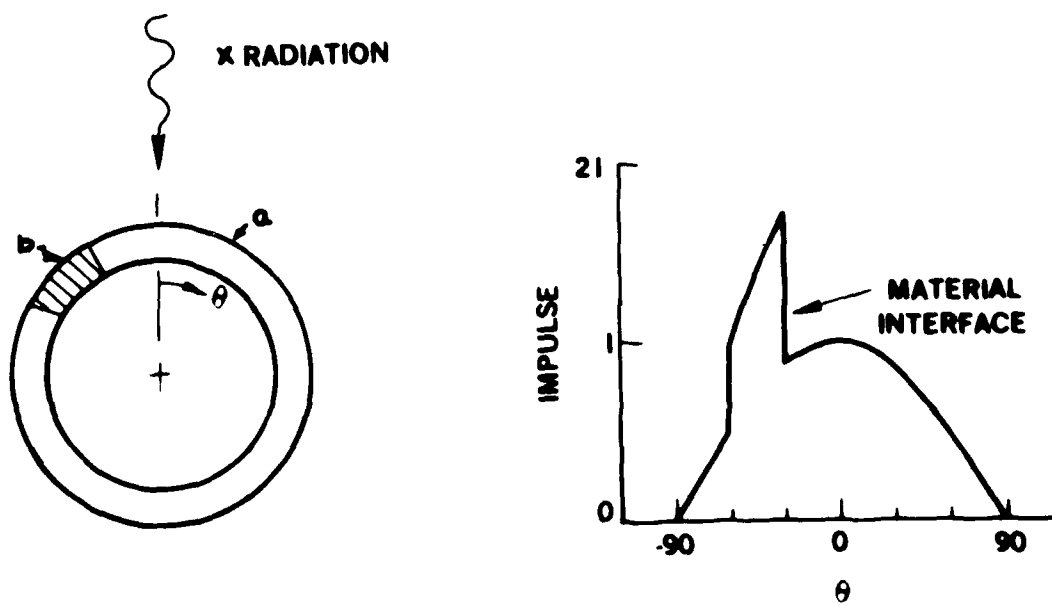


Fig. 1 - Impulse Distribution for a Ring Structure Built From Two Materials

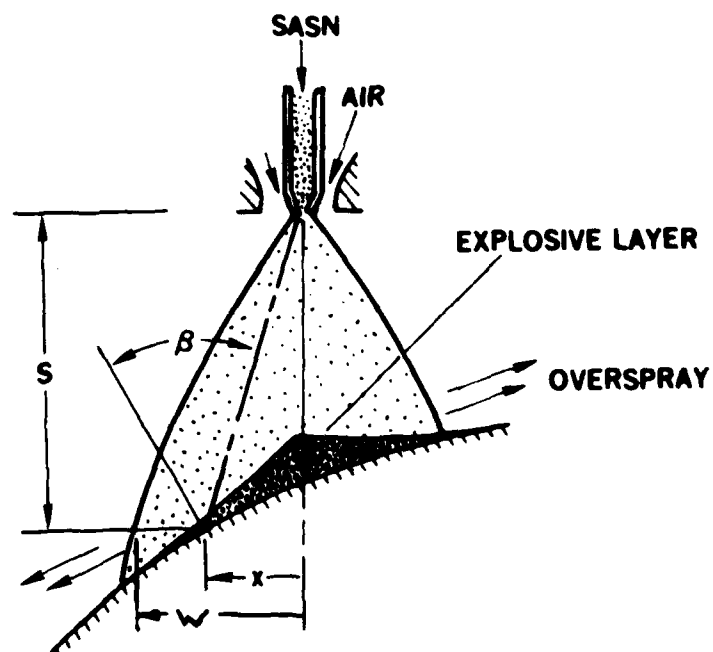


Fig. 2 - Cross Section of a Spray Pass Over a Curved Surface

Several processes must be studied to complete this theory. First, each specific spray head, atomizing air nozzle and atomizing pressure combination distributes the particles of explosive differently. A specific spray gun setup was selected as the standard, (DeVillbiss PH head with a 1.016 mm fluid nozzle at an atomizing pressure of 124 kPa). The function

$$\frac{\left(\frac{dM}{dt}\right)}{A} = f_1(S, X) \quad (4)$$

must be identified empirically where dM/dt is the mass flow rate of explosive thru an area normal to the flow at a position S, X , when the surface is not present.

Drying of the liquid droplets during their flight from the nozzle affects their adherence when they reach the target surface. Very small droplets may lose enough fluid so that they have insufficient momentum to penetrate the gas boundary layer at the target and are therefore carried into the surrounding air as an overspray. Thus, the efficiency of deposition decreases with separation to yield a function

$$E = f_2(S) \quad (5)$$

where E is the deposition efficiency. Conditions within the spray booth including temperature and possibly humidity influence efficiency.

A final process involves an additional decrease of deposition dependent upon the angle of incidence between the arriving spray flux and the surface normal depicted by β in Figure 2. Thus, an efficiency function

$$K = f_3(\beta) \quad (6)$$

dependent upon angle of incidence of the sprayed material as it approaches the target surface is required. In this relatively crude theory, possible interrelationships between these three functions are omitted resulting in an overall functional relationship

$$\frac{M}{A} = \frac{NQ}{V} f_1(S, W) f_2(S) f_3(\beta) \cos\beta. \quad (7)$$

Where the last term, $\cos\beta$, accounts for the larger area presented to the spray flux by a surface inclined to the flux. The theory sought in this paper involves identifying this function.

DEPOSITION MEASUREMENTS

Deposition was measured by placing target strips in front of the spray gun as shown in Figure 3. The static pressure at the spray nozzle was adjusted until a measured flow of 2.08 ml/s was obtained with atomizing air off. The spray gun traverse velocity was set at 125 mm/s. Fluid flow measurements given in Table 1, were taken with the gun stationary before and after completing the spray by capturing material ejected from the nozzle with the atomizing air turned off. After drying, the residual explosive solids were weighed, and the explosive mass concentration of Table 2 calculated. A reduced flow rate observed after the spray process is attributed to coating of the nozzle surface. This occurs as the flow is stopped between each spray pass when a needle valve is inserted through the fluid stream and seats on the nozzle. An explosive coating is pressed onto the nozzle sides restricting flow. The possibility of nozzle flow restriction has not been studied. Explosive mass concentration data of Table 2 indicates that this parameter may be treated as constant over a spray process.



Fig. 3 - Spray Targets for the Deposition Experiment With Strip and Circular Coupons

Three of the spray targets were flat sections placed perpendicular to the nozzle axis and centered on a stream of fluid emitted without atomizing air using both circular coupons 19 mm in diameter and long strips 19 mm wide. Two strips 165 mm long joined at the spray centerline were used at the 152 mm spacing. Three strips, 152 mm long, were placed symmetrically at the 229 mm location, and three strips, 203 mm long, were used at the 304 mm location. The fourth target was inclined to the spray by an angle of 45 degrees with its center 229 mm from the nozzle outlet. In comparison to the coupons, the strips have a much larger ratio of surface area to edge area and give the best indication of total explosive mass deposited across the spray width. In general, the average explosive mass obtained by integrating a curve drawn thru values indicated by small coupons was 10 to 15% less than measured on the strips. The spray gun velocity was set at 127 mm/s and a sequence of 60 spray passes completed in groups of 15 with at least 40 seconds of drying time allowed between each spray pass.

Measured values of areal density are given in Tables 3 through 6. Standard sampling methods were used involving removal and weighing of sprayed coupons. Most coupons were raised slightly above the surface. However, no systematic difference between these samples and flush mounted samples was determined. The scatter between multiple coupons placed on the spray centerline was for some unknown reason larger than is usually obtained. Sample No. 8 was removed, weighed, and replaced after each group of 15 spray passes to obtain the incremental data of Table 3.

Data from the 19 mm wide strips is given in Table 7. These strips were located so that they intercepted almost the complete spray. A negligibly small amount of explosive in the form of dry overspray was deposited beyond the sample ends.

EMPIRICAL THEORY

An empirical description of the spray efficiency on a flat surface located normal to the spray axis can be derived from the flat strip data of Table 7. Thus, in 60 passes over these strips a total explosive mass of 1.096g was emitted over the 19 mm wide strips and the total deposited mass was measured and is given in Table 7. Thus, the efficiency of deposition on a flat surface as a function of separation can be

calculated to give the values of Table 8. This data can be approximated by a linear function

$$E = 0.925 - 0.000512S \quad (8)$$

$$152 \leq S \leq 305 \text{ mm}$$

which applies for a flat surface and the standard Ph nozzle setup.

The width over which material is deposited increases as a function of separation. The values given in Table 9 are representative of the standard setup and a flat surface. This information was obtained using dyed acetone and can be approximated by a parabolic function

$$W = -60.07 + 1.7842S - 0.001894S^2 \quad (9)$$

$$152 \leq S \leq 305 \text{ mm}$$

where W is the spray half width in mm on a flat surface at a center line separation S.

The explosive mass deposition across this width on a flat surface varies as a function of position (X) along the width but was symmetric with a maximum at the center line. The functional dependence was approximated by

$$\frac{M}{A} = \left(\frac{M}{A} \right)_{\text{Max}} \left[\cos \left(\frac{\pi X}{2W} \right) \right]^4 \quad (10)$$

$$-W \leq X \leq W$$

where (M/A)_{max} is the maximum value deposited at the spray centerline.

Rewriting in terms of Eq. (3) gives

$$\frac{M}{A} = \frac{4NOC E}{3WV} \left[\cos \left(\frac{\pi X}{2W} \right) \right]^4 \quad (11)$$

$$-W \leq X \leq W$$

and both E and W are functions of the separation.

The mass distribution computed using this function is compared to measurements in Figure 4. A second comparison is obtained by integrating Eq. (11) over the width of the strip samples to obtain the comparison given in Table 7. The functional dependency has been forced to fit the more accurate total deposition obtained from strip samples. The comparison to the individual coupon measurements is poorer. Reasons for a discrepancy between the coupon and strip samples were not investigated. A second observation from the coupons is that the spray was not exactly centered over the sample holder even though the setup was carefully done. Non-symmetry of dispersal from the atomizing air is a likely cause.

TABLE 1
Flow Data ⁽¹⁾

Sample	t(s)	Flow Rate	
		Vol(ml)	Q(m l/s)
Before Spray	14.5	30.1	2.08
After Spray	14.3	28.1	1.97

(1) Atomizing air was off.

TABLE 2
Explosive Concentration Data

Sample	Vol(ml)	Mass(g)	C(g/l)
Before Spray	30.1	1.809	60.1
After Spray ⁽¹⁾	28.1	1.643	58.5

(1) Some HE Lost While Taking Sample.

TABLE 3
P.H. Nozzle Deposition Data at 152 mm Separation After
60 Passes at 127 mm/s With 124 kPa Atomizing Air ⁽¹⁾

Coupon Number	X(mm) ⁽²⁾	Deposition ⁽³⁾ (g/m ²)
1	-133	4
2	-114	18
3	-95	46
4	-76	112
5	-57	193
6	-38	284
7	-19	330
8	0	372
8 (0-15)	0	(102)
8 (16-30)	0	(102)
8 (31-45)	0	(84)
8 (46-60)	0	(84)
9	19	358
10	38	323
11	57	235
12	76	126
13	95	60
14	114	14
15	133	7
57	0	330 ⁽⁴⁾

(1) Static gage pressure at nozzle inlet.
 (2) Negative positions are to the left in Figure 3.
 (3) Accumulation determined from coupon weight change.
 (4) Explosive chipped during removal.

TABLE 4

P.H. Nozzle Deposition Data at 229 mm Separation After
60 Passes at 127 mm/s and With 124 kPa Atomizing Air

Coupon Number	X (mm)	Deposition (g/m ²)
16	-200	4
17	-171	14
18	-143	32
19	-114	77
20	-86	(1)
21	-57	179
22	-26	221
23	0	249
58	0	225
59	0	246
24	29	239
25	57	197
26	86	140
27	114	88
28	143	46
29	171	4
30	200	4

(1) Coupon dropped during sampling.

TABLE 5

P.H. Nozzle Deposition Data at 305 mm Separation After
60 Passes at 127 mm/s and With 124 kPa Atomizing Air

Coupon Number	X (mm)	Deposition (g/m ²)
31	-229	0
32	-191	25
33	-152	49
34	-114	98
35	-76	137
36	-38	169
37	0	182
60	0	176
61	0	165
38	38	162
39	76	119
40	114	88
41	152	49
42	191	18
43	229	7

TABLE 6

P.H. Nozzle Coupon Data at 45 Degree Inclination After
60 Passes at 127 mm/s With 124 kPa Atomizing Air

Coupon Number	S (mm)	X (mm)	Deposition (g/m ²)
44	354	-108	25
45	336	-90	25
46	300	-72	28
47	282	-54	53
48	264	-36	56
49	247	-18	53
50	229	0	772
62	229	0	736 (1)
51	211	18	109
52	193	36	144
53	175	54	176
54	157	72	165
55	139	90	112
56	121	108	33 (2)

(1) Flush mounted
(2) Small chip

TABLE 7

P.H. Nozzle Data From 19 mm Wide Strips After 60 Passes
at 127 mm/s With 124 kPa Atomizing Air

S (mm)	X (mm)	Measured Deposition (mg)	Computed (1) Deposition (mg)
152	-165 to 0	438	464
152	0 to 165	488	464
Total		926	928
229	-229 to -76	99 (2)	131
229	-76 to 76	641	623
229	76 to 229	137	131
Total		877	885
305	-305 to -102	113	109
305	-102 to 102	626	625
305	102 to 305	101	109
Total		840	843

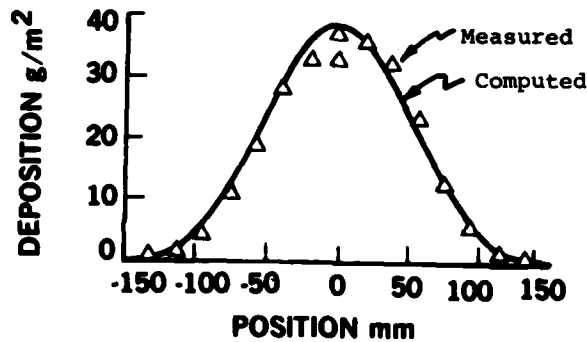
(1) Computed values obtained by integration of Eq. (11).
(2) Sample dropped.

TABLE 8
Deposition Efficiency on a Flat Surface

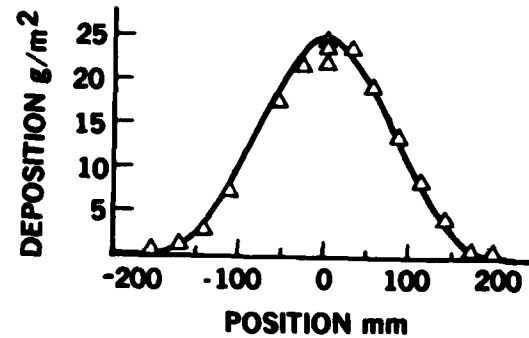
Separation (mm)	Efficiency
152	0.846
229	0.800
305	0.767

TABLE 9
Measured Total Spray Width (2W)

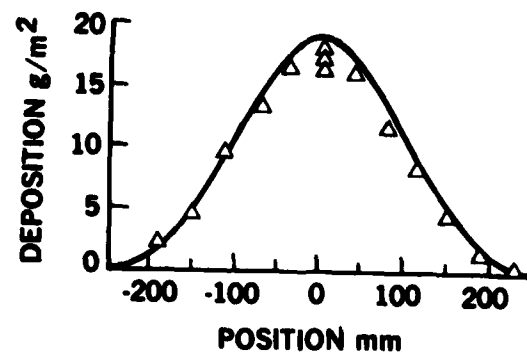
Separation (mm)	Spray Width (mm)
152	339
229	498
305	616



a. 152 mm Separation



b. 229 mm Separation



c. 305 mm Separation

Figure 4 - Computed and Measured Deposition on a Flat Surface at Various Separations

Deposition efficiency is influenced by both the distance separating the gun from the target surface and the angle between the surface normal to the direction in which the spray material is traveling. The distance versus efficiency function has already been found for a flat surface and is given by Eq. (8). The angular efficiency function K can be determined by comparing centered coupon data from Table 4 and data for coupons 50 and 62 in Table 6 which were mounted on the spray centerline at an angle of 45 degrees. The deposition at 45 degrees is given by

$$\left(\frac{M}{A}\right)_{45} = K \left(\frac{M}{A}\right)_0 \cos 45$$

where K is the angular efficiency. Using average values for coupons 50 and 62 then $K = 0.427$. In the absence of additional data, a linear equation is selected. Thus,

$$K = 1 - 0.0127|\beta|; -78.7 \leq \beta \leq 78.7 \quad (12)$$

$$K = 0; \text{ all other } \beta$$

where β is the angle in degrees between the surface normal and the line to the spray nozzle. The linear function is the best that can presently be offered with limited data, and is assumed to apply at all distances and all positions along the spray fan.

A final use of Eq. (12) is to correct the flat plate data to account for angular dispersal at positions along the fan width. Then the spray flux ψ within the flux tube passing from the spray nozzle to a position S, X is given by

$$\psi = \frac{4NQ_C}{3WV} \left(\cos \left(\frac{\pi X}{2W} \right) \right)^4 \left(\frac{1}{(1 - 0.0127|\alpha|) \cos \alpha} \right) \quad (13)$$

$$\alpha = \arctan \frac{X}{S}$$

$$6 \leq S \leq 12$$

$$-W \leq X \leq W$$

where α is the angle between the flat plate normal and the spray nozzle which defines the flux tube. This calculation of the flux term using the various empirical factors results in a calculated mass flow rate somewhat larger than the value actually present and therefore introduces a violation of continuity. This problem results from accumulating small errors.

The material deposited on any surface located at coordinate S, X , is the product of this flux term and the

efficiency terms describing angular and separation efficiency. Thus,

$$\frac{M}{A} = \psi EK \cos \beta \quad (14)$$

$$-78.7 \leq \beta \leq 78.7$$

is the empirically determined function which describes the SASN explosive deposited on a surface placed in front of the spray fan from a PH nozzle with 125 kPa atomizing air pressure.

Eq. (14) can be verified by comparing the calculated deposition for the strip inclined at 45 degrees in Figure 3 with measured values as shown in Figure 5. The excellent agreement is taken as justification for use of Eq. (14) to compute the deposition on other surfaces.

APPLICATIONS

The function of Eq. (14) was used in computer studies of several spray geometries. A major objective was to understand the influence of parameters which could be selected in the design of a particular painting procedure. Several examples will be discussed to illustrate these results.

Flat Surface Subjected to a Uniform Impulse

A relatively common test problem is to produce a uniform load on a flat surface. A sequence of equal numbers of spray passes on uniformly spaced parallel paths produces this loading. Several questions are important to the design including: (1) How accurately must positioning be controlled? (2) What is the widest spacing permitted between each spray gun path? (3) How far must the spray gun traverse beyond the width of the target?

Results for several calculations are given in Figures 6 thru 9 for a standard spray gun setup with 152 mm separation. An acceptably uniform impulse distribution is obtained when either 51 or 102 mm spacing is used while a 127 mm spacing produces unacceptable impulse variation. These plots also show that the last spray gun position must extend about 130 mm beyond the surface to be covered by uniform impulse. Results calculated when all sprays at one location were misplaced by 6.4 mm are given in Figure 9. Errors randomly spaced between -5 and 5 mm affecting all sprays at each location were also studied. Impulse uniformity was similar to that obtained in Figure 9.

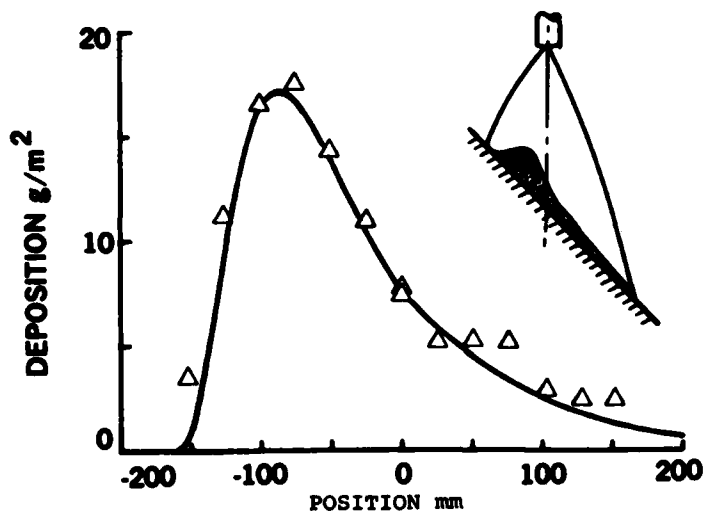


Fig. 5 - Computed and Measured Deposition on a Flat Surface Inclined at 45° with a Center Separation of 229 mm

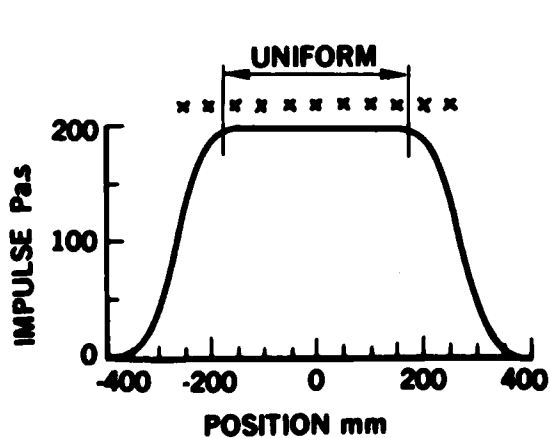


Fig. 6 - Computed Impulse Distribution on a Flat Surface After 20 Spray Passes at Each of 11 (X) Locations Spaced 50.8 mm Apart

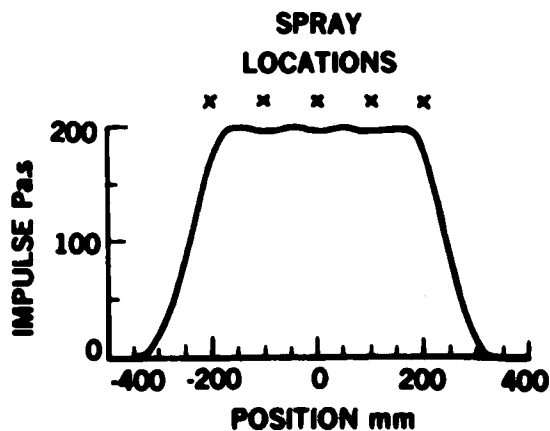


Fig. 7 - Computed Impulse Distribution on a Flat Surface After 40 Spray Passes of Each of 5 Locations Spaced 101.6 mm Apart

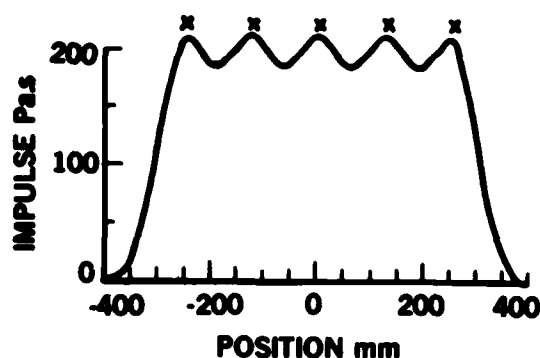


Fig. 8 - Computed Impulse Distribution on a Flat Surface After 50 Spray Passes at Each of 5 Locations Spaced 127 mm Apart

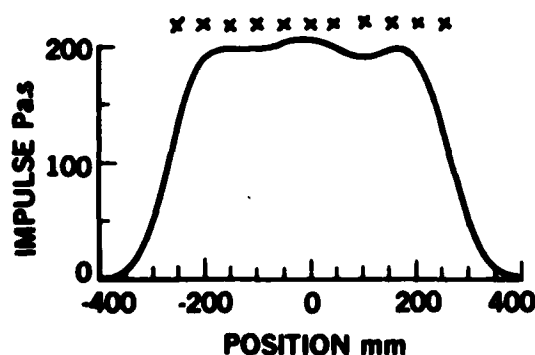


Fig. 9. - Impulse Distribution on a Flat Surface After 20 Spray Passes at Each of 11 Locations. The Spray at 50.8 mm Has Been Positioned with an Error of 6.4 mm

These results suggest that single errors of position should be kept below 6 mm and that random errors of 5 mm are acceptable. The largest spacing between spray locations should be kept to 102 mm or less and the edge spray path should be at least 130 mm outside the surface which will be subjected to uniform impulse.

Overlapping Sprays on Cylindrical or Conical Surfaces

Test specifications on conical or cylindrical surfaces usually involve an

impulse distributed as a $\cos \theta$ function over half the test object surface. Current practice involves spray painting using an aperture which allows explosive to fall on a narrow (~ 15 degrees) surface segment. The loading profile is then built up using a stair step approximation by applying repeated sprays at suitably indexed positions on the surface. When conical shapes are involved the process is inefficient with only 10 to 20% of the sprayed explosive adhering to the target. The case of overlapping sprays with no aperture applied to a cylindrical surface was therefore studied for the case where a $\cos \theta$ impulse distribution is desired. In this setup approximately 30 to 50% of the explosive sprayed should adhere to the target. The cylindrical calculation was then extended to a conical surface by studying cylinders of various diameter. Thus, if the spray gun were moved parallel to a ray of the conical surface traversing from the large to small diameter at a spacing of 152 mm, using the number of passes indicated in Table 10, then results similar to Figure 10 are predicted. This procedure requires that the spray gun be turned off at appropriate positions along the conical axis during its movement from the large to small end.

Studies regarding results of random positioning errors on cylindrical surfaces have also been conducted with results similar to those already discussed. It was concluded that randomly occurring positioning errors of a few degrees can be tolerated.

Deposition Efficiency

Estimates of total explosive utilization are needed to determine the explosive batch size. Overestimates result in wasted SASN which although expensive, cannot be stored for subsequent use. Underestimates require that the partially sprayed test unit be removed and repositioned while coated with dry SASN explosive, a particularly difficult operation. It is therefore useful to investigate efficiency for several types of spray setups.

When flat surfaces are sprayed using overlapping passes, the efficiency can be calculated using Eq. (8). Ordinarily approximately 80% of the explosive adheres to the target surface. Losses due to edge masking and end run-out may be estimated for the specific setup. Previous observations derived from Figures 6 thru 9 are adequate for this purpose.

TABLE 10
Schedule for a 200 COS θ Impulse (Pa.s) On a Conical Surface⁽¹⁾

Angle	Number of Spray Passes										
	Diameter (mm)										
	559 ⁽²⁾	508	457	406	356	305	254	203	152	102	51 ⁽³⁾
0	35	33	31	28	26	23	21	20	18	16	15
+15	33	30	28	26	24	22	20	18	16	14	12
+30	31	29	26	24	22	20	18	16	15	13	12
+45	26	24	23	21	20	18	16	15	13	12	11
+60	20	19	17	16	14	13	12	11	11	11	11
+75	12	11	11	9	8	7	7	6	4	2	0
Total	279	259	241	220	202	183	167	152	136	120	107

(1) Spacing of 152 mm, Atomizing air 124 kPa, velocity of 127 mm/s.
 (2) Impulse function plotted in Figure 10.
 (3) Impulse function plotted in Figure 10.

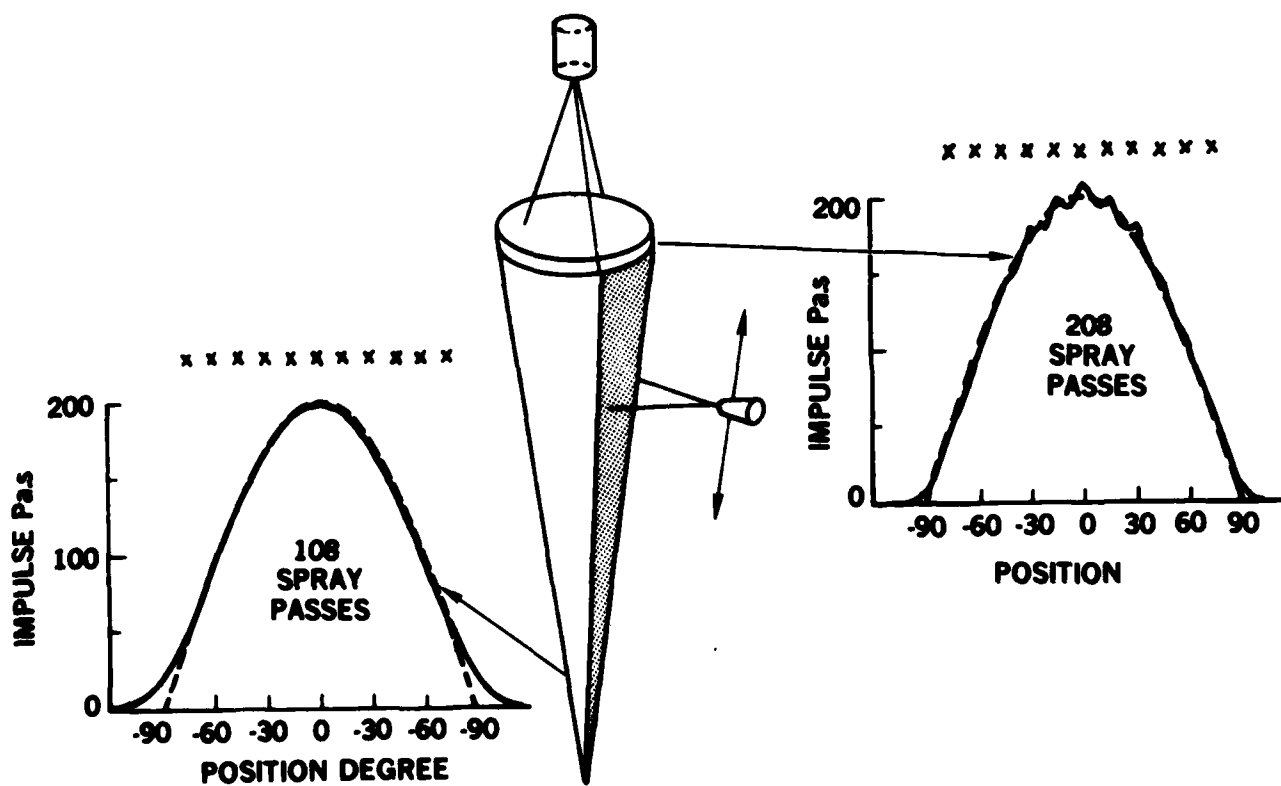


Fig. 10 - Impulse Distribution at Two Diameters Computed for a Conical Object Using the Setup of Table 10. The Desired Impulse is Shown by a Dotted Line

The deposited fraction is defined as the amount of SASN material adhering to the target surface divided by the amount emitted by the spray gun as it passes over the surface. The deposition fraction obtained with a mask placed between the spray fan and a flat target surface was studied by solving Eq. (14) over the area of the slit width. Results are given in Figure 11 where the fraction deposited is plotted as a function of slit fraction for three gun to surface separations. The slit fraction is the width of spray fan passing thru the slit divided by the total spray fan width. This figure indicates that reasonably high efficiencies are obtained provided the slit is at least 40% of the fan width.

The deposition fraction on a cylinder when no mask is used was obtained as a function of radius and minimum separation between the target surface and the spray nozzle. The result is plotted in Figure 12. Note that relatively great losses occur for small radius and that at small radius the efficiency is severely reduced with large separation distances. This figure permits estimates of explosive quantities for cylindrical or conical surfaces provided additional losses due to spray over run and edge masking are included.

The case of spray painting a cylindrical surface while using a slit to pass only material within a fixed angular segment is shown in Figure 13. Three angular segments of 12, 15, and 18 degrees are plotted. Comparison between Figures 12 and 13 indicates that use of an angular slit significantly decreases efficiency in comparison to a similar case when no slit is used. Again small diameters exhibit particularly low efficiencies. These figures may also be used when estimating required quantities of explosive.

Other cases have also been studied including the situation of flat and curved surfaces rotated in front of a spray gun similar to the techniques described in Reference 5. Future work will investigate the possibility of combining a variable traverse velocity in conjunction with control of position and number of passes as a means of deposition control. This work is awaiting a suitable testing requirement.

CONCLUSION

An empirical theory describing spray painting of a SASN explosive layer has been developed and verified for a single inclined flat plate geometry. Important physical parameters which include

explosive concentration in the atomized spray, the deposition profiles for a single pass, with deposition efficiency as a function of spacing, position and incident angle have been incorporated into a numerical calculation of the space dependent explosive deposition for a single pass of the spray apparatus. When implemented into a computation of multiple overlapping passes, which may include the use of masking to intercept unwanted portions of the spray, a reasonably complete prediction is obtained.

Studies of several important geometries including flats, cylinders, and cones have been described. This work suggests improvements in process efficiency as well as new methods for handling difficult shapes. An additional benefit is that consequences of positioning inaccuracies have been estimated. Reasonable positioning tolerances produce acceptable deviations in computed spray results. The completed analysis is a useful tool in selecting appropriate spray application methods during the design of a remotely controlled spray process.

ACKNOWLEDGEMENTS

The careful work of Dave Shirey and Louis Perea who designed and conducted the deposition experiments is greatly appreciated.

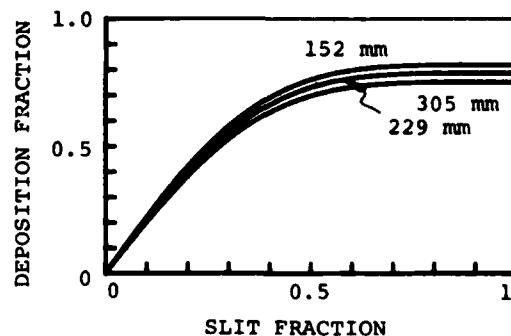


Fig. 11 - Deposition Fraction as a Function of Slit Fraction for Three Separations

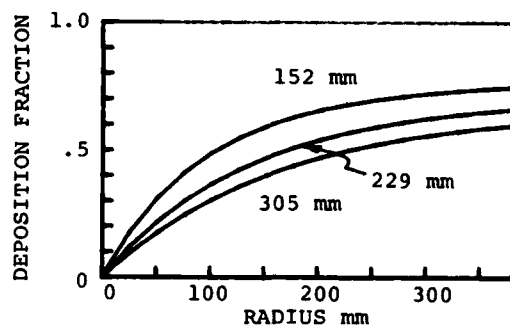
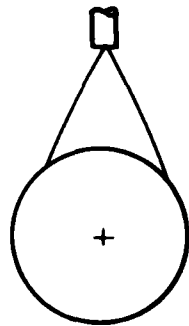


Fig. 12 - Deposition Fraction as a Function of Cylinder Radius for Spray Painting at Three Separations

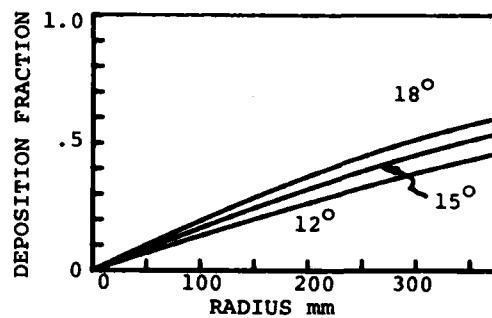
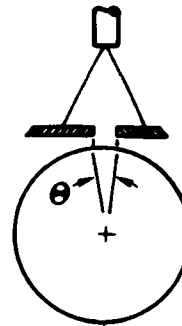


Fig. 13 - Deposition Fraction as a Function of Target Radius and Slit Angle for a Cylinder

REFERENCES

1. F. O. Hoese, C. G. Langhner, and W. E. Baker, "Simultaneous Initiation Over Large Areas of a Spray Deposited Explosive," Experimental Mechanics, Vol. 8, September 1968.
2. G. E. Nevill, Jr., and F. O. Hoese, "Impulse Loading Using Sprayed Silver Acetylide-Silver Nitrate," Experimental Mechanics, September 1965, pp. 294-298.
3. A. B. Wenzel and W. E. Baker, "The Use of Light-Initiated Explosives for Impulsive Loading of Structures," Proc. 16th Annual Meeting of the Institute of Environmental Sciences, Boston, Mass., April 1970.
4. R. A. Benham and F. H. Mathews, "X-ray Simulation With Light-Initiated Explosive," The Shock and Vibration Bulletin, No. 45, Part 4, June 1975.
5. R. A. Benham, "Simulation of X-ray Blowoff Impulse Loading on a Reentry Vehicle Aft End Using Light-Initiated High Explosive," The Shock and Vibration Bulletin, No. 46, Part 1, August 3, 1976.
6. P. B. Higgins, "An Arc Light Source for Initiating Light-Sensitive Explosive," The Shock and Vibration Bulletin, 1976.
7. R. A. Benham, F. H. Mathews and P. B. Higgins, "Application of Light-Initiated Explosive for Simulating X-ray Blowoff Impulse Effects on a Full Scale Reentry Vehicle," The Shock and Vibration Bulletin, No. 47, 1978, Supplement.
8. P. B. Higgins, "An Arc Source for Initiating Light-Sensitive Explosives," The Shock and Vibration Bulletin, No. 46, Part 3, pp. 191, 1977.

9. F. H. Mathews, "A Computational Model Describing the Initiation of Silver Acetylide-Silver Nitrate Explosive by an Intense Light Source," The Shock and Vibration Bulletin, No. 49, 1979.
10. R. A. Benham, "Predicting the Motion of Flyer Plates Driven by Light-Initiated Explosive for Impulse Loading Experiments," The Shock and Vibration Bulletin, No. 50, 1979.
11. P. B. Higgins, F. H. Mathews, and R. A. Benham, "A Non-Contacting Beta Backscatter Gage for Explosive Quantity Measurement," The Shock and Vibration Bulletin, No. 50, Part 4, pp 113, 1980.

SHOCK ANALYSIS

THE RESPONSE SPECTRUM METHOD OF SOLUTION FOR DISPLACEMENT EXCITATION

F. C. Nelson
College of Engineering
Tufts University
Medford, MA 02155

The response spectrum method is formulated in terms of base displacement rather than base acceleration. This allows simpler application of the response spectrum method to spring-mass systems with multiple input motions. The method is extended to systems for which hysteretic damping is incorporated by the use of complex stiffnesses.

INTRODUCTION

Consider an n degree-of-freedom (ndof) spring and mass model where $x_i(t)$ is the absolute displacement of mass i and $y(t)$ is the absolute ground displacement, see Fig. 1.

In the problem of Fig. 1, $y(t)$ is specified and one wishes to determine the $x_i(t)$. Such problems arise in the design of shipboard equipment to resist shock and vibration and the design of mechanical and electrical equipment to resist earthquakes. The conventional approach is to write the laws of motion with respect to the base. The base then becomes fixed, each mass is subjected to an inertial force $m_i \ddot{y}(t)$, and the displacement variables become the relative displacements, $z_i(t)$ - see Fig. 2.

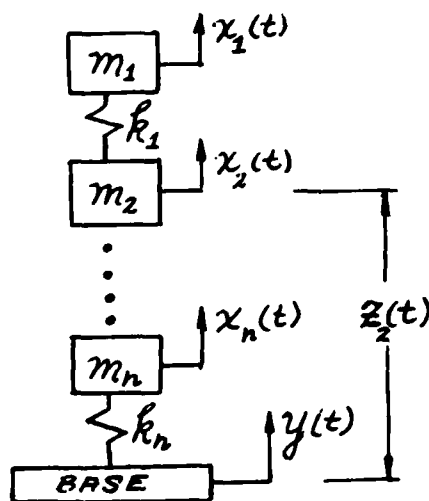


Fig. 1 - Spring-mass system with displacement excitation of the base

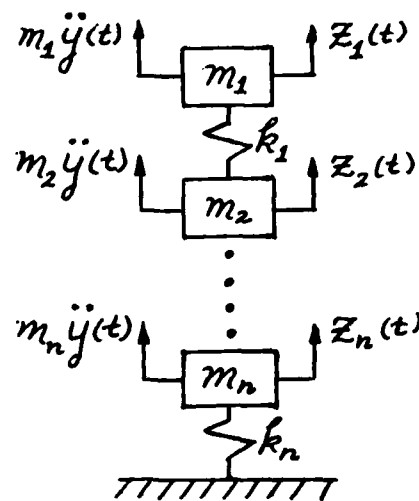


Fig. 2 - Conventional transformation of Fig. 1 into a fixed-base system

One can now proceed with a solution by modal analysis using either the acceleration time history, $\ddot{y}(t)$, directly or using the acceleration response spectrum $A(\omega)$, which is associated with $\ddot{y}(t)$. Since shock and earthquake motion do not have repeatable time histories but do have repeatable shock spectra, it is the latter method which is of general interest. See reference [1] for a discussion of this method.

However, it is possible to formulate the problem of Fig. 1 as shown in Fig. 3; with the base fixed, with only the mass next to the base subjected to a force equal to $k_n y(t)$, and with the displacement variables being the absolute displacements, $x_i(t)$. All that is required is to write the equation of motion with respect to an observer at rest and move the term $k_n y$ to the right-hand side of the n th equation.

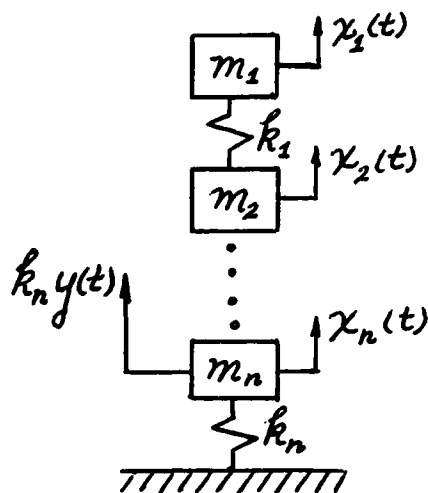


Fig. 3 - Alternative transformation of Fig. 1 into a fixed-base system

This formulation is not widely used because most dynamic analysis computer programs will not accept it. It does have some advantages over the conventional formulation of Fig. 2; e.g., in the seismic analysis of nuclear power plant piping which is supported at many different elevations, it permits the easy incorporation of distinct motions at each support, see reference [2].

The purpose of this paper is to work out the consequences of the formulation of Fig. 3 in such a way that it can be easily incorporated into a computer program and then to modify the formulation to permit the use of the complex stiffness model of hysteretic damping.

DETERMINATION OF RESPONSE

The equations of motion of the system in Fig. 3 are:

$$[m]\ddot{X} + [k]X = k_n y \begin{Bmatrix} 0 \\ 0 \\ \vdots \\ \vdots \\ \vdots \\ 1 \end{Bmatrix} \quad (1)$$

Assume that the eigenvalue problem associated with Eq. (1) has a spectral matrix $[\omega_i]$ and a modal matrix where

$$[\Phi] = [\{\phi_1\} : \{\phi_2\} : \dots : \{\phi_r\}]$$

and $\{\phi_i\}$ is the i th eigenvector with elements $\phi_{r,i}$ $r = 1, \dots, n$. It will be assumed that the $\{\phi_i\}$ are normalized so that $\text{MAX}_r [\phi_{r,i}] = 1$ for each i .

Orthogonality of the eigenvectors requires that

$$[\Phi]^T [m] [\Phi] = [M_i] \quad (2)$$

and

$$[\Phi]^T [k] [\Phi] = [K_i] \quad (3)$$

where M_i are the modal masses and K_i are the modal stiffness. It can be shown that $\omega_i^2 = K_i/M_i$.

Consider the transformation of coordinates

$$\{X(t)\} = [\Phi]\{q(t)\} \quad (4)$$

Eq. (1) becomes

$$[m][\Phi]\{\ddot{q}\} + [k][\Phi]\{q\} = \begin{Bmatrix} 0 \\ 0 \\ \vdots \\ \vdots \\ \vdots \\ 1 \end{Bmatrix} k_n y$$

premultiplying by $[\Phi]^T$ and using (2) and (3) gives

$$[M_i] \{\ddot{q}\} + [K_i] q = [\phi]^T \begin{Bmatrix} 0 \\ 0 \\ \vdots \\ 1 \end{Bmatrix} k_n y. \quad (5)$$

It can be shown that

$$[\phi]^T \begin{Bmatrix} 0 \\ 0 \\ \vdots \\ 1 \end{Bmatrix} = \begin{Bmatrix} \phi_{n,1} \\ \phi_{n,2} \\ \vdots \\ \phi_{n,n} \end{Bmatrix}$$

i.e., a vector composed of the n^{th} element of each $\{\phi_i\}$. Eq. (5) then become

$$[M_i] \begin{Bmatrix} \ddot{q}_1 \\ \ddot{q}_2 \\ \vdots \\ \ddot{q} \end{Bmatrix} + [K_i] \begin{Bmatrix} q_1 \\ q_2 \\ \vdots \\ q_n \end{Bmatrix} = \begin{Bmatrix} \phi_{n,1} \\ \phi_{n,2} \\ \vdots \\ \phi_{n,n} \end{Bmatrix} k_n y(t)$$

which is equivalent to

$$M_i \ddot{q}_i + K_i q_i = \phi_{n,i} k_n y(t) \quad (6)$$

$i = 1, 2, \dots, n$

The response spectrum is the maximum response of an oscillator subjected to a forcing function drawn from the process of interest as a function of the frequency of the oscillator. If the response of interest is the absolute acceleration, the acceleration response spectrum is denoted by $A(\omega)$ where ω is the frequency of the oscillator.

If $A(\omega_1)$ equals $\text{Max} [\ddot{Q}_1(t)]$ where $Q_1(t)$ is the solution to

$$M_1 \ddot{Q}_1 + K_1 Q_1 = K_1 y(t) \quad (7)$$

then linearity requires that

$$\text{Max}_t [\ddot{Q}_1(t)] = \phi_{n,1} A(\omega_1) \frac{k_n}{K_1} \quad (8)$$

where $q_1(t)$ is the solution to Eq. (6).

Equation (4) can be rewritten

$$\ddot{X}_r = \sum_{i=1}^n \phi_{r,i} \ddot{q}_i \quad (9)$$

The acceleration of the r^{th} dof in the i^{th} mode is therefore

$$\ddot{X}_{r,i} = \phi_{r,i} \ddot{q}_i \quad (10)$$

using Eq. (8)

$$\text{Max}_t [\ddot{X}_{r,i}] = \phi_{r,i} \phi_{n,i} A(\omega_1) \frac{k_n}{K_1} \quad (11)$$

For convenience, let

$$\text{Max}_t [\ddot{X}_{r,i}] = R_{r,i} \quad (12)$$

Note that in going from Eq. (10) to Eq. (11), the information about the temporal relationships among the $\text{Max} [\ddot{X}_{r,i}(t)]$ is lost. This loss of information requires that the exact modal recombination rule, Eq. (4), be replaced by an approximate modal recombination rule.

The most widely used recombination rule among the many suggested is the Square-Root-of-the-Sum-of-the-Squares (SRSS) rule. In the SRSS rule

$$A_r = \left[\sum_{i=1}^n R_{r,i}^2 \right]^{1/2} \quad (13)$$

where A_r is expected to be an approximate measure of the maximum absolute acceleration of mass point M_r when all modes are excited by input $y(t)$. The spring forces in mode i can be obtained from

$$F_{r,i} = k_r \frac{[R_{r,i} - R_{r+1,i}]}{\omega_i^2} \quad (14)$$

and, if desired, they can also be combined by the SRSS rule.

Equations (11) and (14) can be the basis for a computer solution of Eq. (1) using the acceleration response spectrum associated with $y(t)$. Of course if $A(\omega)$ is not specified, a separate program will be necessary to compute $A(\omega)$ from $y(t)$ in accordance with Eq. (7). The method encompassed by Eqs. (11) and (14) was developed to solve a multibranch dynamic model which was attached to ground at several places but had a displacement imposed

at only one attachment point. In the case of multiple, distinct inputs, it is better to generalize Eq. (1) as in Ref. [2] and base the solution on the prescribed displacements. In either case, the above method is more suitable than the conventional method.

EFFECT OF DAMPING

So far, the effect of damping has been neglected. In lumped spring-mass models subjected to sinusoidal forcing, hysteretic damping can be included by considering the spring stiffnesses to be complex, i.e.

$$\underline{k} = k_R + ik_I \quad (15)$$

where $(\)$ represents a complex number, $(\)_R$ the real part of the complex number, $(\)_I$ the imaginary part and $i = \sqrt{-1}$. This representation is a mathematical convenience rather than a physical reality...as are, in fact, complex numbers themselves. Hysteretic damping is energy dissipation which is independent of frequency and proportional to the square of the displacement. As such, it is a much better predictor of the ability of metals and polymers to dissipate energy than is linear viscous damping.

Although Eq. (15) is the most common way (it is not the only way) of modeling hysteretic damping, it must be used with caution when the forcing is not sinusoidal. Its use for free vibration or multiple-frequency forcing (such as a shock pulse) is open to question. Experience has indicated that reasonable results are obtained provided the excitation does not contain a strong DC-component, e.g. an earthquake ground acceleration having zero mean value.

Shock response spectra are usually specified with damping as a parameter. In using Eq. (11) one must select the value of $A(\omega_1)$ for the appropriate damping value. If damping is measured by the loss factor η , Eq. (11) can be written

$$\underline{R}_{r,i} = \phi_{r,i} \phi_{n,i} A(\omega_1, \eta_1) \frac{k_n}{K_1} \quad (16)$$

where $\phi_{j,i}$ are the mode shapes of the undamped eigenvalue problem and K_1 is given by

$$K_1 = \{\phi_1\}^T [k]_R \{\phi_1\}.$$

The question then becomes how to find η_1 for each mode.

To answer this question, first consider a single dof system subjected to sinusoidal forcing. The equation of motion is

$$m\ddot{X} + \underline{k} X = \underline{f} \quad (17)$$

where

$$f(t) = \text{Re}[\underline{f}e^{i\omega t}]$$

$$X(t) = \text{Re}[\underline{X}e^{i\omega t}]$$

Letting $\underline{k} = k_R + ik_I$ and defining the loss factor as $\eta = k_I/k_R$, Eq. (17) becomes

$$m\ddot{X} + k_R(1+i\eta)\underline{X} = \underline{f} \quad (18)$$

Now consider an ndof system with

$$[k] = [k]_R + i[k]_I$$

For sinusoidal forcing, Eq. (1) becomes

$$[m]\ddot{\underline{X}} + i[k]_I \underline{X} + [k]_R \underline{X} = \underline{f} \quad (19)$$

where

$$\underline{f} = \underline{k}_n \underline{y} \begin{Bmatrix} 0 \\ 0 \\ \vdots \\ 1 \end{Bmatrix}$$

and

$$y(t) = \text{Re}[ye^{i\omega t}]$$

The generalization of Eq. (4) is

$$\underline{X} = [\phi]\{q\}$$

where $[\phi]$ is the (real) modal matrix derived from the undamped eigenvalue problem.

The above relation, along with Eqs. (2) and (3) transform Eq. (19) into

$$[M_1]\ddot{\underline{q}} + [K_1]\underline{q} + i\{\phi\}^T [k]_I \{\phi\} \underline{q} = [\phi]^T \underline{f}$$

or, for the i^{th} dof,

$$M_1 \ddot{q}_i + K_1 q_i + i\{\phi_1\}^T [k]_I \{\phi_1\} q_i = \{\phi_1\}^T \underline{f}_i \quad (20)$$

Now by comparison of Eq. (20) and Eq. (18), a modal loss factor may be defined as

$$\eta_i = \frac{\{\phi_i\}^T [k]_I \{\phi_i\}}{\{\phi_i\}^T [k]_R \{\phi_i\}} \quad (21)$$

The above derivation assumes that the damping is small so that no significant errors will arise from using the undamped mode shapes.

Equation (21) can be written in the equivalent form

$$\eta_i = \frac{\sum_{j=1}^n (k_j)_I (\phi_{i,j} - \phi_{i,j+1})^2}{\sum_{j=1}^n (k_j)_R (\phi_{i,j} - \phi_{i,j+1})^2} \quad (22)$$

where $(k_j)_I$ is the imaginary part of the complex stiffness k_j in Fig. 3 and $(k_j)_R$ is the real part. Now let $(k_j)_I = \eta_j (k_j)_R$ so that Eq. (22) becomes

$$\eta_i = \frac{\sum_{j=1}^n \eta_j (k_j)_R (\phi_{i,j} - \phi_{i,j+1})^2}{\sum_{j=1}^n (k_j)_R (\phi_{i,j} - \phi_{i,j+1})^2} \quad (23)$$

Equation (23) is obvious from energy consideration: the denominator is the sum of the energies stored in each spring in mode i and the numerator is the sum of the energies dissipated in mode i . As such, Eq. (23) is widely used to estimate modal loss factors since it can be justified on the basis of intuition alone. The formal equivalence between Eq. (23) and Eq. (21) established that Eq. (23) is tantamount to modal superposition using complex stiffnesses.

CONCLUSIONS

This paper has discussed a response spectrum method which is particularly suited for spring-mass systems excited by one or more ground displacements. It offers an alternative to the conventional response spectrum method which is best suited for a single prescribed ground acceleration. The paper also discusses how to incorporate hysteretic damping via complex spring stiffnesses.

REFERENCES

- [1] Biggs, J.M. Introduction to Structural Dynamics, Chapter 6, McGraw-Hill, 1964.
- [2] Chan, A.W., Chen, C.H., and Mitchel, B.J. "Modal Dynamic Analysis of Linear Elastic Systems with Specified Displacement Time Histories," ASME paper 80-C2/PVP-91.

AN IMPROVED RECURSIVE FORMULA FOR CALCULATING SHOCK RESPONSE SPECTRA

David O. Smallwood
Sandia National Laboratories
Albuquerque, New Mexico 87185

Currently used recursive formulas for calculating the shock response spectra are based on an impulse invariant digital simulation of a single degree of freedom system. This simulation can result in significant errors when the natural frequencies are greater than 1/6 the sample rate. It is shown that a ramp invariant simulation results in a recursive filter with one additional filter weight that can be used with good results over a broad frequency range including natural frequencies which exceed the sample rate.

NOMENCLATURE

$x(t)$ = base input displacement of a single-degree-of-freedom system
 $y(t)$ = response displacement of a single-degree-of-freedom acceleration
 $\ddot{x}(t)$ = base input acceleration
 $\ddot{y}(t)$ = response acceleration
 $z(t)$ = relative displacement $y(t) - x(t)$
 ζ = fraction of critical damping
 ω_n = natural frequency of a single-degree-of-freedom system, rad/sec
 s = complex variable
 H = transfer function
 $L[]$ = Laplace transform
 $L^{-1}[]$ = Inverse Laplace transform
 z = z Transform
 z^{-1} = Inverse z transform
 $\omega_d = \omega_n \sqrt{1-\zeta^2}$ = damped natural frequency,
 T = sample interval

$\delta(t)$ = delta function; $\delta(t) = 1$ for $t = 0$, $\delta(t) = 0$ elsewhere
 d_m = digital delta function; $d_m = 1$ for $m = 0$, $d_m = 0$ all other m
SDOF = single degree of freedom
 $u(t)$ = unit step function; $u(t) = 1$ for $t \geq 0$, $u(t) = 0$ for $t < 0$
 t = time

INTRODUCTION

There are many ways to calculate the shock response spectra. A popular technique is to use a digital recursive filter to simulate the single-degree-of-freedom (SDOF) system. The output of the filter using a sampled input is assumed to be a measure of the response of the SDOF system.

The response is then searched for the maximum value. This process is then repeated for each natural frequency of interest. Currently used filters exhibit large errors when the natural frequency exceeds 1/6 the sample rate. This paper will discuss the design of an improved filter which gives much better results at the higher natural frequencies. The companion problem of peak detection of a sampled system will not be discussed in this paper.

MODELS

Absolute acceleration model -- The absolute acceleration model is shown in Fig. 1.

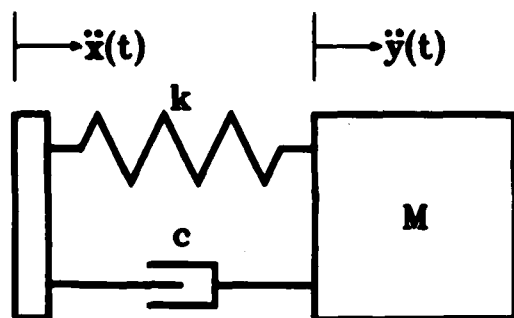


Fig. 1 Absolute acceleration model

The input to the SDOF system is the base acceleration. The response of the system is the absolute acceleration of the mass. The transfer function of this system in the complex Laplace domain is given by

$$H(s) = \frac{2\zeta\omega_n s + \omega_n^2}{s^2 + 2\zeta\omega_n s + \omega_n^2} \quad (1)$$

This is the model most frequently used in shock response spectra calculations.

Relative displacement model -- The relative displacement model is shown in Fig. 2.

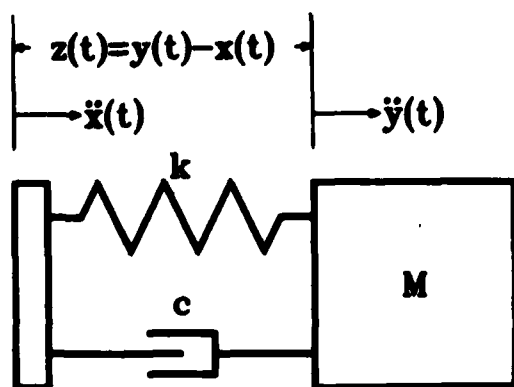


Fig. 2 Relative displacement model

The input to the system is the absolute acceleration of the base. The response of the system is the relative displacement between the base and the mass. The transfer function of this system is given by

$$H(s) = \frac{1}{s^2 + 2\zeta\omega_n s + \omega_n^2} \quad (2)$$

If the relative displacement is expressed in terms of an equivalent static acceleration,

$$\ddot{y}_{eq} = z\omega_n^2 \quad (3)$$

the transfer function becomes,

$$H(s) = \frac{\omega_n^2}{s^2 + 2\zeta\omega_n s + \omega_n^2} \quad (4)$$

The relative displacement model is used when the damage potential (perhaps the stress in the support bracket) can be related to the relative displacement. The equivalent static acceleration is used to keep the input and response in the same physical units. Both models give $H(0) = 1$ and have the same denominator. Equations (1) and (4) will be referred to as the absolute acceleration and the relative displacement models respectively.

SIMULATION OF CONTINUOUS SYSTEMS

Following Stearns [1] a digital simulation will be compared with the continuous system as outlined in Fig. 3.

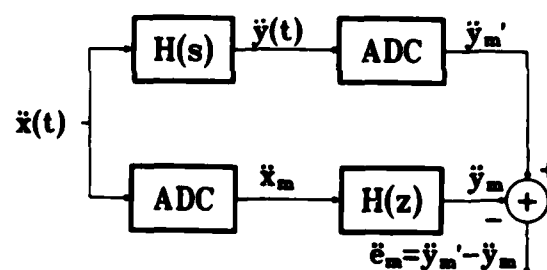


Fig. 3 Simulation of a Continuous System

The output, \ddot{y}_m , of the digital simulation, $H(z)$, will be compared to the sampled output of the continuous system, \ddot{y}_m' . If the sample set $e_m = 0$ for all m 's the simulation is said to be exact.

Impulse invariant simulations -- Stearns shows that if the input is an impulse, i.e.,

$$\ddot{x}(t) = \delta(t),$$

$$\text{and } \ddot{x}_m = d_m,$$

the simulation

$$\tilde{H}_0(z) = Tz[L^{-1}[H(s)]] \quad (5)$$

is exact.

The digital recursive filters given in [2] for the absolute acceleration and relative displacement models can be derived from this formulation. The formulas given in [2] are therefore said to be impulse invariant. It can be shown (using superposition) that if the input is a series of scaled impulses the error of simulation, \tilde{e}_m , will be zero. This is true even though the impulses are not band limited. Also $H(s)$ need not be band limited for the simulation to be exact. In the case of a SDOF simulation, the natural frequency can be equal to or above the sampling frequency.

The shock response spectra of a 1g, .64 ms haversine was calculated (Fig. 4), using an impulse invariant simulation of the absolute acceleration model (eq. 6.96 in [2]). The correct shock spectra should be almost a constant of 1.0 above a few hundred Hz. Note the gradual decline in the computed shock spectra to a minimum at 1000 Hz (one half the sample rate) and then an increase as 2000 Hz (the sample rate) is approached. As a second example, the shock spectra of an exponentially decaying sinusoid was calculated. The decaying sinusoid was modified to reduce the velocity and displacement change [3]. The input acceleration time history sampled at 2000 samples/s is given by

$$\ddot{x}(t) = u(t)e^{-\eta\omega t}\sin\omega t + u(t+\tau)Ae^{-\nu t}\sin\nu(t+\tau),$$

where

$$\begin{aligned} A &= -0.1995 \\ \eta &= .05 \\ \omega &= 2\pi(100) \\ \nu &= 2\pi(10) \\ \tau &= -0.015757. \end{aligned}$$

The shock spectra (Fig. 5) again shows the notch/peak at one half the sample rate and at the sample rate.

The errors cannot be blamed on the sampling theorem as the input is reasonably well band limited. If the input is properly band limited, the response will be band limited even if $H(s)$ is not band limited. The errors have long been recognized and the recursive formulas have not been recommended whenever the sample rate was less than 5 or 6 times

the highest natural frequency. However, the author does not believe that the mechanism of the errors has been well understood.

The errors can be explained using the following argument. Consider, the response to a square wave represented by two impulses. That is, the original square wave is sampled. The function is now represented by a series of scaled impulses at each sampling time. Note that the sample rate is such that only two non-zero samples are observed. Set the natural frequency of the SDOF system equal to one half the sample rate (see Fig. 6).

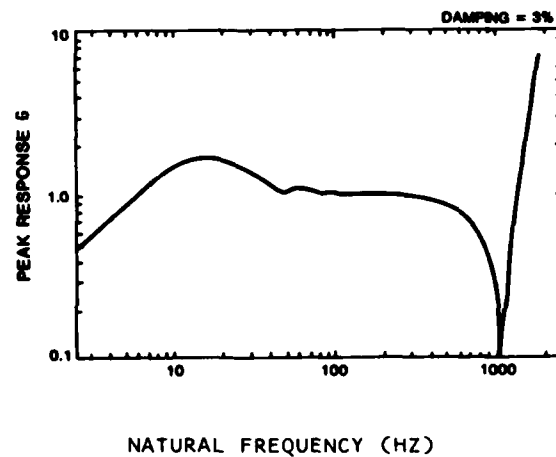


Fig. 4 Shock Response Spectra of a 64 ms Haversine with Unity Amplitude Sampled at 2000 Samples/Sec Using an Impulse Invariant Filter

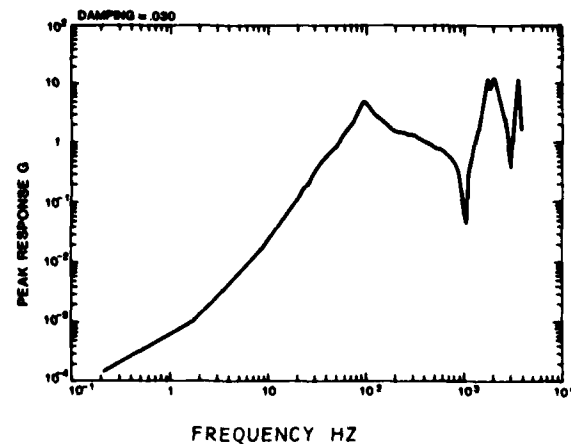


Fig. 5 Shock Response Spectra of a 100 Hz Decaying Sinusoid Sampled at 2000 Samples/Sec Using an Impulse Invariant Filter

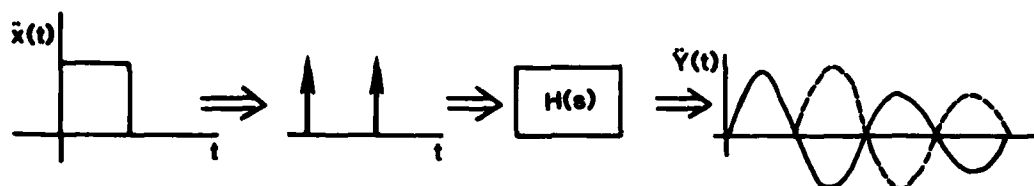


Fig. 6 Response to Two Impulses by a Single Degree of Freedom System

The solid line represents the response to the first impulse and the dashed line represents the response to second impulse. The total response will be the sum of the two curves. Clearly the total response will be quite small except for the first half cycle of response due to the destructive interference of the two impulse responses. The actual response of the system to a square wave will be larger than the response to two impulses. The simulation of the square wave input by two impulses is not very good in this example. This argument can be extended to more complicated waveforms simulated by a series of impulses. In general, using an impulse invariant simulation of a SDOF system, a minimum in the observed response will be found when the natural frequency is near one half the sample rate due to the destructive interference of successive impulses. A maximum (constructive interference) will be found when the natural frequency is near the sample rate.

Ramp invariant simulations [1] -- Let the input to the system be a generalized ramp function;

$$\ddot{x}(t) = A \cdot (t-mT) \cdot u(t-mT),$$

i.e., a ramp with slope A beginning at time $t=mT$. A ramp invariant simulation can then be found from

$$\tilde{H}(z) = \frac{(z-1)^2}{T^2 z} \mathcal{Z} \left[\mathcal{L}^{-1} \left[\frac{H(s)}{s^2} \right] \right]. \quad (6)$$

Using superposition, an input composed of straight lines connecting the sample points will then be an exact simulation.

Eq. 6 yields (after much algebra) the following formulas for the absolute acceleration and relative displacement models.

Absolute acceleration model --

$$\tilde{H}(z) = \frac{b_0 + b_1 z^{-1} + b_2 z^{-2}}{1 - 2Cz^{-1} + E^2 z^{-2}} \quad (7)$$

$$\omega_d = \omega_n \sqrt{1 - \zeta^2}$$

$$E = e^{-\zeta \omega_n T}$$

$$K = T \omega_d$$

$$C = E \cos K$$

$$S = E \sin K$$

$$S' = S/K = E \sin K/K$$

$$b_0 = 1 - S'$$

$$b_1 = 2(S' - C)$$

$$b_2 = E^2 - S'.$$

Relative displacement model --

$$\tilde{H}(z) = \frac{b_0 + b_1 z^{-1} + b_2 z^{-2}}{1 - 2Cz^{-1} + E^2 z^{-2}} \quad (8)$$

$$b_0 = \frac{1}{T \omega_n} \left[2\zeta(C-1) + \frac{(2\zeta^2-1)S}{\sqrt{1-\zeta^2}} + T \omega_n \right]$$

$$b_1 = \frac{1}{T \omega_n} \left[-2CT \omega_n + 2\zeta(1-E^2) - \frac{2(2\zeta^2-1)S}{\sqrt{1-\zeta^2}} \right]$$

$$b_2 = \frac{1}{T \omega_n} \left[E^2(T \omega_n + 2\zeta) - 2\zeta C + \frac{(2\zeta^2-1)S}{\sqrt{1-\zeta^2}} \right].$$

These models can be converted into a recursive formula of the form

$$\ddot{y}_m = b_0 \ddot{y}_m + b_1 \ddot{y}_{m-1} + b_2 \ddot{y}_{m-2} - a_1 \ddot{y}_{m-1} - a_2 \ddot{y}_{m-2}, \quad (9)$$

where

$$a_1 = -2C,$$

$$a_2 = E^2,$$

$$b_0, b_1, b_2 \text{ as given above for the}$$

relative displacement model,
and for the absolute acceleration model.

The denominator has the same form as the impulse invariant simulations given in [2].

When the natural frequency is much less than the sample rate the filter weights become nearly integers i.e.,

$$b_0, b_1, b_2 \rightarrow 0$$

$$a_1 \rightarrow -2$$

$$a_2 \rightarrow 1.$$

The output of the filter can be found more accurately if written in the form

$$\ddot{y}_m = b_0 \ddot{x}_m + b_1 \ddot{x}_{m-1} + b_2 \ddot{x}_{m-2} + \ddot{y}_{m-1} + (\ddot{y}_{m-1} - \ddot{y}_{m-2}) - a'_1 \ddot{y}_{m-1} - a'_2 \ddot{y}_{m-2} \quad (10)$$

where

$$a'_1 = a_1 + 2 \quad (11)$$

$$a'_2 = a_2 - 1. \quad (12)$$

In this form

$$\ddot{y}_m = \ddot{y}_{m-1} + (\text{smaller terms}). \quad (13)$$

Incidentally, the formulas in [2] have the same problem and can be improved by writing them in a similar form. When the natural frequency is much less than the sample rate even double precision calculations will not yield accurate filter weights. The following approximations derived from a power series expansion of the formulas can then be used

$$a'_1 \sim 2\zeta\omega_n T + (\omega_n T)^2(1-2\zeta^2) \quad (14)$$

$$a'_2 \sim -2\zeta\omega_n T + 2\zeta^2(\omega_n T)^2 \quad (15)$$

absolute acceleration model

$$b_0 \sim \zeta\omega_n T + (\omega_n T)^2\left(\frac{1}{6} - \frac{2}{3}\zeta^2\right) \quad (16)$$

$$b_1 \sim \frac{2}{3}(\omega_n T)^2(1-\zeta^2) \quad (17)$$

$$b_2 \sim -\zeta\omega_n T + (\omega_n T)^2\left(\frac{1}{6} + \frac{4}{3}\zeta^2\right) \quad (18)$$

relative displacement model,

$$b_0 \sim (\omega_n T)^2/6 \quad (19)$$

$$b_1 \sim 2(\omega_n T)^2/3 \quad (20)$$

$$b_2 \sim (\omega_n T)^2/6. \quad (21)$$

The ramp invariant filters have one more weight than the impulse invariant filters. (For the impulse invariant filters $b_2=0$). The additional weight requires one more multiply add. Round off errors can cause the filter to be unstable when the natural frequency, ω_n , is small and the damping, ζ , is zero. This can be avoided by not using ζ exactly zero when the natural frequency is small compared to the sample rate.

For the proper calculation of the residual shock response spectra, the response must be calculated for a minimum of one full cycle after the input has ended. The number of samples in one cycle is the inverse of the non-dimensional frequency, $f_n T$. When $f_n T$ is small, this can be a large number of samples. An efficient way to avoid this problem is to reduce the sample rate when calculating the residual response for low natural frequencies.

The shock response spectra for the examples as in the impulse invariant section were calculated using the ramp invariant model as shown in Figs. 7 and 8. The spectra was computed with good accuracy over a non-dimensional frequency range, $f_n T$, of 10^{-4} to 2.0.

CONCLUSIONS

An efficient (requiring 5 multiply-adds per sample point) recursive formula for calculating the shock response spectra has been derived. The formula will give good results over a wide frequency range with a natural frequency of much less than the sample rate to many times the sample rate. The only requirement is that the input waveform is reasonably well band limited to less than the Nyquist frequency.

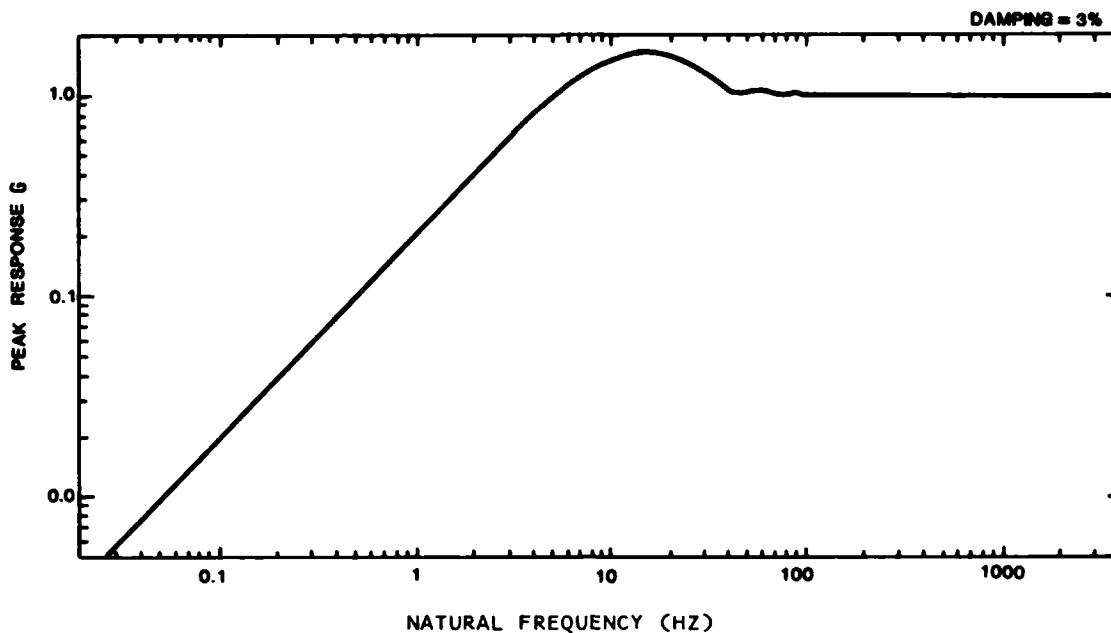


Fig. 7 Shock Response Spectra of a 64 ms Haversine with Unity Amplitude Sampled 2000 Samples/Sec using a Ramp Invariant Filter

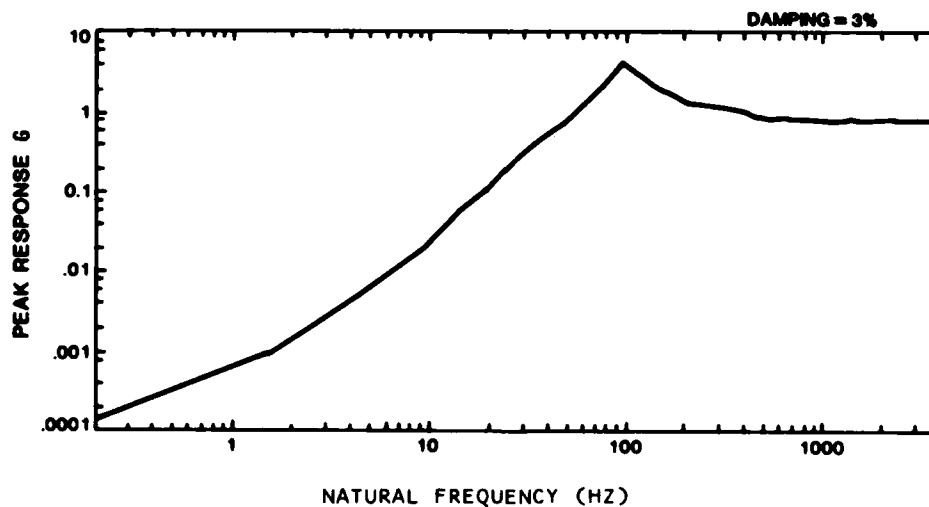


Fig. 8 Shock Response Spectra of a 100 Hz Decaying Sinusoid Sampled at 2000 Samples/Sec Using a Ramp Invariant Filter

REFERENCES

1. S.D. Stearns, Digital Signal Analysis, Hayden, Rochelle Park, NJ 1975
2. R.D. Kelly and G. Richman, Principals and Techniques of Shock Data Analysis, SVM-5, Sec. 6.7 Shock and Vibration

Information Center, Naval Research Laboratory, Washington, D.C. 1969

3. D.O. Smallwood and A.R. Nord, "Matching Shock Spectra with Sums of Decaying Sinusoids Compensated for Shaker Velocity and Displacement Limitations" Shock and Vibration Bulletin No. 44, Part 3, pp 43-56, Aug. 1974.

DISCUSSION

Mr. Rubin (The Aerospace Corp): Regarding the residual matter that you just described. An alternative procedure would be to develop the response and its first derivative at the last time of your input function and then you can predict what the peak will be and the residual immediately. You don't have to go through decimation or any further calculations at all. All you have to do is get the first derivative of the response. It is an initial value problem of free vibration and you can get the answer.

Mr. Smallwood: I agree. It is an alternate way to do it.

A FINITE ELEMENT MODEL FOR FAILURE INITIATION IN SHOCK LOADED STRUCTURAL MATERIALS

David W. Nicholson
Naval Surface Weapons Center
White Oak, Silver Spring, Maryland 20910

The present article reports the basic finite element equations governing the response of a material described by a recently published constitutive model for dynamically loaded ductile structural materials. The main feature of the model is the decomposition of the material response into rate sensitive flow and damage processes. The finite element treatment is based on several assumptions regarding the intraelement and interelement distributions of the flow and damage strains. The derived equations comprise a system of ordinary differential equations in time, requiring the specification of nine material parameters.

INTRODUCTION

In broad terms the work reported here concerns the prediction of structural failure under high dynamic loads, for example due to an explosive attack on a ship. The common approach has been to predict permanent structural deformation, using either empirical results or finite element structural analysis. Criteria based on the deflection magnitude have then been cited as grounds for anticipating the rupture of the structural material. The ultimate objective underlying the present work is to predict directly the onset and termination of the rupture process.

Unfortunately, classical fracture mechanics primarily concerns catastrophic crack propagation in brittle materials, and it does not genuinely address fracture initiation in the ductile structural materials used in various marine applications. To obviate this difficulty, we have formulated a special constitutive model [1]. Here we briefly describe the model and we present the mathematics for its implementation in a finite element code.

More concretely, the constitutive model describes two rate-dependent inelastic processes occurring in ductile structural materials: flow (plastic deformation) and damage

(nucleation, growth and coalescence of microvoids and microcracks). Three vector quantities with dimensions of displacement are to be determined by numerically integrating the time-dependent governing finite element equations: the nodal displacement vector $\underline{\zeta}_g$, the nodal flow parameter vector $\underline{\beta}_g$, and the nodal damage parameter vector $\underline{\gamma}_g$. The governing equations in finite element form are

$$\begin{aligned} M_g \ddot{\underline{\zeta}}_g + (K_{fg} + K_{dg}) \dot{\underline{\zeta}}_g \\ = \underline{P}_g + K_{fg} \underline{\beta}_g + K_{dg} \underline{\gamma}_g \end{aligned}$$

$$\begin{aligned} \dot{\underline{\beta}}_g = \eta_f \phi_f (\underline{\gamma}_g, \underline{\beta}_g) (2\mu \underline{\zeta}_g \\ - (2\mu + c_f) \underline{\beta}_g) \end{aligned}$$

$$\begin{aligned} \dot{\underline{\gamma}}_g = \eta_d \phi_d (\underline{\zeta}_g, \underline{\gamma}_g) (\kappa \underline{\zeta}_g \\ - (\kappa + c_d) \underline{\gamma}_g) \end{aligned}$$

Here M_g , K_{fg} , K_{dg} , ϕ_f and ϕ_d are matrices; \underline{P}_g is the vector of external forces; and η_f , η_d , c_f , c_d , κ and μ are positive material constants. The major

thrust of this paper is simply to sketch the derivation of the governing equations.

A finite element code applying the constitutive model to a rapidly loaded simply supported circular plate is currently being written and we expect to report computational results shortly. In this report, the present paper describes work in progress.

CONSTITUTIVE MODEL

As discussed in Ref. 1, under high loads ductile structural materials experience two inelastic processes: (a) flow, otherwise called plastic deformation, and (b) damage, comprising the nucleation, growth and coalescence of microvoids and microcracks. Further, both of these processes are dynamic in the sense that they are delayed (retarded). The appearance of a crack of significant size, representing the initiation phase of (macroscopic) fracture, corresponds to the accumulation of damage to a critical level.

The governing equations are given as follows.

$$\dot{e}_{ij}^f = \eta_f \langle \phi_f (F_f - k^f) \rangle \frac{\partial F_f}{\partial s_{ij}} \quad (1.1)$$

$$\dot{e}^f = 0 \quad (1.2)$$

$$\dot{e}_{ij}^d = \eta_d \langle \phi_d (F_d - k^d) \rangle \frac{\partial F_d}{\partial s} \quad (1.3)$$

$$\dot{e}_{ij}^d = 0 \quad (1.4)$$

Here e_{ij}^f and e^f are the deviatoric (shear) and isotropic parts of the flow strain ϵ_{ij}^f . Similarly, e_{ij}^d and e^d are the deviatoric and isotropic parts of the damage strain ϵ_{ij}^d . The total strain is the sum of the flow strain, the damage strain and the elastic strain, which is given in terms of the stress by Hooke's law. Formally

$$\epsilon_{ij} = \epsilon_{ij}^e + \epsilon_{ij}^f + \epsilon_{ij}^d \quad (2)$$

where

$$\sigma_{ij} = 2\nu \epsilon_{ij}^e + \lambda \epsilon_{kk}^e \delta_{ij}$$

for σ_{ij} the stress, δ_{ij} the Kronecker tensor, and μ and λ the Lamé coefficients.

Continuing, in Eq. 1, s_{ij} and s are the deviatoric and isotropic (hydrostatic) stresses; ϕ_f , ϕ_d , F_f and F_d are positive material functions; η_f , η_d , k^f and k^d are positive material constants; and the symbols $\langle \cdot \rangle$ are defined by

$$\langle \phi(\psi) \rangle = \begin{cases} \phi & \text{if } \psi \geq 0 \\ 0 & \text{if } \psi < 0. \end{cases}$$

The constitutive model embodies several features.

1. Inelastic strains are used as measures of flow and damage.

2. Flow is a deviatoric (hence volume conserving) process controlled by the deviatoric stress.

3. Damage is an isotropic (dilatational) process controlled by the isotropic stress.

4. Flow and damage are uncoupled.

5. The dynamic (retarded) nature of the flow and damage processes is accommodated by using rate equations with viscosity coefficients η_f and η_d .

6. Threshold conditions, analogous to yield conditions, are used to govern the onset and termination of flow and damage.

7. The fact that η_f and η_d are positive goes a long way to ensuring that both flow and damage are dissipative processes.

Simply speaking, the damage measure e^d represents the relative microvoid and microcrack volume. A macroscopic fracture initiation criterion is introduced in Ref. 1 based on damage strain accumulation to a critical level. Formally,

$$\max_x [e^d] \geq e^*$$

where x refers to points in the body under study.

FINITE ELEMENT FORMULATION

A. Equation of Equilibrium of an Element

For simplicity of illustration, we study the plane triangle shown in Fig. 1 and assume that the displacements u_x and u_y are distributed linearly in the element. Our argument follows the presentation of Ref. 2. Extension to more elaborate elements and displacement models is straightforward, although frequently tedious.

We introduce the nodal displacement vector $\underline{\zeta}$ for the element under study

$$\underline{\zeta} = \begin{Bmatrix} u_x^{(1)} \\ u_y^{(1)} \\ - \\ u_x^{(2)} \\ u_y^{(2)} \\ - \\ u_x^{(3)} \\ u_y^{(3)} \end{Bmatrix}$$

The displacement vector $\underline{u} = \{u_x \ u_y\}^T$ is now approximated according to

$$\underline{u} \sim \bar{\underline{u}} = DC \underline{\zeta} \quad (3.1)$$

where C is a constant matrix and D depends on x and y within the element, and where the superscript T denotes the transpose.

Using the usual kinematic relations, the strain $\underline{\epsilon} = \{\epsilon_{xx} \ \epsilon_{yy} \ \epsilon_{xy}\}^T$ may be written as

$$\underline{\epsilon} = B' * \underline{u}$$

where B' may be called the kinematic operator. Applying B' to $\bar{\underline{u}}$, we obtain an approximate strain $\bar{\underline{\epsilon}}$ according to

$$\underline{\epsilon} \sim \bar{\underline{\epsilon}} = B' * \bar{\underline{u}} = BC \underline{\zeta} \quad (3.2)$$

Here B is a matrix possibly depending on x and y (although not in this case).

Suppose now that the constitutive relation is

$$\underline{\sigma} = \Lambda(\underline{\epsilon}) \text{ where } \underline{\sigma} = \{\sigma_{xx} \ \sigma_{yy} \ \sigma_{xy}\}^T.$$

An approximation for the stress is now given by

$$\underline{\sigma} \sim \bar{\underline{\sigma}} = \Lambda(\bar{\underline{\epsilon}}) \quad (3.3)$$

For equilibrium of the element, the principle of virtual work may be stated in terms of true quantities as

$$\int_V \rho \ddot{\underline{u}}^T \delta \underline{u} dV + \int_V \underline{\sigma}^T \delta \underline{\epsilon} dV = \int_S \underline{\tau}^T \delta \underline{u} dV$$

Here, V is the element volume and S its surface area, $\underline{\tau}$ is the traction applied to the element boundary, ρ is the mass density, $\delta(\cdot)$ is the variational operator, and the superposed dot denotes differentiation with respect to time.

We assume this principle also applies to the approximate quantities:

$$\int_V \rho \bar{\ddot{\underline{u}}}^T \delta \bar{\underline{u}} dV + \int_V \bar{\underline{\sigma}}^T \delta \bar{\underline{\epsilon}} dV = \int_S \bar{\underline{\tau}}^T \delta \bar{\underline{u}} dS \quad (3.4)$$

Hereafter the overbars designating the approximations will not be displayed.

Upon substituting (3.1) into (3.4) the inertial term becomes $\underline{\zeta}^T M \delta \underline{\zeta}$ where M is the consistent mass matrix given by

$$M = \int_V \rho C^T D^T D C dV.$$

Similarly, the forcing term becomes $\underline{P}^T \delta \underline{\zeta}$ where \underline{P} is the consistent load vector given by

$$\underline{P} = \left[\int_S \bar{\underline{\tau}}^T D C dS \right]^T$$

But the second right hand term requires the use of the constitutive model, as discussed in the next section.

B. Application of the Constitutive Model

We first write $\underline{\sigma}$ and $\underline{\epsilon}$ in deviatoric and isotropic components as

$$\underline{\sigma} = \underline{s} + s\theta \quad \underline{\epsilon} = \underline{e} + e\theta$$

where θ is the vectorial counterpart of the Kronecker tensor. Elementary manipulation leads to

$$\underline{\sigma}^T \delta \underline{\varepsilon} = \underline{s}^T \delta \underline{e} + 3s \delta e$$

From the constitutive model

$$\underline{s} = 2\mu(\underline{e} - \underline{e}^f) \quad s = \kappa(e - e^d)$$

where $\kappa = 2\mu + 3\lambda$ is the bulk modulus. Consequently,

$$\begin{aligned} \underline{\sigma}^T \delta \underline{\varepsilon} &= 2\mu \underline{e}^T \delta \underline{e} + 3\kappa e \delta e \\ &\quad - 2\mu \underline{e}^f T \delta \underline{e} - 3\kappa e^d \delta e. \end{aligned} \quad (4.1)$$

By decomposing the kinematic operator in (3.2), we may find a matrix B_0 and a vector b such that

$$\underline{e} = B_0 C \underline{\zeta} \quad (4.2)$$

$$e = b^T C \underline{\zeta} \quad (4.3)$$

We now make a most important assumption, which we call the consistent inelastic assumption.

Namely, we assume that \underline{e}^f and e^d are distributed throughout the element in the same fashion as the corresponding parts of the total strain vector. Hence

$$\underline{e}^f = B_0 C \underline{\beta} \quad (4.4)$$

$$e^d = b^T C \underline{\gamma} \quad (4.5)$$

in terms of new unknown vectors $\underline{\beta}$ and $\underline{\gamma}$, hereafter called the flow and damage parameters. It now follows that

$$\begin{aligned} \int_V \underline{\sigma}^T \delta \underline{\varepsilon} dV &= \underline{\zeta}^T K_f \delta \underline{\zeta} + \underline{\zeta}^T K_d \delta \underline{\zeta} \\ &\quad - \underline{\beta}^T K_f \delta \underline{\zeta} - \underline{\gamma}^T K_d \delta \underline{\zeta} \end{aligned}$$

with

$$K_f = 2\mu \int_V C^T B_0 C dV$$

$$K_d = 3\kappa \int_V C^T b b^T C dV, \{b b^T\}_{ij} = b_i b_j.$$

The matrix $K_e = K_f + K_d$ is nothing but the ordinary stiffness matrix of linear elasticity.

The equilibrium equation for the element under study is now

$$M \ddot{\underline{\zeta}} + (K_f + K_d) \underline{\zeta} = \underline{P} + K_f \underline{\beta} + K_d \underline{\gamma}. \quad (5)$$

In the next section we apply the constitutive model to derive equations governing $\underline{\beta}$ and $\underline{\gamma}$.

C. Constitutive Equations in Finite Element Form

For simplicity of illustration, we use the constitutive relations

$$\dot{\underline{e}}^f = \eta_f < 1 - k^f/F_f > (\underline{s} - c_f \underline{e}^f) \quad (6.1)$$

$$F_f = \left[(\underline{s} - c_f \underline{e}^f)^T (\underline{s} - c_f \underline{e}^f) \right]^{1/2} \quad (6.2)$$

$$\dot{e}^d = \eta_d < 1 - k^d/F_d > (s - c_d e^d) \quad (6.3)$$

$$F_d = \left[(s - c_d e^d)^2 \right]^{1/2} \quad (6.4)$$

The flow relations (6.1, 6.2) comprise the Hohenemser-Prager viscoplasticity model with linear kinematic hardening [3]. Evidently, the relations (6.3, 6.4) are the counterparts for damage.

Recalling that

$$\underline{s} = 2\mu(\underline{e} - \underline{e}^f)$$

$$\underline{e}^f = B_0 C \underline{\beta}$$

$$\underline{e} = B_0 C \underline{\zeta}$$

we introduce the vector $\underline{\psi}_f$ by

$$\underline{\psi}_f = 2\mu \underline{\zeta} - (2\mu + c_f) \underline{\beta}$$

It follows that

$$B_0 C \dot{\underline{\beta}} = \eta_f < 1 - k_f/F_f > B_0 C \underline{\psi}_f.$$

Using integration over the volume of the element, we find

$$\dot{\underline{\beta}} = \eta_f K_f^{-1} L_f \underline{\psi}_f \quad (7.1)$$

where

$$L_f = 2\mu \int_V < 1 - k^f / \bar{F}_f > C^T B_O^T B_O C dv \quad (7.2)$$

For the sake of simplicity, we approximate \bar{F}_f as follows:

$$\begin{aligned} \bar{F}_f &\sim \bar{F}_f = \frac{1}{V^{1/2}} \left[\int_V F_f^2 dv \right]^{1/2} \\ &= \left[\underline{\psi}_f^T K_f \underline{\psi}_f / 2\mu V \right]^{1/2} \end{aligned} \quad (7.3)$$

Of course, numerical integration in (7.2) usually poses no problem. Substituting \bar{F}_f into (7.2) we find

$$L_f = < 1 - k^f / \bar{F}_f > K_f$$

and (7.1) becomes

$$\dot{\underline{\beta}} = \eta_f < 1 - k^f / \bar{F}_f > (2\mu \underline{\zeta} - (2\mu + c_f) \underline{\beta}) \quad (7.4)$$

By similar reasoning, for $\underline{\gamma}$ we may derive

$$\dot{\underline{\gamma}} = \eta_d < 1 - k^d / \bar{F}_d > (\kappa \underline{\zeta} - (\kappa + c_d) \underline{\gamma}) \quad (7.5)$$

$$\bar{F}_d = \left[\underline{\psi}_d^T K_d \underline{\psi}_d / 3\kappa V \right]^{1/2}$$

$$\underline{\psi}_d = \kappa \underline{\zeta} - (\kappa + c_d) \underline{\gamma}.$$

D. Global Equations

The previous sections concerned equilibrium of a given element. Here we consider equilibrium of a collection of elements. The element equations of equilibrium may be combined into a global equilibrium equation using two rules:

1. the elements sharing a node have the same values of $\underline{\zeta}$, $\underline{\beta}$ and $\underline{\gamma}$ at that node;

2. the vector sum of forces exerted at a node by the elements

sharing it is equal to the force applied externally at the node.

The global equilibrium equation now takes on the form

$$\begin{aligned} M_g \underline{\zeta}_g + (K_{fg} + K_{dg}) \underline{\zeta}_g \\ = \underline{P}_g + K_{fg} \underline{\beta}_g + K_{dg} \underline{\gamma}_g \end{aligned} \quad (8.1)$$

where the subscript g stands for global. In reality, it is seldom necessary to assemble the global system matrices explicitly.

A difficulty arises in stating the global form of the constitutive equations. In particular, in their present form the element constitutive equations (7.4) and (7.5) are not necessarily consistent with the requirement (1) for nodal continuity of $\underline{\beta}$ and $\underline{\gamma}$. To obviate this difficulty we use nodal averages over the elements sharing a node. For elements e we rewrite (7.4, 7.5) as

$$\dot{\underline{\beta}} = \phi_f^e (2\mu \underline{\zeta} - (2\mu + c_f) \underline{\beta})$$

$$\dot{\underline{\gamma}} = \phi_f^e (\kappa \underline{\zeta} - (\kappa + c_d) \underline{\gamma})$$

At node n introduce

$$\phi_f^n = \frac{1}{n_e} \sum \phi_f^e$$

$$\phi_d^n = \frac{1}{n_e} \sum \phi_d^e$$

where n_e is the number of elements sharing node n and summation is taken over these elements sharing node n.

The quantities ϕ_f^n and ϕ_d^n can now be assembled into global matrices Φ_f and Φ_d , to yield global constitutive equations in the form

$$\dot{\underline{\beta}}_g = \Phi_f (2\mu \underline{\zeta}_g - (2\mu + c_f) \underline{\beta}_g) \quad (8.2)$$

$$\dot{\underline{\gamma}}_g = \Phi_d (\kappa \underline{\zeta}_g - (\kappa + c_d) \underline{\gamma}_g) \quad (8.3)$$

The material parameters to be specified are: μ , κ , η_f , η_d , c_f , c_d , k^f , k^d and ρ

CONCLUSION

The present article formulates the mathematics underlying the finite element implementation of a constitutive model for fracture initiation in dynamically loaded ductile structural materials. One of the main features of the model is that it decomposes the material response into (uncoupled) flow and damage processes. The basic step in the finite element implementation is the consistent inelastic assumption in which the flow and damage strains are approximated in the same manner as the corresponding parts of the total strain. A nodal continuity requirement is imposed on the flow and damage parameters introduced by the constitutive inelastic assumption. The governing equations in finite element form, comprising a system of ordinary differential equations in time, are given by Eqs. 8.1, 8.2 and 8.3. A special purpose finite element code embodying the constitutive model is in preparation and it should soon lead to illustrative calculations on the deformation and rupture of a rapidly loaded simply supported circular plate.

REFERENCES

1. Nicholson, D. W., "Constitutive Model for Rapidly Damaged Structural Materials," to appear in *Acta Mechanica*
2. Zienkiewicz, O. C., The Finite Element Method, McGraw-Hill, 1977
3. Nicholson, D. W., and Phillips, A., "On the Structure of the Theory of Viscoplasticity," *Int'l J. Sol. Structures*, 1974

DISCUSSION

Voice: Could you describe what kind of an experiment you would do so that you could decompose the incremental stiffness into the damage and flow properties that you need to essentially fit the parameters in your equation?

Mr. Nicholson: I believe that the most likely method for doing that is to use the flat plate impact test results from Sandia or some place and attempt to back the stiffness matrices out of the actual measurements up to point of spall. There have been substantial numbers of tests at Sandia where flyer plates have struck each other causing a spalling process and some of these tests have gone short of the threshold of spalling. That is what you particularly want to look at. There have been examinations of the interior of these plates where void nucleation and growth was quite extensive. So here we have a situation of damage short of the event of coalescence and that is really what we have to examine. There have been empirically minded studies of that problem by Shockley, Seaman and others. I hope to take advantage of the more adhoc treatment of the data that these people have to see if I can state what the flow and damage stiffness matrices should be.

Mr. Pakstys (General Dynamics-Electric Boat): Were your second and third set of matrix equations non-linear?

Mr. Nicholson: They were mildly non-linear.

Mr. Pakstys: Do you have in mind some procedures for getting solutions?

Mr. Nicholson: Yes, I don't believe there is any basic problem with integrating these equations. That is not typical of large systems which are also non-linear.

Mr. Pakstys: You would just be marching in time?

Mr. Nicholson: That is right. It is just going to be marching in time. I hope I can get away with a primarily explicit method but I haven't succeeded yet.

Mr. Pakstys: So you are planning an explicit method?

Mr. Nicholson: Well I did try the Adams-Moulton and the Adams-Bashsmith type methods.

Mr. Pakstys: Have you tried it on one dimensional problems?

Mr. Pakstys: You haven't even tried it?

Mr. Nicholson: Right, but the Adams Bashworth method seemed to introduce instabilities and I think it was just a bad choice. I am attempting to prove the method I am using.

STUDY OF PENETRATION FORCES FOR SUPERSONIC WARHEAD DESIGNS

R. Hassett, J. C. S. Yang*, J. Richardson and H. Walpert
Naval Surface Weapons Center
Silver Spring, Maryland 20910

The purpose of this study was to generate penetration forces to evaluate several preliminary warheads designed to survive severe transient loading conditions at velocities up to 762 mps into water, ship targets, and a wide variety of land targets. A preliminary investigation into each of these mediums was conducted to determine which target medium presented the most difficult applied loading conditions to the warhead structure.

Results were obtained using various methods both analytical and semi-empirical for the expected range of peak deceleration loads experienced by the warhead as it penetrates water, earth and hull targets. The range in magnitude of the deceleration is large because it covers the wide range in diameters, weights, target materials and velocities under consideration. The ship hull penetration provides the most severe loading and therefore was selected as the design criteria for the warheads.

INTRODUCTION

The warhead must be designed to survive severe transient loading conditions at velocities up to 762 mps into water, ship targets, and a wide variety of land targets. A preliminary investigation into each of these mediums was conducted to determine which target medium presented the most difficult applied loading conditions to the warhead structure. The warheads considered were all designed with a blunt

nose (typically 0.6 times the maximum diameter of the warhead), weighed 226.8 or 317.5 kilograms, measured up to 152.4 centimeters in length and between 30.48 and 40.64 centimeters in diameter (see Fig. 1). Two materials were used, AISI 4340 Steel and Titanium 64. Terminal velocities considered were 457 and 762 meters per second.

1.5 CAL OBLIVE
80% BLUNT NOSE
PBXN 103 EXPLOSIVE
WEIGHTS: 226.7 & 317.5 KG TOTAL
MATERIALS: 4340 STEEL & 64 TITANIUM
DIMENSIONS: 40.64 CM x L & D x 152.4 CM

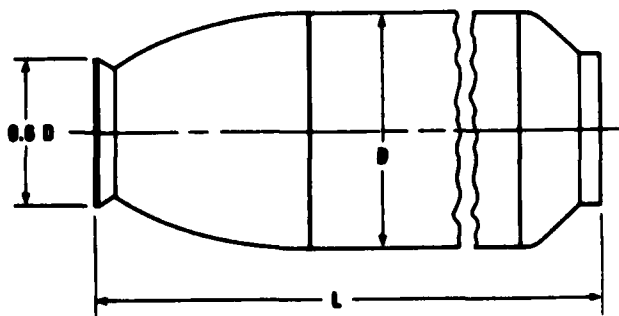


Figure 1: Warhead Design Features

*Consultant, Professor, Mechanical Engineering Dept., University of Maryland, College Park, MD 20742

Various methods, both analytical and semi-empirical, were used to determine the penetration loads on water, earth and ship targets.

* Water entry loads were obtained by analyzing the transient forces on flat disks during water entry. The resulting cavity from the blunt nose warhead is such that it, in essence, appears to be a flat disk as far as the water forces are concerned since the cavity clears the rest of the warhead.

* Earth penetration loads were obtained initially by using some simplified assumptions and empirical results from various experimental tests which were compared to the results obtained using the PENCO computer code. The PENCO computer code was developed by R. S. Bernard and D. C. Creighton, U.S. Army Engineer-Waterways Experiment Station, Vicksburg, Miss.

* Ship penetration loads were obtained using the DEFORM ballistic penetrator deformation model developed by Mr. Rodney Recht of the Denver Research Institute. This model is based on empirical data and DEFORM is a subroutine of the SPM (Ship Penetration Model) used at the David Taylor Naval Ship Research and Development Center, Carderock, Maryland.

Results were obtained for the expected range of peak deceleration loads experienced by the warhead as it penetrates water, earth and hull targets. The range in magnitude of the deceleration is large because it covers the wide range in diameters, weights, materials and velocities under consideration. The ship hull penetration provides the most severe loading and therefore was selected as the design criteria for the warheads.

WATER-ENTRY LOADS

Considerable empirical data are available in the literature regarding transient forces on flat disks during water entry (see Refs. 1 and 2). This data is applicable to all warhead configurations which have blunt nose similar to those in this study. The resulting cavity from this blunt nose is such that it in essence appears to be a flat disk as far as the water forces are concerned since the cavity clears the rest of the warhead.

The behavior of drag coefficient for disks during water-entry is illustrated in Fig. 2-a as a function of penetration distance and entry angle (θ) off the horizontal. It is the sum total of the steady-state drag coefficient which increases to a constant value as the nose becomes wetted and a transient term resulting from virtual mass behavior and effects. The peak drag coefficient as a function of (θ) has been plotted in Fig. 2-b. The peak axial drag force can be expressed as:

$$F_{D \text{ MAX}} = \frac{1}{2} \rho C_{D \text{ MAX}} A V_0^2$$

where

ρ = water density

A = area of blunt nose

V_0 = entry velocity

The peak loads and deceleration are given in Table 1 for a variety of conditions being considered.

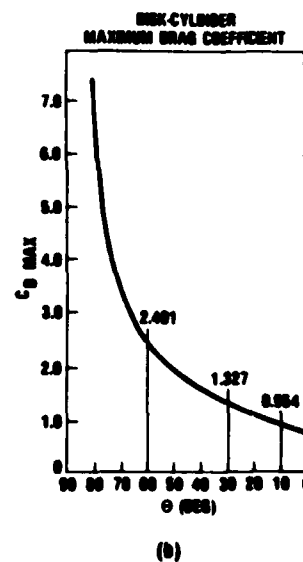
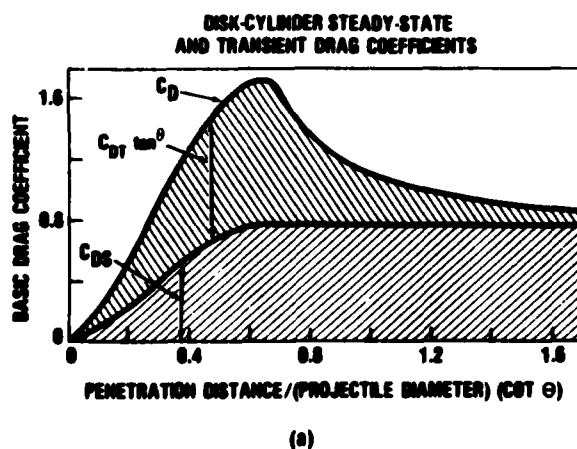


Figure 2: Drag Coefficients for Water Entry

Table 1
Peak Water-Entry Loads

WEIGHT (KG)	VELOCITY (M/SEC)	NOSE DIA (CM)	ENTRY ANGLE (DEGREES)	$C_D \text{ MAX}^1$	$F_D \text{ MAX}^2$ (x 10 DYNES)	a_{MAX} (G'S)
226.8	467.3	2.44	10	0.954	4.9	2157
			30	1.327	6.7	3000
			60	2.401	12.5	5637
	762.2	2.44	10	0.954	13.8	6111
			30	1.327	19.1	8500
			60	2.401	35.6	15933
317.5	467.3	2.44	10	0.954	4.9	1571
			30	1.327	6.7	2186
			60	2.401	12.5	4097
	762.2	2.44	10	0.954	13.8	4429
			30	1.327	19.1	6143
			60	2.401	35.6	11429

NOTES 1. $C_D \text{ MAX} = C_{Ds} + C_{Dt}$
 $= 0.79 + 0.93 \tan \theta$

2. $F_D \text{ MAX} = 1/2 (\rho C_D \text{ MAX}) A V^2$

EARTH-PENETRATION LOADS

Theoretical investigations into projectile impacts with earth-type targets are usually macroscopic penetration studies. The technique used is to assume an equation of motion for the projectile. The constants in this equation are determined by integrating and maximizing the resulting distance equation to yield a penetration depth. Expressing the penetration depth in terms of impact velocity yields an equation which can be fitted to experimentally gathered data.

A generalized equation of motion could be written in the following form:

$$-\frac{d^2 Z}{dt^2} = A + B \frac{dZ}{dt} + CZ + DZ \frac{dZ}{dt} + E \left(\frac{dZ}{dt}\right)^2$$

where Z is the distance along the penetration path.

The coefficients A, B, C, D, E depend on the target material properties, the penetrator geometry and the interaction parameters between penetrator and target material.

Once the mathematical model has been assumed, it is necessary to solve the equation and to express the depth of penetration, D_p , in terms of the impact velocity, V_0 , by substituting the proper boundary conditions:

$$\text{when } t = 0 : \frac{dZ}{dt} = V_0, D_p = 0$$

$$\text{when } Z = D_p : \frac{dZ}{dt} = 0$$

Some of the prediction techniques which predominantly depend on experimental penetration data for the evaluation of the constants are given in Table 2, with the equations for the depth of penetration. Evaluation of the constants used and further details may be found in Refs. 3 and 4.

Table 2
Earth Penetration Loads

GENERAL SEMI-ANALYTICAL:

$$-\frac{d^2 Z}{dt^2} = A + B \frac{dZ}{dt} + CZ + DZ \frac{dZ}{dt} + E \frac{dZ}{dt}^2$$

ROBIN-EULER:

$$\frac{d^2 Z}{dt^2} = A$$

$$D = \frac{V_0^2}{2A}$$

PONCELET:

$$-\frac{d^2 Z}{dt^2} = A + E \left(\frac{dZ}{dt} \right)^2$$

$$D = \frac{1}{2E} \ln \left(1 + \frac{E}{A} V_0^2 \right)$$

PETRY:

$$D = \frac{W}{A} K \log_{10} \left(1 + \frac{V_0^2}{19900} \right)$$

K = SOIL PENETRATION CONSTANT

RESAL:

$$-\frac{d^2 Z}{dt^2} = B \frac{dZ}{dt} + E \left(\frac{dZ}{dt} \right)^2$$

$$B = \frac{1}{E} \ln \left(1 + \frac{E}{B} V_0 \right)$$

ALLEN'S FORCE LAW:

$$-M_p \frac{d^2 Z}{dt^2} = A_0 + B_0 \frac{dZ}{dt} + E_0 \left(\frac{dZ}{dt} \right)^2$$

FOR $V > 305 \text{ M/SEC}$ $A_0 = E_0 = 0$

$$D = M_p (V_0 - C_1) \frac{1}{6 \rho V (\pi A)^{1/2} N_1}$$

PENCO COMPUTER CODE:

CAVITY EXPANSION ANALYSIS CORRECTED FOR
TARGET COMPRESSIBILITY

The equations of penetration were solved to provide the velocity and acceleration as a function of time (see Table 3). Typical constant values were used in these calculations and the results were used as inputs to check on

the validity of the subsequent PENCO penetration analysis. The PENCO compute code was selected as the baseline method for determining deceleration loading.

Table 3
Penetration Equation Solutions

<p><u>ROBINS-EULER:</u> $-\frac{d^2z}{dt^2} = A$ $V = V_0 - At$ $a = -A$</p>	
<p><u>PONCELET:</u> $-\frac{d^2z}{dt^2} = A + E \left(\frac{dz}{dt} \right)^2$ $V = \sqrt{A/E} \tan \left[\tan^{-1} V_0 \sqrt{E/A} - \sqrt{AE} t \right]$ FOR $A > 0$ $a = -A \left\{ 1 + \tan^2 \left[\tan^{-1} V_0 \sqrt{E/A} - \sqrt{AE} t \right] \right\}$ $V = V_0 / (1 + EV_0 t)$ FOR $A = 0$ $a = -EV_0^2 / (1 + EV_0 t)^2$</p>	
<p><u>PETRY:</u> $-\frac{d^2z}{dt^2} = E \left[19.98(10)^3 + \left(\frac{dz}{dt} \right)^2 \right]$ $V = 141.5 \tan \left[\tan^{-1} \frac{V_0}{141.5} - 141.5 Et \right]$ $a = -E \left\{ 19.98(10)^3 + (141.5)^2 \tan^2 \left[\tan^{-1} \frac{V_0}{141.5} - 141.5 Et \right] \right\}$</p>	
<p><u>RESAL:</u> $-\frac{d^2z}{dt^2} = B \frac{dz}{dt} + E \left(\frac{dz}{dt} \right)^2$ $V = B \left[e^{(Bt + c)} - E \right]^{-1}$ WHERE $c = \ln \frac{B + EV_0}{V_0}$ $a = -B^2 \left[e^{(Bt + c)} - E \right]^{-1} \left\{ 1 + E \left[e^{(Bt + c)} - E \right]^{-1} \right\}$</p>	

PENCO: COMPUTER CODE

Program PENCO analyzes the normal impact and penetration of rigid axisymmetric projectiles into layered targets. The projectile penetration theory used in the PENCO computer code for the earth materials is based on an analogy with the expansion of a spherical cavity in a Mohr-Coulomb material. The form of the projectile equation of motion is postulated in accord with empirical observations. However, the force coefficients are obtained directly from the cavity expansion analysis and are expressed in terms of standard engineering properties. The theory is used to make a number of after-the-fact calculations which are compared with full-scale test results.

PENCO uses this theory and incorporates a simple Newtonian integration scheme to solve the projectile equation of motion. The code requires inputs describing the penetrator, impact velocity, target material properties

and integration time step size. The output is transmitted to an external time history output file and includes the projectile's instantaneous velocity, depth, and deceleration, along with the maximum cavity diameter, at selected points in time between problem initialization and problem completion.

PENCO: RESULTS

Projectile penetration studies were conducted on seven warhead designs using the PENCO computer code for two sets of impact velocities, 762 mps and 457 mps. The warhead designs vary in material, steel and titanium, dimension and weight.

In the PENCO computer analysis, the projectiles are modeled as biconic penetrators (see Fig. 3). The blunt nose is obtained by setting the half angle of the nose equal to 90 degrees. The ogive section of the penetrator is approximated by a conical section with a straight line

drawn from the edge of the blunt nose to a point tangential to the profile of the penetrator. This is a reasonable estimation since the cavity expansion is not affected by the excavation behind the blunt nose. The parameters which describe the different projectiles are presented in Table 4. The properties of the soil used are given below:

p = Target mass density = 1.5 gm/cm^3

K = Effective bulk modulus =
 $= 5 \times 10^8 \text{ dynes/cm}^2$

I = Rigidity index = 50

$\phi_1 = \phi_2 = 30 \text{ degrees}$

$C_1 = C_2 = 1.38 \times 10^6 \text{ dynes/cm}^2$

Δ_{max} = Locking strain = 0.1

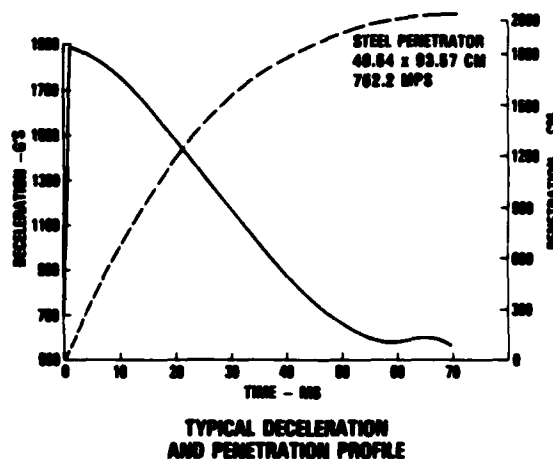
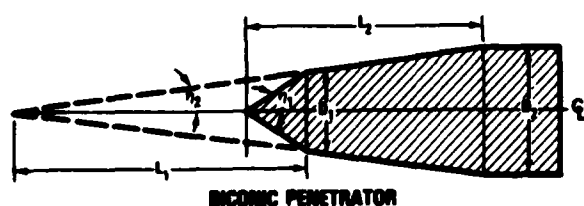


Figure 3
Biconic Penetrator

Table 4
Penetrator Parameters

MATERIAL	DIMENSION (CM)	WEIGHT (KG)	L_1 (CM)	L_2 (CM)	D_1 (CM)	D_2 (CM)	η_1 (DEG)	η_2 (DEG)	$\sin \eta$
STEEL	40.84 x 86.22	222.26	44.68	23.09	23.86	36.18	90	14.94	0.58
STEEL	40.84 x 89.59	312.98	41.15	25.40	23.92	36.88	90	16.21	0.55
STEEL	40.84 x 93.57	312.98	41.27	25.40	24.16	36.03	90	16.32	0.56
STEEL	30.87 x 152.4	317.52	33.20	16.93	16.43	28.89	90	15.49	0.57
STEEL	29.93 x 152.4	317.52	27.35	16.30	17.27	29.46	90	17.53	0.54
TITANIUM	28.23 x 152.4	226.80	32.90	20.32	17.27	27.94	90	14.71	0.54
TITANIUM	28.63 x 152.4	226.80	28.53	15.94	16.93	26.40	90	16.53	0.58

$$\sin \eta = \frac{D_1^2 \sin \eta_1 + (D_2^2 - D_1^2) \sin \eta_2}{D_2^2}$$

Results from the PENCO computer analysis on the maximum deceleration and penetration depth are summarized in Table 5.

Table 5
PENCO Analysis Results for Maximum Penetration and Deceleration

WARHEAD MATERIAL	WARHEAD DIMENSION (CM)	WARHEAD WEIGHT (KG)	MAX DECELERATION (G'S)	MAX PENETRATION (CM)
Vo = 457.3 MPS				
STEEL	40.64 x 66.22	222.2	1421	1015
STEEL	40.64 x 89.59	312.9	1167	1211
STEEL	40.64 x 93.57	312.9	1186	1193
STEEL	30.87 x 152.4	317.5	873	1944
STEEL	29.93 x 152.4	317.5	896	1892
TITANIUM	28.23 x 152.4	226.8	858	1581
TITANIUM	28.63 x 152.4	226.8	775	1718
Vo = 762.2 MPS				
STEEL	40.64 x 66.22	222.2	2264	1742
STEEL	40.64 x 89.59	312.9	1859	2084
STEEL	40.64 x 93.57	312.9	1890	2036
STEEL	30.87 x 152.4	317.5	1101	3275
STEEL	29.93 x 152.4	317.5	1136	3187
TITANIUM	28.23 x 152.4	226.8	1381	2675
TITANIUM	28.63 x 152.4	226.8	1255	2906

TARGET PENETRATION LOADS

DEFORM: COMPUTER CODE

The DEFORM subroutine from the Ship Vulnerability Model (SVM/D) program developed by the David Taylor Naval Ship Research and Development Center (DTNSRDC) and the Denver Research Institute (DRI) was used to analyze these designs for ship target penetration capability. The representative ship target illustrated in Fig. 4 consists of a 1.905 cm thick HY80 plate reinforced by a T-beam and angle member welded cross-ways on the back of the plate. Composite targets such as this are modeled in DEFORM as isotropic infinite flat plates of finite thickness. Extensive semi-analytical and empirical studies conducted at DRI indicate that blunt nose shapes at high velocities

will develop a shear plug during penetration of the plate with peak impact proportional to the mass of the plug. The worst case situation for the target in Fig. 4 would then be the section of the target where the reinforcing members cross and present the largest mass resistance. The mass of this plug was determined to be equivalent to a uniform plate thickness of 3.175 cm which was then used in these calculations.

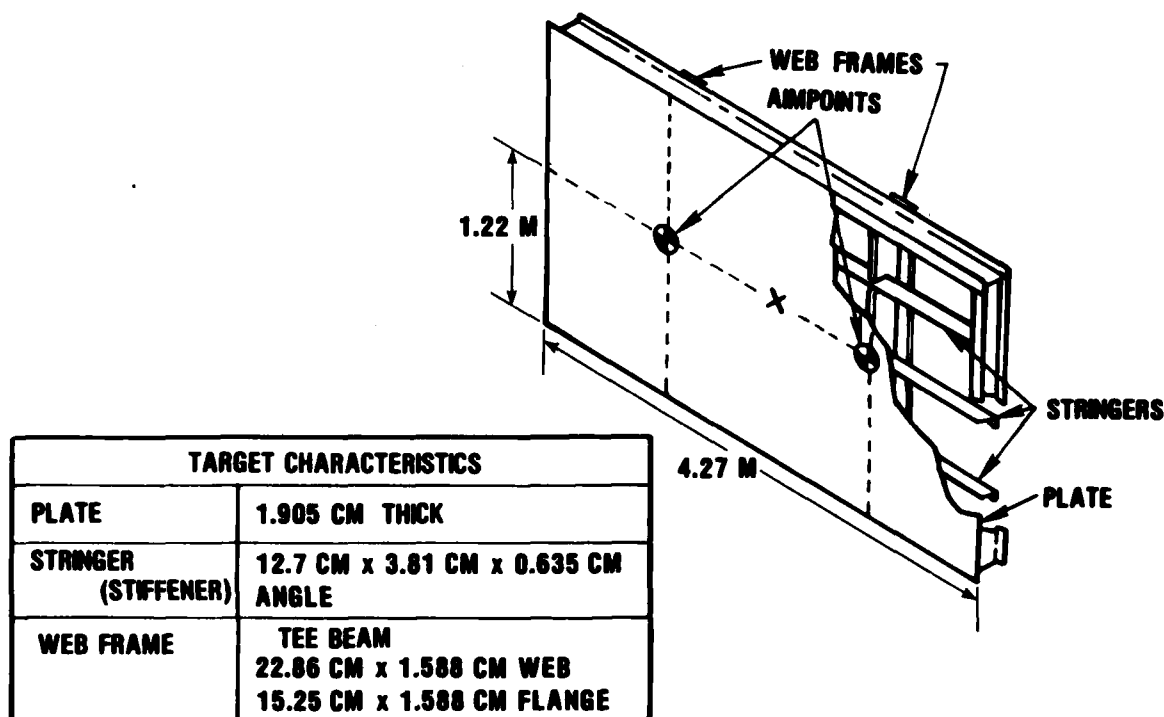


Figure 4
Standard Target

The DEFORM code evaluates stresses and strains in the casing wall at some arbitrary (selected) station, the explosive carried by the projectile and the bond (shear stress) between casing and explosive. The model will consider any nose shape which is axisymmetric (or can be represented by an axisymmetric shape). The penetrator deformation model will predict stresses and plastic strains (due to combined axial and flexural impact loading) in the penetrators. The model also evaluates the maximum g-loading experienced by the penetrator.

The model is empirical. It is based on actual tests of 40MM, and 8 inch projectiles, and Mk 82 bombs. The DEFORM model first predicts the strain based on velocity, plate thickness, diameter and shape of similar 40MM or 8 inch projectiles or Mk 82 bombs. The results are then scaled up to fit the penetrator in question. The stresses and forces are then derived from the strain and other geometric and material properties of the projectile. The stresses and loads predicted may be less accurate since they are deduced from the strain. This is why the strain prediction is used as the main criterion for design purposes.

The strain predictions are correlated with certain general descriptions of warhead

conditions after penetration. Gross deformations can be expected if the predicted strains are 0.25 cm/cm or higher. Functional behavior of the penetrator may be impaired when the predicted strains are above 0.03 cm/cm. A moderate amount of deformation of the walls can also be expected at strains above 0.10 cm/cm. Strains of 0.02 cm/cm or less correspond to ballistic penetrators with little or no damage due to plate penetration. Thus, by designing to a certain strain level, the designer can choose an acceptable damage level for a particular application.

It should be noted that stresses and strains due to axial loading are invalid aft of the station at which maximum deformation occurs. Aft of this point the loads in the warhead will be lower than those predicted by the model. This is due to the shock mitigation (energy absorbed) by the projectile while being deformed.

The model evaluates the maximum value of the resisting force and considers it to be acting at a specific location near the nose; it does not define force magnitude and location as a function of time. Hence, in the immediate vicinity of the nose, the model is not capable of defining bending moments accurately; at stations farther aft this is not a problem.

Fortunately, bending moments are minimal near the nose (where axial loading is maximal) and prediction accuracy does not suffer greatly.

The DEFORM Code provides for modeling a full diameter flat blunt nose or a conical nose but it is not possible to describe the subcalibre flat blunt followed by an ogive used as the warhead shape. To get around this, the warhead was input to DEFORM as if it were the same diameter as the blunt penetrator plate for purposes of calculating loads. The plugging load during hull penetration with the

penetrator plate is significantly higher than the load when the ogive section impacts the hull because the material will petal. Also since these loads do not occur simultaneously, this was considered a realistic design approach.

The material property inputs to the DEFORM code are given for the titanium and steel warheads in Table 6. The final configuration for the steel warheads used a maximum strain of 0.02 cm/cm as the design criteria. The titanium warhead used 0.01 cm/cm/ These values present reasonable structural deformations based on extensive data obtained by DRI.

Table 6
Material Properties Input Into
DEFORM

PROPERTY	STEEL AISI4340	TITANIUM 64 (8% AL, 4% V _o)	EXPLOSIVE PBXN-103
DENSITY	7.834 GM/CM ³	4.706 GM/CM ³	1.855 GM/CM ³
YOUNG'S MODULUS	2.07 x 10 ¹² DYNES/CM ²	1.103 x 10 ¹² DYNES/CM ²	0.689 x 10 ¹² DYNES/CM ²
POISSON'S RATIO	**	**	0.19
DYNAMIC YIELD (COMPRESSION)	- 1.476 x 10 ⁴ KG/CM ²	1.406 x 10 ⁴ KG/CM ²	
WORK-HARDENING COEF	1.828 x 10 ⁴ KG/CM ²	1.624 x 10 ⁴ KG/CM ²	
ULTIMATE STRENGTH	1.125 x 10 ⁴ KG/CM ²	1.09 x 10 ⁴ KG/CM ²	
SHEAR STRENGTH OF METAL-EXPLOSIVE BOND			6.89 x 10 ⁶ DYNES/CM ²
HARDNESS	*		TARGET 240
TARGET THICKNESS			1.905 CM

- * COMPUTED FROM DYNAMIC YIELD AND WORK-HARDENING COEF.
- ** DEFORM HAS VALUE FOR STEEL INTERNAL TO CODE

SUMMARY

The expected range of peak deceleration loads experienced by the warhead as it penetrates water, earth and hull targets are summarized in Table 7. The methods used to determine these loads were described in the preceding sections of this report. The range in magnitude of the deceleration is so large because it covers the range in diameter, weight

and velocity under consideration, and for the case of earth penetration it covers the variation due to the different theories applied. Of the cases analyzed, the ship hull penetration provided the most severe loading condition. Thus, the hull penetration load was selected as the design criteria for the warheads.

Table 7
Penetration Studies

<u>MEDIUM</u>	<u>BASIS OF STUDY</u>	PEAK DECELERATION (G'S)	
		V_0 (MPS)	
		457.3	762.2
WATER	EMPIRICAL (30° IMPACT ANGLE)	2200-3000	6140-8500
SOIL	SEMI-ANALYTIC	1450-8680	2880-17300
	ANALYTIC	670-1420	1100-2260
SHIP TARGET	EMPIRICAL	13000 —	30000

REFERENCES

1. Baldwin, J. L., "An Experimental Investigation of Water Entry," Ph.D. Thesis, U. of Maryland, (1972).
2. May, A., "Forces at Water Impact," Alden Research Laboratory (U.S.) Report, 119-72/SP (1972).
3. Hadala, P. F., "Evaluation of Empirical and Analytical Procedures Used for Predicting the Rigid Body Motion of an Earth Penetrator," Paper S-75-15, U.S. Army Engineer Waterways Experiment Station, Vicksburg, Miss., June 1975.
4. R. Hassett and J. Yang, "The Effect of the Nose Shape on the Penetration on Small Scale Mk 82 Bombs in Soil," Report TR70-261, 1970, Naval Ordnance Laboratory.